

UNITED STATES AIR FORCE
SUMMER RESEARCH PROGRAM -- 1995
GRADUATE STUDENT RESEARCH PROGRAM FINAL REPORTS

VOLUME 10B
WRIGHT LABORATORY

RESEARCH & DEVELOPMENT LABORATORIES
5800 Uplander Way
Culver City, CA 90230-6608

Program Director, RDL
Gary Moore

Program Manager, AFOSR
Major David Hart

Program Manager, RDL
Scott Licoscos

Program Administrator, RDL
Gwendolyn Smith

Reproduced From
Best Available Copy

Submitted to:

19981218 143

AIR FORCE OFFICE OF SCIENTIFIC RESEARCH
Bolling Air Force Base
Washington, D.C.
December 1995

PREFACE

Reports in this volume are numbered consecutively beginning with number 1. Each report is paginated with the report number followed by consecutive page numbers, e.g., 1-1, 1-2, 1-3; 2-1, 2-2, 2-3.

Due to its length, Volume 10 is bound in two parts, 10A and 10B. Volume 10A contains #1-20, and Volume 10B contains reports #21-37. The Table of Contents for Volume 10 is included in both parts.

This document is one of a set of 16 volumes describing the 1995 AFOSR Summer Research Program. The following volumes comprise the set:

<u>VOLUME</u>	<u>TITLE</u>
1	Program Management Report <i>Summer Faculty Research Program (SFRP) Reports</i>
2A & 2B	Armstrong Laboratory
3A & 3B	Phillips Laboratory
4	Rome Laboratory
5A, 5B, & 5C	Wright Laboratory
6A & 6B	Arnold Engineering Development Center, Wilford Hall Medical Center and Air Logistics Centers <i>Graduate Student Research Program (GSRP) Reports</i>
7A & 7B	Armstrong Laboratory
8	Phillips Laboratory
9	Rome Laboratory
10A & 10B	Wright Laboratory Arnold Engineering Development Center, Wilford Hall Medical Center and Air Logistics Centers <i>High School Apprenticeship Program (HSAP) Reports</i>
11	Arnold Engineering Development Center, Wilford Hall Medical Center and Air Logistics Centers
12A & 12B	Armstrong Laboratory
13	Phillips Laboratory
14	Rome Laboratory
15A&15B	Wright Laboratory
16	Arnold Engineering Development Center

GSRP FINAL REPORT TABLE OF CONTENTS**i-xiv**

1. INTRODUCTION	1
2. PARTICIPATION IN THE SUMMER RESEARCH PROGRAM	2
3. RECRUITING AND SELECTION	3
4. SITE VISITS	4
5. HBCU/MI PARTICIPATION	4
6. SRP FUNDING SOURCES	5
7. COMPENSATION FOR PARTICIPATIONS	5
8. CONTENTS OF THE 1995 REPORT	6

APPENDICES:

A. PROGRAM STATISTICAL SUMMARY	A-1
B. SRP EVALUATION RESPONSES	B-1

GSRP FINAL REPORTS

Design of a Fuzzy Logic Controller

**Vikas Mehrotra
Graduate Student
Department of Electrical Engineering**

(until June 1995)
**The Ohio State University
2015 Neil Avenue
Columbus, OH 43210**

(starting September 1995)
**Massachusetts Institute of Technology
MIT Room 38-444
Cambridge, MA 02139**

**Final Report for:
Summer Graduate Student Research Program
Wright Laboratory**

Sponsored by:

**Air Force Office of Scientific Research
Bolling Air Force Base, DC**

and

Wright Laboratory

August 1995

Design of a Fuzzy Logic Controller

Vikas Mehrotra
Graduate Student
Department of Electrical Engineering
The Ohio State University
Massachusetts Institute of Technology

Abstract

A fuzzy logic controller is designed using the Comdisco Signal Processing Worksyste (SPW) software package developed by the Alta Group of Cadence Design Systems, Inc. The design is done using block diagram descriptions of the various components with mathematical and logic functions. Each entity in the design is linked via a heirarchical structure, which is used as part of the complete design. The hardware description language code is generated for each entity, as well as for the entire fuzzy controller. This code is then used with Synopsys to synthesize and optimize the circuit, which will be used in the fabrication of an integrated circuit chip.

The fuzzy controller presented here takes two input variables, error and change of error, and performs the fuzzification using seven triangular membership functions. The fuzzy set centers may be adjusted by the user for both the inputs and the output, but the rule base is fixed for each design. The controller has been successfully simulated in Comdisco for selected inputs. It is first designed with floating point blocks and then converted to fixed point for hardware description language code generation.

Design of a Fuzzy Logic Controller

Vikas Mehrotra

1 Introduction

Fuzzy logic is a method of control that uses imprecise information [1]. It is very useful when a mathematical model does not exist or is too complicated to develop. This is especially true for nonlinear systems. A conventional controller, on the other hand, uses specific information about the system and therefore requires a model. There are at least two advantages of using fuzzy logic in solving control problems. The first is that a precise mathematical model is not needed. The second is that the fuzzy controller is insensitive to small plant changes. Whereas conventional controllers may cause a system to become unstable due to minor variations in the plant parameters, a controller based on fuzzy logic is less likely to become unstable.

2 Basics of Fuzzy Logic

A fuzzy logic controller takes a numerical input, converts it into fuzzy sets, processes the information using a rule base, and then converts the fuzzy output into a crisp numerical value [1]. An important part of using fuzzy logic is to choose the control variables. These are the variables that are used in controlling the process.

The range over which the input variables vary is broken down into control regions whose complete range is called a fuzzy set. The input variables are classified using linguistic names instead of actual values. These linguistic names are the regions of the fuzzy sets. The regions are approximate and they overlap, so a single value of input may be placed into two regions. The amount that a

variable belongs to a certain region is given by its degree of membership. Once the input is fuzzified, a rule base is used to determine the fuzzy output. This rule base consists of if-then statements, and the output depends on where the inputs belong in the fuzzy sets. To get a crisp value at the output, a weighted average method is used in the defuzzification process.

2.1 Design Method

The steps required for the entire process are given below.

1. Fuzzification

In this step, the input control variables are broken down into fuzzy regions or fuzzy sets. The inputs are classified by their corresponding degrees of membership in each region.

2. Rule Base

A rule base, or inference engine, is then used to decide which rules are fired. This rule base is decided by the user and may require some knowledge of the process to be controlled.

3. Defuzzification

In the defuzzification process, the combined degree of membership is found by the product of the degrees of memberships of all the variables. This is known as the sum of products method.

4. Crisp Output

A crisp numerical value for the output is calculated by multiplying the combined degrees of memberships with the center values of the rules that are fired, adding them together, and finally dividing by the total degree of membership. This is known as the weighted average method. Note that the total degree of membership will always be equal to 1 if the inputs are scaled between -1 and 1.

2.2 Fuzzy Logic Example

To get a better understanding of how fuzzy logic works, let's take a look at an example of a fuzzy proportional plus derivative (PD) controller. Let there be two control variables called *error* and *change of error*. For simplicity, define the 7 fuzzy membership function centers to be equally distributed for error, change of error, and the output. Figure 1 shows the membership functions for equally distributed ranges. The regions are referred to as follows:

NL = negative large, NM = negative medium, NS = negative small, ZR = zero, PS = positive small, PM = positive medium, PL = positive large.

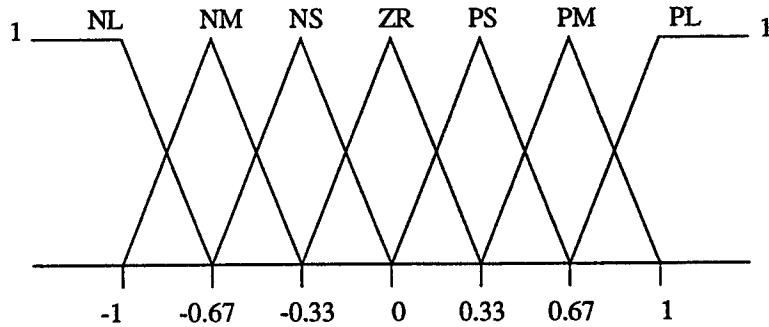


Figure 1: Membership functions

For this example, let the inputs be *error* = 0.50 and *change of error* = -0.25. Let the membership function centers be $NL=-1$, $NM=-\frac{2}{3}$, $NS=-\frac{1}{3}$, $ZR=0$, $PS=\frac{1}{3}$, $PM=\frac{2}{3}$, and $PL=1$. Note that since the inputs and the output are normalized, the degrees of membership for the NL and PL are 1 for inputs extending beyond -1 or 1. Let the rule base be defined as given in Table 1.

Follow the steps given below:

1. Fuzzification

Find the degrees of membership using the functions given in Figure 1.

Figures 2 and 3 show how this is done for the error and change of error.

		Error						
		NL	NM	NS	ZR	PS	PM	PL
NL	NL	NL	NL	NL	NM	NS	ZR	
NM	NL	NL	NL	NM	NS	ZR	PS	
Change of Error	NS	NL	NL	NM	NS	ZR	PS	PM
Error	ZR	NL	NM	NS	ZR	PS	PM	PL
PS	NM	NS	ZR	PS	PM	PL	PL	
PM	NS	ZR	PS	PM	PL	PL	PL	
PL	ZR	PS	PM	PL	PL	PL	PL	

Table 1: Rule base

- error – 50% PS, 50% PM
- change of error – 75% NS, 25% ZR

2. Rule base

Using the rule base given in Table 1, decide which rules will be fired. There are only 2 input variables, so there can be a maximum of 4 rules fired for a single input since there are only 4 combinations. For this example, the rules are summarized below.

If error is PS and change of error is NS, then output is ZR.

If error is PS and change of error is ZR, then output is PS.

If error is PM and change of error is NS, then output is PS.

If error is PM and change of error is ZR, then output is PM.

3. Defuzzification

Find the combined degrees of membership using the sum of products method as given in Table 2. The combined membership is given as the product of the error and change of error memberships.

4. Crisp Output

To get the final numerical output, multiply the combined degrees of mem-

Error Mem.	Change of Error Mem.	Combined Mem.
0.50 PS	0.75 NS	0.375 ZR
0.50 PS	0.25 ZR	0.125 PS
0.50 PM	0.75 NS	0.375 PS
0.50 PM	0.25 ZR	0.125 PM

Table 2: Combined degrees of memberships at the output

berships by their corresponding output centers, add them, and divide by the sum of the degrees of memberships. Since the inputs are normalized, the total degree of membership will always be 1. This step is shown below in Equations 1 and 2.

$$output = \frac{(0.375)(0) + (0.125)(\frac{1}{3}) + (0.375)(\frac{1}{3}) + (0.125)(\frac{2}{3})}{0.375 + 0.125 + 0.375 + 0.125} \quad (1)$$

$$output = 0.25 \quad (2)$$

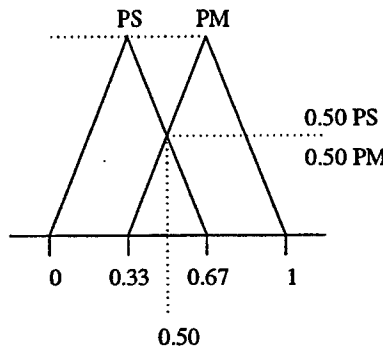


Figure 2: Degrees of membership for error

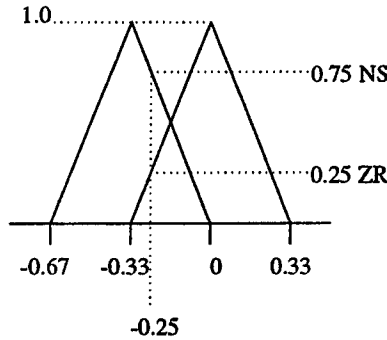


Figure 3: Degrees of membership for change of error

3 Floating Point Block Diagram Implementation

The block diagram implementation of the fuzzy controller has been simulated successfully using the Comdisco Signal Processing Worksystem (SPW) software package [2]. The design presented here consists of floating point inputs and floating point blocks.

3.1 Membership Function Generator

Figure 4 shows a membership function generator. This is a slight modification of the design given in [3]. The output is given as the degree of membership of the input variable for a particular membership function. The description of the comparators and the control switch is given as follows:

- Comparator 1
 $out = 1$ if $x \geq 0$ else $out = 0$
- Comparator 2
 $out = \max(x, 0)$

- Control switch

$$y = x_1 \text{ if } control = 0 \text{ else } y = x_2 \text{ if } control = 1$$

3.2 Description of Membership Function Generator

The inputs are the incoming signal, the constants 0 and 1, and the centers of the region for which the degree of membership is to be calculated as well the centers of the regions on both sides.

The input A represents the center of the region for which the degree of membership is being calculated. Except for NL and PL, inputs B and C are the centers of the regions to the right and to the left of the region for which the degree of membership is being calculated, respectively. For NL and PL, inputs B and C are both equal to the centers of the regions NM and PM, respectively.

Comparator 1 is used to decide whether the input is to the right or left of the center of the membership function. This information is used at the input of the control switch. The slope is chosen from the control switch based on the output of comparator 1. The difference between the input and the fuzzy set center is multiplied by the appropriate slope. To get the degree of membership, an adder is used to shift this result to get a membership between 0 and 1. Comparator 2 returns zero if the the degree of membership is less than or equal to zero.

3.3 Input Centers

To obtain the degree of membership in any region for a particular input, 7 such function generators must be connected. The input centers A, B, and C for the complete membership function generator are shown below in Table 3.

3.4 Fuzzy Logic Controller

The complete system using the fuzzy logic method described in the previous section is built on the Designer Block Diagram Editor (BDE) portion of Comdisco

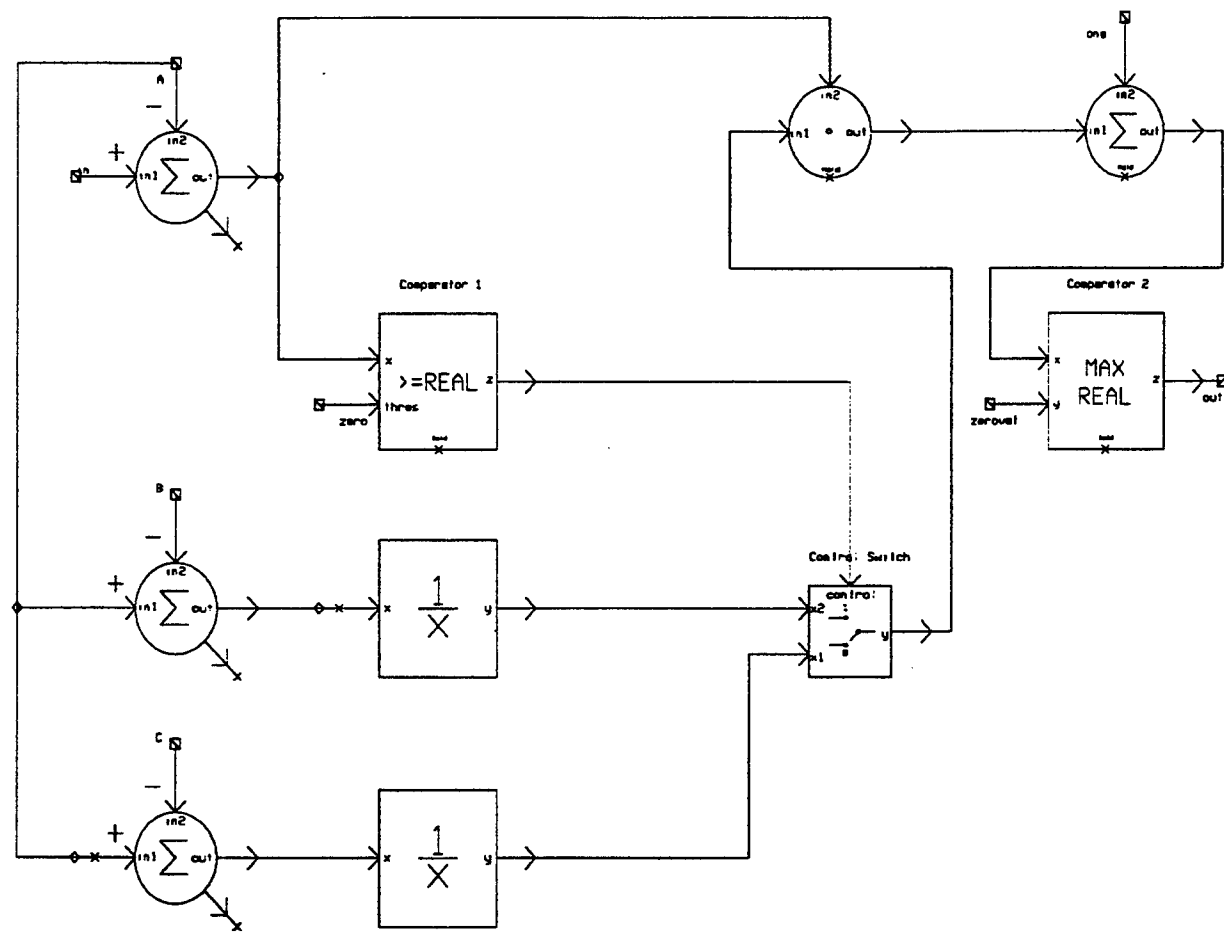


Figure 4: Membership function generator

Region	A	B	C
NL	NL	NM	NM
NM	NM	NS	NL
NS	NS	ZR	NM
ZR	ZR	PS	NS
PS	PS	PM	ZR
PM	PM	PL	PS
PL	PL	PM	PM

Table 3: Input Centers

and shown in Figure 5. This is also similar to the design given in [3]. The top left corner represents the membership function generator for the error input, and the bottom left corner represents the membership function generator for the change of error input. Each block labeled mfg is one membership function and represents the block diagram shown in Figure 4. There are seven outputs from both membership function generators, representing the degrees of memberships in each of the regions. The center of the block diagram contains 49 multipliers to calculate all the combined degrees of memberships. Moving one step to the right, the outputs of the multipliers are added in accordance with the rule base and multiplied with their corresponding output centers. To get the numerical output, the results of these multipliers are then added together. The only disadvantage with this design is that the rule base must be chosen before the circuit is designed. On the other hand, the membership function centers may be changed anytime as necessary. Note that although “wire” is not used to connect the outputs of the membership function generators to the inputs of the multipliers, the signals are connected using “connectors” even though they do not appear to be connected. The same method is used to connect the outputs of the multipliers to the inputs of the adders at the right of the figure.

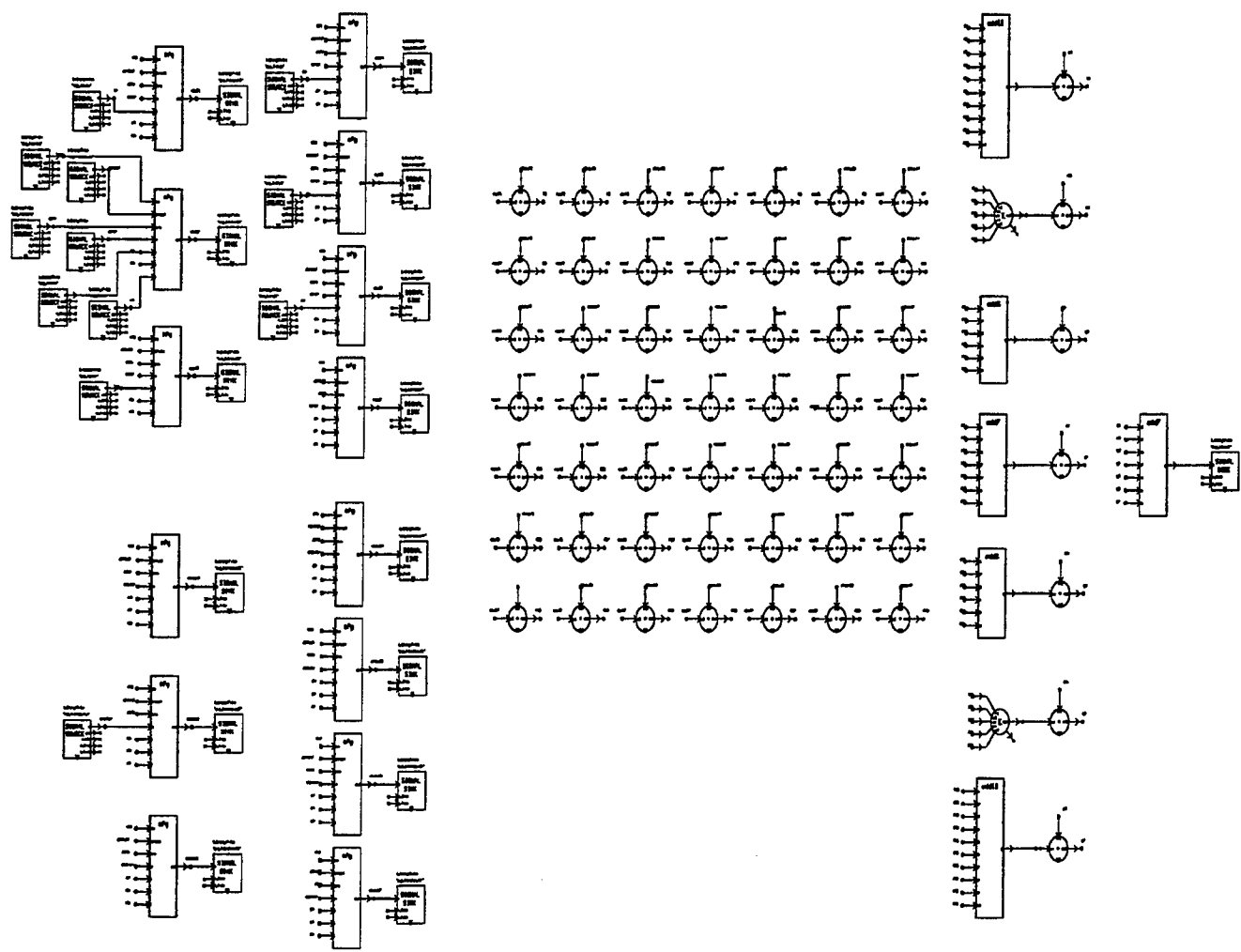


Figure 5: Floating point description of fuzzy logic controller

4 Results

The fuzzy logic controller design has been tested using the Signal Calculator portion of Comdisco. To test the example given above, let's choose the error to be 0.50 and change of error to be -0.25. The output is 0.25 again and shown in Figure 6. As another example, consider the output when both the error and the change of error are varied from -1 to 1 simultaneously. The output should be zero when both the error and change of error are zero, and the magnitude of the output should be largest at the endpoints. This result is shown in Figure 7.

5 Fixed Point Implementation using HDS

5.1 Hardware Design System

The design given above needs to be converted to fixed point blocks so that the VHSIC hardware description language (VHDL) code may be generated. This can then be used with the Synopsys [4] software package to synthesize the circuit. To do this, the Hardware Design System (HDS) package [5] available on Comdisco will be used. The inputs are chosen to be of the form $<12,4,t>$, where 12 is the number of total bits, 4 is the number of integer bits, and t is the two's complement representation.

5.2 Modifications

Some of the blocks that were used in the floating point design will have to be changed since they are not available on HDS. These include the reciprocator and the comparator 2 blocks. The reciprocator is first replaced by a divider circuit. Comparator 2 is replaced by comparator 1 and a control switch. The block diagram for this is shown in Figure 8.

However, the VHDL link does not support even the divider circuit. The membership function generator is further modified by eliminating the 2 sub-

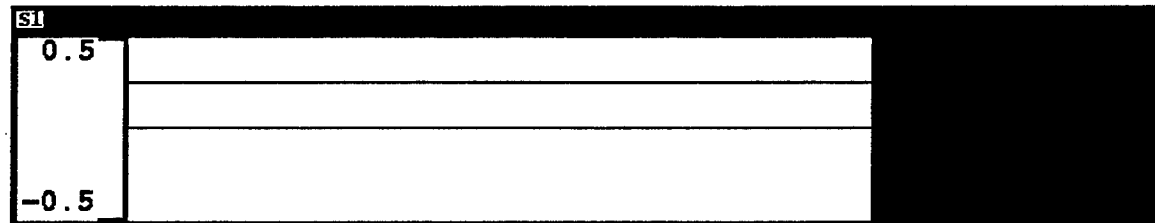


Figure 6: Output from example given above

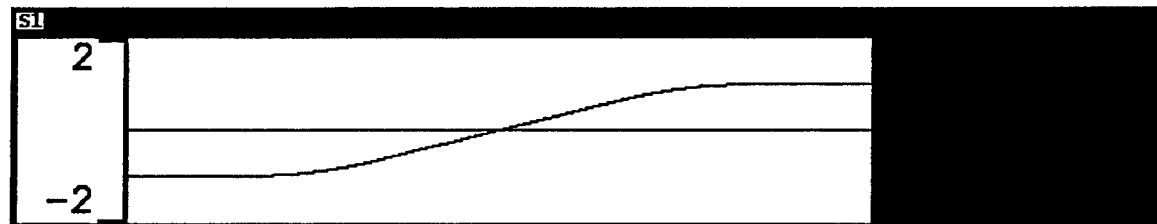


Figure 7: Output with varying the error and change of error from -1 to 1

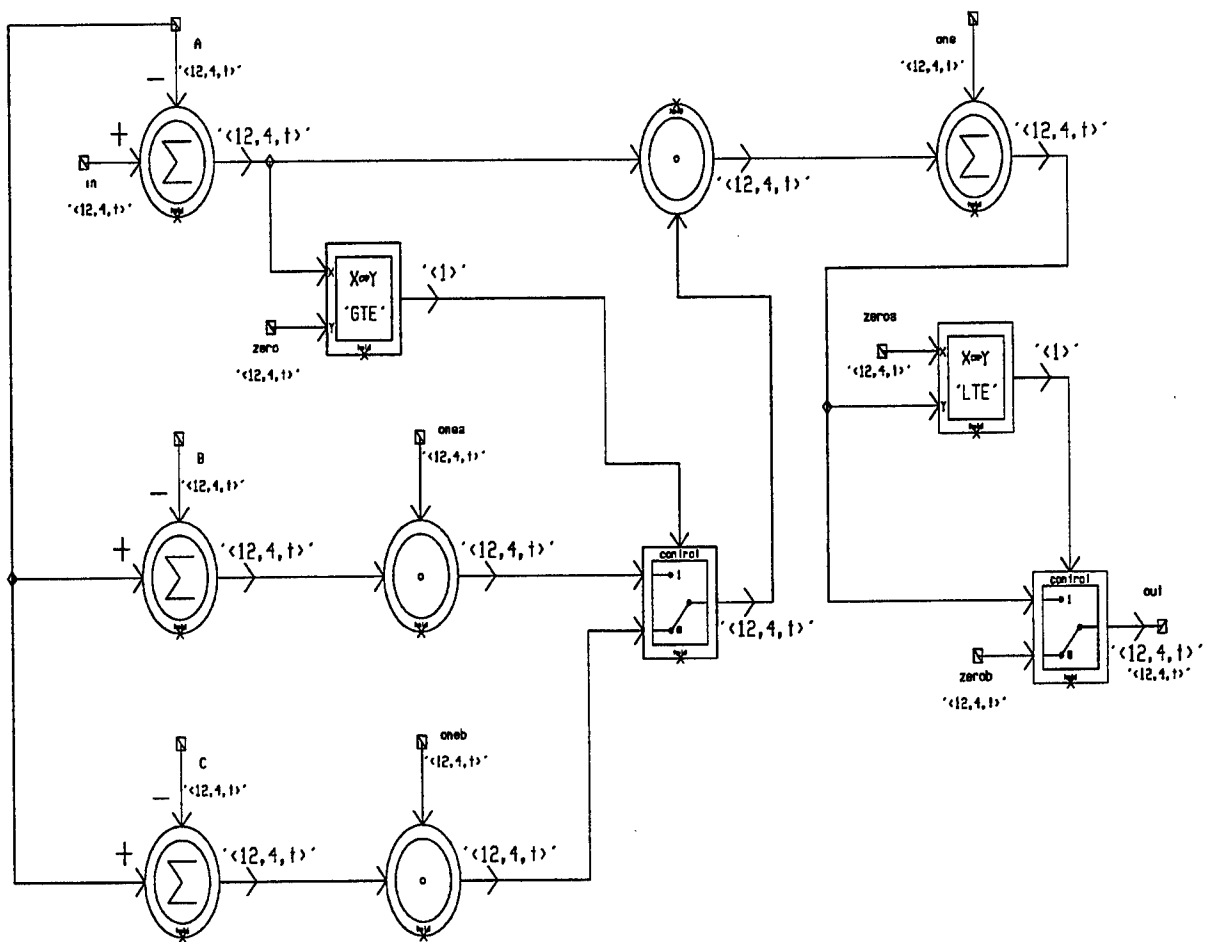


Figure 8: First modification of membership function generator

tractors and 2 dividers. These values must be calculated and input by the user. For a particular simulation, though, these are just constants that must be calculated only once. The membership function generator used in the fixed point design is given in Figure 9.

To generate the VHDL code for Synopsys, there are 3 hierarchical stages into which the design must be divided. The membership function generator and the adders and multipliers are referred to submodules. The code must first be generated for each of these separately. Then all of the submodules must be connected and linked together into a group. This is the next level in the hierarchy. Finally, the testbench model is composed of the group, along with the signal sources and sinks. The group and the testbench models are shown in Figures 10 and 11, respectively. The design presented here has been synthesized successfully in Synopsys.

To compare the two designs, the error and change of error are varied between -1 and 1 again. The same result is obtained for the fixed point design as for the floating point design whose result is shown in Figure 7.

6 Conclusion

A fuzzy logic controller has been designed and tested on Comdisco using the BDE and Signal Calculator. The design proposed in [3] has been used with minor modifications. The results from this design were found to be as expected. The advantage of using the Comdisco software package is that only a functional description of the circuit is required. By using mathematical and logical descriptions of the components used in the design, one can get an idea of how the circuit will function before actually proceeding with the circuit design.

Another advantage of using Comdisco is that the hardware description language code is generated from HDS. This is very useful for circuit synthesis in Synopsys.

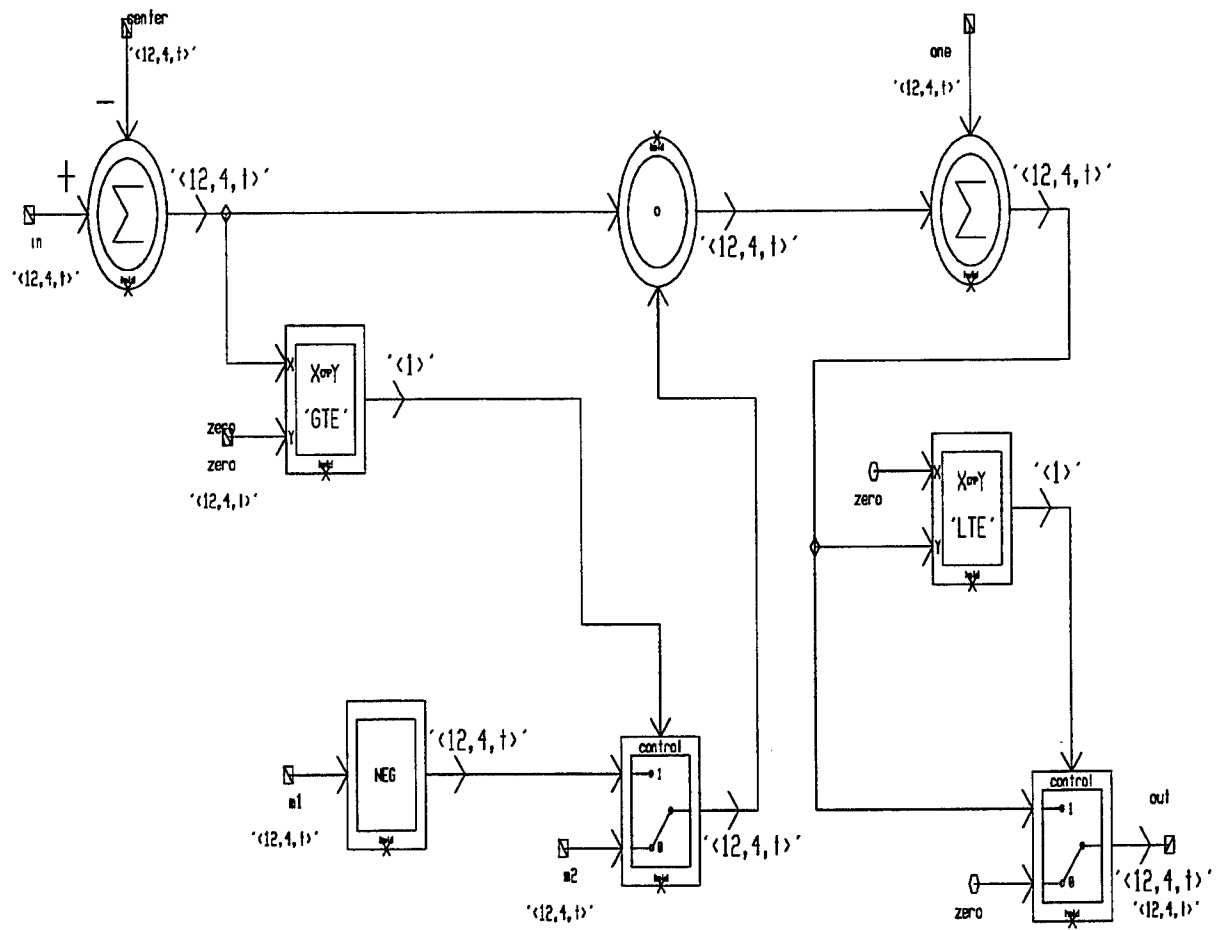


Figure 9: Second modification of membership function generator

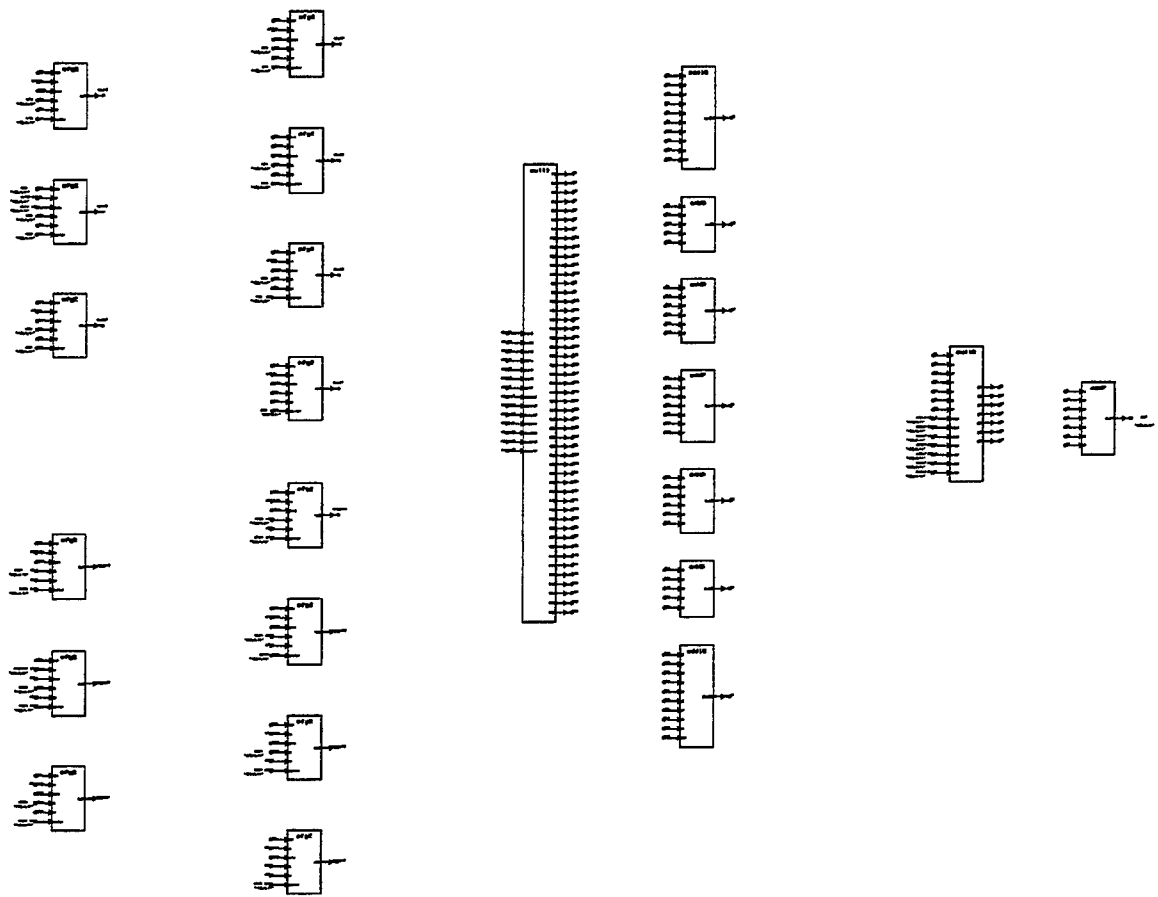


Figure 10: Fixed point group level description of fuzzy logic controller

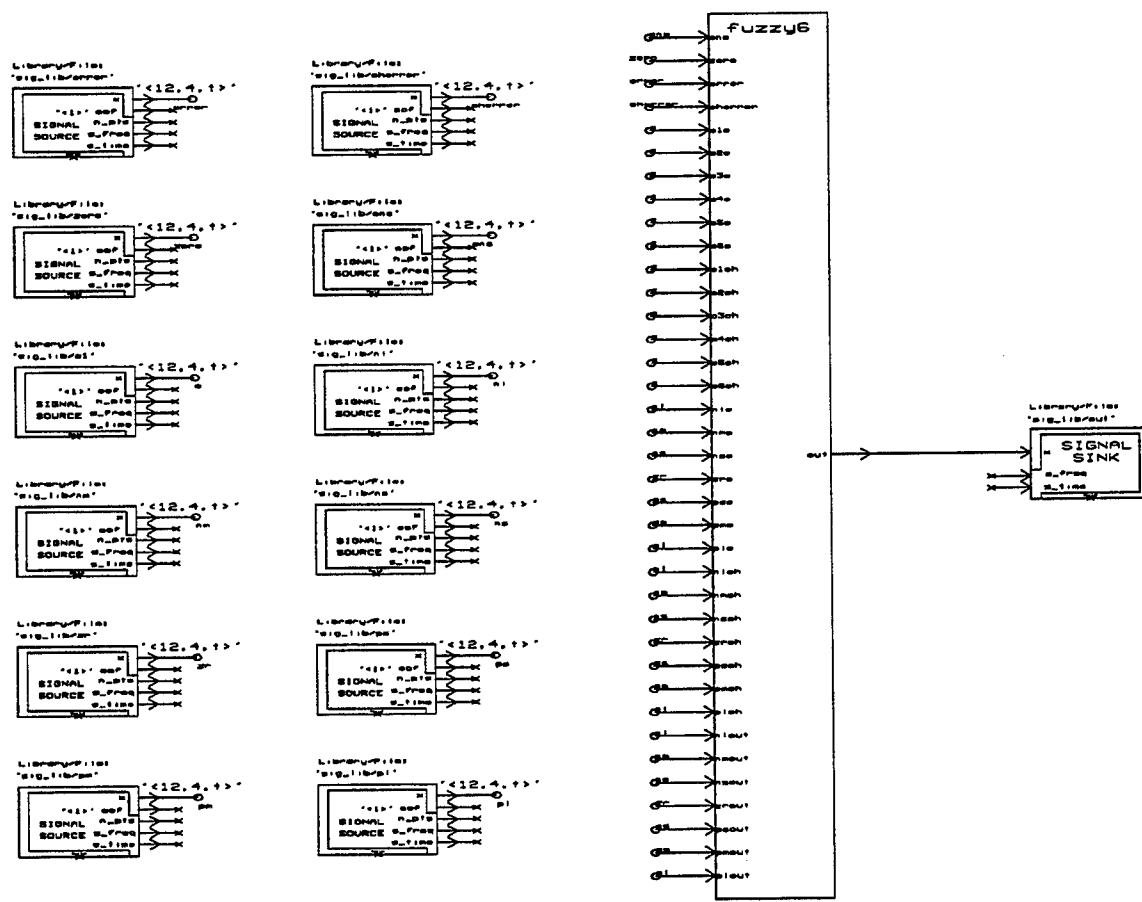


Figure 11: Fixed point testbench level description of fuzzy logic controller

References

- [1] E. Cox, "Fuzzy Fundamentals," *IEEE Spectrum*, pp. 58-61, October 1992.
- [2] *Signal Processing Worksystem User's Guide and Tutorial*. Alta Group of Cadence Design Systems, Inc., June 1994.
- [3] V. Shah, "Design and Implementation of High Speed Fuzzy Logic Controllers," Master's thesis, Wright State University, Department of Computer Science and Engineering, 1994.
- [4] *Design Analyzer*. Synopsys, Inc., April 1995.
- [5] *SPW - The DSP Framework Hardware Design System User's Guide*. Comdisco Systems, Inc., January 1993.

**MISSILE AUTOPILOT DESIGN
BASED ON A UNIFIED SPECTRAL THEORY
FOR LINEAR TIME-VARYING SYSTEMS**

Michael C. Mickle
Candidate for Doctor of Philosophy
Department of Electrical and Computer Engineering

with

J. Jim Zhu
Assistant Professor
Department of Electrical and Computer Engineering

Louisiana State University
Baton Rouge, LA 70803
Email: zhu@sun-ra.rspip.lsu.edu

Final Report for:
Summer Graduate Research Program
Wright Laboratory

Sponsored by:
Air Force Office of Scientific Research
Bolling Air Force Base, DC

and

Wright Laboratory

July 1995

**MISSILE AUTOPILOT DESIGN
BASED ON A UNIFIED SPECTRAL THEORY
FOR LINEAR TIME-VARYING SYSTEMS**

Michael C. Mickle

Candidate for Doctor of Philosophy

Department of Electrical and Computer Engineering

Louisiana State University

Abstract

This report presents design and simulation case studies of a missile autopilot for angle of attack and nominal acceleration tracking using a recently developed Extended-Mean Assignment (EMA) control technique for linear time-varying (LTV) systems. The EMA control technique is based on a new eigenvalue concept, called SD-eigenvalue, for LTV systems. Closed-loop stability is achieved by the assignment of the extended-mean of these time-varying SD-eigenvalues to the left-half complex plane in a way similar to the eigenvalue (pole) assignment technique for linear time invariant (LTI) systems. Salient features of the tracking controller include: (i) good tracking performance for arbitrary trajectories without any scheduling of the constant design parameters throughout the entire operating range of the Mach, (ii) implementation of the inverse pitch dynamics using a static neural network, (iii) time-varying EMA control gains to improve tracking performance, and (vi) a time-varying bandwidth command shaping filter that effectively reduces the actuator rate while maintaining good tracking response for both smooth and abrupt trajectories. Although the autopilot was designed only for nominal aerodynamic coefficients and constant trajectories, excellent performance was verified for $\pm 50\%$ variations in the aerodynamic coefficients, and for arbitrary command trajectories.

**MISSILE AUTOPILOT DESIGN
BASED ON A UNIFIED SPECTRAL THEORY
FOR LINEAR TIME-VARYING SYSTEMS**

Michael C. Mickle

1. Introduction

This report presents design and simulation case studies of a missile autopilot design using a recently developed Extended-Mean Assignment (EMA) control technique for linear time-varying (LTV) systems. The EMA control technique is very similar to the conventional pole placement design for linear time-invariant (LTI) systems, but based on a new, time-varying Series D-eigenvalue (SD-eigenvalue) concept [1]-[4]. The autopilot is to control the nonlinear time-varying pitch-axis dynamics of a hypothetical tail-controlled missile, which has been used as a benchmark in a number of recent studies on nonlinear gain-scheduling design techniques [5]-[7]. In [1] the principle and design technique were presented for an EMA controller that uses complex-valued SD-eigenvalues to avoid singularities known as finite-escapes. The nonlinear pitch dynamics of the missile was rendered into a linear time-varying one via the classical linearization along a nominal trajectory, and followed by a linear coordinate transformation to make it tractable by the EMA control technique. Simulation validation of the zero input stability was also presented there.

In this report, we present the design and simulation study of trajectory tracking using the complex-valued EMA controller. A radical departure from the conventional design philosophy is that nonlinearity and time-variance are not treated as nuisances, but purposely utilized to accomplish design objectives beyond the capability of LTI controllers. Salient features of the EMA tracking controller include: (i) good tracking performance for arbitrary trajectories without any scheduling of the constant design parameters throughout the entire operating range of the Mach, (ii) implementation of the inverse pitch dynamics using a static neural network, (iii) time-varying EMA control gains to improve tracking performance, and (vi) a time-varying bandwidth command shaping filter that effectively reduces the actuator rate while maintaining good tracking response for both smooth and abrupt trajectories.

For completeness, Section 2 recapitulates the main results presented in [1]. Section 3 details the design and implementation of the EMA tracking controller, including: the Radial Basis Function (RBF) neural network based inverse plant model, the time-varying EMA command logic, and the time-varying bandwidth command shaping filter. Two Normal Acceleration (NA) tracking system configurations are designed; both are centered around an Angle of Attack (AOA) tracking subsystem. One configuration uses an AOA state observer to estimate the AOA tracking error from that of the NA measurement. The other uses the AOA subsystem as an inner loop, and employs a Proportional-Integral (PI) controller for the NA outer loop tracking. In Section 4, simulation case studies are presented for: (i) AOA tracking of step trajectories with constant EMA commands, and with nominal

and $\pm 50\%$ variations in the aerodynamic coefficients, (ii) AOA tracking of sinusoidal trajectories with both constant and variable EMA commands, and with nominal and $\pm 50\%$ variations in the aerodynamic coefficients, (iii) NA tracking of both step and sinusoidal trajectories using an AOA state observer, and (iv) NA tracking of both step and sinusoidal trajectories using AOA inner loop. Section 5 concludes this report with a summary of the results and suggestions for further studies on tracking of arbitrary normal acceleration trajectories using a dynamic neural network based “pseudo-inverse” of the non-minimum phase plant model.

2. Preliminaries

This section summarizes the main results of [1]. Interested readers are referred to [1] for detailed derivations and the missile model parameters. It is noted that some typos found in [1] are corrected here.

2.1 Complex-valued EMA controller

The EMA control technique is based on a new SD-eigenvalue concept for LTV systems in a way similar to the conventional pole placement design method for LTI systems. Let $D = d/dt$ be the derivative operator. A 2nd-order LTV system

$$\ddot{y} + \alpha_2(t)\dot{y} + \alpha_1(t)y = u \quad (2.1)$$

can be written in an operator form $\mathcal{D}_\alpha\{y\} = u$ where

$$\begin{aligned} \mathcal{D}_\alpha &= D^2 + \alpha_2(t)D + \alpha_1(t) \\ &= (D - \lambda_2(t))(D - \lambda_1(t)) \end{aligned} \quad (2.2)$$

is known as a *polynomial differential operator* (PDO), and the factorization is known as *Cauchy-Floquet factorization*. The scalar functions $\lambda_1(t), \lambda_2(t)$ are called *Series D-eigenvalues (SD-eigenvalues)* for the LTV system (2.1). The SD-eigenvalues satisfy a set of (nonlinear, differential) SD-characteristic equations

$$\begin{aligned} \dot{\lambda}_1 + \lambda_1^2 + \alpha_2(t)\lambda_1 + \alpha_1(t) &= 0 \\ \lambda_2 &= -\alpha_2(t) - \lambda_1 \end{aligned} \quad (2.3)$$

Note that, in general, $\lambda_1(t), \lambda_2(t)$ are non-commutative, nonunique, and may be complex-valued. In the latter case, they form an *affine complex-conjugate pair* [6]

$$\begin{aligned} \lambda_1(t) &= \sigma_1(t) + j\omega(t) \\ \lambda_2(t) &= \sigma_2(t) - j\omega(t) \end{aligned} \quad (2.4)$$

where $\omega(t)$ satisfies

$$\dot{\omega} = (\sigma_2(t) - \sigma_1(t))\omega \quad (2.5)$$

Now define the extended-mean (EM) value of an integrable function $\lambda(t)$ by

$$\text{em}\{\lambda(t)\} = \limsup_{(t-t_0) \rightarrow \infty} \frac{1}{t-t_0} \int_{t_0}^t \lambda(\tau) d\tau \quad (2.6)$$

Then the LTV system is exponentially stable if the EM values of $\lambda_1(t), \lambda_2(t)$ are in the LHP of \mathbb{C} , i.e.

$$\text{em}\{\text{Re}(\lambda_i(t))\} < 0, \quad i = 1, 2 \quad (2.7)$$

Thus, if the LTV system (2.1) is unstable, a feedback control law

$$u(t) = k_1(t)y(t) + k_2(t)\dot{y}(t) \quad (2.8)$$

can be synthesized so that SD-eigenvalues $\gamma_1(t)$, $\gamma_2(t)$ of the closed-loop system $\mathcal{D}_\eta\{y\} = 0$ where

$$\begin{aligned} \mathcal{D}_\eta &= D^2 + \eta_2(t)D + \eta_1(t) \\ &= (D - \gamma_2(t))(D - \gamma_1(t)) \end{aligned} \quad (2.9)$$

with

$$\eta_i = \alpha_i(t) - k_i(t)$$

has the desired EM values $C_i(t)$. These desired EM values can be achieved using LTI tracking control methods to drive the EMA error

$$\epsilon_i(t) = \text{em}\{\gamma_i(t)\} - C_i(t) \rightarrow 0 \quad (2.10)$$

exponentially, thereby rendering a LTV control problem to a LTI one.

A nuisance in the previously developed EMA controller is that the SD-eigenvalues may have finite singularities known as finite escapes. Even though some methods have been developed to circumvent the problem, they are either restricted to 2nd-order systems only, or merely render the infinite values in $\lambda_i(t)$ to finite peaks that will eventually show up in the controlled motion.

In a recent paper [2], it is proven that for LTV systems with piecewise smooth coefficients, there always exist piecewise smooth SD-eigenvalues free of finite escapes. However, these well-behaved SD-eigenvalues are often complex-valued. A condition for the SD-eigenvalues of a 2nd-order LTV system to be well behaved is to allow complex-valued solutions

$$\lambda_{1,2}(t) = \sigma_{1,2}(t) \pm j\omega(t) \quad (2.11)$$

for (2.3) when the discriminant

$$\theta = 2\dot{\alpha}(t) + \alpha_2^2(t) - 4\alpha_1(t) \leq 0 \quad (2.12)$$

Otherwise, let

$$\lambda_{1,2}(t) = \sigma_{1,2}(t) \pm \omega(t) \quad (2.13)$$

By substituting (2.11)-(2.13) into (2.3), the SD-characteristic equation becomes:

$$\begin{aligned} \dot{\sigma}_1 + \sigma_1^2 + \alpha_2(t)\sigma_1 + \alpha_1 + \text{sgn}(\theta)\omega^2 &= 0 \\ \sigma_2 &= -\alpha_2(t) - \sigma_1 \\ \dot{\omega} &= (\sigma_2(t) - \sigma_1(t))\omega \end{aligned} \quad (2.14)$$

These equations give the following useful relationship

$$\begin{aligned} \alpha_1(t) &= -\dot{\sigma}_1(t) + \sigma_1(t)\sigma_2(t) - \text{sgn}(\theta)\omega^2(t) \\ \alpha_2(t) &= -(\sigma_1(t) + \sigma_2(t)) \end{aligned} \quad (2.15)$$

Since only the EM values of the real-parts of the closed-loop SD-eigenvalues $\gamma_i(t)$ determine stability, we can still use real-valued EM compensating signals $\mu_i(t)$. This results in complex-valued closed-loop SD-eigenvalues $\gamma_i(t) = \psi_i(t) \pm j\phi(t)$, which prevents finite-escapes in the closed-loop systems, and allows design freedom in closed-loop dynamic behavior. Thus, we have

$$\begin{aligned} \gamma_i(t) &= (\sigma_i(t) + \mu_i(t)) \pm j\phi(t) \\ &= \psi_i(t) \pm j\phi(t) \end{aligned} \quad (2.16)$$

where $\phi(t)$ satisfies

$$\dot{\phi} = (\psi_2(t) - \psi_1(t))\phi \quad (2.17)$$

Note that the same relationship (2.15) holds for $\eta_i(t)$ and $\gamma_i(t)$. Thus, the LTV feedback control gains $k_i(t)$ are given by

$$\begin{aligned} k_1 &= \alpha_1 - \eta_1 = \dot{\mu}_1 - \sigma_1\mu_2 - \sigma_2\mu_1 - \mu_1\mu_2 - \text{sgn}(\theta)\omega^2 - \phi^2 \\ k_2 &= \mu_1 + \mu_2 \end{aligned} \quad (2.18)$$

where the sign for $\phi^2(t)$ has been fixed to obtain damped oscillatory impulse response for the closed loop system. The overall implementation diagram for the complex-valued EMA controller is given in Figure 1. Interested readers should compare it to the original EMA controller given in [4].

2.2 Dynamic model of the missile airframe

We now consider a hypothetical tail-controlled missile whose pitch-axis dynamics are described by

$$\begin{aligned} \dot{\alpha}(t) &= K_\alpha M(t) C_n[\alpha(t), \delta(t), M(t)] \cos(\alpha(t)) + q(t) \\ \dot{q}(t) &= K_q M^2(t) C_m[\alpha(t), \delta(t), M(t)] \\ \eta_z(t) &= K_z M^2(t) C_n[\alpha(t), q(t), \delta(t), M(t)] \end{aligned} \quad (2.19)$$

where $\alpha(t)$ is the angle-of-attack (AOA), $q(t)$ is the pitch-rate, $\delta(t)$ is the tail-fin deflection angle, $\eta_z(t)$ is the normal acceleration (NA), and $M(t)$ is the Mach number. The aerodynamic lift coefficient C_n and the pitch moment coefficient C_m are modeled by

$$\begin{aligned} C_n[\alpha, \delta, M] &= a_n \alpha^3 + b_n \alpha |\alpha| + c_n (2 - \frac{M}{3}) \alpha + d_n \delta \\ C_m[\alpha, q, \delta, M] &= a_m \alpha^3 + b_m \alpha |\alpha| + c_m (-7 + \frac{8M}{3}) \alpha + d_m \delta \end{aligned} \quad (2.20)$$

The tail-fin actuator dynamics is described by

$$\frac{d}{dt} \begin{bmatrix} \delta(t) \\ \dot{\delta}(t) \end{bmatrix} = \begin{bmatrix} 0 & 1 \\ -\omega_a^2 & -2\zeta\omega_a \end{bmatrix} \begin{bmatrix} \delta(t) \\ \dot{\delta}(t) \end{bmatrix} + \begin{bmatrix} 0 \\ \omega_a^2 \end{bmatrix} \delta_c(t) \quad (2.21)$$

where $\delta_c(t)$ is the commanded tail-fin deflection angle.

The values of the various constant parameters in the dynamic equations (2.19)-(2.21) can be found in [1] and [5]-[7], so they are omitted here. This missile model has been used as a benchmark in a number of recent studies on nonlinear gain-scheduling design techniques [5]-[7]. It is noted that in general the pitch moment coefficient C_m depends on the pitch rate q . This dependence is absent in the model (2.19) in the previous studies, and in this study as well. However, since for tail fin controlled pitch dynamics this dependence has a stabilizing effect, the performance should be improved when a controller designed with the model (2.19) is applied to the more accurate model.

Let $\eta_c(t)$ be the commanded NA trajectory, $\bar{\alpha}(t)$ be the corresponding nominal AOA trajectory, and $\bar{\delta}(t)$ be the required nominal control input. By applying the standard linearization along a nominal trajectory, followed by a linear coordinate transformation, a linear time-varying tracking error model was derived in [1] as follows

$$\ddot{z}_1 + \alpha_2(t)\dot{z}_1 + \alpha_1(t)z_1 = u \quad (2.22a)$$

$$b_1(t)\dot{v} + [b_1 + b_2(t)]v = u \quad (2.22b)$$

$$y = c(t)z_1 + d(t)v \quad (2.22c)$$

where

$$z_1(t) = \alpha(t) - \bar{\alpha}(t) \quad (2.23)$$

$$y(t) = \eta_z(t) - \eta_c(t) \quad (2.24)$$

$$v(t) = \delta(t) - \bar{\delta}(t) \quad (2.25)$$

and

$$\alpha_1(t) = -[\dot{a}_{11}(t) + a_{21}(t)] \quad (2.26)$$

$$\alpha_2(t) = -a_{11}(t) \quad (2.27)$$

$$b_1(t) = K_\alpha M(t)d_n \cos(\bar{\xi}_1(t)) \quad (2.28)$$

$$b_2(t) = K_q d_m M^2(t) \quad (2.29)$$

$$c(t) = K_z M^2(t)[3a_n \bar{\xi}_1^2(t) + 2b_n |\bar{\xi}_1(t)| + c_n(2 - \frac{M(t)}{3})] \quad (2.30)$$

$$d(t) = d_n K_z M^2(t) \quad (2.31)$$

where

$$a_{11}(t) = K_\alpha M(t)[(3a_n \bar{\xi}_1^2(t) + 2b_n |\bar{\xi}_1(t)| + c_n(2 - \frac{M(t)}{3})) \cos(\bar{\xi}_1(t)) - (a_n \bar{\xi}_1^3(t) + b_n |\bar{\xi}_1(t)| \bar{\xi}_1(t) + c_n(2 - \frac{M(t)}{3}) \bar{\xi}_1(t) + d_n \bar{\delta}(t)) \sin(\bar{\xi}_1(t))] \quad (2.32)$$

$$a_{21}(t) = K_q M^2(t)[3a_m \bar{\xi}_1^2(t) + 2b_m |\bar{\xi}_1(t)| + c_m(-7 + \frac{8M(t)}{3})] \quad (2.33)$$

This model is readily tractable by the EMA control technique, and will be used for the subsequent angle-of-attack tracking and normal acceleration tracking studies.

3. EMA Autopilot Design

To take advantage of the minimum phase zero-dynamics in AOA, and the LTV model (2.22) for AOA dynamics that is readily controlled by the EMA technique, the (nonminimum phase) normal acceleration (NA) tracking is achieved via an AOA tracking subsystem shown in Figure 3.1. Based on this AOA tracking subsystem, two NA tracking system configurations are proposed: one uses an observer to estimate the AOA tracking error from the NA tracking error, as shown in Figure 3.2; the other uses a PI controller to generate the AOA tracking command from the NA tracking error, as shown in Figure 3.3. The design of subsystem components are described below.

3.1 Time-Varying Bandwidth (TVB) Command Shaping Filter

Due to the stringent requirements on tracking performance and actuator rate limit, all three system configurations in Figures 3.1-3.3 require a tracking command shaping filter, which is not shown in the figures. The filter should greatly reduce the acceleration and rate of an abrupt command trajectory, whereas it should have little effect on smooth trajectories that can be tracked within the actuator limits. These two requirements cannot be

achieved with a fixed-parameter filter. For instance, the AOA tracking subsystem can track a 0.5 Hz, 0.3 radians amplitude sine wave within the ± 8.7 rad/sec (500°/sec) actuator rate limits without any command shaping. However, the same system tracks a step command of 0.3 radians magnitude accurately, but requires a maximum actuator rate of 17,500 rad/sec. When a 3rd-order LTI Bessel filter with a bandwidth $\omega_n = 10$ is applied to the step tracking command, the actuator rate is reduced to within the limits with a satisfactory tracking performance, but the sinusoidal tracking then has an unnecessary tracking delay of 0.25 second, or a 45° phase lag.

To resolve this problem, a novel 2nd-order, LTV filter with a *variable bandwidth* is designed. The impulse response of the filter is chosen to be of the form

$$h(t) = A \exp(-\zeta \int \omega_n(t) dt) \cos(\int \omega_d(t) dt + \phi) \quad (3.1)$$

where ζ is a constant damping coefficient, ϕ is a constant depending on ζ , and $\omega_d(t)$ is related to $\omega_n(t)$ by

$$\omega_d(t) = \omega_n(t) \sqrt{1 - \zeta^2}$$

For a constant ω_n , this is the familiar 2nd-order LTI filter that has a damped oscillatory impulse response for $0 < \zeta < 1$. The dynamical equation of the filter is given by

$$\ddot{c}_{out} + a_2(t) \dot{c}_{out} + a_1(t) c_{out} = c_{in} \quad (3.2)$$

where c_{in} and c_{out} are the command input and the shaped command output. The time-varying system coefficients $a_1(t)$, $a_2(t)$ and the associated Parallel D-eigenvalues (PD-eigenvalues) $\rho_i(t)$ are given by [3]

$$a_1(t) = \omega_n^2(t) \quad (3.3)$$

$$a_2(t) = - \left[2\zeta\omega_n(t) + \frac{\dot{\omega}_n(t)}{\omega_n(t)} \right] \quad (3.4)$$

$$\rho_{1,2}(t) = -\zeta\omega_n(t) \pm j\omega_d(t) \quad (3.5)$$

Thus, the filter is well-defined if $\omega_n(t) > 0$, and is exponentially and BIBO stable if and only if, in addition to $\omega_n(t) > 0$, $\zeta > 0$. Incidentally, it is interesting to note that under this stability condition, the filter can be stable while $a_2(t)$ is negative when $\omega_n(t)$ decreases at a fast rate, which implies that a “frozen-time” eigenvalue is in the right-half-plane of \mathbb{C} !

For the application at hand, the damping factor $\zeta = 1$ is chosen, and the filter bandwidth $\omega_n(t)$ and its rate $\dot{\omega}_n(t)$ are generated from

$$\dot{\omega}_n(t) + 2\zeta_0\omega_0\dot{\omega}_n(t) + \omega_0^2\omega_n(t) = \omega_0^2 r_\omega(t) \quad (3.6)$$

where ζ_0, ω_0 are design parameters that determine how $\omega_n(t)$ follows the bandwidth command $r_\omega(t)$, which is in turn determined by the following command shaping logic:

$$r_\omega(t) = \omega_{n0} - a \cdot \text{sat}(b \cdot \text{ddzone}(d \cdot |\ddot{c}_{out}(t)|)) \quad (3.7)$$

where ω_{n0} is the maximum bandwidth, a, b, d are constant design parameters which determine how the bandwidth is reduced from the maximum ω_{n0} when $|\dot{c}_{out}(t)|$ exceeds a predefined threshold set by the saturation function $\text{sat}(\cdot)$ and deadzone function $\text{ddzone}(\cdot)$, which are defined in the usual way.

Figures 3.7, 3.8 show the step and sine responses, respectively, of the TVB filter with a maximum $\omega_n(t) = \omega_{n0} = 100$, and minimum $\omega_n(t) = 5$, along with the responses of a 2nd-order LTI filter with a fixed $\omega_n = 100$ and a 3rd-order Bessel filter with a fixed $\omega_n = 10$. The corresponding filter parameters $a_1(t)$ and $a_2(t)$ are given in Figures 3.9, 3.10, respectively, which clearly show how the bandwidth is drastically reduced during the initial transient of an applied command trajectory.

3.2 Neural Network Based Dynamic Inverse

Nonlinear tracking by linearization along a nominal trajectory calls for an inverse model of the plant input/output dynamics to generate the required nominal control input. It is well known that when the plant has nonminimum phase zero-dynamics, such as the case of NA tracking, the inverse model is unstable. Consequently, “perfect tracking” is not possible. However, if the plant is stable, it is possible to find the inverse for constant input and output trajectories. The error in the nominal control for a variable trajectory is then to be compensated for by the tracking error controller, provided that the error is sufficiently small so that the linearization remains valid.

The nominal control for a constant trajectory is implemented by a Radial Basis Function (RBF) neural network (NN). Two static RBF NNs are trained, one generates the nominal fin deflection $\bar{\delta}$ for nominal AOA $\bar{\alpha}$, and the other generates both the nominal fin deflection $\bar{\delta}$ and nominal AOA $\bar{\alpha}$ for nominal NA. The former is used in the systems shown in Figures 3.1 and 3.3, and the latter is used in the system shown in Figure 3.2. The training data for the network was acquired from the MATLAB function `trim` which locates the equilibrium points of the missile model, *i.e.* the nominal tail fin deflection required to achieve the desired output (AOA or NA). These data were then used to train a RBF NN via the MATLAB function `solverb`. The training of a RBF NN with some 200 neurons required an order of 10^{10} FLOPs using the Unix version Neural Networks Toolbox Version 1.0 for MATLAB. Shown in Figures 3.4 and 3.5 are the desired inverse mapping of $\bar{\alpha} \mapsto \bar{\delta}$ and a 200-neuron RBF NN implementation, respectively. The error surface between these two is plotted in Figure 3.6, where it can be seen that, except at a few peripheral points outside the operating range, the errors are below 0.01 (radians). This error magnitude is readily accommodated by the EMA tracking controller.

The RBF NN offers several advantages over other NNs. In general, it provides quicker training than networks such as the Multi-layer Network and does not have the problem of local minima. It provides smooth generalization between known data points, as opposed to the zeroth-order generalization of the CMAC. Also, it requires fewer neurons than CMAC. However, it shares CMAC's problem of exponential growth of the number of weights with respect to number of inputs, and is thus limited as a practical solution to problems with smaller number of inputs. It is noted that in practice, training data can be obtained directly from wind tunnel or flight tests. Although it takes significant amounts of time and computations for a comprehensive training, the localization of its receptive fields and the small number of weights makes the RBF NN ideal for on-line training, using the off-line training as the

initial states. This will greatly increase the accuracy and robustness of the overall tracking system in the presence of parameter uncertainties. These facts make the RBF well suited to the problem of generating a constant nominal control.

3.3 AOA Tracking Subsystem

The center piece and the novelty of the AOA tracking subsystem is the complex-valued EMA controller whose design was detailed in [1] and recapitulated in Section 2 of this report. It is noted that the design was greatly simplified owing to the fact that the AOA zero-dynamics (2.22b) is stable, as verified in [1] using the extended-mean stability criterion on SD-eigenvalues.

As the closed-loop stability is guaranteed by the extended-mean stability criterion, the extended-mean assignment commands (EMAC) $c_i(t)$ in the EMA controller need not be constant, as long as in the average they stay in the LHP of \mathbf{C} . This salient feature may be advantageous in cases where control energy is a prime concern while performance may be sacrificed during noncritical maneuverings. To test this concept, a variable EMAC logic is defined as follows

$$c_i(t) = c_{i0} + g \frac{\epsilon(t)}{\epsilon_0} \exp\left(-\frac{\epsilon(t)}{\epsilon_0}\right) \quad (3.8)$$

where $\epsilon(t)$ is the tracking error, ϵ_0 is a predetermined tracking error threshold, c_{i0} is the minimum EMAC, and g is a design constant that, when added to c_{i0} , determines the maximum EMAC. This EMAC logic generates the maximum EMAC when the tracking error $\epsilon(t)$ is equal to ϵ_0 , and reduces to the minimum EMAC when $\epsilon(t)$ is either zero or infinity. This EMAC logic was implemented and tested in the simulation studies presented below.

3.4 AOA Observer for NA Tracking System

The missile guidance system typically generates a NA command profile. Thus, despite the suitability of the AOA dynamic model (2.22) for EMA control, and its nonminimum phase zero dynamics, it is often desirable to track the NA. It is, therefore, important to translate the AOA tracking strategy into a NA tracking controller. Since the EMA controller was designed to eliminate the tracking error in AOA, and NA is related to AOA and the tail fin deflection via a nonlinear algebraic mapping, it is natural to design a nonlinear time-varying state observer that estimates the AOA error from the measurement of the NA error. This is accomplished by inverting the linearized output error equation (2.22c). A lowpass filtered differentiator is used to estimate the AOA error rate. It is noted that the observer performance could be improved by using a static neural network to approximate the nonlinear relation between the NA and AOA errors. Other ways of implementing the observer were discussed in [1].

It is noted that this NA tracking strategy circumvents the nonminimum phase problem of NA tracking implicitly, and yields good results when the mapping between the NA and AOA errors is accurate. This method is

applicable to other nonminimum phase tracking problems, and may be termed *algebraic output redefinition*, as opposed to the (dynamic) output redefinition method proposed in [8].

3.5 AOA Inner-Loop for NA Tracking System

A second normal acceleration tracking structure currently being studied uses the AOA tracking subsystem as an inner loop for NA tracking, and employs a PI controller for the NA outer loop. The advantage of this strategy is that the integrated NA error would allow for zero steady state error to a step command. However, this option still requires further research to justify the outer-loop stability, and to improve transient performance deterioration due to the integral control. Only preliminary simulation results are shown below to exemplify the idea and problems.

4. Simulation Case Studies

Simulation studies were performed to validate the design. The TVB command shaping filter was used for all the cases, so that no actuator amplitude or rate limiter was used. The constant design parameters used in the EMA controller were fixed for all the cases at $k_{i0} = -100$, $k_{i1} = 0$, $k_{i2} = -10$.

Case 1: AOA Step Trajectory Tracking

The AOA EMA control provides remarkable results for step command tracking. Figure 4.1 displays a three-second piecewise constant AOA tracking command, the TVB filtered command, and the AOA output. Figure 4.2 shows the corresponding tail fin deflection rate which is well within the 8.7 rad/sec design constraint. Without the TVB filter, the EMA controller accurately tracks step commands, but the actuator rate reaches 17,000 rad/sec. Thus, the TVB filter is essential for limiting the actuator to achievable rates. The output tail deflection is also limited but as figure 4.3 indicates this was an inconsequential constraint. Figure 4.4 shows the results of simulations of the four possible combinations of $\pm 50\%$ variations in the two aerodynamic coefficients $C_n(t)$, $C_m(t)$. Clearly, the AOA still accurately tracks the desired trajectory for all four cases, indicating excellent robustness of the closed-loop system.

Case 2: AOA Variable Trajectory Tracking

Although the neural network was trained to generate a nominal control input only for static or step commands, the proposed controller configuration can track arbitrary trajectories because of the EMA section's ability to accommodate errors in the nominal control input. Also, the EMA assignment command need not be a constant. Thus, figures 4.5-4.11 compare the results for TVB filtered sinusoidal tracking with both constant and variable EMA command. Shown together in figure 4.5 are: the AOA tracking command, the TVB filtered command, the AOA output with constant EMA command at 20, and with variable EMA command between 10 ~ 20 as defined in (3.8). It clearly shows the remarkable tracking performance. The filtered command has very little magnitude dampening and phase change, demonstrating how little the effect of the TVB filter has on a smooth trajectory comparing to its effect on the step command in the preceding case. Figure 4.7 shows the usefulness of the command filter for minimizing control rate and Figure 4.8 shows the corresponding fin deflection.

Shown in Figure 4.6 are the constant and variable EMA commands (EMAC). It can be seen that the variable EMAC indeed reduces to the minimum level of -10 when there is need for strenuous control action. Figures 4.9 and 4.10 show the corresponding feedback gains $k_1(t)$, $k_2(t)$, respectively, for both constant and variable EMAC. The tracking performance under constant and variable EMAC are almost indistinguishable in Figure 4.5, but Figure 4.11 indicates that in a long run the latter indeed saves control energy. .

As above, the robustness of the closed-loop system were tested for both constant and variable EMA commands under all four possible combinations of $\pm 50\%$ error in the two aerodynamic coefficients $C_n(t)$, $C_m(t)$. The results are shown in figure 4.12 which contains the eight test outputs together with the commanded trajectory. Once again, these results are very good.

Finally, the time-varying coefficients $\alpha_1(t)$, $\alpha_2(t)$ in the linearized AOA error dynamics (2.22), and the Mach profile as an important source of the time varying coefficients in the pitch airframe model, are shown in Figures 4.13-4.15 for the constant EMA command simulation. It is remarkable that no constant design parameters need to be scheduled for the entire operating range of the Mach from 2.6 to 1.9, $\alpha_1(t)$ between -25 to 260 , and $\alpha_2(t)$ between 0.52 to 1.27 , during the 10 seconds sinusoidal AOA maneuvering, and in the presence of $\pm 50\%$ parameter variation. This is one of the most significant advantage of the EMA controller.

Case 3: NA Tracking Using AOA State Observer

Since in this case, the NA tracking is achieved via a nonlinear algebraic mapping to the AOA tracking, we show in Figures 4.16 and 4.17 only the NA tracking performance results for a step and sine trajectory, respectively. Each figure shows the NA command, the TVB filtered command and the NA output. While no design effort was explicitly directed to the nonminimum phase behavior of the NA tracking, the performances in both cases are remarkable. It was noted during the simulation studies that the NA tracking is very sensitive to variations in the acceleration (curvature) of the tracking command. Thus the performance can be further improved by fine tuning the time-varying bandwidth command logic as given by (3.7), which causes some curvature fluctuation in the filtered command.

Case 4: NA Tracking Using AOA Inner-Loop

As mentioned earlier, this case is currently being studied, so only some preliminary results are shown in Figures 4.18 and 4.19 for step and sinusoidal NA command tracking performance. It is noted that the amplitude of the commands are smaller than that in the previous case, because large command amplitude caused instability. Also in Figure 4.18 a noticeable steady state tracking error is observed, but it indeed converges to zero very slowly, as expected from a Type I system. The sine command tracking result in Figure 4.19 also shows a significant delay. All these problems are due to the intrinsic properties of the integral control, and the limitation of the LTI PI controller in the (nonminimum phase, time-varying) outer loop. Remedies are being investigate at the time of writing.

5. Summary and Conclusions

In this report we have presented the design and simulation study of a missile angle of attack and normal acceleration tracking autopilot using a recently developed extended-mean assignment (EMA) control technique. A radical departure from the conventional design philosophy is that nonlinearity and time-variance of the dynamical systems are not treated as nuances. They are exploited purposely to accomplish design objectives beyond the reach of linear time-invariant control techniques. Salient features of the EMA tracking controller include: (i) good tracking performance for arbitrary trajectories without any scheduling of the constant design parameters throughout the entire operating range of the Mach, (ii) implementation of the inverse pitch dynamics using a static neural network, (iii) time-varying EMA control gains to improve tracking performance, and (vi) a time-varying bandwidth command shaping filter that effectively reduces the actuator rate while maintaining good tracking response for both smooth and abrupt trajectories. Simulation results have shown that the EMA control technique, though still in its embryonic stage, has become a viable design tool for realistic control problems.

Further studies are planned to: (i) implement on-line training of the neural network based inverse plant model to improve tracking accuracy and robustness, (ii) fine tune the time-varying bandwidth command shaping filter to improve the tracking transient performance, (iii) improve the performance of normal acceleration tracking using the angle of attack tracking as inner loop, and (iv) implement a dynamic neural network based "pseudo-inverse" of nonminimum phase plants for arbitrary trajectory tracking. It is noted that this research is only an initial effort to apply the new unified spectral theory and the EMA control technique for LTV systems to practical control problems such as missile autopilot design. The autopilot designed herein is limited to planar maneuvering only. Design of higher order EMA controllers for multivariable, higher degrees of freedom autopilot is significantly more challenging, and is planned as a long term research goal. Exploring other forms of controllers utilizing the time-varying SD- and PD-eigenvalues is also a long term research goal.

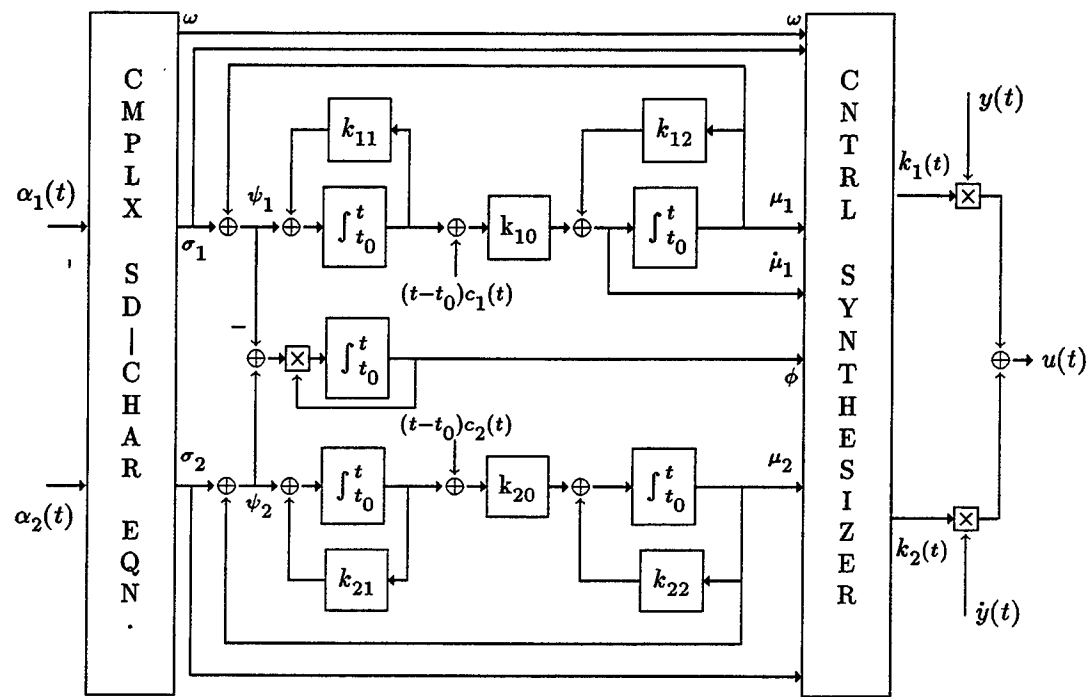


Figure 2.1 The complex-valued EMA controller

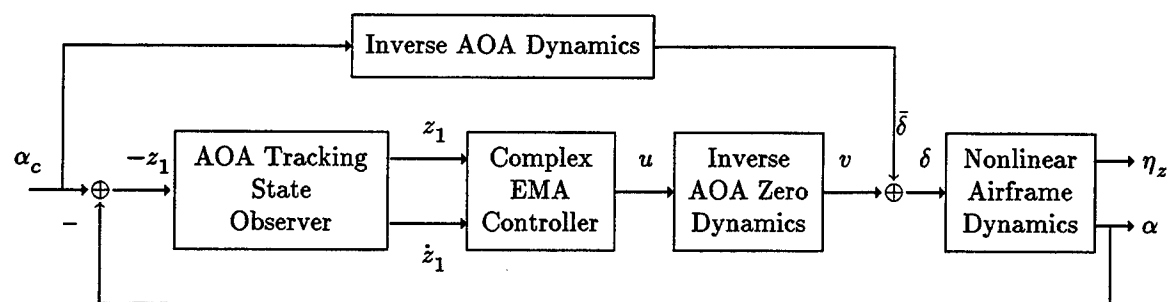


Figure 3.1 AOA Tracking Subsystem

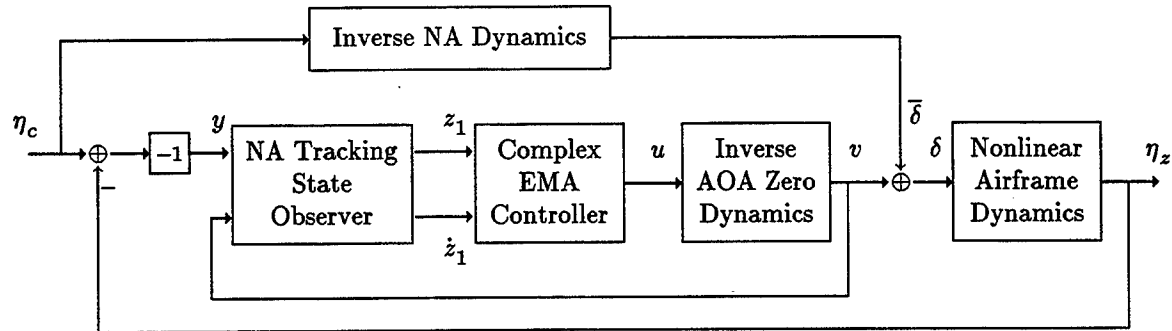


Figure 3.2 NA Tracking System Using AOA State Observer

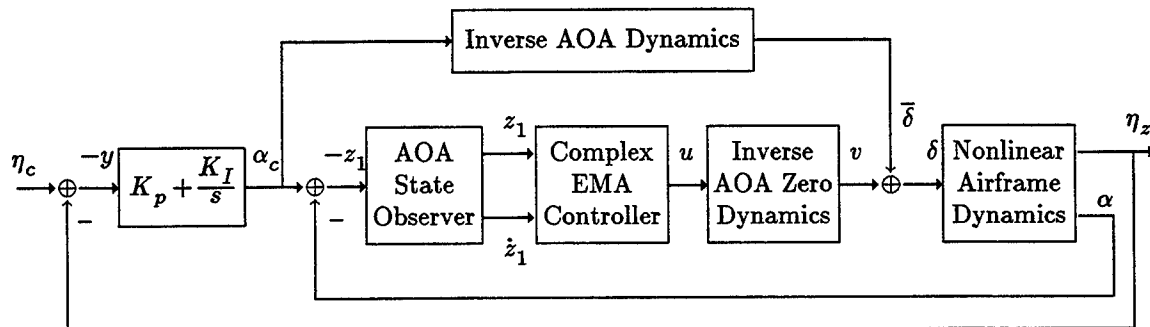


Figure 3.3 NA Tracking System Using AOA Inner-Loop

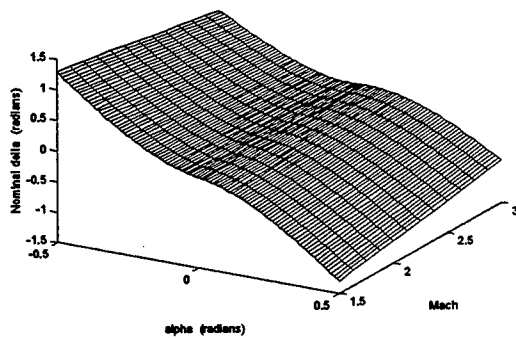


Figure 3.4 The Desired $\bar{\alpha} \mapsto \bar{\delta}$ Mapping

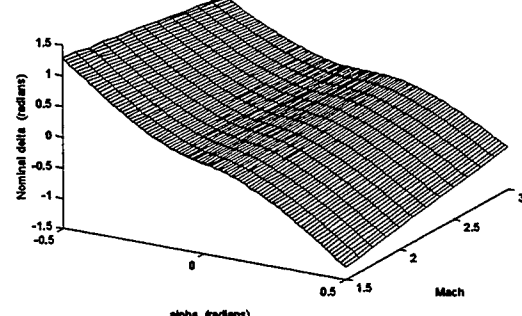


Figure 3.4 The RBF NN $\bar{\alpha} \mapsto \bar{\delta}$ Mapping

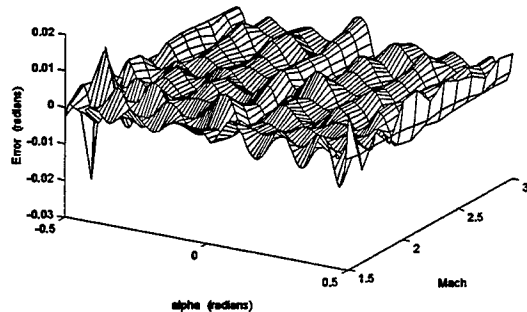


Figure 3.6 Error Surface of the RBF NN $\bar{\alpha} \mapsto \bar{\delta}$ mapping

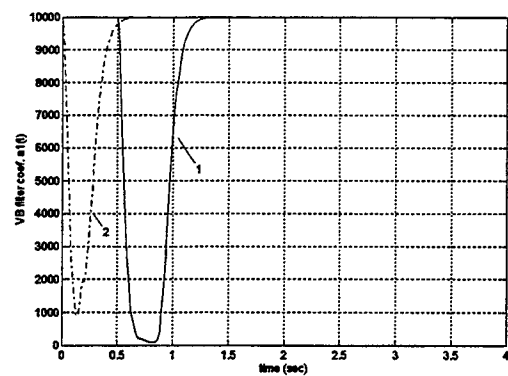


Figure 3.7 Time-varying TVB filter coefficient $a_1(t)$
1—Step command, 2—Sine command

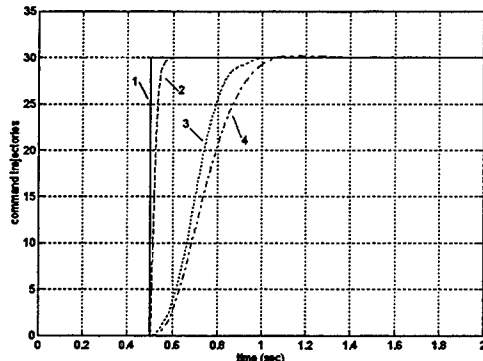


Figure 3.5 TVB Filter Step Response
1—Command, 2—2nd-order LTI filter
3—TVB filter, 4—3rd-order Bessel filter

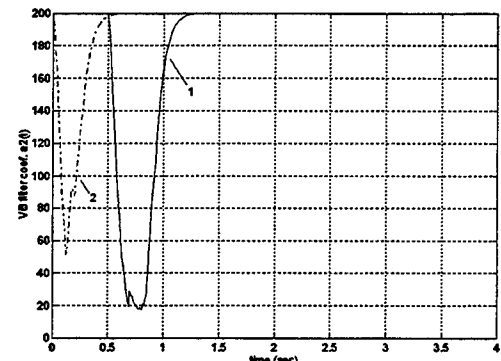


Figure 3.8 Time-varying TVB filter coefficient $a_2(t)$
1—Step command, 2—Sine command

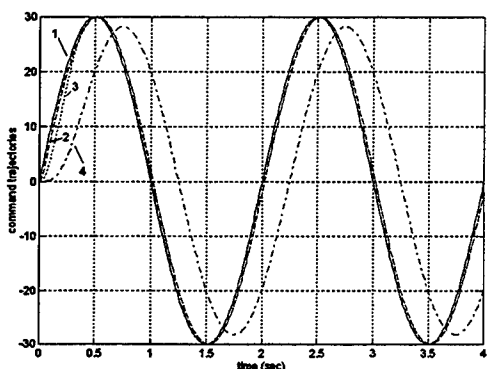


Figure 3.6 TVB Filter Sine Response
1—Command, 2—2nd-order LTI filter
3—TVB filter, 4—3rd-order Bessel filter

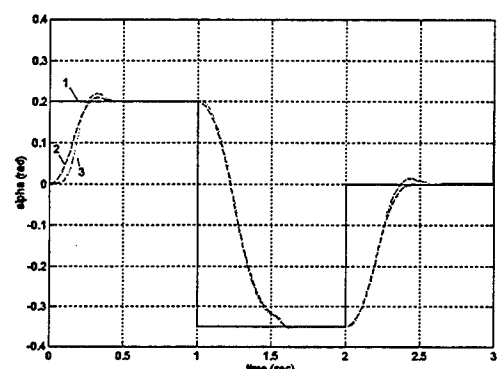


Figure 4.1 Step Trajectory Tracking Performance
1—AOA command, 2—TVB filtered AOA command
3—AOA output

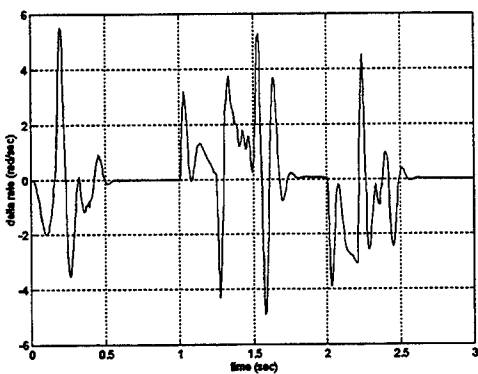


Figure 4.2 Actuator Rate

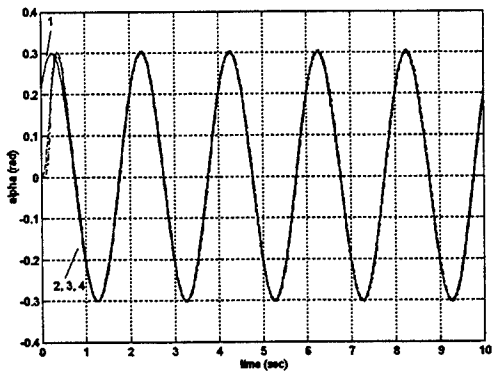


Figure 4.5 Sine Trajectory Tracking Performance
 1—AOA command, 2—TVB filtered AOA command
 3—Result for Const. EMAC, 4—Result for variable EMAC

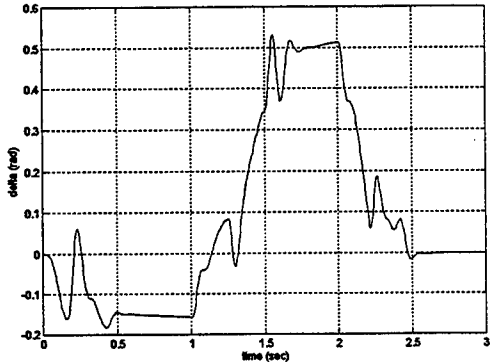


Figure 4.3 Actuator Output

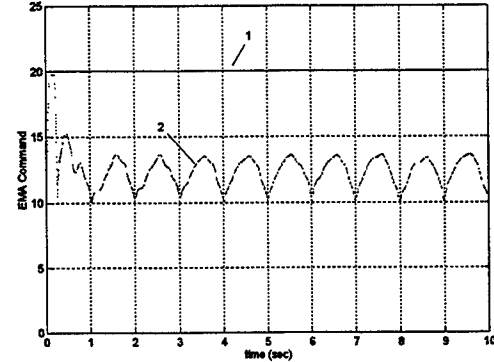


Figure 4.6 Constant vs. Variable EMA Command
 1—Constant EMA command, 2—Variable EMA command

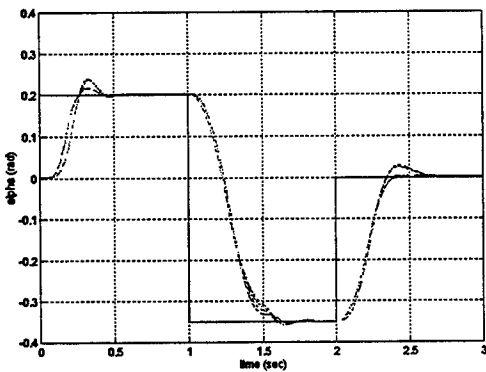


Figure 4.4 Robustness Test — $\pm 50\%$ variation on C_m, C_n

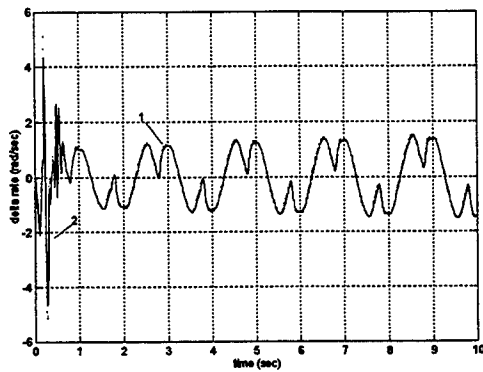


Figure 4.7 Actuator Rate
 1—Result for const. EMAC, 2—Result for variable EMAC

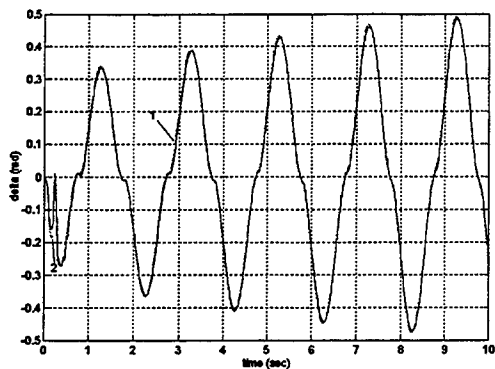


Figure 4.8 Actuator Output
1—Result for const. EMAC, 2—Result for variable EMAC

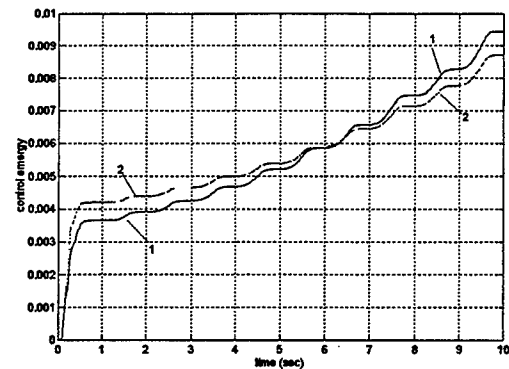


Figure 4.11 Tracking Error Control Energy
1—Result for const. EMAC, 2—Result for variable EMAC

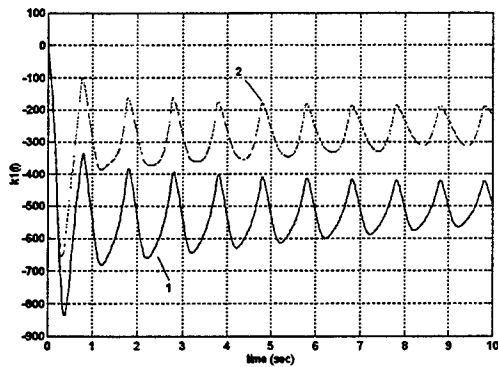


Figure 4.9 Feedback Gain $k_1(t)$
1—Result for const. EMAC, 2—Result for variable EMAC

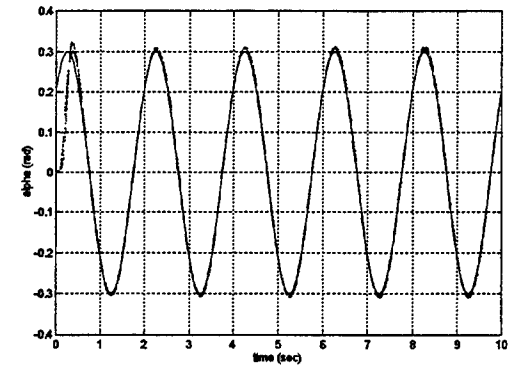


Figure 4.12 Robustness Test
Constant and Variable EMAC, $\pm 50\%$ on C_m, C_n

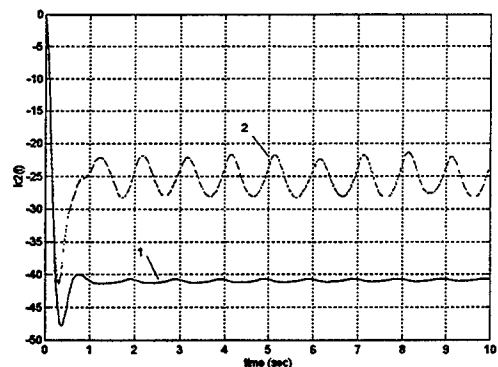


Figure 4.10 Feedback Gain $k_2(t)$
1—Result for const. EMAC, 2—Result for variable EMAC

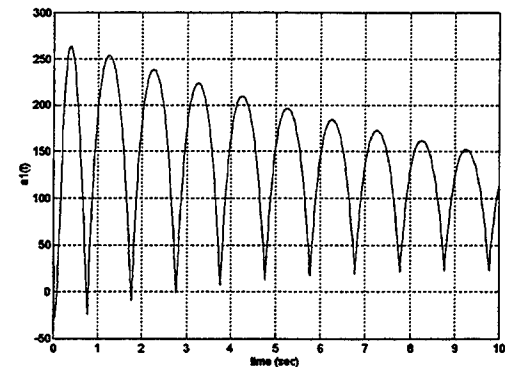


Figure 4.13 Plant Coefficient $\alpha_1(t)$ — Constant EMAC

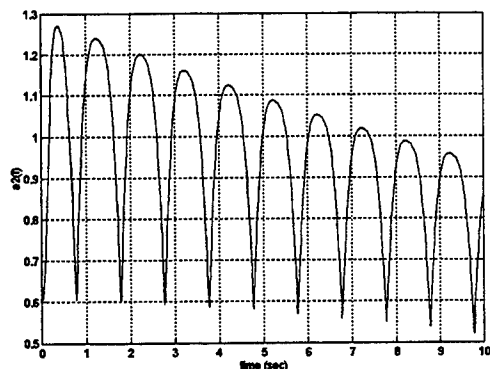


Figure 4.14 Plant Coefficient $\alpha_2(t)$ — Constant EMAC

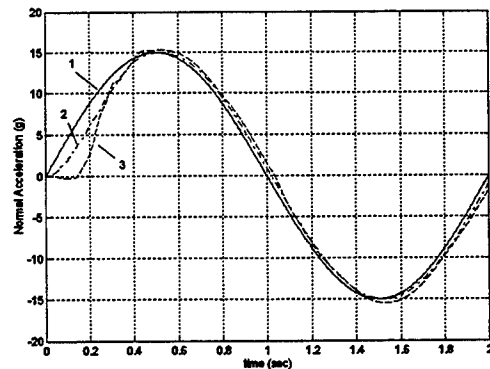


Figure 4.17 NA Sine Trajectory Tracking Performance
— AOA observer
1—NA command, 2—TVB filtered NA com. 3—NA output

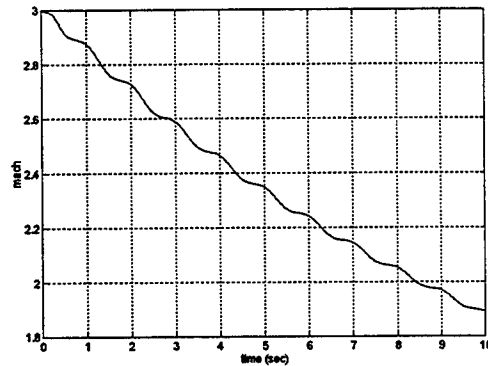


Figure 4.15 Mach Profile — Constant EMAC

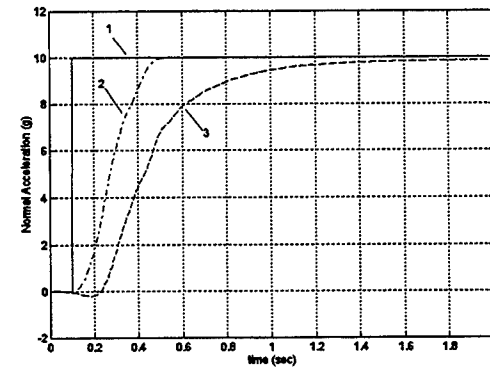


Figure 4.18 NA Step Trajectory Tracking Performance
— AOA inner-loop
1—NA command, 2—TVB filtered NA com. 3—NA output

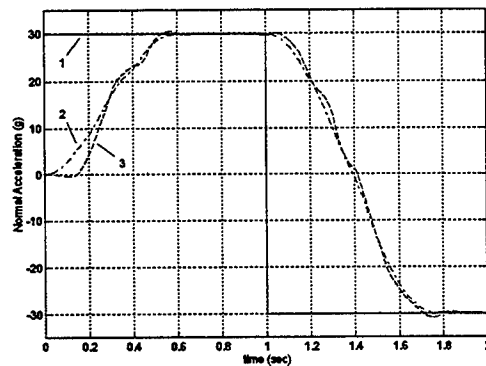


Figure 4.16 NA Step Trajectory Tracking Performance
— AOA observer
1—NA command, 2—TVB filtered NA com. 3—NA output

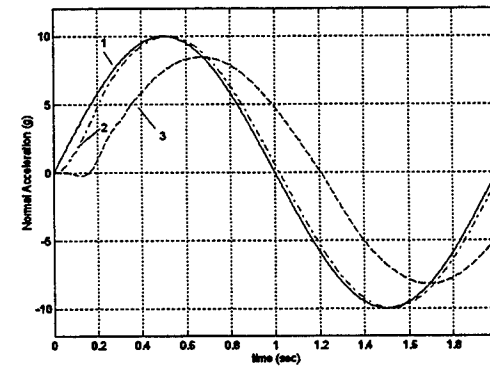


Figure 4.19 NA Sine Trajectory Tracking Performance
— AOA inner-loop
1—NA command, 2—TVB filtered NA com., 3—NA output

References

- [1] Zhu, J. and Mickle, M. C., "Missile Autopilot Design Using the Extended-Mean Assignment Control, Part I: Stability," *Proc., 27th IEEE SSST*, 247-251, March 1995.
- [2] Zhu, J. "Well-defined Series and Parallel D-Spectra for Linear Time-Varying Systems," *Proc. Amer. Control Conference*, 734-738, Baltimore, MD, June, 1994.
- [3] Zhu, J. and Johnson, C. D. "Unified Canonical Forms for Matrices Over a Differential Ring," *Linear Algebra and Its Appl.*, Vol. 147, 201-248, March 1991.
- [4] Zhu, J. and Xiao, W., "Intelligent Control of Time-Varying Dynamical Systems Using CMAC Artificial Neural Network," *Mathematical and Computer Modeling*, Special Issue on Neural Networks, Vol. 21, No. 1/2, 89-107, 1995.
- [5] White, D. P., Wozniak, J. G. and Lawrence, D. A., "Missile Autopilot Design Using a Gain Scheduling Technique," *Proc., 26th IEEE SSST*, 606-610, March, 1994.
- [6] Lawrence, D. A. and Rugh, W. J., "Gain Scheduling Dynamic Linear Controllers for a Nonlinear Plant," *Proc. the 32nd IEEE CDC*, 1024-1029, Dec. 1993.
- [7] Nichols, R. A., Reichert, R. T. Rugh W. J., "Gain Scheduling for H-Infinity Controllers: A Flight Control Example," *IEEE Trans. on Control Systems Technology*, Vol. 1, No. 2, 69-79, 1993.
- [8] Gopalswamy, S. and Hedrick, J. K., "Control of a High Performance Aircraft with Unacceptable Zerodynamics," *Proc. 1992 ACC*, 1834-1838, June, 1992.

Acknowledgment:

The author gratefully acknowledge the Air Force Office of Scientific Research, Bolling Air Force Base, and the Wright Laboratory, Eglin Air Force Base for financial support during this research. The author sincerely thanks Dr. J. Cloutier, who served as the focal point of this research, Major C. Mracek, Dr. R. Zachery and Mr. J. Evers of the MNAG branch for their inspiration and valuable discussions during this work. The author also appreciates technical support from Mr. M. Vanden-Heuvel and Ms. D. Harto of the MNAG branch.

**FATIGUE CRACK GROWTH THROUGH EXFOLIATION CORROSION
IN ALUMINUM ALLOY 7075-T651**

Thomas B. Mills
Graduate Student
Department of Mechanical Engineering

University of Utah
3209 MEB
Salt Lake City, UT 84112

Clare A. Paul
Wright Laboratory
Fatigue, Fracture, & Reliability Section

Final Report for:
Graduate Student Research Program
Wright Laboratory

Sponsored by:
Air Force Office of Scientific Research
Bolling Air Force Base, DC

and

Wright Laboratory, Flight Dynamics Directorate
Fatigue, Fracture, & Reliability Section

November 1995

FATIGUE CRACK GROWTH THROUGH EXFOLIATION CORROSION IN ALUMINUM ALLOY 7075-T651

Thomas B. Mills
Graduate Student
Department of Mechanical Engineering
University of Utah

Clare A. Paul
Wright Laboratory
Fatigue, Fracture, & Reliability Section

ABSTRACT

Exfoliation corrosion is a potentially severe form of corrosion that frequently affects high-strength aluminum, particularly 2xxx- and 7xxx-series alloys. Exfoliation degrades components such as sheets, plates, and extrusions that have highly elongated grain structures. This form of corrosion appears as a flaky lifting of the surface, but it can also attack a material sub-surface, such as within fastener holes, and may not be immediately detectable. The problem of exfoliation corrosion in high-strength aluminum alloys has been traced to the presence of copper and zinc, which are both primary strengthening elements. Copper also has been blamed on increased susceptibility to pitting and stress corrosion cracking in these alloys.

While several methods have been developed over the last few decades to evaluate the susceptibility of high-strength aluminum alloys to exfoliation corrosion, few attempts have been made to investigate the effects of this form of corrosion on the fatigue performance of these materials. Therefore, a preliminary study was conducted to determine the effects of exfoliation corrosion on the fatigue response of 7075-T651 aluminum alloy plate.

Fatigue crack growth experiments were conducted in both dry air and humid air environments on specimens exhibiting either no corrosion damage or exfoliation damage approximately 0.008 inch in depth on one surface. The fatigue lives of the corroded specimens were as much as three times shorter than their uncorroded counterparts. The increase in crack growth rates evident in the corroded specimens during the dry air series of experiments were statistically significant below 7 ksi $\sqrt{\text{in.}}$ A similar difference seemed to exist in the wet air conditions, but no statistical evaluation was conducted since time precluded the completion of more than one corroded/humid air test.

The data suggest that the acceleration in crack growth rate caused by the corrosion can not be solely explained by the loss in thickness. It is suspected, as others have proposed, that embrittlement in the material may be responsible for part of the growth rate difference. However, future experiments coupled with extensive fractography will be necessary to clarify this issue.

FATIGUE CRACK GROWTH THROUGH EXFOLIATION CORROSION IN ALUMINUM ALLOY 7075-T651

Thomas B. Mills and Clare A. Paul

1.0 INTRODUCTION

The C/KC-135 family of aircraft first entered service in the United States Air Force (USAF) in 1957. A large fleet of these aircraft is still maintained and operated by the USAF, but despite the fleet's age in years, these aircraft have not accumulated a large number of flight hours (hence, cycles). Thus, these aircraft are still fairly young in terms of use, and this is encouraging since the KC-135 will undoubtedly be required to endure many more years of service. If the continued use of these aircraft is to be successful, however, many problems will have to be dealt with effectively.

One of these problems is nature. Nature inevitably gets its way regardless of the time an aircraft is airborne, and its influence on the KC-135 is no exception. Many of these 38-year-old airframes are suffering from corrosion problems, and this raises many complicated issues. For instance, since the KC-135 is a low-time aircraft, much of the corrosion damage occurs while the aircraft is parked on the tarmac. The corrosion damage which accumulates during these idle times (precorrosion) may be affecting material and structural response characteristics such as residual life, residual strength, and crack growth behavior. Unfortunately, barring a few exceptions [1-7] precorrosion effects on these characteristics have not been widely studied, so the severity of potential problems is still largely unknown.

To help add some information to the deficient precorrosion/fatigue database, fatigue and corrosion fatigue studies were conducted on panels of 7075-T651 aluminum. Some of the panels were precorroded using a standard test solution known as EXCO.

Many researchers have worked to determine the effects of other types of corrosion, mainly pitting, on the fatigue response of high strength aluminum alloys. Also, the literature is deluged with studies of environmentally assisted crack propagation mechanisms such as stress corrosion cracking and corrosion fatigue. Exfoliation is an extremely common form of corrosion that occurs in all types of aircraft, but its significance continues to be undermined. Exfoliation's interaction with other failure modes, such as fatigue, needs to be understood more completely.

The *Compilation of ASTM Standard Definitions* defines exfoliation corrosion as the following:

"Corrosion that proceeds laterally from the sites of initiation along planes parallel to the surface, generally at grain boundaries, forming corrosion products that force metal away from the body of the material, giving rise to a layered appearance" [8].

Since the 1940s, several test methods have been developed to evaluate the susceptibility of copper containing aluminum alloys (such as 2024, 7075, and 7178) to exfoliation corrosion. Because of the success of these test methods, the susceptibility of these alloys to exfoliation corrosion is now

well documented, but the literature addressing the corresponding effects on structural integrity appears to be deficient. Thus, these authors elected to investigate the effects of this type of corrosion on the fatigue response of alloy 7075-T651 in quarter-inch plate by applying cyclic loads to exfoliated panels and determining the change in crack growth rates through the corroded sections. The procedures used to introduce the corrosion damage and fatigue loads are discussed shortly. Furthermore, the results of these experiments illustrate a need to revise the current views on exfoliation corrosion. However, a brief background of exfoliation in high-strength aluminum alloys precedes these discussions.

2.0 BACKGROUND of EXFOLIATION STUDIES

As mentioned earlier, exfoliation corrosion is a specific form of intergranular corrosion that affects materials with a highly elongated grain structure. Such materials are often used in the construction of aircraft in the form of sheets, plates, and extrusions. This failure mode plagues the high-strength aluminum alloys used in these applications, and the reasons for this are discussed below.

2.1 *Exfoliation Susceptibility*

Copper-containing aluminum alloys are particularly susceptible to exfoliation, a specific type of intergranular corrosion, because of their high activity in the galvanic series. The galvanic couples that cause intergranular attack in Al-Zn-Mg-Cu alloys are inherent to these materials. The driving potentials are shared between the grain bodies and grain boundaries in these alloys and are a result of the heat treatment processes necessary to achieve the remarkably high strengths characteristic of 2xxx- and 7xxx-series aluminum. The heat treatment processes cause the copper and zinc in solution to migrate away from the grain boundaries. Since aluminum is anodic to copper in the galvanic series, the grain boundaries preferentially corrode leading to a phenomena known as intergranular corrosion.

Since 1968, many researchers have developed methods to determine the susceptibility of high-strength aluminum alloys to intergranular attack, particularly exfoliation [9,10]. However, the EXCO test solution was later adopted into *ASTM Standard G34-72, Standard Test Method for Exfoliation Susceptibility in 7xxx-Series Copper Containing Alloys*, later *G34-90* [11]. Note that the key word here is "susceptibility." Neither the EXCO test nor the other tests make an attempt at evaluating the effects of exfoliation corrosion on the structural integrity of these materials, be the applied loads sustained or dynamic. In fact, it appears that very little work has been done to evaluate these effects, possibly because the problem of exfoliation is often regarded as minimal as will be evident in the following paragraph.

2.2 *Deficiencies in the Current Views of Exfoliation Corrosion*

The *ASM Handbook on Corrosion* states that exfoliation corrosion has been of interest for several decades because susceptibility to intergranular attack is considered a prerequisite to stress corrosion cracking (SCC) [12]. However, this reference continues by explaining that exfoliation itself is not of concern because it is a surface phenomenon that is *easily detectable*, that it *proceeds to only a limited depth*, and that *does not result in sudden failures* as does SCC. This author finds that discussion unsatisfactory for a number of reasons:

- 1) Aircraft structural members have been completely consumed by exfoliation corrosion nullifying the limited depth argument [13].
- 2) Many aircraft structural components that suffer from exfoliation corrosion (such as stringers and internal surfaces of wing skins) are hidden from view and are, by default, not readily inspectable. Consequently, damage may only be discovered every few years during heavy maintenance checks [13].
- 3) While failure from exfoliation has not proved to be sudden, resulting damage has been shown to cause sufficient stress concentrations to nucleate *multiple* fatigue cracks, and therefore, may be viewed as a multiple-site damage (MSD) mechanism [1,4].
- 4) Studies have shown that fatigue crack growth rates through exfoliated material can be higher than in uncorroded material [2].

2.3 Studies of Exfoliation/Fatigue Interactions

The experience referenced in item three above came from an investigation by Shaffer et al. into cracks detected in the wing spar cap of a Navy air-sea rescue aircraft. Fatigue life in the exfoliated material was reduced up to 70%, and metallographic examination of the post-test specimens showed that the corroded laminar paths were preferential sites for fatigue crack nucleation. The exfoliation problems originated deep inside rivet holes that suffered pitting attack under crevice corrosion conditions. The resulting corrosion damage was undetectable by normal visual observation, and in all cases, the intergranular corrosion cracks propagated from corrosion pits. As many as twenty cracks were detected (via ultrasonic inspection) emanating from a given area.

The multiple-site damage generating nature of exfoliation corrosion was further affirmed by Mills in precorrosion/fatigue, stress-life tests. The damage reduced the fatigue life of 7075-T651 dogbone specimens at least 20 times. The undamaged specimens did not fail after 5,000,000 cycles and reached an end-of-test condition. The corroded specimens failed, on average, at 250,000 cycles [4].

In 1991, Chubb et. al. [2] investigated crack growth behavior in precorroded aluminum alloys. Specimens were manufactured from 7178-T6 and 2024-T351 aluminum panels pulled from an aircraft that had been in service for fifteen years. Exfoliation damage was introduced artificially using the EXCO solution (outlined later), and the materials were tested in both wet and dry air.

In the 7178-T6 material, the wet-air condition showed an increased crack growth rate compared to the dry-air condition, and the presence of exfoliation corrosion further increased the crack growth rate. In the dry air tests, exfoliation corrosion accelerated crack growth rates by a factor of three. This effect was not as detectable in the 2024-T351 specimens.

Chubb et. al. expanded this work somewhat in 1994 [3] and investigated the effects of exfoliation on fracture toughness in 7178-T6. The tests were of the crack growth resistance curve (or R-curve) variety, and they concluded that exfoliation corrosion had a limited effect on the toughness. Other efforts in this study focused on determining the cause for the accelerated growth rates (which varied between factors of two and five in the dry-air condition); however,

Chubb concluded that the effects of exfoliation on fatigue “cannot be fully explained by a single mechanism such as loss of section thickness, hydrogen charging or other chemical effects.”

A study conducted Hoeppner et al. in 1994 [5] showed that service corrosion on 2024-T3 aluminum panels pulled from a KC-135 aircraft undergoing maintenance had widely variable effects on crack growth rates as compared to uncorroded service panels. In some cases, growth rates were two or three times higher in the corroded material, but in other cases, little difference was seen.

Koch, Hagerdorn, and Berens [6] studied precorrosion effects on crack growth in both 2024-T3 and 7075-T6. They concluded that precorrosion did not affect crack propagation rates in the 2024 material but accelerated rates in the 7075 material. As Chubb found [2,3], changes in stress intensity did not completely explain the accelerated growth rates. Koch attributed the remaining difference to hydrogen-assisted fracture.

Schuering and Grandt conducted crack growth experiments using material from wing skin and fuselage panels of retired KC-135 aircraft [7]. These studies showed that moderate precorrosion damage in alloy 2024-T3 accelerated the crack growth rates ($R = +0.1$) in that material compared to handbook data. These investigators also conducted crack growth rate experiments in 7075-T6 and 2024-T3 but at a higher stress ratio ($R = +0.5$). They concluded that the corrosion effects diminished at the higher R value as compared to handbook data. Again, as Chubb [2,3] and Koch [5] found, the increases in crack growth rates reported by Schuering could not be linked solely to an increase in stress intensity associated with the corrosion damage.

The work presented in this report further supports the findings of Chubb, Koch, and Schuering, and these results mark (in part) the avenues that must be traveled to better understand exfoliation corrosion with regard to structural integrity and aviation safety. All of the experimental procedures, results, and recommendations are detailed in upcoming sections.

3.0 TEST PROGRAM

3.1 Specimen Design

The coupons were designed in accordance to *ASTM Standard E 647-93, A Method for Determining Fatigue Crack Growth Rates in Metallic Materials* [14]. The specimens were 12 inches long, three inches wide, and were fabricated from quarter-inch, 7075-T651 aluminum plate. They contained a 0.600 inch center notch that was cut using a wire electro-discharge machining (EDM) process. Load direction on the specimens was oriented in the longitudinal grain direction, and crack propagation was limited to the long transverse grain direction.

3.2 Test Matrix

The original goal of this experimental program was to evaluate twenty fatigue crack growth specimens subjected to four combinations of conditions. A list of the different material and environment conditions and combinations follows:

- Five dry air tests without previous corrosion damage.
- Five high humidity tests without previous corrosion damage.

- Five dry air tests with exfoliation damage.
- Five high humidity tests with exfoliation damage.
- **Total number of tests: 20**

Each specimen carried an identification number, and this number contained information about the chemical environment and corroded condition. For instance, the tests conducted in dry air using the specimens with no corrosion damage carried the prefix of **DAU** (for Dry Air Uncorroded). Similarly, the humid air companions to the uncorroded tests were denoted by **HAU**. The exfoliated counterparts to the above two chemical environments carried the prefixes of **DAE** and **HAE**.

As was just mentioned, the original goal was to test twenty specimens. However, unforeseen complications made this goal unattainable, and the test program was limited to thirteen specimens. The specimens tested are summarized in section four.

3.2 Introducing Exfoliation Damage

In order to introduce exfoliation corrosion damage in certain specimens, some were subjected to an EXCO solution as outlined in *ASTM Standard G 34-90, Standard Test Method for Evaluating the Susceptibility to Exfoliation Corrosion of 2xxx- and 7xxx-series Aluminum Alloys*. The other specimens were tested in the as-received condition. The EXCO solution, outlined below, produces exfoliation damage rapidly in the plate form of alloy 7075. Depth of attack consuming 3-5% of the cross section was achieved in approximately 52 hours. After the specimens were corroded, they were placed in concentrated nitric acid (70%-wt) for thirty minutes. This step passivated the aluminum and halted the corrosive action of the EXCO solution. Finally, the specimens were rinsed repeatedly using tap water to remove the nitric acid. Most of the specimen surface area was covered in paraffin wax to protect it from the precorrosion process. Approximately a 1.5 sqin. area on either side of the notch was corroded in line with the expected crack path (Figure 1).

The EXCO solution used to exfoliate the specimens consisted of sodium chloride (NaCl), potassium nitrate (KNO₃), and nitric acid (HNO₃) in the following concentrations:

- 1) NaCl (4.0 M; 234 g/ℓ),
- 2) KNO₃ (0.5 M; 50 g/ℓ), and
- 3) HNO₃ (0.1 M; 6.3 ml/ℓ).

The chemicals were reagent grade, and they were all mixed with 18 MΩ deionized water. According to Standard G 34, this solution has an initial apparent pH of 0.4 which increases to approximately 4 after 48 hours [11]. The damage wrought after 52 hours of exposure to the EXCO solution was similar to level "D" as explained in the standard noting considerable depth of penetration into the metal.

3.3 Mechanical Testing

The specimens were tested in a ten-kilopound-capacity load frame. The load frame was equipped with a ten-kip actuator and load cell and was complimented with 22 kip hydraulic grips from Material Test Systems (MTS). An MTS 407 Controller was used to supply the load signal, and crack progress was monitored using a myriad of techniques. Optical microscopes were used in all tests, but were particularly useful in determining the agreement of data collected via Krak-Gages and clip gages (discussed shortly).

Maximum, minimum, and mean load data were all collected using a NEFF 470 data acquisition system in conjunction with Labview II software. The NEFF also was used to accumulate Krak-Gage information and clip-gage information, depending on the type of automated crack length monitor used.

The specimens were subjected to a sinusoidal wave and an initial stress intensity (after precrack) of 5.5 ksi $\sqrt{\text{inch}}$. The frequencies used in the testing were 1 and 10 Hz, and their use in different conditions is shown in Table 1 below. The procedures discussed in ASTM Standard E 647-93 were followed for precracking operations.

Operation	DAU Tests	HAU Tests	DAE Tests	HAE Test
Precrack f (Hz)	10	10	10	10
Test f (Hz)	10	1	10	1

Table 1: Test frequency (Hz) for various experimental conditions.

3.4 Data Collection and Reduction Methods

Two methods for automatically obtaining crack length information were used in these fatigue experiments. These were the Krak-gage and the clip gage. In addition to these instruments, an optical microscope was used to check the performance of the automated equipment.

3.4.1 Krak-gages

Krak-gages, developed by Hartrun, are essentially thin foil gages that report crack length as a function of the increase in resistance in the gage. As the condition of the gage progresses from uncracked to fully cracked, the resistance increases approximately 1 Ohm, and this increase is linearly related to the crack length. The output of the gage exhibits a small amount of non-linearity at short crack lengths, but this problem is easily absorbed by the precracking process which, in this case, extended fatigue cracks a total of 0.050 inch from each end of the machined notch in the M(T) specimen.

High temperature (-HT) gages were selected for this study because, according to the manufacturer, they were more stable and, therefore, produced more accurate readings. The gages were affixed to the specimens using adhesive supplied with the gages.

3.4.2 Clip Gage (Compliance Measurements)

The second instrument used to automatically monitor crack growth during these experiments was the clip gage. An MTS 632.01 clip gage was mounted on the center line of the specimens so that it spanned the center notch. The gage was held in place using steel knife-edges which were attached to the specimen using M-Bond 200 strain gage cement.

The principle behind compliance-based crack measurement is rather simple; however, the equations used to calculate these values are not so simple. Fortunately, several investigators have worked extensively on this problem, and the relationships can be found in *ASTM E 647*.

Compliance-based crack measurement exploits the fact that as a crack extends through a specimen being subjected to load control, the displacement of the specimen increases. This displacement can be measured using a clip gage. Data from the clip gage and from the test frame's load cell are used to produce a load-displacement plot.

By retrieving the reciprocal slope from the linear portion of the load-displacement plot, and by using the specimen thickness and an estimate of tensile elastic modulus, the normalized compliance can be estimated:

$$\text{Normalized Compliance} = \frac{EBV_Y}{P}$$

where; B=thickness, V_Y =gage displacement, P=load, and E=modulus.

Then, by using the equations outlined in *ASTM Standard E 647*, crack length can be calculated. The equations used are shown below:

$$x = 1 - e^{-\frac{\sqrt{(EBC + \eta)(EBC - \eta + c_1\eta + c_2\eta^{c_3})}}{2.141}}$$

where; $C = V_Y/P$ =compliance, $\eta = 2Y/W$ =nondimensional gage length, and c_1 , c_2 , and c_3 are constants dependent on loading conditions. In this case, $c_1=c_2=c_3=0$.

The value x is then substituted into the following polynomial to yield crack length.

$$2a = W(1.06905x + 0.588106x^2 - 1.01885x^3 + 0.36169x^4)$$

This procedure yields $2a$ vs. N data, and these data can then be reduced to crack growth rate curves by using a number of numerical methods and curve fits. These growth rate data were reduced using the secant method.

4.0 EXPERIMENTAL RESULTS and DISCUSSION

The results of these experiments reveal some interesting trends. The discussion will be divided amongst three basic areas:

- revelations of the data,
- success of the different crack length monitoring techniques, and
- macroscopic observations of the specimen fracture behavior.

A discussion of the observed changes in crack growth rates and fatigue lives between the different experimental conditions is offered first. Most of these discussions will focus on the dry air testing since two-thirds of the specimens tested during the program were represented by that environmental condition. The humid air testing (the remainder of which still will be done) showed some interesting trends, but too little data were generated to make any solid conclusions. Therefore, unless otherwise stated, please assume that the discussion refers to the dry air tests.

4.1 Changes in Fatigue Lives and Crack Growth Rates

The fatigue lives of all the samples were recorded, and the relationship between crack length and cycles were compared. The mean lives for the different test conditions varied from the dry air/uncorroded (control group) by factors of 1.89 to 3.18. From Figure 3, which shows 2a vs. N, these vast differences in fatigue lives are evident. Notice how the slopes for the corroded specimens initially climb much steeper than the curves for the uncorroded specimens. As the cracks reach greater lengths in the corroded material, the slopes of the 2a vs. N curves appear to approach those of the uncorroded data. In other words, it appears that the cracks in the corroded material spent less time in the lower stress intensity regimes. These results are again reflected in the crack growth rate curves.

The fatigue crack growth curves (Figure 4) show the accelerated crack growth rates (at the lower stress intensities) in the corroded material. It appears that as one moves down the $da/dN-\Delta K$ curves, the corroded and uncorroded data (dry air) separate at approximately 10 ksi $\sqrt{\text{in}}$. Near 5 ksi $\sqrt{\text{inch}}$, the apparent maximum difference in crack growth rate is represented by a factor of three. The values of crack growth rate between the DAU and DAE tests appear to be significantly different up to the alternating stress intensity of 7 ksi $\sqrt{\text{in}}$. This fact is shown in Figure 5, as the DAE data points fall outside of the 5%-95% confidence interval calculated for the DAU data.

A similar trend is seen in the specimens subjected to high humidity during fatigue testing. The growth rate curves (moving down from higher stress intensity) appear to diverge at an approximate value of 12 ksi $\sqrt{\text{in}}$. Unfortunately, since time constraints yielded only one specimen that had been tested in the corroded/high humidity condition (HAE-01), it was difficult to draw many conclusions. However, it seems as if a similar trend between the corroded and uncorroded specimens in both the dry and wet environments exists. These interactions certainly warrant further research.

The growth rate differences between the wet and dry uncorroded specimens are readily apparent from Figure 4. As a rule, the families of curves parallel each other throughout the complete stress intensity range, and the approximate difference in growth rates is a factor of two. Finally, a large difference exists between the crack growth rates of the DAU tests and the HAE test, particularly

at lower stress intensities such as 6 ksi $\sqrt{\text{inch}}$. At this stress intensity level, the HAE crack velocity is nearly one order of magnitude higher than the in the DAU samples.

4.2 Success of Optical Microscopes, Krak-gages, and Compliance

The optical microscopes primarily served as watchdogs over the Krak-gage output and Clip-gage-derived crack length data. In other words, this well-proven device simply verified that the data from the automated systems were believable. The progress of the first four DAU tests was monitored solely with the traveling microscopes, as the automated data acquisition system was not on line yet. However, as soon as the NEFF 470 system and related software had been modified to collect the Krak-gage and clip gage data, the optical scopes assumed the watchdog role.

The Krak-gages seemed to work very well, and the optical data collected on one face of specimen DAU-05 agreed nicely with the Krak-gage data. The biggest advantage to using the Krak-gages was the simplicity of the output. As the specimen cracked, the gages cracked, and the output signal was displayed directly as crack length (mm) on the Fractomat signal processor. The Fractomat also featured limit detectors which could be set to stop the test after a crack reached a desired length.

The drawbacks to using the HT gages was that they were brittle and fragile and somewhat costly. Preparation time was longer than that necessary to prepare a specimen for compliance readings, as the setup time for Krak-gages was usually two days as opposed to 30 minutes. Another disadvantage of the Krak-gages was that the surfaces to which they were bonded needed to be extremely smooth. Therefore, it was not possible to bond the Krak-gages to the corroded side of the specimens. This arrangement was not ideal since it was desired to observe whether or not the crack front on the corroded surface grew faster than the crack front nearer to the uncorroded surface. Also, the condition of the corroded surface forbade the use of an optical microscope to accurately determine the crack length in those regions, as it proved too difficult to resolve the crack tip.

With these disadvantages in mind, it was decided to rely heavily on compliance as a better technique for automated data acquisition. The advantage of this system was that the output of the clip gage could be related to average crack length. This fact and others are discussed in the next paragraph.

The compliance-based crack length measurements were much more difficult to calculate than the Krak-gage output. Fortunately, this drawback was outweighed by the ease of setup. Location of the knife edges on the specimen face is imperative for the successful use of the compliance equations, as the crack length calculated from compliance information is heavily dependent on this "gage length." Since the knife edges were glued on, it was impossible to know exactly what the value for gage length was for each test. Therefore, optical data were recorded early in the test, and the gage length used in the compliance calculations was adjusted to yield the appropriate crack lengths. After this correction was completed, the optical "check data" and the compliance readings agreed relatively well. The compliance-based crack lengths were typically a few thousandths longer than the optical lengths, but this discrepancy is easily absorbed by a number of observations.

- It was often difficult to resolve the precise location of the crack tips using the optical microscope.
- The cracks in the corroded specimens typically grew faster on the corroded face than on the uncorroded face (optical measurements were taken on the uncorroded face).
- The cracks tended to tunnel in the center of the specimen's cross-section. This process was captured by the compliance readings but was not observable through the optical scope.

In hindsight, it would have been better to mechanically fasten the knife edges to the specimen faces thus reducing the variability in the gage length. This would have made it possible to characterize the accuracy of the compliance technique.

4.3 Macroscopic Observations of the Fracture Behavior

Finally, some simple macroscopic observations of the fracture behavior suggest an embrittlement effect of the precorrosion. Although additional testing and fractographic examination through a scanning electron microscope are definitely necessary to fully support the possibility of embrittlement, some discussion is still offered to promote thought.

As the cracks grew from the center notch, fracture occurred on a plane perpendicular to the applied load. When the cracks extended to greater length, crack rotation occurred, and subsequent propagation occurred as slant, or shear, fracture. However, crack rotation was delayed in the humid air tests and at the corroded surfaces of the exfoliated specimens. Table 2 shows the approximate crack length and corresponding alternating stress intensity at which rotation began for the different conditions. The row in the table labeled "surface" refers to the corroded and uncorroded surfaces of the DAE and HAE tests only.

Test type	DAU	HAU	DAE		HAE	
Surface			Uncorroded	Corroded	Uncorroded	Corroded
ksi $\sqrt{\text{in.}}$	11.0	14.9	11.0	14.9	14.9	19.0
2a (inch)	1.97	2.36	1.97	2.36	2.36	2.60

Table 2: Stress intensities and crack lengths at which crack rotation occurred

Earlier studies of the corrosion fatigue behavior of aluminum alloys have discussed similar findings. In 1972, Krupp, Hoeppner, and Walker [15] reported that in aggressive environments, high crack rates occur without measurable crack rotation. This paper continues by stating that in thinner materials near the point of crack rotation, the combined effects of cyclic rate and corrosive environments diminish. Thus, subsequent crack growth is driven more by the stress intensity.

In 1981, Vogelesang [16] researched this phenomenon further and concluded that aggressive environments suppress shear lip formation. He stated that the environment reduced the stress necessary for fracture and promoted tensile mode cracking, and he observed that this crack rotation was diminished in both plane stress and plane strain conditions. From these results, he concluded that a correlation between stress state and cracking mode did not exist.

From the data generated in this testing program, it is apparent that, in general, precorrosion has an effect on crack rotation akin to that of aggressive chemical environments. Table 2 shows that crack rotation at the corroded surfaces in the DAE tests occurred at approximately 15 ksi $\sqrt{\text{in.}}$. This is the same stress intensity at which the cracks rotated in the humid air tests. When precorrosion damage was superimposed upon the humid air environment, shear lip formation was delayed even more and did not occur until the alternating stress intensity value reached 19 ksi $\sqrt{\text{in.}}$

The suppression of shear lips on the precorroded surfaces of the DAE and HAE specimens could be explained as follows: First, as stated in [15], crack rotation is thought to occur when the stress state at the crack tip shifts from triaxial to biaxial. This shift may be viewed as having taken place when the plastic zone increases in size from the triaxial to the biaxial state. It is possible that the corrosion damage at the surface maintained a triaxial stress state at that crack tip long after the side of the crack at the uncorroded surface had rotated. Furthermore, any embrittlement of the material near the surface would suppress plastic flow and, hence, the formation of shear lips. Perhaps a combination of these two factors is to blame for the delayed onset of crack rotation observed in these experiments.

5.0 CONCLUSIONS

The results of this study yield the following conclusions:

- 1) Fatigue lives of corroded specimens were reduced by factors ranging from two to three compared to the DAU baseline specimens. Examination of the $2a$ vs. N curves showed that the initial slopes were much steeper in the corroded cases.
- 2) Precorrosion damage in the form of exfoliation accelerates the fatigue crack growth rates in 7075-T651 aluminum at lower stress intensities. In a dry air environment, the ratio is represented by a factor of 3 at an alternating stress intensity of approximately 5 ksi $\sqrt{\text{in.}}$. As the stress intensity increases, however, the effects of precorrosion appear to diminish. At approximately 7 ksi $\sqrt{\text{in.}}$, the differences in growth rate become statistically insignificant.
- 3) The addition of a more aggressive environment (humid air) to the scenario results in a still greater increase in growth rate, and the contribution of corrosion damage is still discernible in the midst of the humid air effects. The crack growth rates in the best case (dry air/uncorroded) and the worst case (humid air/exfoliated) initially differ by an order of magnitude.
- 4) Increases in stress intensity caused by the reduction in cross section from corrosion do not completely account for the increases in crack growth rates shown at lower stress intensity values.

- 5) Crack rotation (shear lip formation) was delayed both by the introduction of precorrosion damage and the humid air environment. The contribution of the humid air was expected and is well documented. However, the reasons behind the similar effect from precorrosion are more mysterious. This effect could be a result of increased complexity of the crack tip stress state near the corroded surface, or it could be a result of embrittlement. A combination of these two effects also may be responsible.
- 6) Crack-gages yield accurate surface crack growth rate information. However, the necessity for a smooth surface for gage application precludes their use on corroded material.
- 7) Compliance techniques yield more useful information in the crack growth of precorroded material since crack tunneling and asymmetric crack growth between corroded and uncorroded surfaces can be detected.

6.0 RECOMMENDATIONS

The following recommendations are designed to help obtain more concrete data on the effects of precorrosion on crack growth rates in 7075-T6 aluminum.

- 1) Constant-K tests would offer distinct advantages over increasing-K tests as future experiments are used investigate growth rates at stress intensities both below and above the point where the pilot data "converge." By collecting numerous data points, increased statistical confidence in the differences will be gained via the large sample size.
- 2) Fractographic investigations of failed specimens must be conducted to search for evidence of embrittlement. Changes in the micromechanisms of fracture as distance from the corroded surface increases may be a good indication of embrittlement.
- 3) Some of the specimens should be "baked" before fatigue testing in an attempt to drive off any hydrogen or other species that may be embrittling the material. This added step may reduce increases in crack growth rates to the point that stress intensity-based (reduction in thickness) adjustments solely explain any remaining differences. It would be useful to observe the shear lip formation to see if the baking shifts the crack rotation point.
- 4) Chemicals other than EXCO should be used along with the latter to preocorrode different specimens. Any embrittling in the specimens could be the result of the extreme severity of the EXCO solution. Corrosion induced by artificial acid rain or simply 3.5% salt water, for instance, may yield very different results.
- 5) Crack nucleation mechanisms associated with precorrosion damage need to be more closely examined and the impacts on structure determined. These effects are a large source of concern with regards to structural integrity and aviation safety.

7.0 REFERENCES

[1] Shaffer, I. S., Sebastian, J. C., Rosenfeld, M. S., and Ketcham, S. J., "Corrosion and Fatigue Studies of Extruded 7075-T6 Spar Caps," *Journal of Materials*, JMLSA, Vol. 3, No. 2, June 1968, pp. 400-424.

[2] Chubb, J. P., Morad, T. A., Hockenhull, B. S., Bristow, J. W., "The Effect of Exfoliation Corrosion on the Fatigue Behavior of Structural Aluminum Alloys," *Structural Integrity of Aging Airplanes*, 1991, pp. 87-97.

[3] Chubb, J. P., Morad, T. A., Hockenhull, B. S., Bristow, J. W., "The Effect of Exfoliation Corrosion on the Fracture and Fatigue Behavior of 7178-T6 Aluminum," *Int. J. Fatigue*, Vol. 17, No. 1, 1995, pp. 49-54.

[4] Mills, T. B., "The Effects of Exfoliation Corrosion on the Fatigue Response of 7075-T651 Aluminum Plate," Master's Thesis, University of Utah, June 1995.

[5] Mills, T. B., Magda, D. J., Kinyon, S. E, Hoeppner, D. W., "Fatigue Crack Growth and Residual Strength Analyses of Service-Corroded 2024-T3 Aluminum Fuselage Panels" Report to Oklahoma City Air Logistics Center and Boeing Defense & Space Group, University of Utah, May 1995.

[6] Schuering, J. N., Grandt, A. F., "An Evaluation of Aging Aircraft Material Properties," Presented at 1995 ASME Structural Integrity of Aging Aircraft Winter Annual Meeting, San Francisco, CA, 1995.

[7] Koch, G. H., Hagerdorn, E. L., Berens, A. P., "Effect of Preexisting Corrosion on Fatigue Cracking of Aluminum Alloys 2024-T3 and 7075-T6," Final Report to Flight Dynamics Directorate, WPAFB, August 1995.

[8] Compilation of ASTM Standard Definitions, 6th ed., ASTM, 1986, pg. 283.

[9] Sprowls, D. O., Walsh, J. D., and Shumaker, M. B., "Simplified Exfoliation Testing of Aluminum Alloys," *Localized Corrosion—Cause of Metal Failure*, ASTM STP 516, American Society for Testing and Materials, 1972, pp. 38-65.

[10] Romans, H. B., "An Accelerated Laboratory Test to Determine the Exfoliation Corrosion Resistance of Aluminum Alloys," *Materials Research and Standards*, MTRSA, Vol. 9, No. 11, 1969, pg. 31.

[11] ASTM Standard G34-90, "Standard Test Method for Exfoliation Susceptibility in 7xxx Series Copper Containing Alloys," 1990.

[12] Metals Handbook, 9th ed., Vol. 13, *Corrosion*, American Society for Metals, Metals Park, Ohio, 1985, pp. 584-609.

[13] Author's personal experience, Tinker Air Force Base, Oklahoma City, OK, June 1993.

[14] ASTM Standard E 647-93, "Standard Test Method for Measurement of Fatigue Crack Growth Rates", American Society of Testing and Materials, Philadelphia, 1993.

[15] Krupp, W. E., Hoeppner, D. W., Walker, E. K., "Crack Propagation of Aluminum Alloys in Corrosive Environments," *Corrosion Fatigue, NACE-2*, 1972, pp. 468-483.

[16] Vogelesang, L. B., "Fatigue Crack Growth in Aluminum Alloys," Report LR-324, Delft University of Technology, June 1981.

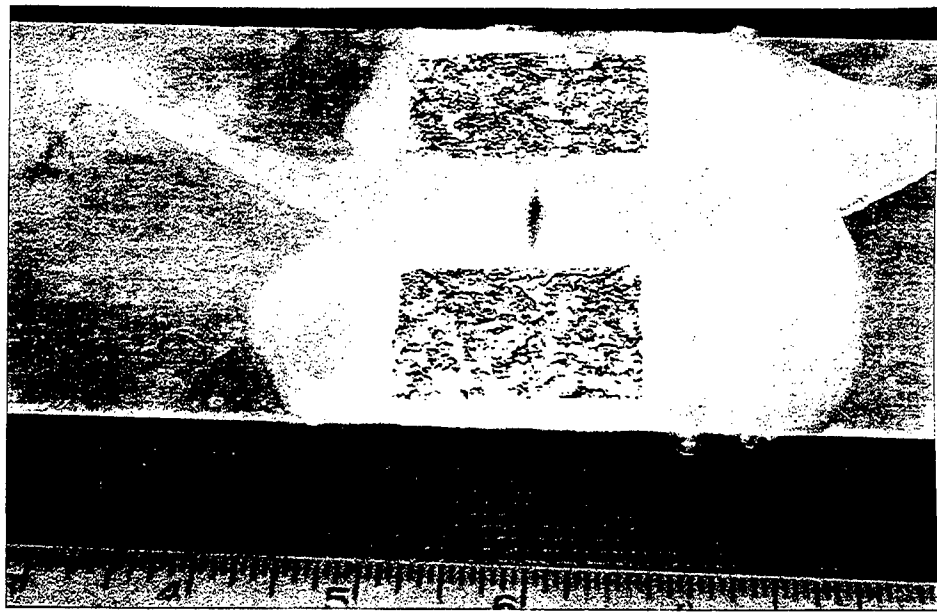


Figure 1: Specimen after exposure to EXCO solution. Note exfoliation damage and wax coating.

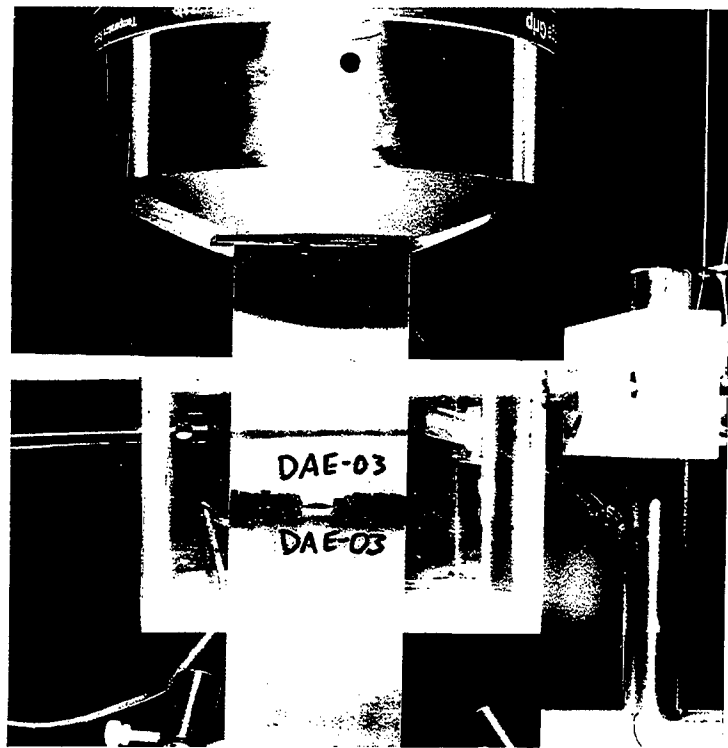


Figure 2: Specimen in load frame showing uncorroded surface and environmental chamber.

Figure 3: 2a vs. N Comparison for Dry Air and Humid Air, Uncorroded and Exfoliated, 7075-T651 Aluminum

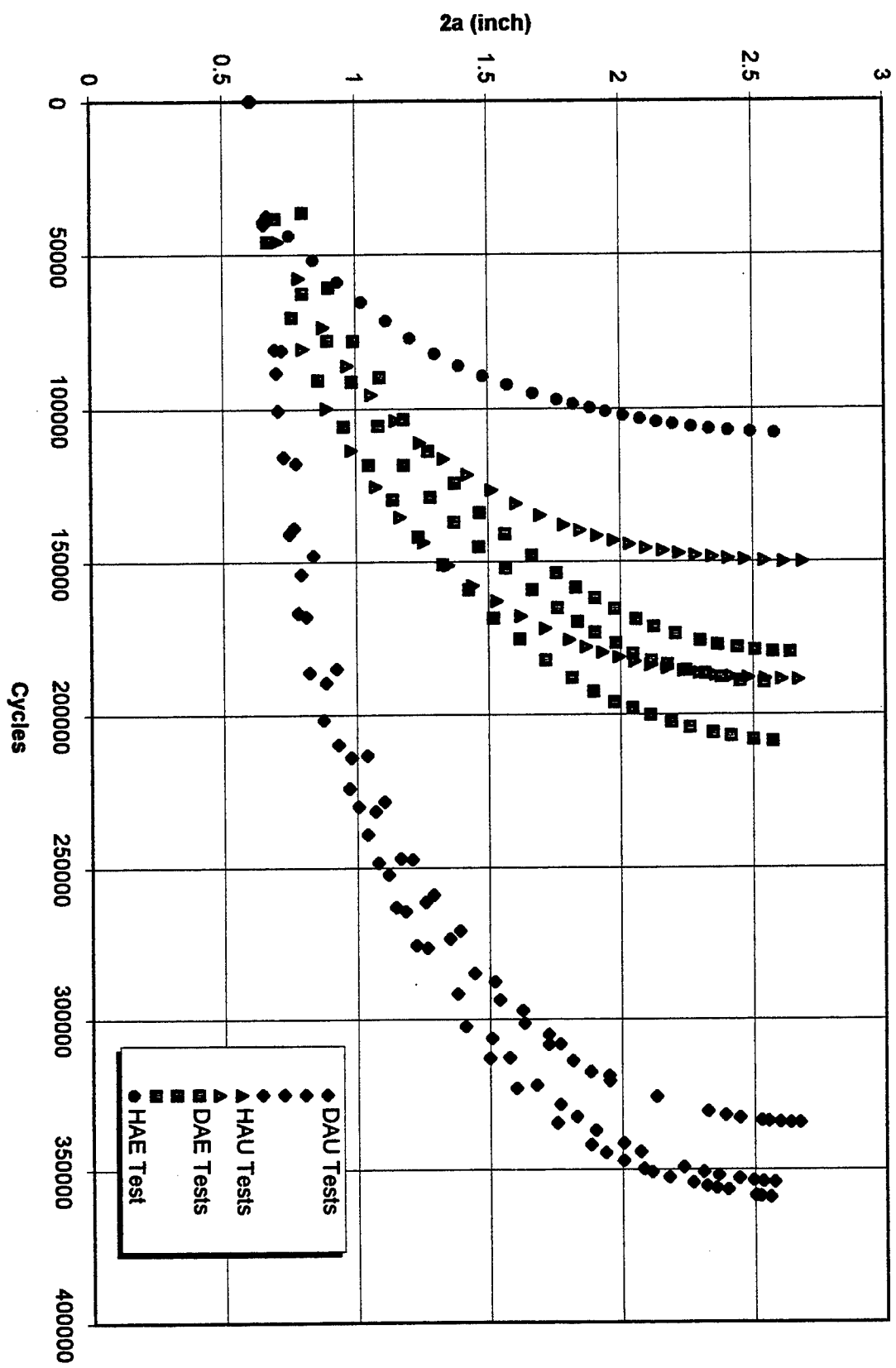
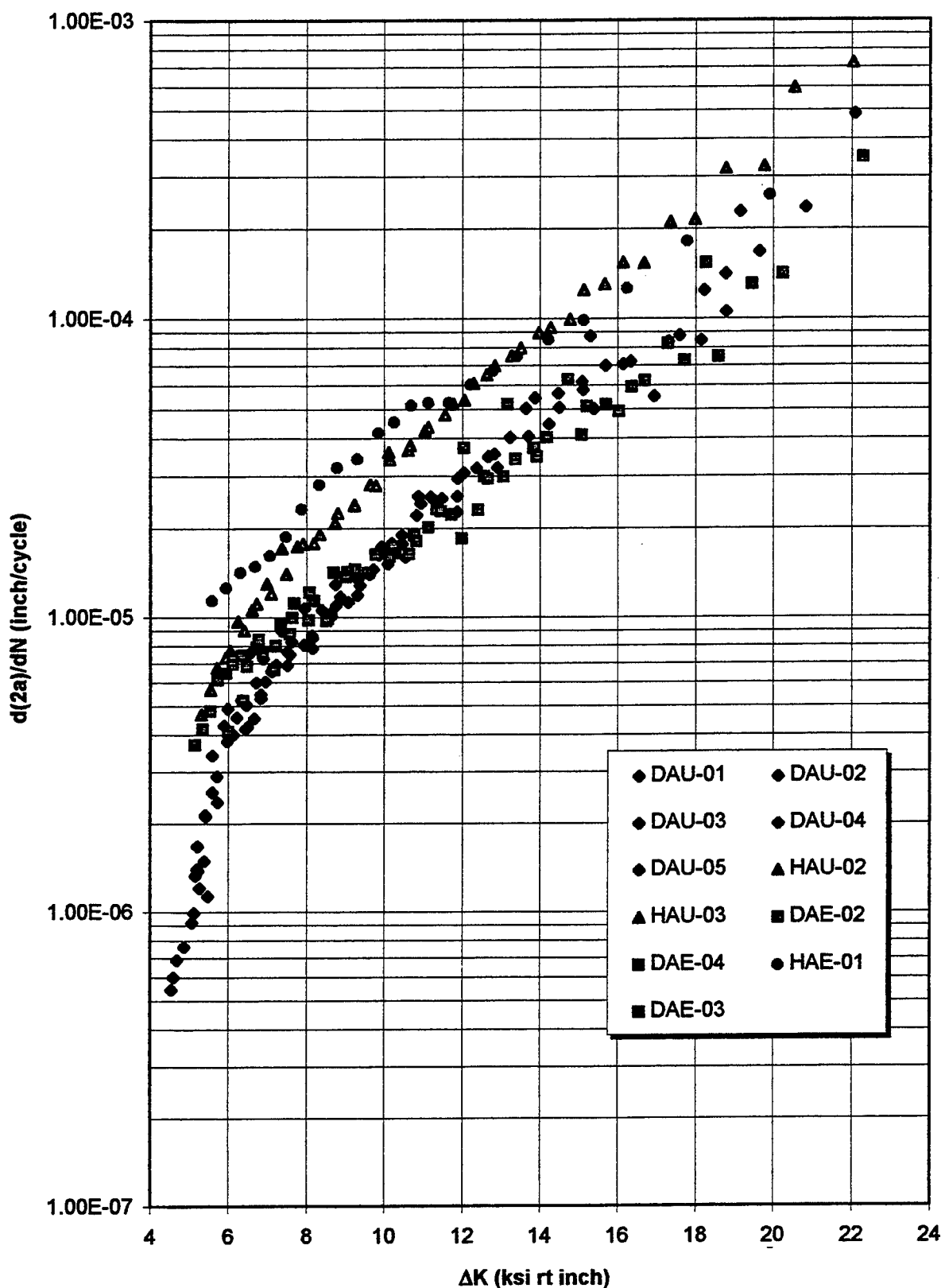
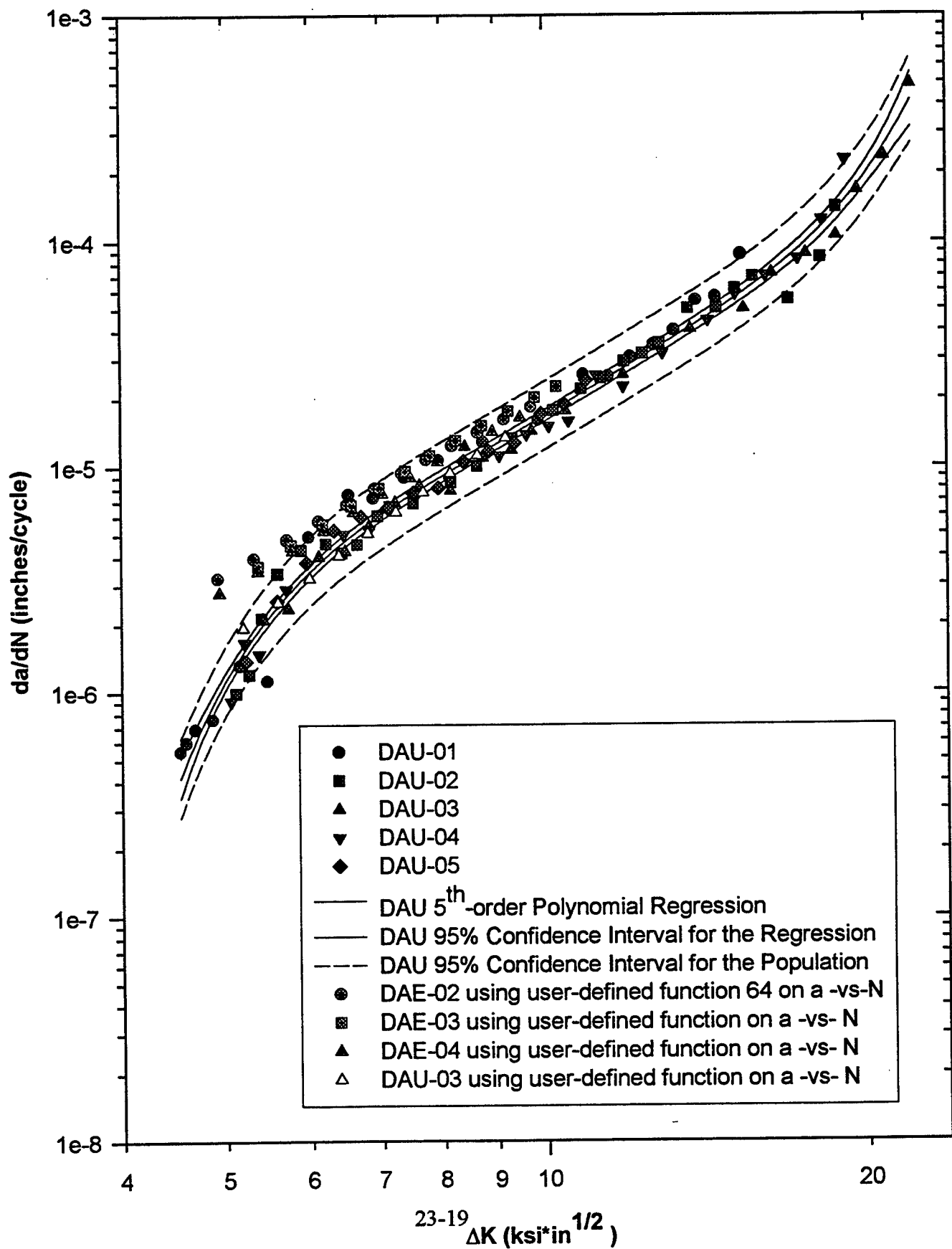


Figure 4: $d(2a)/dN$ vs. ΔK , 075-T651 Al, Corroded and Uncorroded



Effect of Prior Corrosion on Crack Growth Rate



Toward a Quantitative View of Solute-Fluid Interactions
in Supercritical Fluids

Emily D. Niemeyer
State University of New York at Buffalo
Natural Sciences and Mathematics Complex
Buffalo, NY 14260-3000

Final Report for:
Graduate Student Research Program

Sponsored by:
Air Force Office of Scientific Research
Bolling AFB
Washington D.C.

and

Wright Laboratory

October 1995

Table of Contents

Introduction	24-3
Motivation for the Work	24-4
Experimental	24-5
Results and Discussion	24-8
Future Work	24-9
References	24-10
Figure Captions	24-12

Introduction

As aircraft have become increasingly complex, the onboard fuel supply has played an important role in not only powering the aircraft, but also in cooling aircraft components. Often, the fuel is subjected to high temperatures which can potentially cause it to become supercritical. Once the fuel is raised above its critical temperature, key factors which govern the stability and performance of the fuel within the aircraft are altered. It is therefore imperative to understand the interactions which occur in these supercritical fuels in order to determine how they govern the overall performance of the aircraft. Basic research on the interactions occurring between a dissolved solute in a simple supercritical fluid system can provide fundamental insight into the interactions between solutes dissolved in more complex systems, such as supercritical aviation fuels. By developing a better molecular-level view of solute-solute and solute-fluid intermolecular interactions and dynamics in supercritical fluids, one will be poised to better control and optimize these fuels for Air Force applications.

Every pure substance exhibits a critical temperature (T_c) and pressure (P_c) defining its characteristic critical point. Below the critical point, the liquid and gas phases can exist in equilibrium; above the critical point, the two phases coalesce into a single phase - a supercritical fluid. A supercritical fluid retains many desirable properties of both gases and liquids such as favorable mass transport and increased solvation.¹ Moreover, the physicochemical properties of a supercritical fluid (e.g., refractive index (n), dielectric constant (ϵ), density (ρ), and viscosity (η)) are intermediate between those of a gas or liquid *and* can be tuned by slight changes in temperature and pressure. Thus, supercritical fluids represent completely tunable solvents.

One of the more interesting phenomena that has been observed in supercritical fluids is the increased interaction between a solute and fluid in proximity to the fluid critical point. This is often termed “solute-solvent clustering”² or “molecular charisma”.³ This solute-fluid clustering has been studied extensively using spectroscopic methods, theoretical models, and simulations.²⁻¹⁰ Supercritical fluid clustering has been shown to directly affect chemical reaction rates,^{4,5} solute conformational equilibria,⁶ and extraction processes.⁷ These clusters are also known to be dynamic in nature and constantly exchanging fluid molecules with the bulk on a very short time scale (ps-fs).⁸ The aforementioned works suggest that solute-fluid clustering is understood in part, but there is still little *molecular-level* information on solute-fluid clustering.

Motivation for the Work

The presence of clustering has been confirmed experimentally^{2-7,10} and theoretically^{8,9} but many details are still lacking. For example, although fluorescence studies have shown there to be solute-fluid clustering about an excited-state molecule, there is still much debate about the magnitude of these solute-fluid clusters and there is little evidence at all about solute-fluid clustering in the ground *and* excited state of the same species.¹⁰ Much of this information “void” arises because many of the key dynamical processes are very fast (<<ns).

Ultrafast laser spectroscopy is a tool that can provide specific information about fast phenomena occurring between a spectroscopically active solute and its local environment (e.g., solute-fluid clustering). Moreover, ultrafast techniques allow one to probe the ground and excited state on a fast time scale.^{11,12} Therefore, the goal of this summer project was to follow *directly* the ground- and excited-state dynamics, using ultrafast pump-probe spectroscopy, of a model solute in a supercritical fluid as we systematically adjust the physicochemical properties

of the fluid with pressure. By developing a view of the fundamental interactions occurring within simple supercritical solvent systems, existing models can then be applied to more complex systems (i.e., supercritical aviation fuels).

It was our desire to first study a simplified solute-solvent system before beginning measurements in a supercritical fluid. The model system that we chose for this work involved an infrared dye (HITCI and IR-125) in a liquid solvent (methanol). These and similar probes have been previously studied¹³⁻¹⁵ and the excited-state lifetime of IR-125 in methanol has been determined.¹³ In addition, the excitation and emission wavelengths for these probes are easily accessible directly with our laser system.

Experimental

The basic pump-probe setup constructed at Wright-Patterson Air Force Base (WPAFB) is shown in Figure 1. Briefly, a CW argon-ion laser (AL) was used to pump two mode-locked ps Ti:sapphire lasers ($\lambda = 765$ nm) with matched repetition rates. The pump beam is optically chopped at 3 kHz (OC) to minimize low frequency noise contributions. The pump beam is delayed by means of an optical delay line (DL) containing a retro-reflector coupled to a controlled stepper-motor. Pump and probe beams are then combined and crossed in the optical sample cell using a short focal length lens (L). After interacting with the sample in the cell, the pump beam is then blocked (i.e., dumped) using a spatial filter and the probe passed through a small optical iris (I). The probe beam is ultimately focused onto a photodiode (PD) using a short focal length lens, and the signal detected subsequently at the frequency of the modulated pump (3 kHz) using a lock-in amplifier (LIA), and processed by a PC. The cross-correlation function has been measured to determine the time resolution of the system using the second harmonic

generation technique as discussed by Fleming¹¹ and was found to be about 4 ps for ground-state recovery measurements.

The optical cell used was a 1 mm pathlength quartz optical flow cell. The cell was temperature controlled at 22 °C throughout these experiments and an infinitely dilute solution of HITCI in methanol was constantly circulated through the cell during the experiment.

Pump-probe spectroscopy inherently allows measurements of ground- and excited-state information using ground-state recovery and stimulated-emission measurements, respectively.^{11,12} In a ground-state recovery experiment, a pump laser illuminates the sample using a powerful modulated pulse (ps or fs) which produces enough molecules in the excited state to deplete the ground-state population (Figure 2). If the much weaker unmodulated probe pulse (tuned to the same wavelength as the pump) arrives before the pump pulse (termed “negative time”) the probe will be absorbed by the sample but no pump-induced *modulation* on the probe beam is detected by the detection electronics (Figure 2A). When the probe pulse passes through the sample a very short time following the pump (Figure 2B), it is transmitted more by the sample because the ground state has been bleached by the pump. As the probe is further delayed in time with respect to the pump, the probe will be absorbed as the excited-state species return to the ground state. In practice, the probe pulse is designed to be increasingly delayed in time relative to the modulated pump (Figure 2C), and the increased absorbance attenuation of the probe used to map out the entire ultrafast ground-state recovery process (Figure 2D). Pump and probe pulses for ground-state recovery measurements are most often chosen at the solute absorption maximum (Figure 3).

By continuing to pump into the absorbance band and simply tuning the probe pulse to the

sample emission band, the resulting stimulated emission intensity is proportional to the fluorescence intensity. As a result, this configuration can be used to determine the excited-state system dynamics (Figure 3). In the so-called two-color pump-probe experiment, one again delays the probe pulse with respect to the pump and traces out the decay process (*vide supra*).

One-color pump-probe spectroscopy (the more difficult experiment) was used initially to determine the ground-state recovery of the HITCI in methanol system. Because of measurement difficulties associated with thermal lensing of the sample (*vide infra*), the actual ground-state recovery of HITCI in methanol was not determined during my stay at WPAFB.

Before beginning two-color pump-probe measurements to determine the time-resolved excited-state decay kinetics, we first determined the excited-state fluorescent lifetime of IR-125 using time-correlated single photon counting (TCSPC) technique. Time-correlated single-photon counting has several advantages for determination of fluorescent lifetimes.¹⁶ Although the time-resolution is less than that achieved with pump-probe spectroscopy, TCSPC generally has good time resolution, typically to about 50 ps. High-quality electronic components necessary for TCSPC measurements are common and commercially available. In addition, TCSPC is a very sensitive technique and can detect even very dilute solutions of fluorophores. Figure 4 presents a schematic of the TCSPC instrument constructed at WPAFB for fluorescent lifetime measurements of IR-125 in methanol. Briefly, a CW Ar⁺ laser (AL) is used to pump a single ps Ti:sapphire laser (TSL) ($\lambda = 730$ nm). The mode-locked output is then pulse-picked (PP) at 4 MHZ. A small portion of the beam is sent to a photodiode (PD) which is used to start the time-to-amplitude converter (TAC). The remaining portion of the beam is polarized (P) at magic angle conditions (54.7°) and focused into the temperature-controlled (22 °C) sample cell.

The resulting fluorescence ($\lambda = 840$ nm) was detected at 90° and after polarization selection (P) at the magic angle, was focused onto a monochromator (M) for wavelength selection and the subsequent signal was detected by a microchannel plate photomultiplier tube (MCP-PMT) and sent to the timing electronics. The instrument response function were determined by using a light scatterer in place of the IR-125 sample. Typical instrument response times were found to be around 40-50 ps.

Preparations were made to begin supercritical fluid experiments. The system and high-pressure cell have been described in detail elsewhere.¹⁷ Briefly, SFC grade CO₂ was purified using an 2 μ m filter and gas filter before charging a high-pressure microprocessor-controlled syringe pump (ISCO). A pressure transducer was used to monitor the system pressure (0.35% full scale accuracy) and to test for leaks. The stainless steel cell has four quartz windows sealed into a temperature-controlled body using teflon o-rings.

Results and Discussion

One-color pump-probe measurements (3 kHz modulation) were made for HITCI in methanol but anomalous results were obtained. It has since been discovered that, although precautions were taken against such, thermal lensing was occurring within the original samples. A thermal lens arises due to changes in refractive index caused by heating of the sample by the focused pulsed laser beam. Although the sample was flowed through the cell, thermal lensing was still affecting the measurements. Dr. James R. Gord (WPAFB) and Dr. William L. Weaver (Systems Research Laboratories, Inc.) have subsequently found that by modulating the pump beam at a much higher frequency (~ 1 MHZ), the thermal lens problem can be alleviated.¹⁸

A typical time-resolved TCSPC decay trace for IR-125 in methanol is shown in Figure 5.

Preliminary data analysis shows this system to conform to a single exponential fit, recovering a fluorescent lifetime of 490 ps. This result is similar to those obtained by Soper et al.¹³ for the same system and confirm that our TCSPC experimental setup is valid.

Initial two-color pump-probe measurements were made, but due to experimental difficulties, definitive results were not obtained for the IR-125/methanol system.

Future Work

Although work began on the road toward using pump-probe spectroscopy to determine molecular-level interactions occurring in supercritical fluids, there were problems encountered which precluded reaching such lofty goals. Over the course of this summer research program, we were able to construct and test a one-color and two-color pump-probe spectrometer and a time-correlated single-photon counting system. Results to date have been very encouraging and illustrate the power of this methodology. In the future, we plan to use tools developed at WPAFB as a jump point for work on supercritical fluids. We are now planning for continuing these supercritical fluid experiments in conjunction with personnel at WPAFB. An AFOSR Summer Research Extension Program Proposal entitled "A Molecular-Level View of Solvation in Supercritical Fluid Systems" has been submitted to allow this and other collaboration between our group at SUNY-Buffalo and the WPAFB team.

References

1. Franck, E.U. *Ber. Bunsenges. Phys. Chem.*, **1988**, 88, 820.
2. Kim, S.; Johnston, K.P. *AIChE J.*, **1987**, 33, 1603.
3. Eckert, C.A.; Knutson, B.L. *Fluid Phase Equil.*, **1993**, 83, 93.
4. Rhodes, T.A.; O'Shea, K.; Bennett, G.; Johnston, K.P.; Fox, M.A. *J. Phys. Chem.*, **1995**, 99, 9903.
5. Wu, B.C.; Klein, M.T.; Sandler, S.I. *Ind. Eng. Chem. Res.*, **1991**, 30, 822.
6. Kazarian, S.G.; Poliakoff, M. *J. Phys. Chem.*, **1995**, 99, 8624.
7. Hawthorne, S.B.; Yang, Y.; Miller, D.J. *Anal. Chem.*, **1994**, 66, 2912.
8. Petsche, I.B.; Debenedetti, P.G. *J. Chem. Phys.*, **1989**, 91, 7075.
9. O'Brien, J.A.; Randolph, T.W.; Carlier, C.; Ganapathy, S. *AIChE J.*, **1993**, 39, 1061.
10. Rice, J.K.; Niemeyer, E.D.; Dunbar, R.A.; Bright, F.V. *J. Am. Chem. Soc.*, **1995**, 117, 5832.
11. Fleming, G.R. *Chemical Applications of Ultrafast Spectroscopy*, Oxford University Press: New York, **1986**.
12. Wirth, M.J. *Anal. Chem.*, **1990**, 62, 270A.
13. Soper, S.A.; Mattingly, Q.L. *J. Am. Chem. Soc.*, **1994**, 116, 3744.
14. Soper, S.A.; Mattingly, Q.L.; Vegunta, P. *Anal. Chem.*, **1993**, 65, 740.
15. Thompson, R.B.; Frisoli, J.K.; Lakowicz, J.R. *Anal. Chem.*, **1992**, 64, 2075.
16. Lackowicz, J.R. *Principles of Fluorescence Spectroscopy*, Plenum Press: New York, 3rd ed., **1986**.
17. Betts, T.A.; Zagrobelny, J.; Bright, F.V. *J. Supercrit. Fluids*, **1992**, 5, 48.

18. Gord, J.R.; Weaver, W.L.; Niemeyer, E.D.; Bright, F.V. 22nd Annual Federation of Analytical Chemistry and Spectroscopy Society (FACSS) Meeting, Cincinnati, OH, October 15-20, paper no. 033.

Figure Captions

Figure 1: Schematic of the pump-probe spectrometer constructed at WPAFB as part of my AFOSR-sponsored Summer Research Program. Abbreviations: AL, Ar⁺ laser (25W); BS, beam splitter; TSL, titanium sapphire laser; OC, optical chopper; DL, delay line; L, lens; S, sample cell; I, iris; SF, spatial filter; PD, photodiode; and LIA, lock-in amplifier.

Figure 2: Schematic of the pump-probe experiment. (Panel A) Probe pulse arrives in the sample before the pump pulse. (Panel B) Probe and pump pulse are nearly overlapping in time. (Panel C) Probe pulse arrives after pump pulse and is delayed in time (several pulse sequences are shown). (Panel D) Hypothetical decay trace as determined by pump-probe spectroscopy.

Figure 3: Simplified analyte absorption and emission spectra.

Figure 4: Schematic of the time-correlated single-photon counting apparatus. Abbreviations: AL, Ar⁺ laser; TSL, titanium sapphire laser; BS, beam splitter; PP, pulse picker; PD, photodiode; PTD, pico-timing discriminator; D, delay box; TAC, time-to-amplitude converter; P, polarizer; S, sample; M, monochromator; MCP-PMT, microchannel plate photomultiplier tube; PA, pre-amplifier; MCA, multichannel analyzer; and PC, personal computer.

Figure 5: TCSPC excited-state fluorescence intensity decay trace for IR-125 in methanol generated using time-correlated single-photon counting. The instrument response function is also shown.

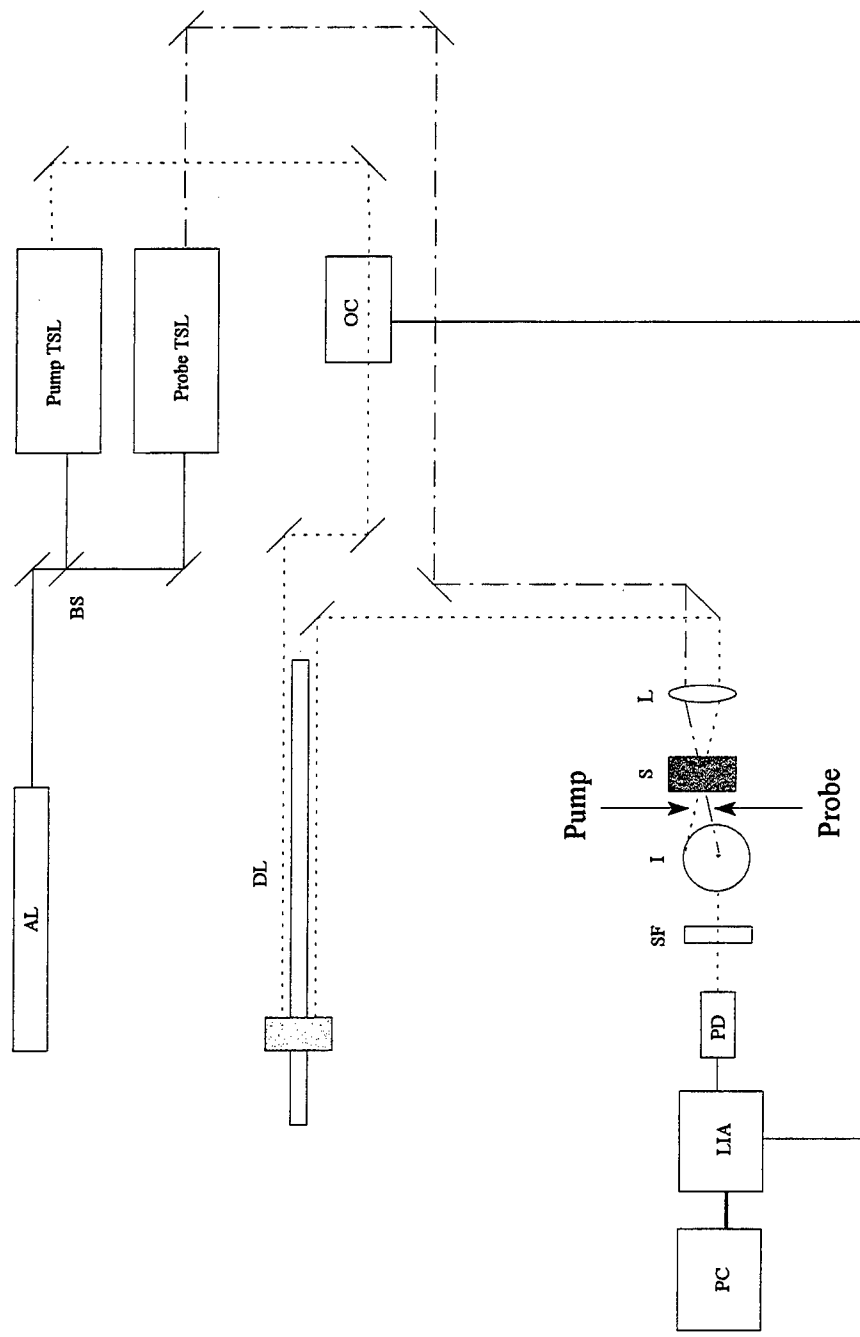


Figure 1

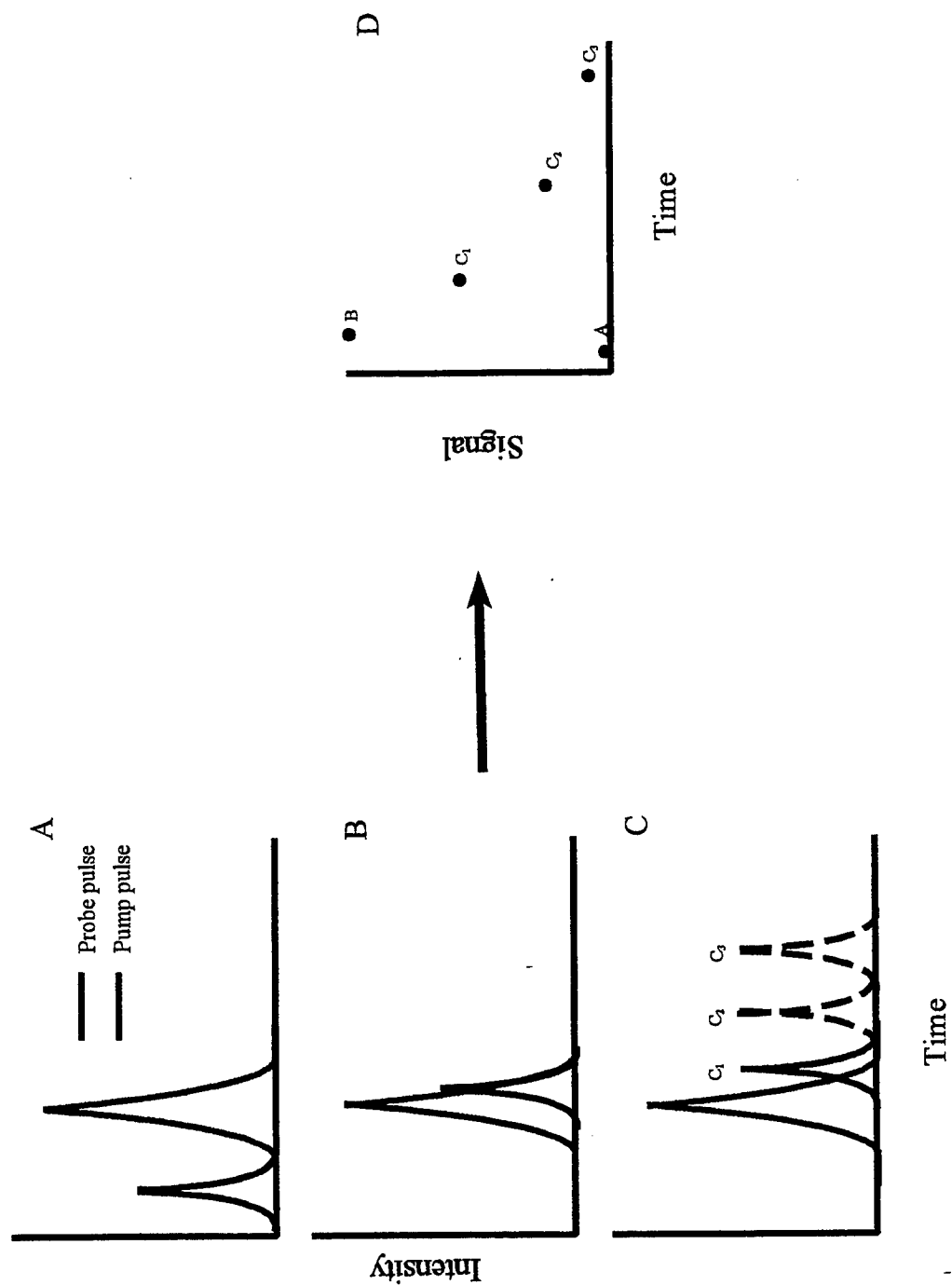


Figure 2

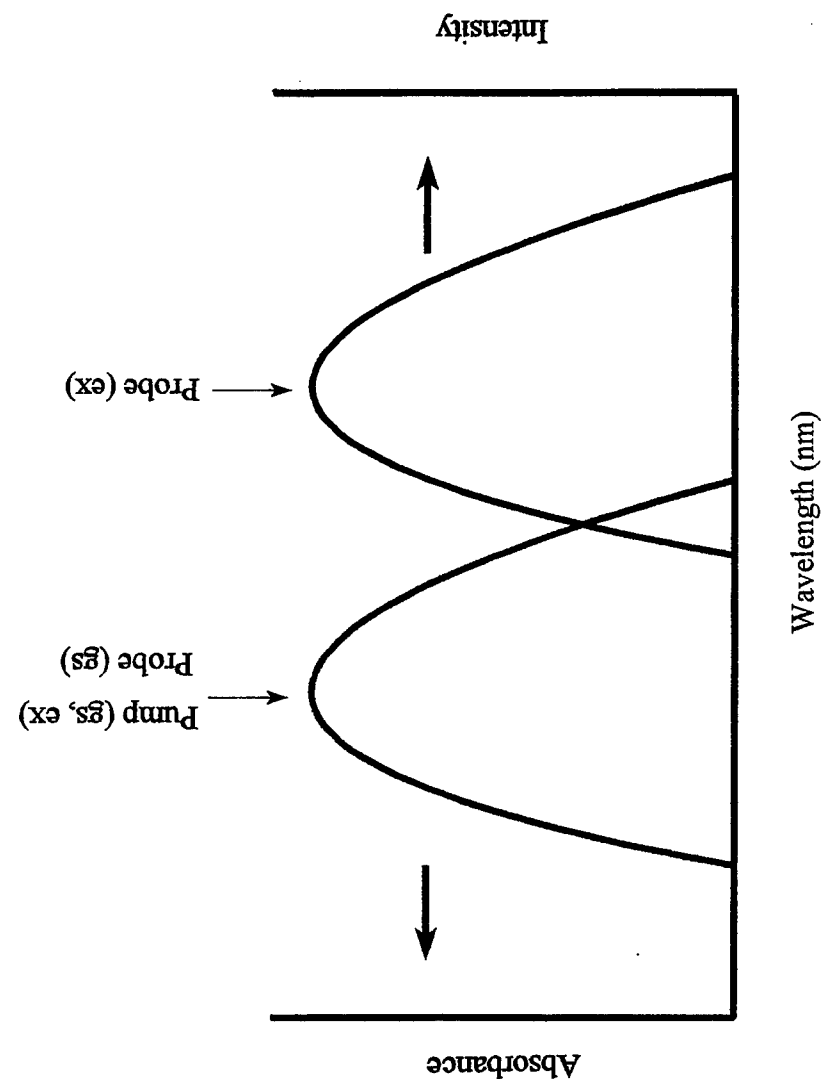


Figure 3

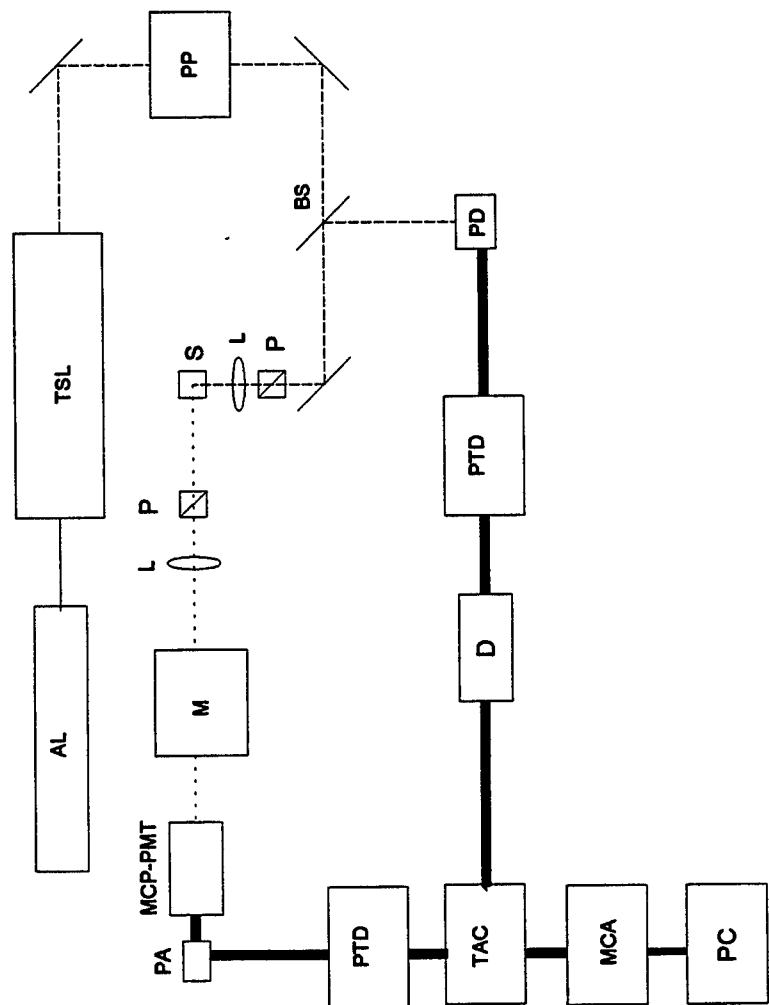


Figure 4

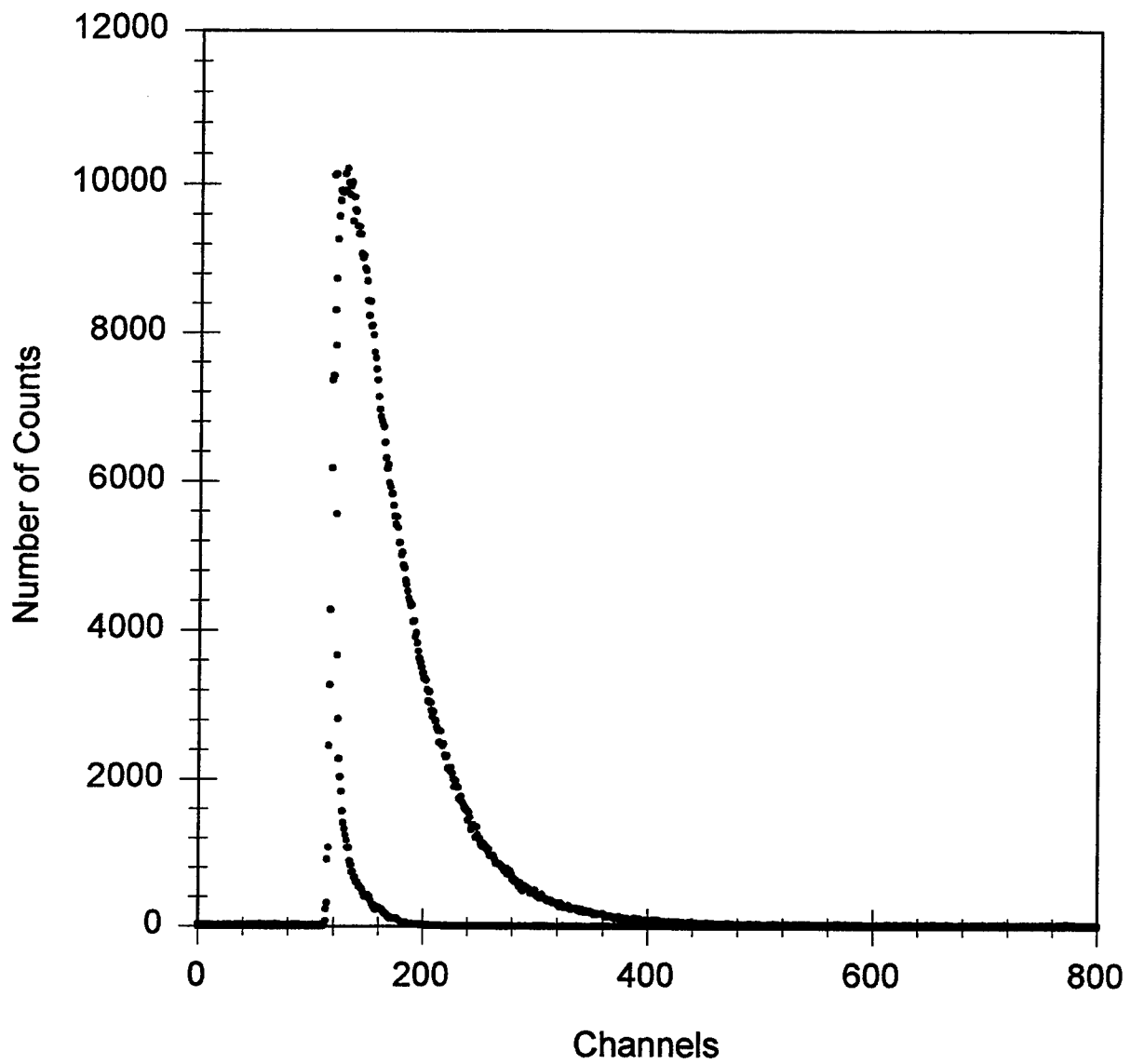


Figure 5

ON THE OPTIMIZATION OF BINARY PHASE ONLY
FILTERS USING GENETIC ALGORITHMS

Robert Vincent Opalecky
Teaching Fellow
Department of Mathematics

University of North Texas
Denton, Texas 76203

Final Report for
Graduate Student Research Program
Wright Laboratory

Sponsored by
Air Force Office of Scientific Research
Bolling Air Force Base, Washington DC

August 1995

ON THE OPTIMIZATION OF BINARY PHASE ONLY
FILTERS USING GENETIC ALGORITHMS

Robert Vincent Opalecky
Teaching Fellow
Department of Mathematics
University of North Texas

Abstract

A genetic algorithm is defined and employed as a search algorithm for binary phase only filters used for image recognition and discrimination. When a population of binary strings is used, the setup for such an algorithm is simple, but the efficiency of a genetic algorithm search suffers from the size of the search space and the time required to evaluate the fitness function. Search results are presented, and a comparison with another simple search techniques is made.

ON THE OPTIMIZATION OF BINARY PHASE ONLY
FILTERS USING GENETIC ALGORITHMS

Robert Vincent Opalecky

1 Introduction

A genetic algorithm (GA) is a search technique that may be applied to a variety of optimization problems. Though most, if not all of the underlying mathematical principles behind the operation of genetic algorithms still remain a mystery, experimental results seem to justify their study and application. One of the simplest and most natural types of problem for a GA to be used on is the optimization of a function $f : \{0, 1\}^N \rightarrow R$. Given N , the dimension of the binary space to be searched, there are assertions about the population size needed to get a general GA to locate a global maximum. The notion is that there is a need to mix aspects of fairly good solutions to obtain better solutions. A huge population will probably contain all of the needed characteristics. Whether or not these assertions are correct, it is easy to formulate a problem large enough to make to make large population sizes almost impossible to implement. This is the case in binary filter design.

Most procedures in spatial filter design start with some sort of matched filter, weighted averages of match filters, or altered versions of these. So to offset the prohibitive cost of using a very large population, a much smaller population made up of perturbations of a version of a matched filter is used. Even so, given a training set of M images, if the function to be optimized needs information from all of the correlations with a given filter, in order to perform L iterations of a GA with a population of K filters we must perform MKL cross correlations. While this is linear in each parameter, if the population is merely one thousand and the training set has ten images, one hundred iterations of the

GA will require one million correlations. This will require at least one million two dimensional FFT's, and many more, depending on the implementation. The problem can becomes large very quickly. If a very small population is used, the problem of inbreeding arises, the so called "premature convergence". With a small number of iterations, the population is not given a fair chance to increase the function value. After all, every algorithm has minimal run times necessary for any semblance of convergence. Hence the algorithm is inherently compute intensive.

2 The Optical Correlation Simulation

The following is a description of the optical correlation simulation used throughout the genetic algorithm runs performed. Basically, optical correlation with a phase only filter consists of passing an optical signal through a Fourier transforming lens, and altering the signal with a filter via a spatial light modulator which changes the phases of certain frequencies by certain amounts. The resulting signal then passes through another Fourier transforming lens and onto a detector where the resulting intensities are measured. The goal of our filter design is to concentrate as much of the signal as possible at the center of the detector if the signal is to be recognized, and to disperse the light evenly throughout the correlation plane if the signal is not to be recognized, especially if a signal is specifically to be rejected. In the simulation process, both target input signals and filters are regarded as 128 by 128 arrays of complex numbers. This size is chosen to correspond to some existing spatial light modulators. The correlations all are performed on 256 by 256 arrays to simulate the passage of the potentially unbounded signal through a square aperture. Therefore it is necessary to first put the input into the formats described below prior to correlating.

2.1 Data

The targets are 128 by 128 pixel images of an M60 tank or of an M113 armored vehicle taken at various angles from a fixed distance and elevation. Each pixel is one of 256 intensity values. The target will be zero padded in a 256 by 256 complex array, but first one of the following actions is performed. One of the preprocesses is straightforward; the intensities are converted into amplitudes (taking square roots), and regarded as complex numbers. This will be referred to as amplitude input imagery. The other preprocess assigns to each intensity a complex number of modulus one via the one to one map $x \rightarrow e^{i\pi x/255}$. This will be referred to as phase encoded input. The benefit of phase encoding input is that there is no attenuation of the light in the correlator as it passes the first phase of the correlation, and the energy in any such signal is a constant. Once the target is preprocessed, it is zero padded in a 256 by 256 complex array so that the image is in the center. That is, if the preprocessed image is regarded as a function $g : Z_{128} \times Z_{128} \rightarrow C$, then the zero padded function is $f : Z_{256} \times Z_{256} \rightarrow C$ where $f(x, y) = g(x - 64, y - 64)$ if $64 \leq x, y < 192$, and $f(x, y) = 0$ otherwise. A 128 by 128 filter array p is expanded to a 256 by 256 array P for the correlation by setting $P(2x, 2y) = P(2x + 1, 2y) = P(2x, 2y + 1) = P(2x + 1, 2y + 1) = p(x, y)$ for all $0 \leq x, y < 128$. This square replication is the frequency space equivalent to the zero padding done to the target images.

2.2 The Correlation and SCR Function

The correlation is done using 256 by 256 two dimensional complex Fourier transforms. The transform of a target is taken, the resulting array is multiplied pointwise by the filter's values and inverse transformed. The amplitudes squared of the elements of the final array represent the intensities of the light on the cor-

relation plane. Symbolically, for an image f and a filter P , the process is

$$f \rightarrow \mathcal{F}(f) \rightarrow \mathcal{F}(f) \cdot P \rightarrow \mathcal{F}^{-1}(\mathcal{F}(f) \cdot P) \rightarrow \left\{ \left| (\mathcal{F}^{-1}(\mathcal{F}(f) \cdot P))(x, y) \right|^2 \right\}_{x, y \in Z_{256}}$$

where \mathcal{F} is the two dimensional Fourier transform operator and \cdot is pointwise multiplication of the arrays (as opposed to matrix multiplication). In practice, only the values over the detector face are seen, the detector face being the 128 by 128 region in the center of the correlation plane. Thus anything outside of this region is often ignored. There is, however no real reason to do so. Since the arrays have an even dimension, there is no natural center. Thus we choose one of the four ‘center’ pixels, namely (128, 128) to be the origin of the discrete plane. For a zero padded target image, whenever the correlation plane intensity is sufficiently high at the origin, as defined above, we consider the filter to have recognized the target. A threshold level cannot be defined universally, but there are hardware requirements and thresholding schemes to help dictate what is acceptable. In the problem at hand we will not concern ourselves with threshold levels per se. Instead we will look at how well a given filter recognizes a set of targets versus how well it rejects some other set. We will now define a general signal to clutter ratio function for a given set of images. Suppose $f_1, f_2, \dots, f_M, f_{M+1}, \dots, f_N$, $0 < M \leq N$, is a set of images. We will consider the first M images as true images to be recognized, and the last $N - M$ images as false images to be rejected by a filter. For each k , $1 \leq k \leq N$, choose disjoint regions R_k and B_k in the discrete plane. The B_k are regions in which we want large intensities. The R_k are regions in which large intensities are distinctly not wanted. Once these regions are chosen, we may define a function SCR whose value at a filter P is

$$SCR(P) = \frac{\max_{1 \leq k \leq N} \min_{(x, y) \in B_k} |\mathcal{F}^{-1}(\mathcal{F}(f_k) \cdot P)(x, y)|^2}{\max_{1 \leq k \leq N} \max_{(x, y) \in R_k} |\mathcal{F}^{-1}(\mathcal{F}(f_k) \cdot P)(x, y)|^2}$$

wherever this exists. Typically, the B_k will be a small region about the origin, or the origin itself, for true targets, and empty for false targets. The R_k are

usually the complement of the B_k or empty for true targets, and for false targets the R_k are either the detector face or the whole plane.

3 Genetic Algorithms

A genetic algorithm (GA) is a process on a population of vectors designed to mimic natural selection. Each set has a fixed number of positions and a fixed range of values allowable in these positions. Generally there are four steps common to any GA; evaluation of strength, replication, crossover, and mutation. In the first phase, a function assigns a numerical value to each element of the population to gauge its fitness. Based upon this, the second phase chooses members of the population to be replicated, and how many times, in a temporary population. Thus a stronger member will probably be represented with one or more copies of itself, while a weaker member will probably be weeded out. In the third phase, members of the temporary population swap some of their genes according to some crossover scheme. Finally, individual genes are given the opportunity to randomly mutate. This completes one iteration. The new population is now processed again from step one. The hope is that the maximum of the fitness values will increase over time, perhaps finding a global maximum of the fitness function.

3.1 The Fitness Function and Initial Population

Naturally, for any given GA we need to know the function to be optimized, which will dictate the nature of the population. We also need to know how to generate an initial population for the algorithm. In the problem at hand, we are interested in designing binary phase only filters for target recognition and discrimination. So first choose a set of images to be recognized and a set of images to be rejected by the filters to be designed. Therefore one natural choice

of function for optimization is some form of the SCR function described above. In every experiment, the regions B_k were chosen as the center pixel for true targets and empty for false targets. The regions R_k were varied, so in each case it will be necessary to identify what the choices made were. Nevertheless, the general fitness function used, notation as in the previous section, is

$$SCR(P) = \frac{\max_{1 \leq k \leq N} |\mathcal{F}^{-1}(\mathcal{F}(f_k) \cdot P)(128, 128)|^2}{\max_{1 \leq k \leq N} \max_{(x,y) \in R_k} |\mathcal{F}^{-1}(\mathcal{F}(f_k) \cdot P)(x, y)|^2}.$$

The population should consist of spatial filters, in particular binary phase only filters. The filters are taken so as to work in our simulation, thus are 128 by 128 arrays.

An initial population is now generated. A matched filter with complex entries for the true target images is made. This is only a crude initial guess, so if a place contains a zero reset it, say to one, to avoid any frequency stops. The elements are then normalized to produce a phase only filter P . For each θ , $0 \leq \theta < \pi$, a binary version P_θ of P is made by setting

$$P_\theta(x, y) = \begin{cases} -1 & \theta - \pi < \text{Arg}(P(x, y)) \leq 0 \\ 1 & \text{otherwise} \end{cases}.$$

Choose θ such that $SCR(P_\theta)$ is as large as possible. This will be used as an initial filter. Each member of the population is generated by copying this filter and then mutating 128 entries at random, that is choosing a random index and replacing 1 with -1 or vice versa.

3.2 The Replication and Crossover Phases

Replication is performed using a simple double tournament scheme. The filters in the population are paired off at random. For each pair, the member of the pair with the higher SCR is given a berth in the temporary population, the other is not. This is done twice, so that the population size is maintained. Two

passes also guarantees that the filter with the highest SCR is copied twice, and that the filter with the lowest SCR is discarded.

For the crossover phase, the filters in the new population are again paired off at random. Regarding the filters as 128 by 128 arrays, they are randomly partitioned into nine rectangular regions apiece in an obvious way. Each region in one of the filters of a pair corresponds to a region in the same location with the same size in the other filter of the pair. Each of the regions is exchanged between the pair with a probability of $\frac{1}{3}$.

3.3 The Mutation Phase

Each bit in each filter is now given the opportunity to mutate, to change from 1 to -1 or vice versa. The mutation probability is initially set to zero, so there are no mutations in the first generation. If the highest SCR in a successive generation is less than or equal to the highest SCR yet seen in any prior generation, the mutation probability is increased by $\frac{1}{16384}$, or an expectation of one additional mutation for each member of the population. If the new highest SCR is greater than any yet seen, the mutation probability is set back to zero. Thus for a given generation the probability of any given bit mutating is $\frac{k}{16384}$, where k is either the number of generations since an all time high was reached, or a predefined maximum integer, whichever is less. The limit used in the trials is ten.

It should be noted that there is no good reason why the mutation rate should not be fixed, as in most simple GA's. The rational for using this scheme is that it allows successful recombinations to become population elements without mutation. Only when a population's strength is in question will the higher mutation be tried to lift its strength. However, if recombination is not working on the population, it is doubtful that an extreme mutation rate will help.

3.4 Termination

No termination conditions were used, though several logical choices could have been made. There are intuitive and common conditions for ending a trial including finding an acceptably high SCR, passing some set number of function evaluations or generations, or having the population become too similar, gauged by some similarity test.

In the trials performed, the implied termination condition was time. No trial lasted less than 50 or more than 200 generations, which is acceptable to me. Large population need almost as many iterations to start improving as small populations, but take much longer to execute. Thus more time is needed to merely start improving. But if a GA search is to be practical, the time needed for a given improvement is important. Therefore searches were sometimes terminated due to the feeble progress versus the adequate time allotted.

4 Search Results

All of the trials were performed under the scheme as explained above. The variations from trial to trial are due to differing training sets, input method, population size, and the variant of the *SCR* function used. Each of these needs to be mentioned before any trial can make sense. The selection, crossover, and mutation operators are always as above. There may be better, more efficient, operators available, but these seem not only acceptable, but rather much better than some tried.

Usually multiple runs were performed using a given setup. These often used very small populations or a severely limited number of iterations to test the parameters or to investigate the size of the SCR's to expect. Other times multiple runs were performed with identical setups. The trials below are among the largest and longest trials attempted, and are invariably typical of the types

of behaviors seen throughout. Invariably, duplicate trials or mock-up trials behaved in very similar ways. That is, there does not seem to be any sensitivity to initial conditions, where two different populations generated will find two radically different filters.

4.1 Initial Trials

For the first trials the training set was made up of five binarized views of an M60 model at 0, 1, 2, 3, and 4 degrees off of head on for target recognition, with the same five binary views of an M113 used for discrimination. The fitness function used takes the R_k to be the detector face for false targets, and the detector face minus a five by five box about the center for true targets. As always, the B_k are empty for false targets and just the center pixel for true targets. The phase only matched filter was created and immediately showed its bad character. The initial binary filter had a correlation peak intensity of 31.39 at the origin for the first true target, while for the rest of the true targets the next least intensity was 77.58.

A GA trial with a population of one thousand was performed. The best SCR in the initial population was 5.44. After 47 generations, the best SCR had improved to 13.06. However, for the filter with the best SCR, the center correlation peak for the first target had gone down an intensity of only 19.67 while the next smallest for the true targets was 53.86. While the SCR had more than doubled, the inconsistency in recognition from the first filter had persisted, and can be argued to have gotten worse. The run was terminated at this point. In every other trial using the same initial filter, the result was similar. The growth of the SCR was slight and slow, and the filters produced had much poorer recognition of the first target than for the rest of the true targets.

The suspect phase-only matched filter was given briefly to an optimization program written by Robert Kallman for Wright Laboratory which very quickly evened out the peak intensities among the true targets. The binary version of

this filter had a minimum peak intensity of 64.86 with a next lowest peak at 64.94. A GA trial was performed using this new filter to initialize a population of five hundred. The initial best SCR was 9.88. By the sixth generation, the best SCR in the population had reached 13.52. By the fourty seventh generation, the best SCR was 29.80 and in the same number of function evaluations as the first trial, a filter with SCR of 34.19 was found. The smallest recognition intensity was 42.65 and the largest false target correlation intensity anywhere was 1.19.

The good performance of the GA on the improved filter was heartening, so attempt were made to improve the "bad" binary matched filter using a GA. In one attempt, a fitness function was used to select for a filter that would produce a high percentage of energy in the five by five box about the center in the correlation plane. In other attempts, minimum correlation peak intensity from the true targets was used as the fitness function. No GA run was able, regardless of population size or time allotted, to pick up the minimum peak intensity to a degree comparable to two iterations of Kallman's algorithm. The progress made was slow and tended to slow down more as generations passed. The most successful trial put the lowest correlation peak just over 40 after around fifty generations, compared to a peak intensity of over 50 on the first iteration for Kallman's algorithm.

Furthermore, it appears as if the consideration of clutter within the true target correlation planes did little. Even the filters that had some relative problem recognizing the first true target gave satisfactorily small intensities throughout the entire plane for all false targets, almost always less than the clutter in the true target's correlations. The natural suspicion is that the full potential of the target discrimination is not being exploited. So after many trials, the fitness function was chosen to ignore true target intensities when calculating clutter. In discrimination trials, ignoring true target clutter in the *SCR* function worked almost as well as using a medium sized box about the center, say 31 by 31, for damping the clutter. Thus the box was dropped entirely.

As a footnote, I should mention that during the early 'playing around' with the algorithm, a filter with SCR of over 60 was found by repeatedly reseeding the GA with better and better filters. The problem arising was that the new population more often than not would have best SCR less than its parent, and the new search would not quickly find a filter as good in any short amount of time. However, the trial and error method with the GA found the 'best' filter I saw for this training set.

4.2 Other Trials

The images used were five views of a M60 from 0, 1, 2, 3, and 4 degrees off of head on, with the same five views of an M113 for discrimination. The images have been quantized to 256 intensity values and centered in a blank field. The *SCR* function is defined by choosing the center pixel alone for the B_k and empty R_k on the true targets, and choosing empty B_k and R_k equal to the detector face for false targets.

In the first case, the images were read as arrays of amplitudes in an ordinary way. The binary matched filter made seemed better than the one used in the trials above, so the GA was used to improve it. A population of five hundred was tried first. The best SCR in the initial population was 4.032. After fifty generations, the best filter in the population had a SCR of 14.54, and after one hundred generations a filter with SCR of 16.25 had been found. This performance was only marginally better than the trials on the binary images with the other fitness function, but had been done with only half of the population. So a long trial with a population of one thousand was run on the binary matched filter. The first best SCR was 4.545, owing to the larger population. After fifty generations, the best SCR in the population was 14.48, but better growth continued for more generations than before, so the final best filter found at one hundred generations had an SCR of 20.03. Remember however that the second run took just less than twice the time as the first to execute the same number

of generations, so while our final search was better, the efficiency of the second search was initially very poor.

For the second set of trials, the image's intensity at each pixel was put through the function $x \mapsto \exp(i\pi x/255)$. Since each intensity is a nonnegative integer less than 256, this function maps our images to images consisting of complex numbers of modulus one in the interval $[0, \pi]$ of the circle in a one-to-one fashion. Once this phase encoding is performed, the correlations are done on the new images. The binary matched filter for the phase-encoded images was made and seemed adequate for improvement with the GA. A trial with population five hundred was again tried first. The initial best SCR in the population was 6.142. After fifty generations a filter with an SCR of 19.36 had been found, and after one hundred generations, 21.92. The next trial with population one thousand was performed for contrast with the amplitude input search, but was left running for a full two hundred generations. The initial best SCR in the population was 6.383. After fifty generations, a filter with SCR of 20.07 was found. After one hundred generations, a filter with an SCR of 22.64 was found. The final best filter found after two hundred generations had an SCR of 26.77.

The general behavior of these and other trials leads to the basic supposition that the maximum return of the algorithm is a function of both population size and generations run, and not merely the number of correlations performed. For example, the trials performed with a population of five hundred reached certain levels twice as fast as the population one thousand runs due to the need to perform only half the function evaluations. However, the smaller populations stagnate more quickly than larger ones. Thus the larger populations seem to hold more potential, though achieve it far more slowly. The problem to be dealt with in filter design is balancing the need for a small population with the potential of a very large population, particularly when the potential gains and minimal population size is unknown. As it would take a population of ten

thousand roughly twenty hours to find a filter comparable to one found by a population of five hundred in one hour, the promise of the large population being able to continue for five times the generations of the small population before stagnating is not very appealing for very practical reasons.

4.3 The Hillclimber

As a contrast to the GA, a simple hillclimbing algorithm was employed to search for an optimal filter in the phase-encoded target recognition problem stated above. The idea is very simple. The binary phase only matched filter for the training set is created. Then a single pixel is changed from 1 to -1 or vice versa. If the change increases the SCR, it is kept, otherwise it is changed back. Continue with a different pixel.

The actual algorithm used keeps four counters. All start from the center frequency pixel, which is the top left (or just past bottom right) pixel in the filter. One counter moves down until it hits the bottom row, then goes back to the top, moving one column over to the right. Another moves to the right until it hits the right edge, at which point it moves back to the left edge and then moves one row down. Two of the counters start at the bottom right pixel, but move in a similar fashion. One moves up then left, the other moves left, then up. At each stage, the pixels at the counter positions are flipped and the SCR considered, one at a time. My hope is that considering four positions where the frequency information is likely to be similar may aid the search. This also causes a lot of redundant flipping of pixels usually not found in the simple hillclimber prototype, using up extra time in an already slow algorithm. I decided to use it anyway, hoping that the extra flips may aid the search.

As it turned out, one pass across the entire filter, redundancy and all, took only nine hours. Contrast this with the over thirteen hours for a GA run with a population five hundred for one hundred generations, using the same processor and the same simulation. Add to this the fact that the filter found had a SCR of

over 34, compared to the 26 found by the two hundred generation GA, and the conclusion I reached was that the slow methodical algorithm worked faster and better than the quasi-random GA search, especially given the times involved.

5 Conclusion

It is indeed true that in every trial, the genetic algorithm searched for and found filters that were significant improvements over the binary phase only matched filters used to seed the populations. However, at times the GA was incapable of improving a very good filter, or sometimes even a mediocre filter. The main problems are memory and speed constraints. But even if any machine limitations did not exist, there would still be a problem with the lack of understanding of the reasons why the algorithm seems to work at all. If more of the mathematics were firmly understood, the schemes to improve upon this class of algorithm would have more direction. Short of this, there are still a plethora of possibilities for schemes to be tested via trial and error, or parametric studies.

The greatest question left unanswered by using a GA on a problem of this size is whether there is indeed a process of some sort artificially selecting binary schemes out of presented possibilities due to strength, as supposed, or if the GA is merely a controlled random search programmed to keep its successes, and only appears to be doing anything other than blind guessing. In the favor of the GA, the one used outperformed every pseudo-random search attempted, either random perturbation or randomization inside of the GA. To the discredit of the algorithm, each directed search outperformed the GA in a much shorter amount of time; be it the hillclimber, conscious combinations of short GA runs, or the optimization routines written by Dr. Kallman. All in all, the random nature of the algorithm may well be its strength, but it needs to be understood better so that it may be harnessed and directed to be much more efficient.

IMPROVING THE SPEED AND ACCURACY OF THE 3-D SCANNER

**Brian E. Oskey
Graduate Student
Department of Electrical Engineering**

**Wright State University
Dayton, OH 45435**

**Final Report for:
Graduate Student Research Program
Wright Laboratory**

**Sponsored by:
Air Force Office of Scientific Research
Bolling Air Force Base, DC**

and

**Wright Laboratory
Wright Patterson AFB**

September 1995

IMPROVING THE SPEED AND ACCURACY OF THE 3-D SCANNER

Brian E. Oskey
Graduate Student
Department of Electrical Engineering
Wright State University

Abstract

A laser and camera were mounted on one side of a rotatable arch to implement the non-contact, active triangulation, 3-D scanning method. The success of the process is dependent on the alignment and calibration of the system. The laser and camera must be aligned with the motor shaft, the axis with which the arch rotates about, in order to obtain an accurate output. Calibrating the system is also necessary to correct for distortions caused by the system components. The previous alignment and calibration procedures were found to be slow, inaccurate due to human error, and difficult to repeat. The redesigned procedures were implemented and have showed vast improvements in time, accuracy, repeatability, and can be easily accomplished with one person.

IMPROVING THE SPEED AND ACCURACY OF THE 3-D SCANNER

Brian E. Oskey

Introduction

The need for 3-D scanning has grown over the past few years. Applications for this technology exist in the military, manufacturing, entertainment, and medical fields. In order for the system to be acceptable, the entire scanning process (alignment, calibration, scanning, data processing) must be fast, accurate, and easy to use. The entire 3-D scanning system was studied in order to improve these performance measures.

There are several techniques used to perform 3-D scanning. The technique used in this study is non-contact, active triangulation. The system is composed of a laser and camera mounted on one side of a rotatable arch. The system's speed is dependent on both hardware and software developments. The accuracy of the process is dependent on the system's alignment and calibration techniques.

The system's speed can be divided into pre-scanning, scanning, and post-scanning times. Hardware developments will be considered for scanning and pre-scanning improvements. The development of software will be used to further improve the post-scanning and pre-scanning times.

The system's accuracy is divided into two sections: alignment and calibration. The post-processing uses cylindrical coordinate information to paste the individual images together; therefore, determining the true center is crucial to the accuracy of the final image. The alignment procedure should ensure that the laser line and camera center are in line with the shaft of the arch. Any misalignments will cause distortion within the image. For example, scanning a string with a misaligned system will result in an image of a cone rather than a cylinder. Calibration is also important to achieve the desired output. Much of the distortion is due to the lens, the CCD's AD conversion, and the perspective viewpoint of the camera. A mapping procedure was used to associate a distorted point on the computer screen to a known point in the real world. The accuracy and sensitivity of this mapping procedure was studied in much detail. Inaccuracies within this procedure result in an image that appears to be accurate until further

analysis reveals that the image is 'stretched' or 'squashed'.

Methodology

The overall speed of the system was evaluated at each of its three stages: pre-scanning, scanning, and post-scanning. The time improvements associated with the pre-scanning stage (alignment and calibration) will be addressed in the accuracy section since they are directly related. After examining the system's bottlenecks for the scanning stage, hardware upgrades for the frame grabber and motor are the most logical choices. The scan time with the current system can take as long as 2 hours when scanning an object every $.5^\circ$ (720 images). An upgraded system should produce more acceptable scan times. Improvements to the post-scanning time can be seen by carefully evaluating the existing software. Through code optimization and rewriting some routines, significant time results should be realized.

The system's accuracy can be improved by conducting experiments with the existing alignment and calibration techniques. The existing alignment procedure is stated below:

Camera/Shaft Alignment

1. A plumb line was hung from the center of the motor shaft, the axis of the system. This will serve as an extension of the shaft, see Figure 1.

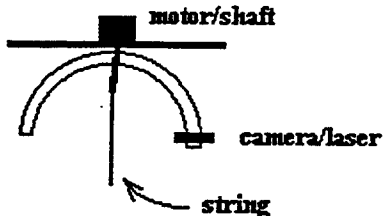


Figure 1

2. Since the mounting of the shaft is not perfect (not perpendicular with the earth), the string must be forced into a position in which it lies on the system's axis. This was done with the aid of the camera at the 12 and 6 o'clock positions and at the 3 and 9 o'clock positions. For example, if the camera views the string at pixel row 250 from the 12 o'clock position and views the string at row 230 from the 6 o'clock position,

then the string must be manually positioned to pixel row 240 $\left(\frac{(250 - 230)}{2} + 230 \right)$, see Figure 2.

**String viewed from different angles
(camera mounted on its side)**

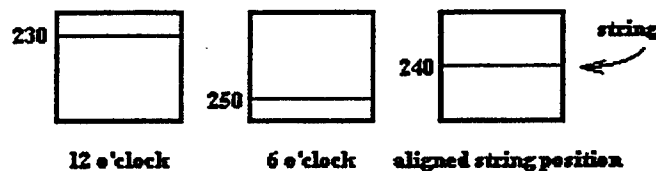


Figure 2

After several repetitions of this step from different positions along the circumference, the string should lie on the axis (the same pixel location for every point along the circumference).

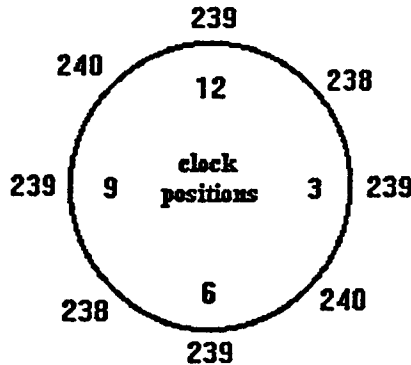
3. Camera adjustments should now be made such that the string is in the center of the screen (row 239) and parallel.
4. Repeat step 2 to ensure alignment.

Laser/Camera/Shaft Alignment

1. Turn laser on and adjust mirror (3 axis adjustment) such that the laser line illuminates the string.
2. Rotate the arch and observe to ensure that the laser remains on the string. Any fading indicates misalignment.

The current process can become tedious since any correction in one direction can cause an error in another direction. A program was developed which evaluates scanned images of the string. The benefits of this program include: determining the pixel center before any string positioning is done, ensuring that the center is met at every point on the circumference, and confirming that the system has maintained alignment. This program also discovered a counterbalancing problem with the arch. This was discovered after aligning the string to pixel row 239 from the 12-3-6-9 o'clock positions. If the system was properly aligned, then all other points along the circumference should also lie at 239. The output of the alignment

program produced the following results, see Figure 3. Through trial and error, weights were placed on the



Top view of the arch path

Figure 3

arch opposite the camera/laser mounting. The resulting alignment showed improvement at each position except the 10-11 o'clock regions remained 240. A perfect alignment may be impossible through trial and error because of weight shifting problems when the arch rotates.

After alignment, the calibration procedure must be performed to correct for distortions in the final image. One calibration surface is necessary for range (distance from the system's axis) and one is necessary for height. The creation of these calibration surfaces involves the mapping of a point on the computer screen to a 3-D point in the real world. To achieve complete accuracy, each pixel value should be mapped to a point in the real world, but this would be very slow ($480 \times 512 = 245,760$ pixels) and inefficient. To prevent the mapping of all points, a method was developed by Power and Xue where a few points would be mapped and the rest would be interpolated [1]. The interpolation was accomplished through non-linear means, a second order equation. This model was justified since a second order relationship accounts for warping due to optics and other system imperfections. The mapping process was very susceptible to human error and took approximately an hour to complete. In addition, the repeatability of this process was not acceptable. Several new procedures were developed using the quadratic model as its foundation.

The existing method creates a 3-D calibration surface by choosing nine pixel values to map. The points are fitted to a quadratic model in the horizontal direction and then in the vertical direction to complete the interpolation of the entire process, see Figure 4. An alternative to this method consisted of

Interpolation with 2nd Order Model

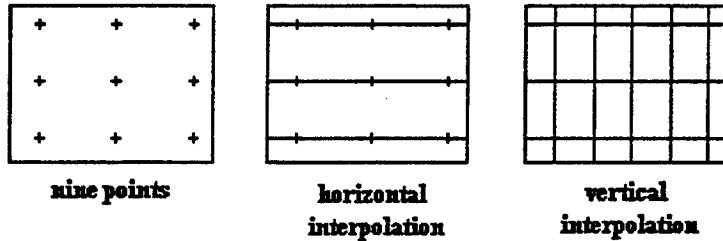


Figure 4

choosing three real world points (at the same range but with different heights). These points could then be moved to three different ranges to obtain the nine points. Now, the tedious process of finding the real world points is replaced by easily finding the pixel values. Finding the pixel values required the user to move a cursor until the pixel with the maximum intensity was found. This method was faster (10 minutes), more accurate (less human error), and repeatable. The problems with this procedure included the determination of the true pixel value and the accuracy of the real world range measurements. This method was further improved by additional computer intervention. The number of fixed points was increased from three to nine points so now range measurements are eliminated and only one image is necessary to collect the points. A program was also written to quickly and accurately find the nine points by way of a center of mass algorithm. This new procedure was extremely fast only taking a few minutes to set up the nine points, record an image, and run the program.

All procedures that were developed used the quadratic model as its foundation. Some questions have been raised about the accuracy and validity of this model. The quadratic model is currently performed with three points, a determined system. If more points were collected and the system were over determined, the calibration's accuracy may be improved through optimization techniques. The model itself is also questioned. The lens distortion is quadratic in nature; however, with other distortions present, it can not be stated with any validity that the quadratic model is the best model. The foundation was laid to

prove or disprove these assumptions by way of a preliminary experiment. The experiment was done to achieve the 'truth' data. Once the 'truth' data has been obtained, the calibration results can be compared with various models in an attempt to minimize the error.

The basic premise behind obtaining the 'truth' data involves the sampling theory. If the calibration surface is sampled at a high enough rate, the surface can be digitized without aliasing. The calibration surface was sampled at a high rate to ensure the accuracy of the surface. A column of 19 pins spaced .5" apart was translated in 2" increments towards the camera (the column will eventually be attached to a motorized slider whose position is fed back to a computer allowing images to be collected while in motion). This effectively sampled the 300 x 512 region used when collecting the images and can be seen in figure 5. As the slider moves toward the camera, less sampled points are obtainable due to the camera's perspective viewpoint. After the computer locates all the points for each picture, the digital signal is transformed back to a real analog signal. The conversion to analog was done through Matlab's cubic spline function. The program's speed was compromised for the resulting high accuracy.

Results

One goal of this study was to speed up the entire 3-D scanning process. A faster frame grabber, 30 images/sec, and a stronger motor were suggested to reduce the scan time to a minute or less. Due to money and time, these suggestions were unable to be implemented. Programs were optimized to reduce the time necessary for the post-scanning stage. For large scans (720 images), the processing time for the old method took approximately 3.5-4 hours. With the new procedure, the processing time for the same scan was only 45 minutes (using a 486, 50 MHz computer). The process could be performed even faster on a top of the line computer (pentium, 100 MHz) with a newer version of C++ which optimizes code.

The new alignment procedure can not only be done faster but also with a higher degree of accuracy. The old alignment procedure originally took 2 people and approximately 1.5 hours to complete. With the addition of the alignment checking program, the procedure can now be done faster, with higher

Sampling Pattern

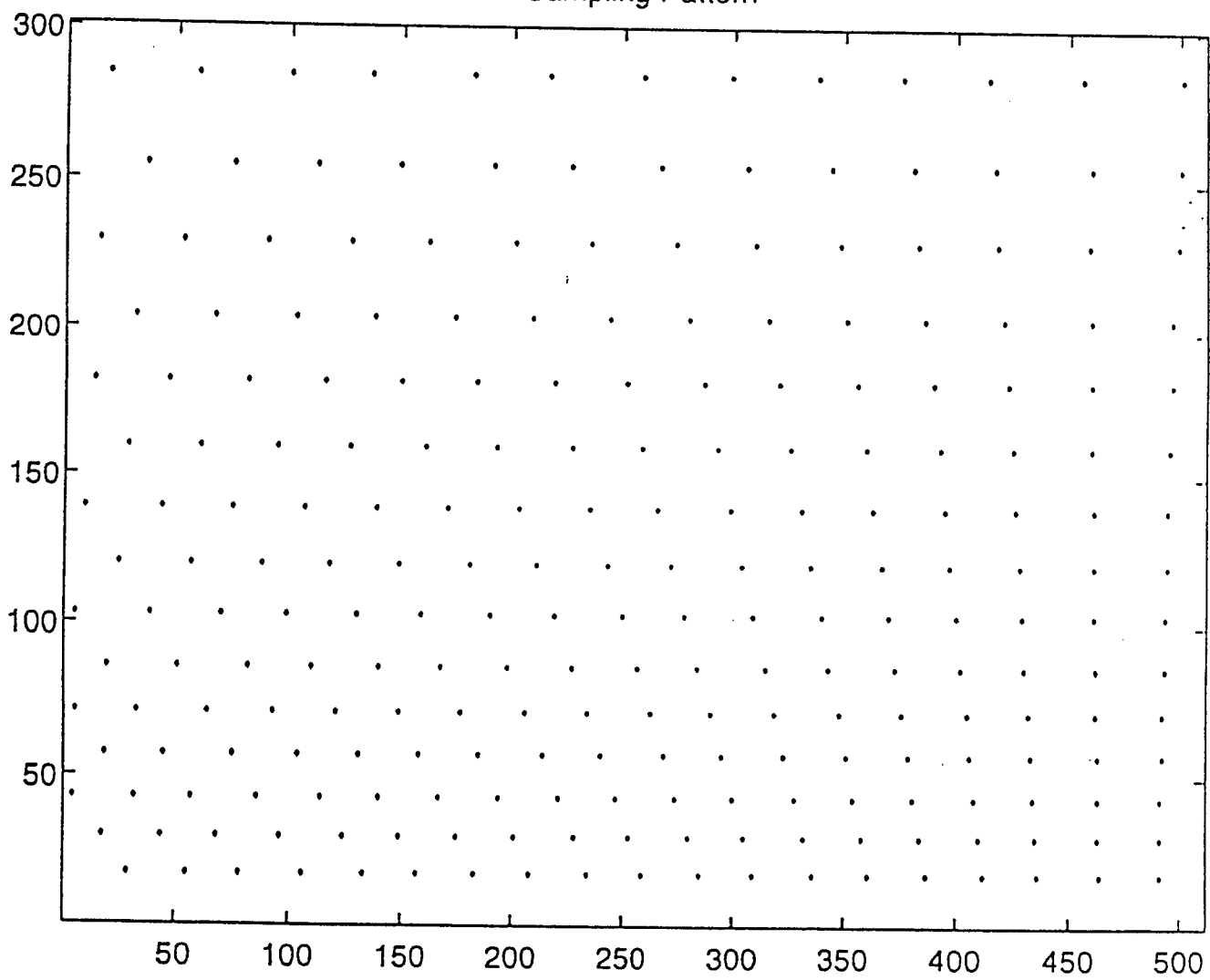


Figure 5

accuracy, and more often. This program also uncovered a balancing problem with the arch that has gone undetected up to this point. Balancing the arch was a long, tedious process and hopefully will not be necessary before each alignment. Once the balancing has been done, the alignment procedure should be completed in approximately 30 minutes. The accuracy of the overall alignment can be seen when the laser is positioned on the string. Any fading of the laser line on the string, while the arch is rotating, is an indication of an alignment problem and will compromise the accuracy of the 3-D image.

The calibration process experienced incredible improvements both in accuracy and speed. The original method, which took two people and 1.5 hours to complete, was plagued by measurement and human error. The new methods require 1 person and 5 minutes to complete. The reduction of human error and speed improvements result from the intervention of a computer program which finds pixel values and creates the two calibration surfaces. With the elimination of human errors, the accuracy is now dependent on the model used to create the surface, quadratic in this case. Different models as well as different ways to use these models should be studied and categorized according to speed, accuracy, and repeatability. The results of a preliminary experiment are discussed below.

The 'truth' data was collected with the existing equipment, a manual sliding column which contained 19 white pins spaced .5" apart. The calibration surfaces were created with this data by using Matlab's cubic spline routine. Another set of calibration surfaces were created with nine points of the 'truth' and the quadratic model program. A 360 line scan of a truck was performed and the resulting 3-D images were compared. The image created with 'truth' data resulted in an image whose dimensions were accurate with the real object, see Figure 6. The image created with the quadratic model appeared to have a double image of the windshield, and after analyzing its dimensions, the truck was found to be elongated, see Figure 7. The calibration surfaces were then compared to find their relative error. The error between the height surfaces was minimal, .1"-.2" maximum, see Figure 8. However, the range surface was much more sensitive to error than the height map, see Figure 9.

The sensitivity of the placement of these nine points was tested. Choosing the nine points closer to the center of the 300 x 512 region resulted in a better representation at the center than at the edges.

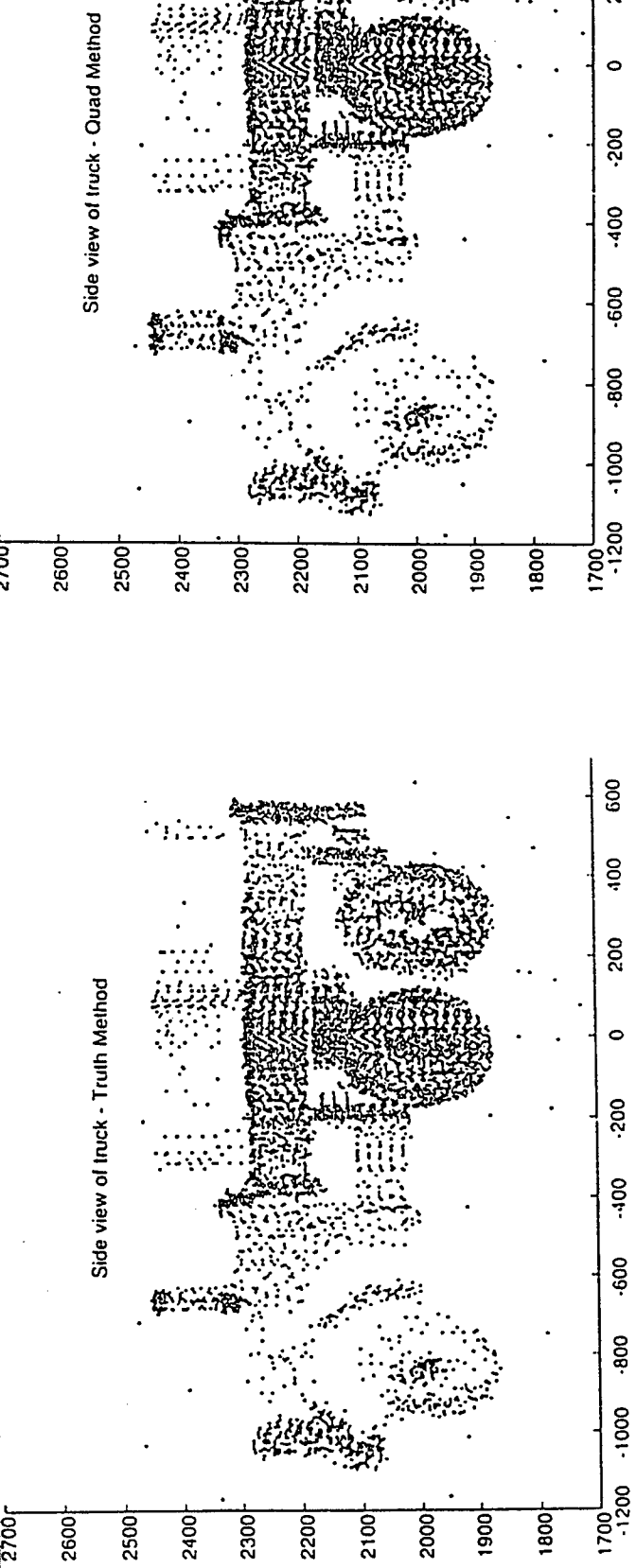


Figure 6

Height Error... TRUTH-ESTIMATED

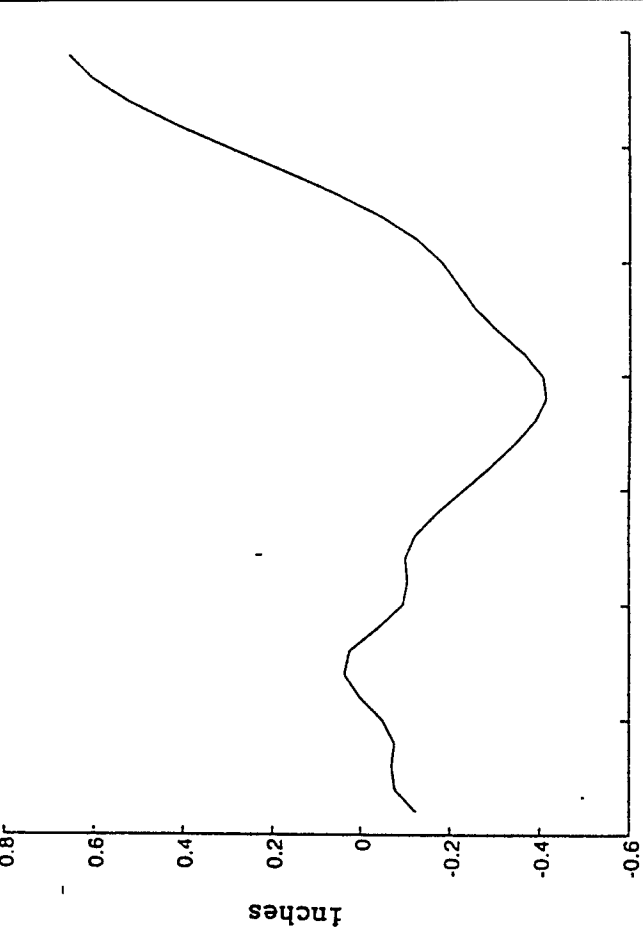


Figure 7

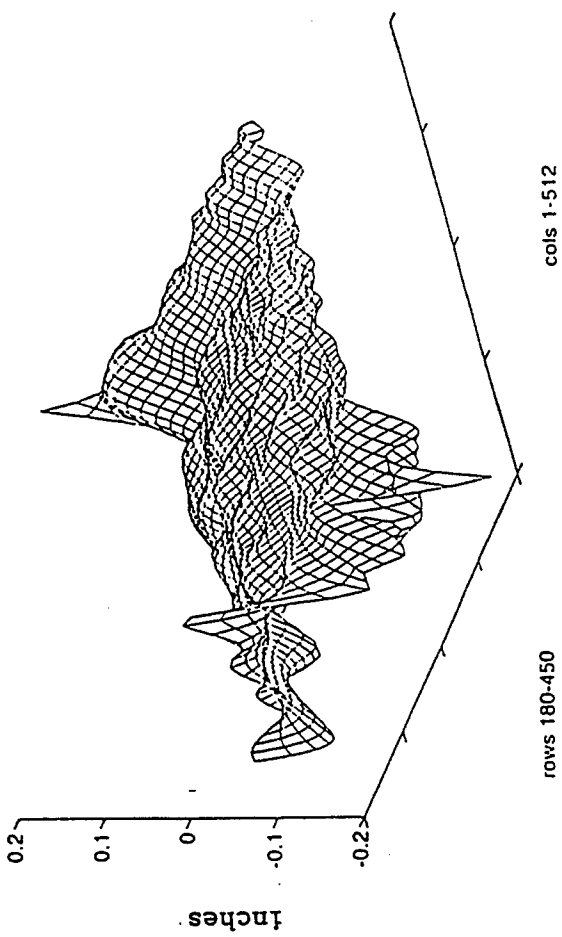


Figure 8

Figure 9

Choosing the nine points near the edges results in an averaging of the surface error. To summarize, randomly choosing 9 points is not reliable enough. The high sensitivity will produce unpredictable results depending on the size and characteristics of the object.

Conclusion

The speed and accuracy improvements accomplished through this study have made the 3-D scanner easier and efficient to use when performing scans or testing new ideas. Future work includes further study of the calibration surface. The quadratic model produced accurate results sometimes, but a more dependable, less sensitive, model is desired for higher accuracy. The optimal model may not contain the highest accuracy. With higher accuracy comes slower processing times, thus, it is necessary to know the performance measures of each method. Choosing the optimal model now becomes dependent on the application of the 3-D scanner. Another goal for the future is to completely eliminate the alignment procedure. The alignment is necessary because the system uses the cylindrical coordinate system. Another system currently being studied is based on a x, y, z coordinate system, which needs calibrated but not aligned. Although this system looks promising, no conclusions have been reached.

Bibliography

[1] Power, Greg and Kefu Xue. "A Non-Linear Transform Technique for a Camera and Laser 3-D Scanner". Proc. of IEEE, NAECON. Dayton, OH. May 1995.

Creating a HTML Document

Lesley Ann Pérez
Research Associate
Department of Civil Engineering

The Ohio State University
Columbus, OH 43210

Final Report for:
Graduate Summer Research Program
Wright Laboratory

Sponsored by:
Air Force Office of Scientific Research
Bolling Air Force Base, DC

and

Wright Laboratory

September 1995

CREATING A HTML DOCUMENT

Lesley Ann Pérez

Research Associate

Department of Civil Engineering

The tools necessary for the development of a HTML file were collected. This paper consists of a compilation of information necessary to create a homepage, the HTML file and the homepage itself. All the needed information was obtained through the Internet. Files required for the homepage were downloaded into a the directory from which it operates. The set of commands necessary in the creation of the homepage are shown within the HTML file as comments.

CREATING A HTML DOCUMENT

Lesley Ann Pérez

INTRODUCTION

In a very short time, the Internet has affected the lives of millions of people. The Internet is a worldwide network of computer networks. Current statistics show that there are about three million hosts (essentially a computer connected to the Internet) on the Net, which equates to more than 30 million people actually using the system worldwide.

Some of the uses of the Internet are electronic mail, file transfer, information browsing and retrieval, social communication and news gathering. Universities and colleges, government departments, big corporate concerns, commercial on-line services, even political parties, are all connected, and use the Net on a daily basis.

Nowadays the internet also include personal documents or personal homepages. One of the purposes of a homepage is to collect all the useful information found in the Internet into single document that you can easily refer to. Another purpose is a means for letting people know who you are. This makes the Internet a very powerfull tool since it connects people around the world.

METHODOLOGY

The first important step to creating a good HTML document for your homepage is finding a good HTML editor. A HTML (HyperText Markup Language) document is an ASCII text file that contains embedded HTML tags. In general, the HTML tags are used to identify the structure of the document and to identify hyperlinks and their associated URLs. The next thing to do is learn about HTM, the standard language used to bring documents to your screen. It is not necessary to have a HTML editor since the editing can be accomplished on any simple word processor. However, a good editor makes it much easier. The following address contains a list of HTML editors, download programs and other information.

http://www.yahoo.com/Computers_and_Internet/Internet/World_Wide_Web/HTML_Editors/

RESULTS:

The following is an example of the HTML file developed for the homepage and itself. This homepage can not be accessed yet but, it will soon be put into a server. HTML commands are explained within the HTML file.

The HTML file

```
<!--*****  
HTML editor for the Macintosh was used in writing this text document.  
To find the latest version of the HTML editor:  
http://dragon.acadiau.ca/~giles/HTML\_Editor/Documentation.html  
*****-->  
  
<!--*****  
HTML tags are encapsulated within less-than(<) and greater-than(>) brackets. Some of the tags are single-element tags that can stand by themselves. Other tags are used in pairs. The ending tag is created by adding a forward slash (/) to the beginning tag  
(except for the comment tag: <!--comment-->).  
The syntax is : <tag>object</tag>  
*****-->  
<title>Bryan's Homepage</title><title>|</title><title>|</title><title></title><title></title><title>|</title>  
<title>|</title><title>|</title><title></title><title>|</title><title>|</title><title>B|</title><title>BR|</title>  
<title>|</title><title>BRY|</title><title>BRYA|</title><title>BRYAN|</title><title>BRYAN F|</title><title>
```

BRYAN FO-</title><title>BRYAN FOO</title><title>BRYAN FOOS</title><title>BRYAN
FOOS'</title><title>BRYAN FOOS'S</title><title>BRYAN FOOS'S H-</title><title>BRYAN
FOOS'S HO</title><title>BRYAN FOOS'S HOME</title><title>BRYAN FOOS'S HOME/</title>
<title>BRYAN FOOS'S HOME-</title><title>BRYAN FOOS'S HOMEPA</title><title>BRYAN
FOOS'S HOMEPAI</title><title>BRYAN FOOS'S HOMEPAGE</title><title>BRYAN FOOS'S
HOMEPAG</title><title>BRYAN FOOS'S HOMEPA</title><title>BRYAN FOOS'S HOME-
</title><title>BRYAN FOOS'S HOME</title><title>BRYAN FOOS'S HOM</title><title>BRYAN
FOOS'S HO</title><title>BRYAN FOOS'S H-</title><title>BRYAN FOOS'S</title><title>BRYAN
FOOS'</title><title>BRYAN FOOS</title>
<title>BRYAN FOO</title><title>BRYAN FO-</title><title>BRYAN F</title> <title>
BRYAN</title><title>BRYA</title><title>BRY-</title><title>BR</title><title>Bl</title>
<title>l</title><title>l</title><title>-</title><title>/</title><title>\</title><title>\</title><title>-\
<title><title>l</title><title>l</title>
<title>-----B</title><title>-----BR</title>
<title>-----BRY</title><title>-----BRYA</title>
<title>-----BRYAN</title><title>-----BRYAN </title>
<title>-----BRYAN F</title><title>-----BRYAN FO</title>
<title>-----BRYAN FOO</title><title>-----BRYAN FOOS</title>
<title>-----BRYAN FOOS'</title><title>-----BRYAN FOOS'S</title>
<title>-----BRYAN FOOS'S </title><title>-----BRYAN FOOS'S H</title>
<title>-----BRYAN FOOS'S HO</title><title>-----BRYAN FOOS'S HOM</title>
<title>-----BRYAN FOOS'S HOME</title><title>-----BRYAN FOOS'S HOMEPA</title>
<title>-----BRYAN FOOS'S HOMEPAI</title><title>-----BRYAN FOOS'S HOMEPAG</title>
<title>-----BRYAN FOOS'S HOMEPAGE</title>

The title tag pair is used once per document and identifies the title of the document. Animated titles are created by using multiple title tags

*****-->

<body bgcolor="#e6e8fa"><body bgcolor="#e6e8fa"><body bgcolor="#e6e8fa"><body
bgcolor="#e6e8fa"><body bgcolor="#e6e8fa"><body bgcolor="#e6e8fa"><body
bgcolor="#e6e8fa"><body bgcolor="#8c1717"><body bgcolor="#8c1717"><body bgcolor="#8c1717"><body
bgcolor="#8c1717"><body bgcolor="#8c1717"><body bgcolor="#8c1717"><body
bgcolor="#8c1717"><body bgcolor="#e6e8fa"><body bgcolor="#e6e8fa">

```
<body bgcolor="#e6e8fa"><body bgcolor="#e6e8fa"><body bgcolor="#e6e8fa"><body bgcolor="#e6e8fa">
<body bgcolor="#e6e8fa"><body bgcolor="#8c1717"><body bgcolor="#8c1717"><body bgcolor=
"#8c1717"><body bgcolor="#8c1717"><body bgcolor="#8c1717"><body bgcolor="#8c1717">
<body bgcolor="#8c1717"><body bgcolor="#8c1717"><body bgcolor="#e6e8fa"><body bgcolor=
"#000000"><body bgcolor="#8c1717"><body bgcolor="#000000"><body bgcolor="#e6e8fa"><body
bgcolor="#000000"><body bgcolor="#8c1717"><body bgcolor="#000000"><body bgcolor=
"#e6e8fa"><body bgcolor="#000000"><body bgcolor="#8c1717"><body bgcolor="#000000"><body
bgcolor="#e6e8fa"><body bgcolor="#000000"><body bgcolor="#8c1717"><body bgcolor="#000000">
<body bgcolor="#e6e8fa"><body bgcolor="#000000"><body bgcolor="#8c1717"><body
bgcolor="#000000">
<!-----*****----->
```

This is an example of a fade-in. By using enough body bgcolor tags the screen goes through the series of colors specified. Netscape uses a theoretical color scheme in which each color is represented from 00 to FF in hexadecimal. Making a total of 16,777,216 colors. The following is a list of some colors.

```
* #000000=black * #00ff00=green * #8c1717=scarlet
* #ff0000=red * #cococo=grey * #e6e8fa=sylver
* #00ff00=blue * #ffff00=yellow * #ff7f00=orange
* #a62a2a=brown * #ffffff=white * #ff00ff=magenta
*****-->
```

```
<!-----*****----->
```

Formatting tools:

b-bold text (coded in pairs, closing tag with a /).

UL-indents a line. (coded in pairs).

I-italic text (coded in pairs).

!-comments(coded in pairs).

blink- makes the background of the letters blink.(coded in pairs)

p-indicates the ending of a paragraph or line.

```
*****-->
```

```
<body background="903s7b2color" text="#ff6ec7" link="#123ecf" vlink="#000000" alink="#ff0000">
```

```
<!-----*****----->
```

One of the most important HTML tagging pairs creates a hyperlink to another document or Internet resource. Generically, the Anchor tagging pair is used as

follows:

anchor-text

These commands set the background and the color of the text in the document.

- * **LINK** is just a regular, never before visited link.
- * **VLINK** is a previously viewed link
- * **ALINK** is an active link (The color when you click on it).

(any of these options can be omitted)

Some background files could be found at: <http://www.nashville.net/~carl/htmlguide/index.html> or by typing in "Netscape backgrounds colors" on the search window. The background used in this homepage is a scanned image saved as gif file and put into the same directory as this text.

*****-->

!--*****

IMG SRC displays an in-line image(that is, an image next to text) that is in a gif format. Loading of the image slows down the display of the document. When you see an image or graphic that you like on another homepage you can easily downloaded to your directory by:

- * clicking the mouse down on the desired image and holding it until a pop-up menu appears.
- * selecting "Save this Image As..." from the pop-up menu.
- * when prompted, save the file with an appropriate name and location.

*****-->

<hr size=5 width=100% align=center><hr size=4 width=75% align=center>
<hr size=3 width=50% align=center><hr size=2 width=25% align=center>

!--*****

Hr inserts a shadow line in order to separate subsections of the homepage. Hr NOSHADe produces a black line. This shadow line could be ALIGNed either left, right or at the center. SIZE determines the thickness of the line (ranges from 1-7)and WIDTH refersto the total length of the line.

*****-->

```
<center><h1>Bryan's Homepage</h1></center>
```

```
<IMG SRC="lifter.gif">
```

```
<IMG SRC="constnew.gif">
```

```
<!--*****-->
```

Headers indicate a level of structure in your document. Headers range from H1(biggest) to H6(smallest), and are coded in pairs.

```
*****-->
```

```
<center><b><blink><font size=15> I<a href="http://www.pinc.com/phantom "> link </a> . . . therefore I  
am.</b></blink><br></center></font>
```

```
<hr>
```

```
<font size=3>You are the<IMG SRC="http:info.mcc.ac.uk/cgi-bin/counter?UID&width=5"> person to  
access this page since <B>9/18/95.</B></font>
```

```
<hr>
```

```
<a href="photoscript"></a>Hi! My name is Bryan Foos, and  
welcome to my homepage. Click <a href="personal">HERE</a> or on the drawing to see a real picture of  
me and other personal information, or click<a href="voice.wav"> here </a>to hear me talk.<p>
```

```
<!--*****-->
```

a href is a parameter that specifies the document that's being pointed to.

In this case the in-line graphic of Bryan links to an external much larger
image. By doing this the downloading is not delayed w large in-line images.

```
*****-->
```

```
<a href="#cool"><I>Click here</I></a> to skip ahead to the <I>really cool stuff.</I><p>
```

```
Curious about this background? <a href="backscript"><I>Click here to find out what the background  
is.</I></a><p>
```

```
<!--*****-->
```

In this case a href is linking to specific sections within your document

```
*****-->
```

```
Click here to see some <a href="Airforce2"><I>cool Air Force pictures</I></a><p>
```

```
<hr>
```

```
<a href="http://www.wl.wpafb.af.mil/welcome.html"></a>I am employed by  
<a href="http://www.wl.wpafb.af.mil/welcome.html"><I>Wright Laboratories</I></a> at Wright  
Patterson AFB near <a href="http://www.firstnet.net/dayton/Welcome.html"><I>Dayton</I></a> <a  
href="http://www.yahoo.com/Government/States/Ohio/"><I>Ohio</I></a><p>
```

<hr>

I work in the <I>Materials Lab</I> which is one of several Labs within Wright Labs. <p>

<hr>

<h3>My own personal references!</h3>

As a student at Ohio State and a research engineer at Wright Patterson AFB, I have been the author or co-author of the following:<p>

"Damage in Graphite/Epoxy Plates Subjected to Low Velocity Impact"--

Final report published in 1988.

"Strain Distribution in Composite Coupons Under Tension"--Final

report published in 1989.

<hr>

<h3>A list of some interesting sights:</h3>

ARPA home page

AirForceLINK

ArmyLINK

Want to make some extra <p>

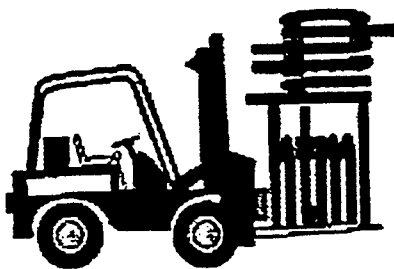
<hr size=5 width=100% align=center> <hr size=4 width=75% align=center>

<hr size=3 width=50% align=center> <hr size=2 width=25% align=center>

Click _HERE to see my resume<p>

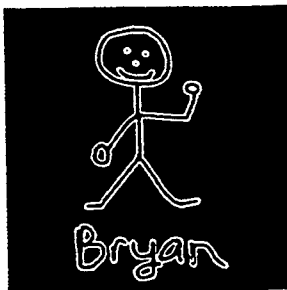
<h2><cite>Foos@ml.wpafb.wpafb.af.mil</h2></cite>

Bryan's Homepage



THIS PAGE IS UNDER CONSTRUCTION. PLEASE WATCH YOUR STEPS!!

I link . . . therefore I am.



Hi! My name is Bryan Foos, and welcome to my homepage. Click [HERE](#) or on the drawing to see a real picture of me and other personal information, or click [here](#) to hear me talk.

[Click here](#) to skip ahead to the *really cool stuff*.

Curious about this background? [Click here to find out what the background is.](#)

[Click here](#) to see some *cool Air Force pictures*



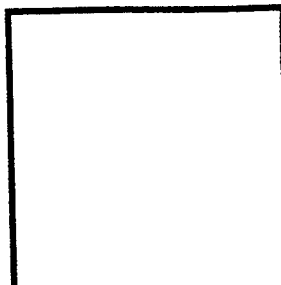
I am employed by [Wright Laboratories](#) at Wright Patterson AFB near [Dayton, Ohio](#).



I work in the Materials Lab, which is one of several Labs within Wright Labs.



I am currently working on my PhD in Civil Engineering at The Ohio State University. I also attended there for my bachelors and masters degrees, which were also in Civil Engineering.



And here is the 90's version of OSU's symbol, plus go on a Tour of the Campus

My own personal references!

As a student at Ohio State and a research engineer at Wright Patterson AFB, I have been the author or co-author of the following:

- "Damage in Graphite/Epoxy Plates Subjected to Low Velocity Impact"--Final report published in 1988.
- "Strain Distribution in Composite Coupons Under Tension"--Final report published in 1989.
- "Experimental Determination of Damage Initiation Resulting From Low Velocity Impact of Composites," with Dr. William E. Wolfe--Final report published 1991.
- "The Effect of Tab Orientation on the Distribution of Strains in Composite Specimens," with Dr. William E. Wolfe and Dr. Ranbir S. Sandhu--Published by ASTM, 1992.
- "Research Proposal on Thermal Stress Analysis of Composite Laminates"--Published 1993.

A list of some interesting sights:

- [List of WWW servers](#)
- [Library of Congress](#)
- [Federal Information Center](#)
- [United Nations Information Services](#)
- [OSD home page](#)
- [OSD guide to organizations and functions](#)
- [C3I home page](#)
- [DDR&E home page](#)
- [DTSE&E home page](#)
- [ACOWEB – OSD\(A&T\) home page](#)
- [DTIC home page](#)
- [DTIC acquisition information home page](#)
- [DOD information systems technology insertion home page](#)
- [Technology Reinvestment Project \(TRP\) home page](#)
- [ARPA home page](#)
- [AirForceLINK](#)
- [ArmyLINK](#)
- [Navy home page](#)
- [NAVYonline home page](#)
- [The Silent Service](#)
- [USMC home page](#)
- [DEFENSELINK LOCATOR -- Coast Guard home page](#)
- [Defense Acquisition University \(DAU\) home page](#)
- [Comprehensive Approach to Reusable Defense Software \(CARDS\) home page](#)

• [Corporate Information Management \(CIM\) Help Desk home page](#)

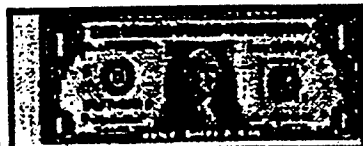
• [Joint Services Conference on Professional Ethics home page](#)

• [Air Force WWW Clearinghouse](#)

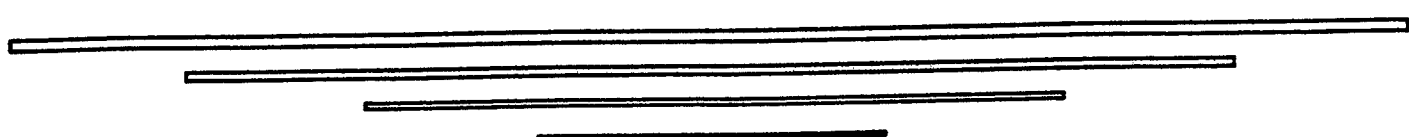
• [DefenseLINK](#)

• [DISA-JEXE \(DOD Software Environment Dept\) home page](#)

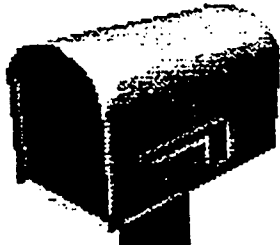
• [United States Air Force WWW Servers](#)



Want to make some extra



Click [HERE](#) to see my resume



Foos@ml.wpafb.wpafb.af.mil

CONCLUSION:

The process of creating a HTML file can be done through commands found in the system. One could take advantage of the interactive and multimedia capabilites of the Internet. On-line forms, graphics, sound, and video could be added to homepages and its creativity can be unlimited. As one can see, the Internet has proven to be one of the most powerful tools for information exchange.

REFERENCES:

Beginner's Guide to HTML

<http://www.gnn.com/gnn/wic/html.03.html>

HTML Glosary & Guide

<http://www.lehigh.edu/~kaf3/guides/kenhtml.html>

HTML Tutorial

<http://www-pcd.stanford.edu/mogens/intro/tutorial.html>

The 256 Colors of Netscape

<http://www.soest.hawaii.edu/bob/Netscape.colors.html>

Downloading Graphics

<http://hakatai.mcli.dist.maricopa.edu/tut/help-dl.html>

Netscapesound how-to

<http://www.xmission.com/~len/va/netsound.html>

HTML Editors for the Macintosh

http://dragon/acadiau.ca/~giles/HTML_Editor/Documentation.html

List of WWW servers

http://www.fir.com/www/us_gov.html

DTSE&E homepage

<http://www.acq.osd.mil/te/>

TEMPERATURE VISUALIZATION OF A ROTATING DISK FLOW FIELD
USING THERMOCHROMIC LIQUID CRYSTALS

Lon H. Preston
Graduate Student
Department of Mechanical Engineering

The Pennsylvania State University
128 Reber Bldg.
University Park, PA 16802

Final Report for:
Graduate Student Research Program
Wright Laboratory

Sponsored by:
Air Force Office of Scientific Research
Bolling Air Force Base, DC

September 1995

TEMPERATURE VISUALIZATION OF A ROTATING DISK FLOW FIELD
USING THERMOCHROMIC LIQUID CRYSTALS

Lon H. Preston
Graduate Student
Department of Mechanical Engineering
The Pennsylvania State University

Abstract

It is recognized that that turbine disk design requires specific knowledge of heat transfer processes to predict stresses and disk life. This study examines the effect of radial outflow coolant air on heat transfer processes on a heated, rotating disk. A major consideration is the stability of the flow field, which, in actual turbines, is affected by the ingress of hot combustion gases and the flowrate of coolant air. The rotating configurations include rotor-stator, co-rotating, and counter-rotating disks. A program was initiated which has the objective of temperature visualization of the flow field using thermochromic liquid crystals. A liquid crystal coating is applied to the heated rotating disk. The project considers the application and calibration of liquid crystal coatings, illumination of the surface and color temperature acquisition software.

TEMPERATURE VISUALIZATION OF A ROTATING DISK FLOW FIELD USING THERMOCHROMIC LIQUID CRYSTALS

Lon H. Preston

Introduction

In advanced design gas turbine engines, air bled from the compressor is used to cool the turbine disks and seal the cavity against ingress of hot gases. The proper design of a turbine should include specific knowledge of its temperature in order to accurately predict stresses and the life of the disk. The knowledge should include the effect of the rotating flow field within the disk cavity on such parameters as the heat transfer, the disk friction, and the mass flow required to seal the cavity.

Rotating disk systems may be conveniently classified in three categories: co-rotating (where both disks rotate in the same direction), counter-rotating (with rotation in the opposite direction), and rotor-stator (where one disk rotates and the other remains stationary). Each type of flow field may be found in state-of-the-art gas turbines. Figure 1 illustrates the air-cooling in a turbine with a rotor-stator configuration and with co-rotating disks. Figure 2 illustrates the air-cooling of a counter-rotating turbine. This paper presents the results of an experimental investigation of the flow field for counter-rotating disks. The study specifically focuses on turbulent heat transfer measurements on a heated disk.

The complexity of the flow field arises from centrifugal and Coriolis forces, as well as boundary layer growth. An early investigation of the counter-rotating case by Batchelor (1951) argued that for laminar flow between infinite disks, radial outward flow at the boundary layer would be attended by radial inward flow along a shear layer between cores counter-rotating with some angular velocity Ω . In contrast, Stewartson (1953) predicted that the central core of fluid would not rotate. Recent studies by Gan et al. (1993) indicate that laminar boundary layer growth is present up to local rotational Re of 1.1×10^5 . No evidence is found for a central shear layer and counter-rotating cores. Owen (1988) shows that the structure of the flow field with radial outflow appears as in Figure 3. The incoming fluid is entrained into the boundary layers on the disks. After the fluid is entrained, Ekman layers form on the disks. For non-symmetric heating, the flow in each layer will not be the same. The Ekman layer equations are derived (Owen, 1988) with respect to the rotating frame and indicate the predominance of Coriolis forces.

Gan et al (1993) define the dimensionless parameters which specify the system variables. A typical rotating disk configuration is shown in Fig. 4. The dimensionless radii x and x_a are

$$x = \frac{r}{b}, \quad x_a = \frac{a}{b}.$$

A shrouded cavity requires two dimensions. The distance between the two disks s is defined by the gap ratio G , given as

$$G = \frac{s}{b}.$$

The clearance between the shroud and the rotating disk is given by the shroud clearance parameter G_c , where G_c is defined as

$$G_c = \frac{s_c}{b}.$$

Two Reynolds numbers are defined for the rotational flow and the axial flow, given respectively as

$$Re_\phi = \frac{\rho \Omega b^2}{\mu} \quad Re_z = \frac{\rho W b}{\mu}.$$

In this study, a superposed radial outflow of cooling air is examined, and this is defined by a nondimensional flow rate parameter C_w , given by

$$C_w = \frac{\dot{m}}{\mu b}.$$

Two parameters which have engineering relevance are the moment and pressure coefficients, C_m and C_p .

Gan defines the frictional moment as follows, with M being the frictional moment on the disk,

$$C_m = \frac{M}{\frac{1}{2} \rho \Omega^2 b^5}.$$

The pressure coefficient is given as

$$C_p = \frac{\Delta p}{\frac{1}{2} \rho U^2}.$$

The heat transfer coefficient is characterized by the Nusselt number and the modified Nusselt number, defined as

$$Nu = \frac{q_o r}{k(T_s - T_{ref})} \quad Nu^* = \frac{q_o r}{k(T_s - T_{s,ad})}.$$

The ingress of hot turbine gases into the rotor cavity is related to the minimum flow rate necessary to prevent ingestion. Under actual turbine operating conditions, some degree of ingestion usually occurs, so the sealing effectiveness parameter ϕ is given by

$$\phi = \frac{C_w}{C_w + C_{w,min}}.$$

In this study, a heated disk is used, and buoyancy effects must be considered in regard to convection. The local Grashof number is given as

$$Gr_x = \frac{\rho^2 \Omega^2 r^4 \beta \Delta T}{\mu^2} = \beta \Delta T (x^2 \text{Re}_\phi)^2,$$

with ΔT being the difference between inlet cooling air temperature and local disk surface temperature. The Coriolis forces are accounted for by the Rossby number, given as

$$Ro = \frac{\dot{m}}{2\pi \rho r^2 g \Omega}.$$

Objectives

The objectives of this program are to examine the variables of cooling air flow rate and heating on the rotating flow field, including an assessment of shroud clearance and gap spacing on these parameters. Visualization of the temperature distribution is to be performed through video acquisition of the color response of thermochromic liquids crystals on the heated disk surface. A secondary objective is to establish in-house facilities for application and calibration of liquid crystal surfaces.

Liquid Crystal Thermography

Visualization of a temperature field is a powerful technique which gives the researcher insight into the structure of the flow and convective heat transfer processes. Although the properties of liquid crystals have been known for a century, the use of temperature sensitive liquid crystals to determine convective heat transfer coefficients has given promising results only in recent years (Kasagi et al, 1988).

Conventional temperature measurement devices such as thermocouples have been employed for this purpose but are inconvenient for visualization of large areas since many point readings are required. The response time for a surface temperature measure is much slower because the thermocouple is often embedded just beneath the surface. The advantages of liquid crystals include the following (Kasagi et al, 1988):

1. Easily handled and inexpensive
2. Small but predictable effect on the flow field
3. Nearly instantaneous measurement
4. Satisfactory accuracy and resolution

A liquid crystal is an organic substance which exhibits behavior between an isotropic liquid and a nonisotropic crystalline solid. The transition from one phase to the other can occur from changes in shear stress, electromagnetic fields, pressure, as well as temperature changes. Temperature sensitive, or thermochromic, liquid crystals are the subject of this study. The liquid crystal may be classified in three groups, according to optical behavior and molecular arrangement (Farina et al, 1994): smectic, nematic, and cholesteric, shown in Fig. 5. The particular optical characteristics of these structures are circular dichroism and rotary polarization. The former gives the liquid crystal a color response at its event temperature, and the latter polarizes the reflected light.

A significant part of this study is the relation of the color response of a liquid crystal and the corresponding temperature. Liquid crystals are specified largely on the basis of two parameters: the event temperature and the temperature bandwidth. The event temperature is the point at which color is visibly reflected, and the bandwidth is the temperature range over which color is visible. For example, the liquid crystal used in this study is specified as R45C5, which means a event temperature of 45 C and a 5 C temperature range. The bandwidth parameter is used to further characterize two classes of liquid crystals: narrow-band and wide-band. Narrow-band crystals have a range of 2 C or less, while the wide band temperature is any range above 2 C (Farina et al 1994).

Calibration of thermochromic liquid crystals is dependent on several factors. The color response of a liquid crystal is affected by the angle of observation and the angle of illumination, and a calibration system must meet this requirement. Kasagi et al (1988) note that liquid crystal applications are stable for

approximately one year. Accuracy of the temperature response may remain longer, but the color brilliance will fade. Several factors which hasten the loss of color are UV light, fluorescent lights, and high temperatures.

Liquid Crystal Calibration Facility

In-house liquid crystal application and calibration are a major objective of this project. A common methodology of calibrating liquid crystals is to apply a linear temperature gradient over a test strip. WL/POTT has initiated liquid crystal calibration through implementation of a system developed at Stanford University (Farina et al 1994). The system in its entirety includes color acquisition software which is coupled to Sony DXC-151 video camera with RGB output. The imaging subsystem is comprised of a Matrox IM-1280 Base Board EISA version with RTP (Real Time Processor) and CLD (Color Digitizer). The illumination equipment consists of a Moritex MHF-150L white light source and a Moritex MRG61-1500S fiber optic ring light. Crossed polarizing filters are provided for the camera and the light ring. The software allows transient temperature study with multiple frame grabbing, as well as steady state analysis.

A calibration unit compatible with the requirements of the system was constructed and is shown in Fig. 6. A copper calibration bar measuring 10 in. x 2 in. is fitted with 19 thermocouples (Type J, 30 gage); the calibration test strips are slightly smaller in size, $9\frac{7}{8}$ in. x $1\frac{7}{8}$ in., in accordance with the standards of the Stanford calibration system. A temperature distribution is created across the bar by flat plate heaters (Omega, 150 W). The hot end consists of one heating element, and the other end consists water-cooled aluminum block which is interposed between the calibration bar and the heater element. The heater element is provided at the cool end as a means of fine-tuning; in some cases, this proves more convenient than adjusting water flow, as a very small flowrate is required for the temperature distribution typical of most liquid crystals.

The housing for the liquid crystal calibration unit provides insulation on all surfaces surrounding the calibration bar. A layer of 4 in. hard insulating foam creates an isothermal zone beneath the calibration bar, assuring that all virtually all heat is dissipated upwards or laterally. The calibration bar and heaters

rest on balsa wood platform on top of the foam block. The balsa wood provides lateral insulation and is preferred due to a 3x higher thermal conductivity compared to other woods. The viewing port consists of a balsa frame holding two panes of anti-reflectance glass. The port prevents free convection from still air and eliminates much of the reflected illumination light. The unit is controlled by two Omega CN76000 process controllers and is capable of temperatures up to 90 C, allowing calibration of nearly all liquid crystal paints.

In-house application of liquid crystals is done with an artist's airbrush. Hallcrest black substrate paint and liquid crystal paint R45C5W are used in the present study. The application method (Farina et al. 1994) requires the application of the substrate, followed by light coats of liquid crystal paint to achieve a uniform coat that is approximately 30-50 μm thick. Thinned paints and a brushing pressure of 20-25 psi are found to be adequate. Calibration test strips are made at the same time as surface application; the strips are painted on black (exposed and developed) photographic paper.

Experimental Apparatus

The experimental apparatus has been documented in a previous AFOSR report (Ervin, 1992). Figure 7 shows a schematic illustration of the rotating disk unit. Two disks are set in pillow block bearings and are each 24 in. in diameter. The disks are independently powered by variable-speed 3-phase motors, which are controlled by frequency modulators. The unit is capable of speeds to approximately 1000 rpm and offers the choice of co-rotating, counter-rotating, or the rotor-stator configuration.

The unit was modified to permit study of the change in shroud clearance. The modifications are applied to the heated disk. The heated disk assembly consists of a 24 in. diameter aluminum shell, which is bolted to a flange on the rotating shaft. The heated disk is illustrated in Fig. 8. It consists of three laminations: a heating elements which is photoetched to provide even coverage of 90% of the disk area. The heating element is embedded within electrically resistive circuit board. The outer surface is capped with thin inconel foil, which is oxidation resistant and has constant emissivity over a wide temperature range (Ervin, 1992). The unit is fitted with thermocouples (Type J, 30 gage) to allow a secondary method of temperature acquisition. Sixteen thermocouples are available for measurement, as shown in Fig. 9. They are attached just beneath the inconel surface with thermal conducting epoxy. The liquid crystal

coating is applied over the inconel foil surface. Currently, a maximum of five thermocouple readings can be taken through a slip ring. Power to heated disk is through a German-silver slip ring which can pass a maximum of 80 A at 1000 rpm (Ervin, 1992). A rheostat controls the 440 V (3 phase) power supply. The heat emitted from the disk is determined from a shunt connected to the slip ring.

The remaining disk is constructed from plexiglass to permit optical access. A shroud is attached to the periphery of the disk to simulate a rotating turbine cavity. At present, one configuration is available. The cooling air is exhausted into the cavity from a 15 hp blower connected to a plenum chamber. Flow rates are determined from an orifice plate, pressure transducers, and a thermocouple, which are placed upstream.

Status of the Program

The rotating disk unit has been modified for liquid crystal temperature visualization. The heated disk is fitted with additional thermocouples and is remounted to permit variation in shroud clearance. The rotating disk unit has been tested and qualified to give uniform heating on the disk surface at steady state operation for speeds up to approximately 1000 rpm. The in-house facilities for liquid crystal application and calibration have been established and validated through preliminary testing. The facility now stands practically ready for data acquisition. Problems related to the commercial source code for the color temperature acquisition software have unfortunately prevented the acquisition of actual data during the time period allotted. These problems are expected to be resolved shortly; thus, arrangements for continuation of this program have been made.

Acknowledgments

The author wishes to express his thanks to the following:

- AFOSR, for financial support of this research
- RDL, for fine management of the Graduate Student Research Program
- Drs. Richard B. Rivir and Charles D. MacArthur (WL/POTT) for excellent and patient supervision of this project
- Greg Cala (WL/POTT) and David Pestian (UDRI) for their generous assistance
- Chris Murawski (WL/POTT), Shichuan Ou (WL/POTT), and John Schmoll (UDRI) for helpful advice and comments related to the project

References

Batchelor, G.K., "Notes on a class of the Navier-Stokes equations representing steady rotationally-symmetric flow," *Quart. Journal Mech. Appl. Math.*, Vol. 4, 1951.

Ervin, J.S., "Turbulent Heat Transfer in Counter-Rotating Disks with Thermographic Phosphor Temperature Determination," AFOSR Summer Faculty Report, 1992.

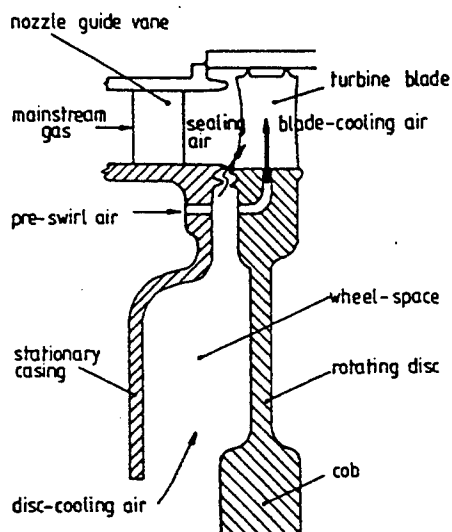
Farina, D.J. and Moffatt, R.J., *A System for Making Temperature Measurements Using Thermochromic Liquid Crystals*, Report No. HMT-48, Stanford University, Sept. 1994.

Gan, X., Kilic, M., and Owen, J.M., "Flow and Heat Transfer Between Gas-Turbine Disc," ASME Paper #93-GT-25

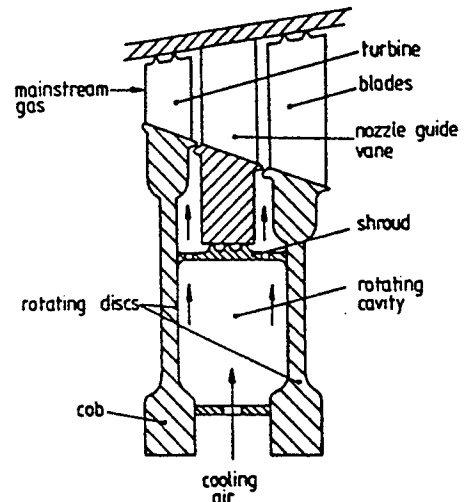
Kasagi, N., Moffatt, R.J., Hirata, M., *Liquid Crystals*, Wiley, New York, p. 105-123.

Owen, J.M., "Air-cooled gas-turbine disks: a review of recent research," *Int. Journal of Heat and Fluid Flow*, Vol. 9, No. 4, Dec. 1988.

Stewartson, K., "On the flow between two rotating coaxial disks," *Proceedings Camb. Phil. Soc.*, Vol. 49, 1953.

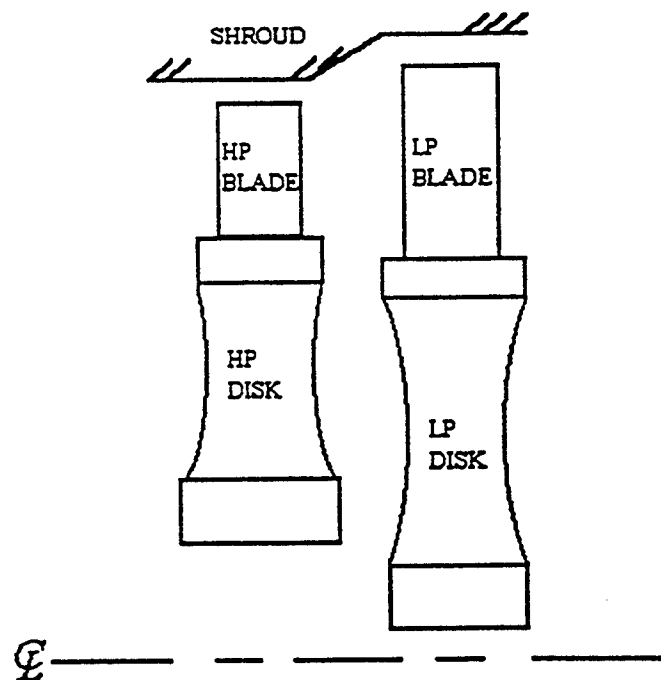


(a) Cooling flows between a turbine disc and a stationary casing.



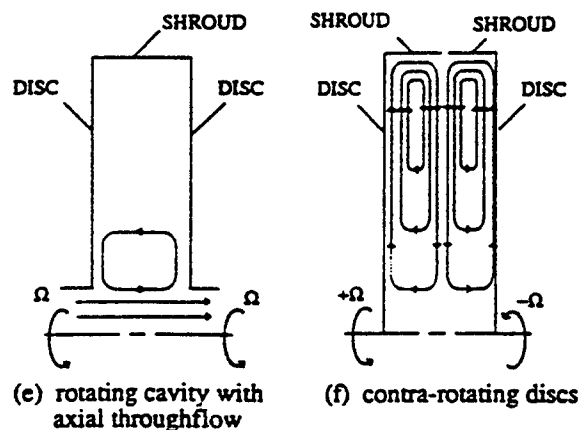
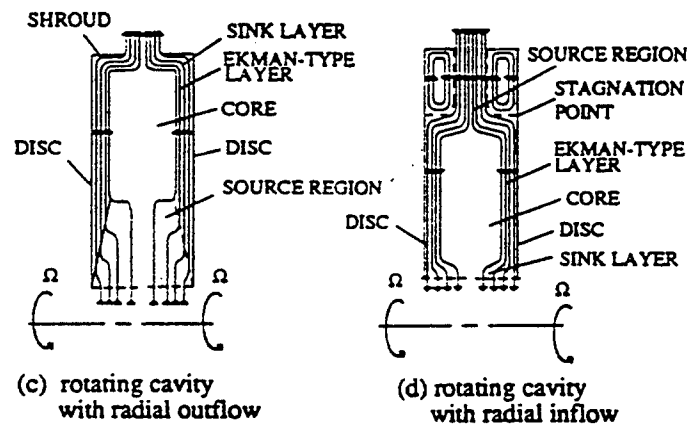
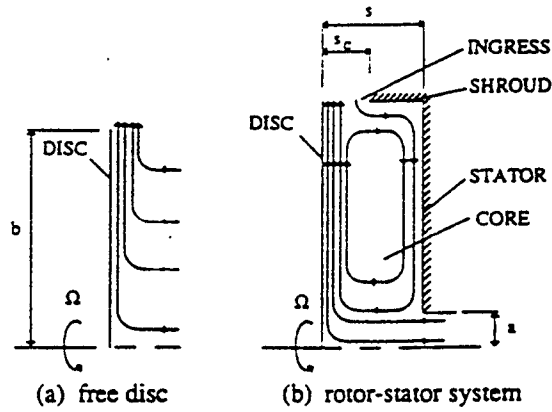
(b) Cooling flow between corotating turbine discs.

Figure 1 (from Owen, 1988)



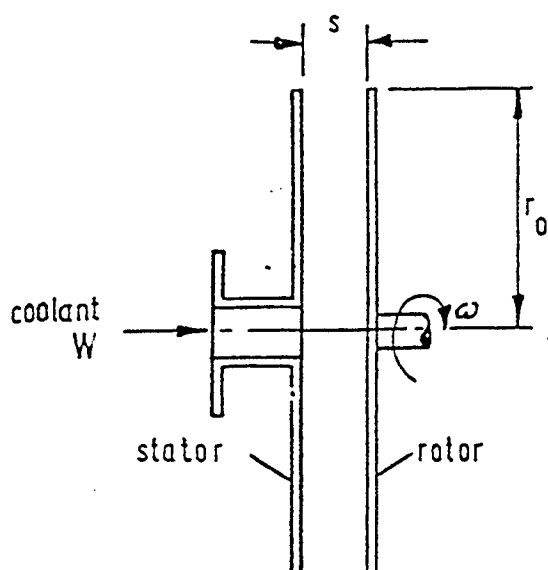
Counter-Rotating, Vaneless Design

Figure 2 (from Ervin, 1992)

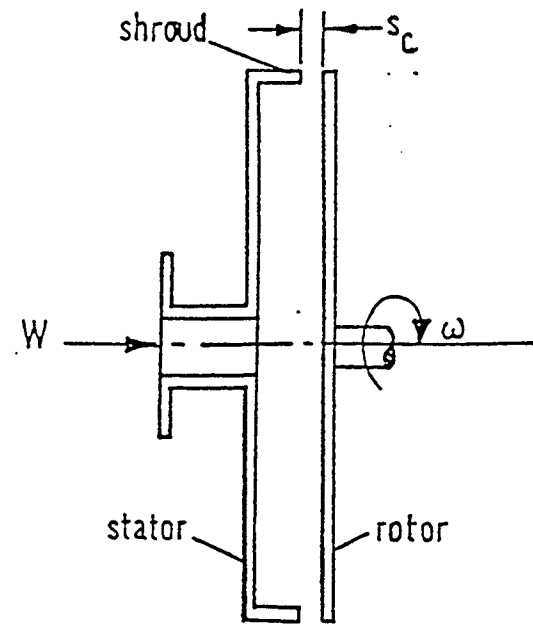


Schematic diagram of rotating-disc systems

Figure 3 (from Gan et al., 1993)

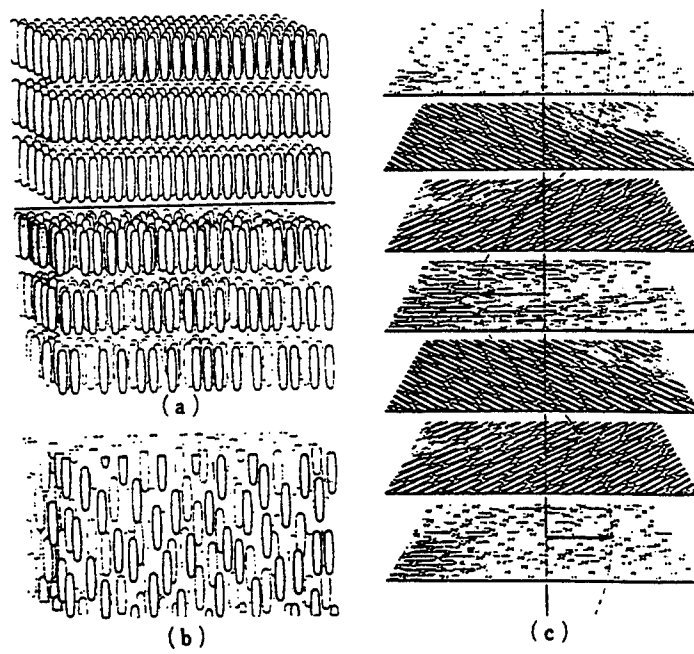


Unshrouded rotating disk model



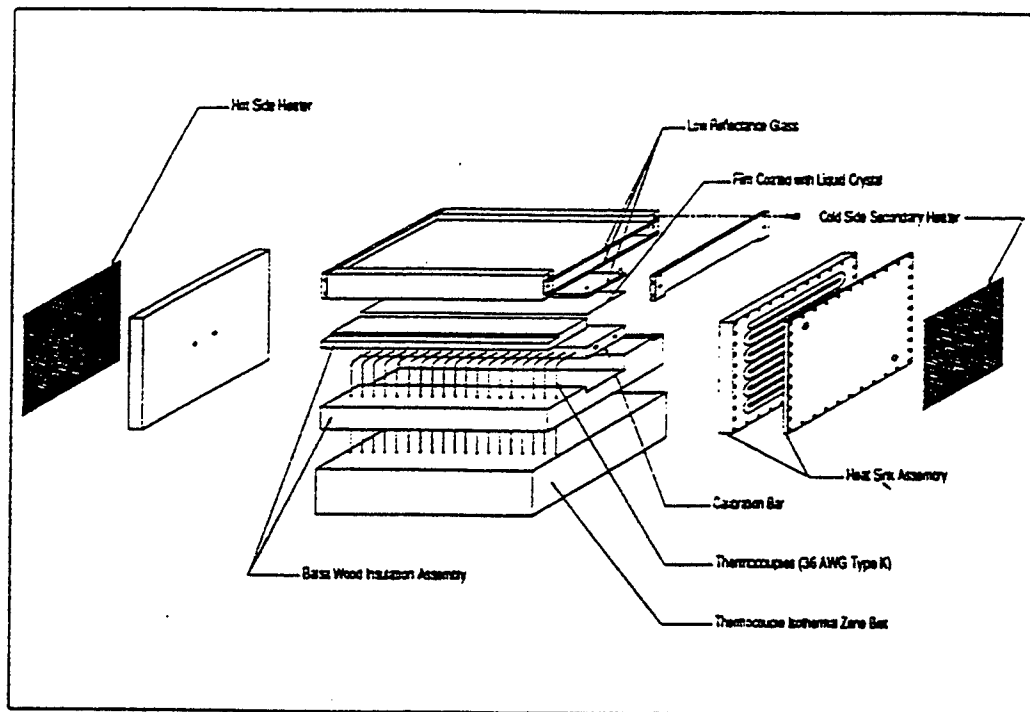
Shrouded rotating disk model

Figure 4

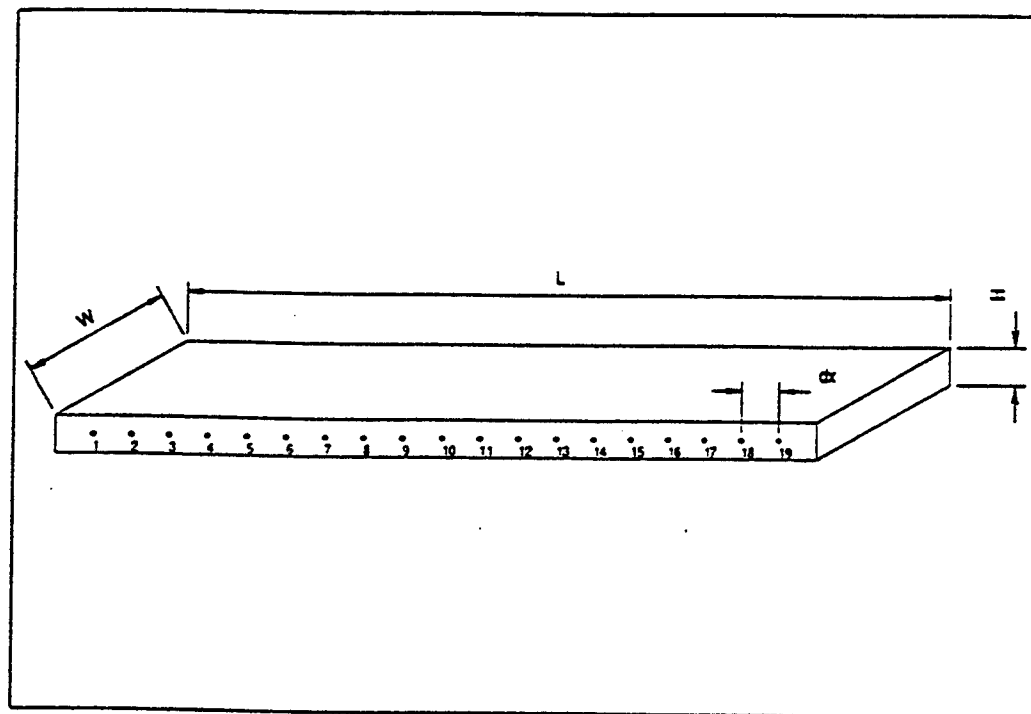


Molecular arrangements of liquid crystals: (a) Smectic; (b) nematic; (c) cholesteric

Figure 5 (from Kasagi et al., 1988)

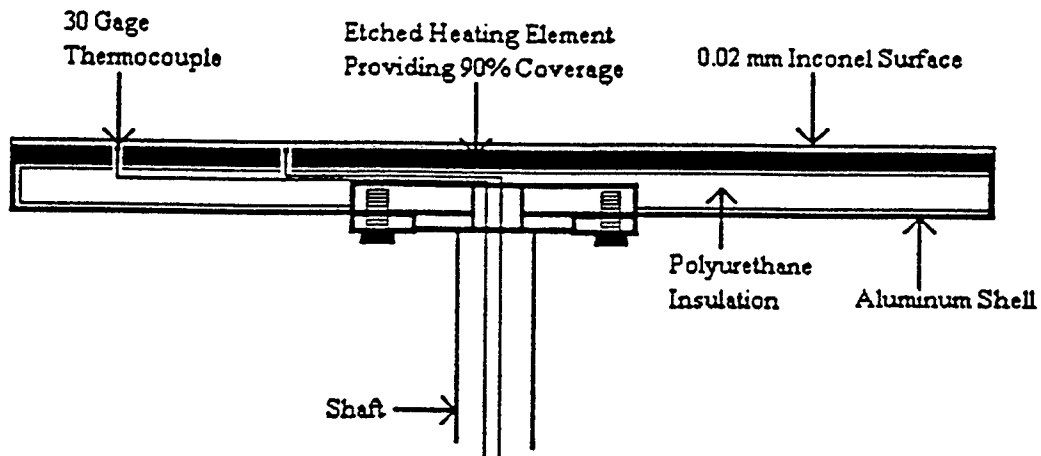


Exploded view of TLC calibration test rig.



Calibration bar.

Figure 6 (from Farina et al., 1994)



Sectional View of Disk For Uniform Heating

Figure 7 (from Ervin, 1992)

THERMOCOUPLE LOCATIONS

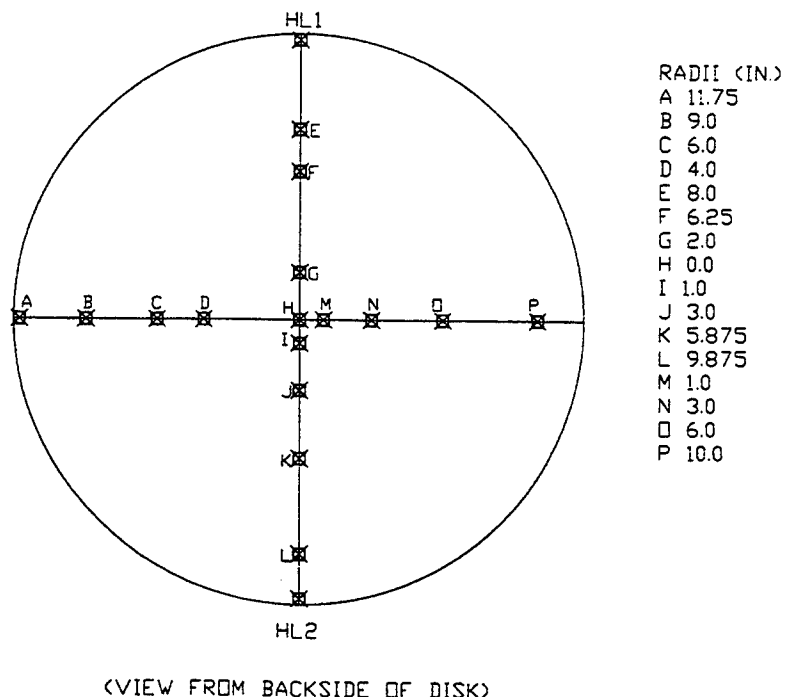


Figure 9

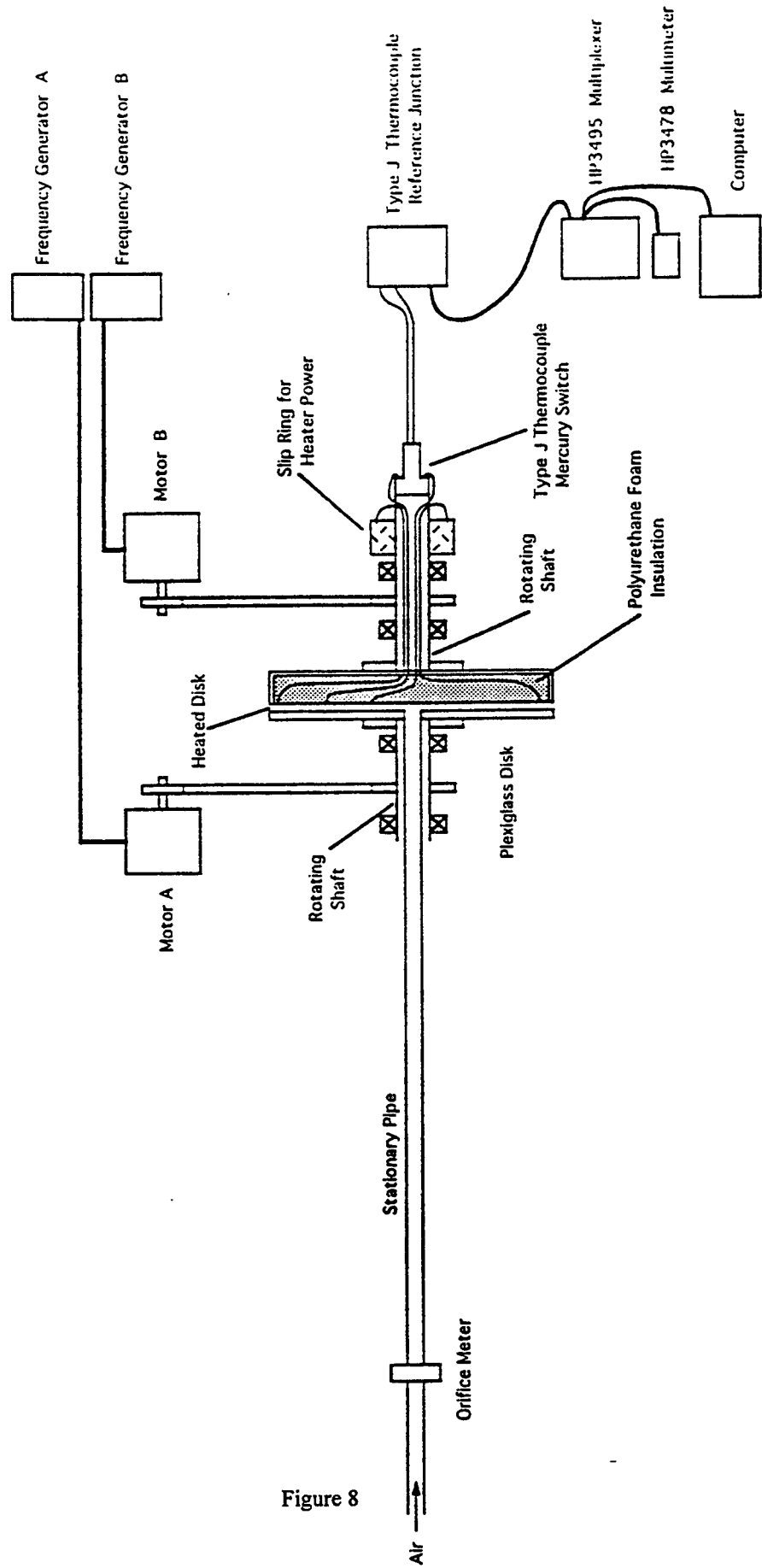


Figure 8

NO REPORT

B. Randolph

**DETERMINATION OF PLUGGING VELOCITY
OF 1018 STEEL, 6061-T6 ALUMINUM, AND TITANIUM 6% Al-4% V**

Keith M. Roessig
Graduate Student
Department of Aerospace & Mechanical Engineering

University Of Notre Dame
365 Fitzpatrick Hall
Notre Dame, IN 46556

Final Report for:
Graduate Student Research Program
Wright Laboratory

Sponsored by:
Air Force Office of Scientific Research
Eglin Air Force Base, Florida
and
Wright Laboratory / Armament Directorate

August 1995

DETERMINATION OF PLUGGING VELOCITY
OF 1018 STEEL, 6061-T6 ALUMINUM, AND TITANIUM 6% Al-4% V

Keith M. Roessig
Graduate Student
Department of Aerospace & Mechanical Engineering
University of Notre Dame

Abstract

Plugging velocity of 1018 steel, 6061-T6 aluminum, and titanium 6% Al-4% V were determined for perpendicular impact of plate specimens by a cylindrical projectile. Careful consideration was given to the geometry of the projectile and specimen while the effect of the clearance between the die and projectile upon the plugging velocity was investigated. A 30 mm powder gun was used at Eglin AFB, Florida at the Advanced Warhead Experimentation Facility (AWEF) under the Armament Directorate to conduct the high velocity, above 100m/s, punch tests of this experiment. Test shots were fired at 6061-T6 aluminum and 1018 steel specimens with varying clearances. The shots for the titanium will be conducted at the University of Notre Dame. For the largest clearance of about 2 inches, the aluminum samples were found to fail completely in shear above 150 m/s, while the 1018 specimens failed by shear down to 110 m/s with this same clearance. At smaller clearances, both metals failed completely in shear down to 85 m/s. So far, the higher strength metals have lower plugging velocities, and the smaller clearances also give lower plugging velocities. These findings are in good agreement with current understanding of shear localization, but more tests must be performed before any details of failure modes can be discussed.

DETERMINATION OF PLUGGING VELOCITY OF 1018 STEEL, 6061-T6 ALUMINUM, AND TITANIUM 6% Al-4% V

Keith M. Roessig

1 Introduction

Adiabatic shear banding has become a well known, if not always well understood, phenomenon in materials. First observations of shear localization date back to 1878 (Johnson, 1987), and since then many investigations have been reported (Massey, 1921, Zener et al, 1944, Rodgers, 1979). Generally, formation of adiabatic shear bands has been attributed to thermal softening of the material at high strain rates. As the material deforms, plastic work is converted to heat, and the material softens due to this heating. If thermal softening is greater than strain hardening or strain rate hardening, localization occurs. Usually the time scale is small so that heat conduction is not a factor during the deformation. Because there is negligible conductive cooling, temperatures can become very high indeed.

Shear banding depends upon many different parameters including material properties and loading geometry. A low heat conduction coefficient aids in the formation of shear bands, as do low strain and strain rate hardening and high thermal softening. Another major factor is the strength of the material. Higher strength materials will require greater work to be done to reach a given amount of plastic strain. This work is converted to heat, so the high strength material will absorb more heat. Assuming no difference in heat capacity, this excess heat causes the material to reach higher temperatures, thus allowing thermal softening to occur more readily.

Some work has been done on the microstructure of metals within adiabatic shear localizations. The evolution of the microstructure is not always clearly understood, but the structure of the band itself yields some clues to the formation of the band. It is clear that evidence of phase transformation in adiabatic shear banding exists (Wingrove, 1971), however, few conclusions about the role of microstructure in shear initiation can be found. Further work may be required.

Plugging is the process in terminal ballistics in which failure occurs in a shear dominated mode. The clearance between the projectile and any support is very large, so in effect it is an infinite plate. Usually plugging occurs at large impact velocity, depending upon the material. Punching, on the other hand, requires a very small clearance, and usually occurs in manufacturing. Punching velocities are small and the failure is again largely dominated by shear since the die prevents any bending deformation. Figure 1 shows the difference between the punching and plugging. The punching incorporates the die and small clearances while plugging happens with a very large clearance.

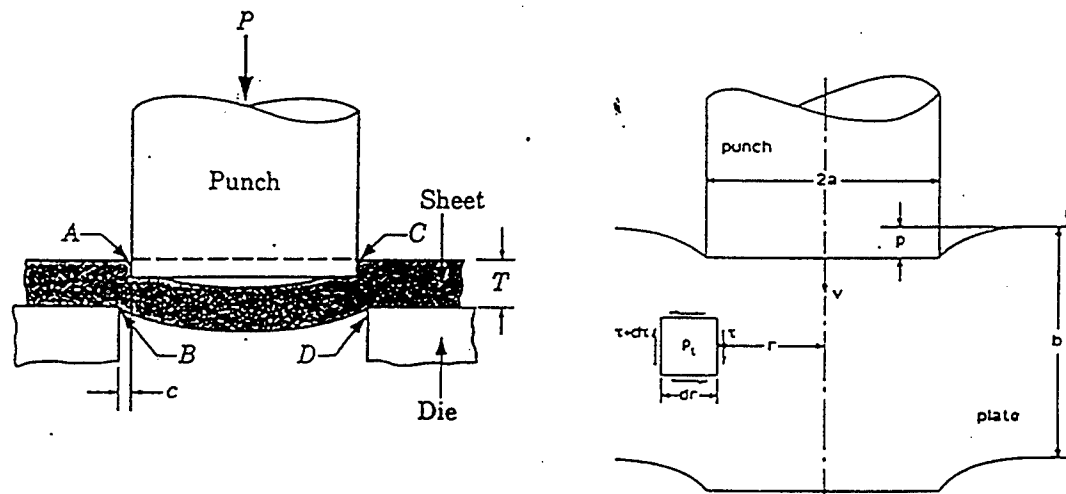


Figure 1: Geometries of punching and plugging operations

The transition between punching and plugging is of interest (Lindholm, 1971). At intermediate clearances, the velocities required to produce a shear dominated failure should be below plugging velocities. Figure 2 shows the ideal plugging velocity curves for two metals. At zero clearance, the velocity should be close to zero, and the velocities should increase with clearance until the plugging velocity is reached. As stated above, higher strength materials should shear localize more readily, giving them a lower plugging velocity. For the same reason, lower strength materials should have a higher plugging velocity.

Of course, there is not a distinct velocity where the failure mode changes from bending to shear. There is

a transition period where both modes are prominent. Figure 3 is a more realistic view of what the plugging velocity curve is expected to be. Below a certain velocity, the failure will be dominated by the bending mode. Above a higher velocity, the failure mode is mainly shear, but in between is the transition area.

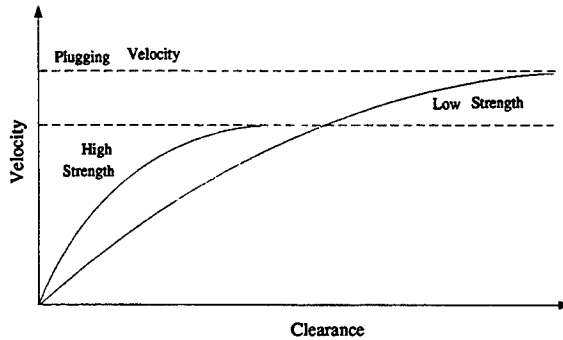


Figure 2: Ideal plugging velocity curve for two different metals

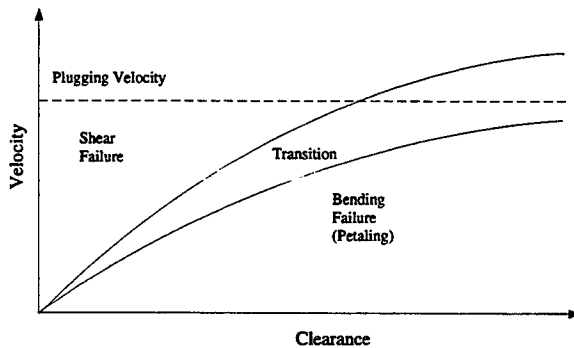


Figure 3: Real plugging velocity curve

In this paper the effect of the clearance between the punching element and the die on the plugging velocity of the specimen is examined with the intention of finding curves such as those shown in Figure 3 for each material. Three materials are examined: 1018 steel, 6061-T6 aluminum, and Titanium 6% Al - 4% V (Ti 6-4). During the summer at Eglin AFB, only the higher velocity tests, above 100 m/s, will be completed

because of the velocity limits imposed by the powder gun. The low velocity shots will be completed at the University of Notre Dame with an air gun. The air gun allows a greater precision and repeatability with the lower velocities, below 100 m/s.

2 Internal Ballistics

One very important part of this experiment is the use of the 30-mm gun used to launch the projectiles. Much of the design of the experiment is based upon the geometry of the gun. The advantages and limitations of the gun also become the advantages and limitations of the experiment. The maximum or minimum velocities attainable by the gun and projectile combination define the ranges in which the plugging velocities can be determined. Safety is always an issue with any experiment, but more so when the transport and use of gunpowder is required. For these reasons, the subject of internal ballistics becomes an important topic and must be understood so that the experiment can be performed.

The most essential part of this topic is obtaining a velocity-powder curve for the projectile. This will also help in deciding which is the best powder to use for the specific application. Many factors influence the velocity curve, including the chemical properties of the powder, the projectile weight, and the packaging of the powder in the gun.

This last factor includes the amount of powder used as well as the capacity of the canister in which the powder is placed. Using a large casing and little powder will result in a poor burn for two reasons. First, as the powder burns, the gases must expand to fill the canister, leading to a decrease in pressure before the gases can do work on the projectile. A lower pressure also leads to a less efficient or even incomplete burn. The second reason is that the spit tube, where the primer is contained, is about one inch long in the 30mm casing, and the powder must extend beyond the spit tube or it may not ignite at all. This problem can be solved by packing cotton behind the powder to bring it close to the primer, but this also may lead to a poor burning performance. The powder must be packed tightly around the spit tube for peak efficiency, and using a cotton filler may prevent a proper ignition and burn.

The chemical properties of the powder and the weight of the projectile are also of concern. With a heavier

projectile, a slower burning powder must be used. This is to prevent the pressure behind the projectile from reaching the critical pressure of the breech itself. A heavier projectile takes longer to accelerate, so a fast burning powder will build a very large pressure behind the projectile. This pressure may be high enough to blow the breech from the barrel, possibly causing fragmentation of the breech. A slower burning powder allows the projectile to start moving before burning is complete, so the gases can expand and the pressure remains below a critical value. This is not to say that the slower burning powder is less energetic, the same velocities can be reached with either powder, but the peak pressures will be different. A diagram illustrating this point can be seen in Figure 4 below. Curve 1 shows the pressures for a fast burn powder. The gases are generated very quickly, and so the pressure builds before the projectile has time to accelerate. Once the projectile does move, the powder has completed its combustion, so the pressure drops rapidly since no new gases are being generated. The second curve is the preferred burn. The powder initiates, but the projectile has time to accelerate before the powder completes its burn. The powder continues to burn as the projectile moves, so the pressure remains high. The preferred burn also completely burns the powder before the projectile leaves the barrel. If the powder burns too slowly, the projectile will leave the barrel before the powder completes its burn. In this situation, curve 3, the pressure will be too low to allow a complete burn, and only a fraction of the chemical energy is used to accelerate the projectile. Once the projectile leaves the barrel, the unburnt powder will have no effect on the velocity of the projectile. This is due to the fact that the gasses being produced can now expand outward around the projectile into the atmosphere, which will not produce enough pressure to further propel the projectile. This type of burn is very unpredictable. For all the reasons above, the correct powder is crucial to the predictability and repeatability of the velocities from a powder gun.

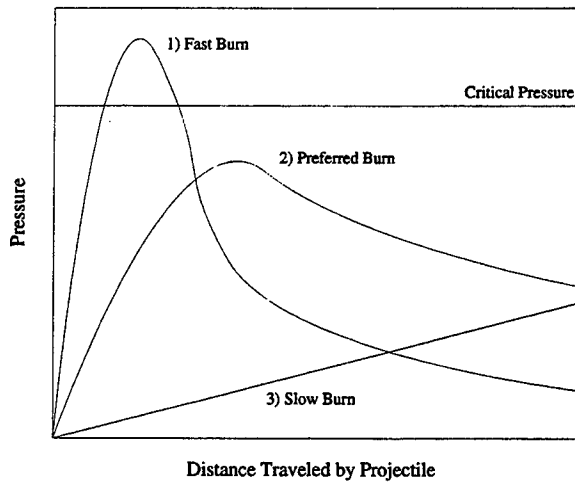


Figure 4: Pressure vs. distance during projectile acceleration

In this experiment, various powders were used, including M1, Red Dot, 30mm Propellant, and Hodgdon 870. Shown below in Figure 5 is the velocity vs. powder mass curve for all different powders used during the experiments. The M1 powder was tried alone as well as mixed with the Red Dot powder to improve its slow burn characteristics. Alone, the M1 burned too slow, as in curve 3 of Fig. 4, and was very inconsistent when charges below 40g were used. 30mm Propellant was then used. It burned much more cleanly, but the supply of this powder was deemed unstable due to its age and was made no longer available. A mixture of small amounts of Red Dot, a much faster burning powder, and M1 was used to improve the burning characteristics, and this combination proved to be more reliable but unsatisfactory. Problems associated with mixing and loading the powder prevented its continued use. Finally, Hodgdon 870, or H870, was chosen for the remainder of the tests. This powder is generally used for large caliber rifles; it has a much faster burn rate than for large bore military guns, but slower than for a hand gun. Powder masses of 8 to 10 g were used, and fairly consistent velocities resulted from similar powder loads. These loads were used to perform the punch test described in the next section.

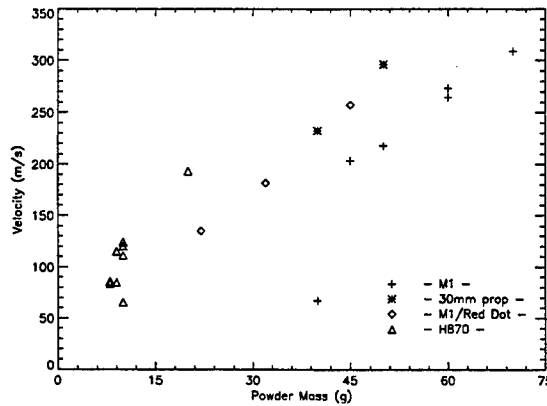


Figure 5: Powder-velocity curve for various gun powders

3 Experimental Procedures

Plugging/punching of the specimen was produced by the impact of a projectile launched from a 30-mm powder gun. The specimens were bolted onto a die and support setup that allowed the clearance to be varied. A soft-catch box made of wood was filled with celotex and sand bags and placed behind the die assembly so that the projectile and plug could be recovered and examined. An overview of the placement of the components can be seen below in Figure 6.

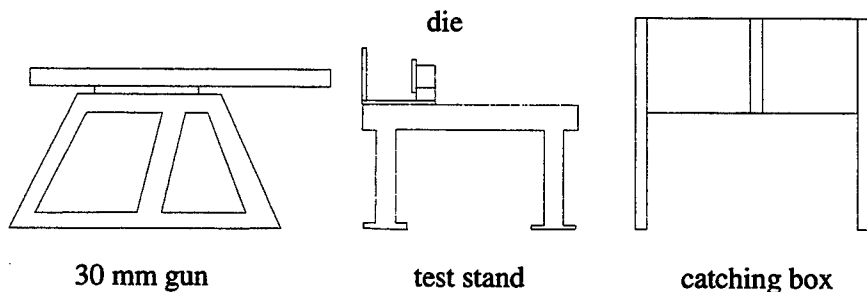


Figure 6: Experimental setup

The die was constructed with an inner diameter of 5.25 inches, so that the maximum clearance could be just over 2 inches with a 30mm diameter projectile. Within this 5.25 inch hole, inserts could be placed that would decrease the effective clearance between the die and the projectile. A protective steel plate was put between the specimen and the 30-mm gun to prevent any adverse effects from the air blast of the barrel. This air is traveling at high velocities along with the projectile, and must not be allowed to interact with the specimen, which needs to be isolated from all outside interactions other than the impact. The inserts were made of a hardened 4340 steel, the die was constructed of armor plate. The rest of the assembly was made of 1018 steel. A diagram of the die is given in Figure 7. The inserts can be placed inside the die to reduce the clearance. These inserts just slide in, but the specimens are then bolted onto the die to keep the parts in place. This assembly is then bolted onto a test stand, shown in Figure 6.

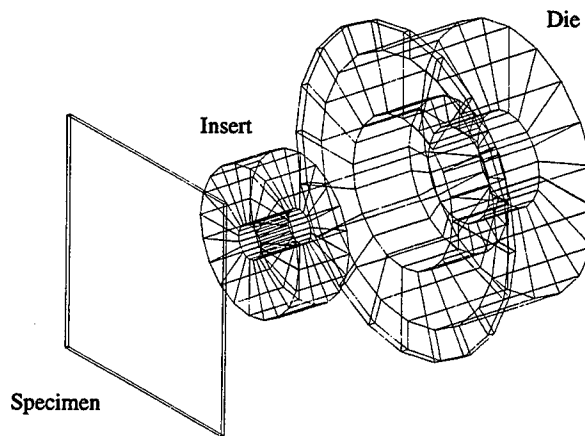


Figure 7: Exploded view of the specimen, insert, and die

The projectile itself was a 6.25 inch long cylinder given a diameter equal to the diameter of the barrel for two reasons. First, the diameter should be large compared to the thickness of the plate to minimize any complex wave interaction between events on diametrically opposed sides of the projectile. Second, the shots were easier to perform because no sabots would have to be designed to keep the projectile aligned while still inside the barrel. These sabots would then only have to be removed during the flight of the projectile,

which would again complicate the experiment. The projectile was constructed of a hardened 4340 steel. The corners of the cylinder were given a radius of curvature of 0.01 inches. This was specified since this could be another factor which may influence the localization process, and it was designed to be kept constant.

The muzzle velocities of the projectile were measured with pressure transducers placed in two holes tapped into the barrel of the gun. These holes were in place before the experiment was designed, and exist for exactly this purpose. The specimen was placed approximately 18 inches in front of the barrel so that the velocity drop due to drag would be negligible.

The tests were started with the 6061-T6 aluminum specimens without any inserts in the die. The plugging velocity with the largest clearance was assumed to be the greatest, so once the plugging velocity was determined at this clearance, the velocities at lower clearances would be easier to find, since an upper bound was given from the previous clearance. The first shot was at 200 m/s, and a binary testing method was to be used. If 200 m/s was too small, then the velocity would be doubled to 400 m/s and so on. Once shear localization occurred, two limit velocities were known, and this range could be halved with each successive shot. This procedure was followed until this range was within tolerance desired for the plugging velocity.

The same procedure was to be used for the 1018 steel and the Ti 6-4. The smaller inserts and the Ti 6-4 were not used in the experiments at Eglin AFB for two reasons. First, the lower velocities required by the smaller inserts and the titanium specimens are harder to achieve on the powder gun, but these tests will be concluded with an air gun back at the University of Notre Dame. Second, time constraints allowed only a given amount of test shots, so the high velocities were used exclusively at Eglin AFB.

All material properties were obtained from the Aerospace Metals Handbook and the ASM Handbook and are given in Table 3.

Table 1: Material Properties

Property	6061-T6 Al	1018 Steel	Ti 6-4
S_{yld} (ksi)	40	60	120
S_{ult} (ksi)	45	70	130
E ($\times 10^6$ psi)	10	29	16
ρ (lbf/in ³)	0.098	0.283	0.160
c_p (Btu/lb-ft)	0.23	0.107	0.125

4 Results & Discussion

For the punch tests performed at AWEF, as stated above, only the high velocities were used. Most of these velocities were on the order of 100 m/s and above. The highest velocities tested on the aluminum specimen were on the order of 300 m/s. The clearance used at these velocities was the largest one, about 2 inches, and the failure mode of the specimen was completely shear. There was almost no bending deformation, and the plug sides show the shear failure clearly. With lower velocities, approximately 125 m/s, the aluminum specimen shows a transition to a bending failure mode. Radial cracks formed in the plate around the impact region. Large out of plane deformation is also seen at these velocities.

The steel specimens with the same clearance showed shear failure at much lower velocities than the aluminum. At about 110 m/s, the failure mode is still completely shear. Out of plane deformation is very prominent, but no radial cracks began to form.

A smaller clearance of 3/8 inches was also tested with velocities between 85 and 100 m/s. Both materials failed in shear in these conditions, and out of plane deformation was much smaller due to the decreased clearance. Graphs showing the velocities used and type of failures seen at the different clearances can be seen below in Figures 8 and 9.

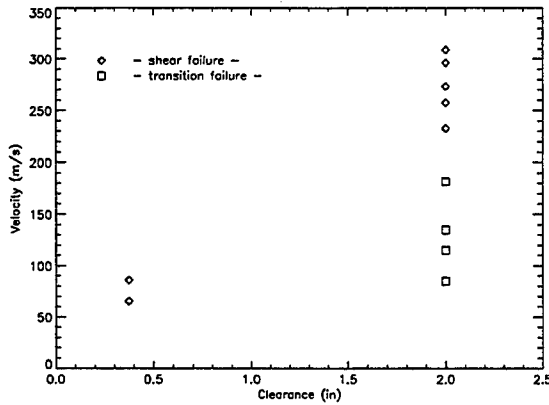


Figure 8: Failure modes at different velocities for 6061-T6 Al

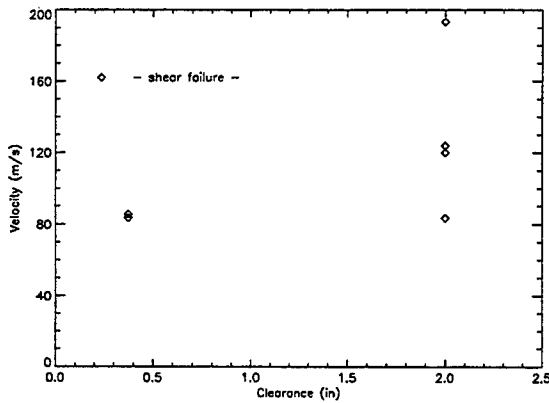


Figure 9: Failure modes at different velocities for 1018 Steel

The graphs in Figure 8 and 9 are definitely not complete, but they do confirm some of the assumptions made before the experiment began. First, the plugging velocity for the higher strength steel is lower than that for the low strength aluminum. Larger deformations occur for the aluminum, and radial cracks appear for much higher velocities, about 150 m/s. The 1018 steel, on the other hand, shows no cracks down to 110 m/s range of velocities. For the Ti 6-4, it is expected that the plugging velocity be even lower than that for the 1018 steel since the Ti 6-4 has a much higher yield and ultimate tensile strength. Recall from the introduction that higher strength often leads to greater heat generation and higher temperatures resulting

in easier localization (All things being equal). Second, both the materials tested showed a shear dominated failure when the clearance was decreased to 3/8 inches, while at similar velocities, a transition failure for aluminum was observed with the 2 inch clearance. For the 1018 steel at velocities between 85-100 m/s and a 2 inch clearance, a much larger out of plane deformation was observed, but the failure was still shear dominated. This supports the assumption that the plugging velocity will decrease with decreasing clearances between the die and projectile.

From the graph, the assumed trends in the plugging velocities do look like they are valid. Of course, there are many tests yet to be completed. The remaining inserts as well as all the tests for the Ti 6-4 must still be completed. For this reason, further conclusions cannot be made at this time about the dependence of the plugging velocity on clearance. One thing is for certain, this clearance plays a major role in the shear band formation in metal specimens.

5 Finite Element Analysis

The finite element program ABAQUS was used to do some simple modeling of this test. The purpose behind a finite element analysis is to understand the role of the clearance in the initiation of localization within the specimen. In the experiment described above, there was no possibility of high speed photography of the localization due to the axisymmetry of the deformation. There is no good view of the mechanical processes involved. With ABAQUS, ideally the failure process can be modeled at the initiation point and then understood more clearly. Simulations could then substitute for instrumentation.

An axisymmetric grid was set up, with the beginning of the analysis starting with the impact. For this reason, the initial position of the projectile was in contact with the specimen. A no slip condition was imposed upon the contact surface, and separation was not allowed. Both of these simplifications were made to reduce the computing effort.

Within the analysis, many material parameters were included to model the specimens accurately. Strain hardening, strain rate hardening, and thermal softening data can all be included in the ABAQUS input deck. Strain hardening was included by specifying the yield strength, and then the strength of the material

depending upon the plastic strain. These are given as data points, and ABAQUS interpolates linearly for conditions between the given values. Thermal softening is specified in the same way. The yield strength and strain hardening data are input for specific temperatures, and again ABAQUS interpolates between the given temperatures. Strain rate hardening uses a power law in which the exponent and a constant are provided by the user. These parameters can also vary with temperature. For these materials, the Johnson/Cook constitutive law was tabulated using values measured at Eglin AFB.

By giving the projectile nodes an initial velocity, the impact can be simulated. Due to time constraints and computing facilities, only a fairly coarse grid was used. Also, the time step required during large plastic deformations can be very small, so an adaptive time increment was used. This leads to large numbers of time increments for the analysis, using large amounts of computer resources. Since the initiation of shear localization is of interest, the analysis was not designed to allow full penetration of the specimen.

The many attempts to use ABAQUS did not result in shear localization. This was determined to be caused by the poor modeling of the constitutive law for the metals. The strain rate hardening data used prevented the non-linear solver for plastic deformation from converging. For this reason, no results from ABAQUS are included here. This work will also be continued at the University of Notre Dame. Shear localization can be modeled using ABAQUS as has been demonstrated recently at the University of Notre Dame (Spicciati, 1995). The constitutive laws must be carefully chosen before this work will be completed successfully. Approximate values for the material properties will be used.

6 Conclusions

This project examines the effect of the clearance between the die and projectile upon the shear localization of the specimen.

A 30 mm powder gun was used at Eglin AFB, Florida to conduct high velocity tests of this experiment. These velocities are above 100 m/s. Test shots were fired at 6061-T6 aluminum and 1018 steel specimens with varying clearances. A soft-catch box was used to capture the projectile and plug for examination. The lower velocities, below 100 m/s, will be completed with an air gun at the University of Notre Dame. The air

gun allows more predictable and repeatable velocities.

The aluminum samples were found to fail completely in shear above about 150 m/s. Below this velocity to about 100 m/s, it is in a transition between shear and bending failure at a clearance of about 2 in. The 1018 specimens failed in a shear dominated mode even down to 110 m/s with this same clearance. At smaller clearances, both metals failed in a shear mode down to 85 m/s.

These findings are in good agreement with expected results, but the tests must be concluded before any general statements can be made. So far, the higher strength metals have lower plugging velocities, and the smaller clearances also give lower plugging velocities.

References

1. *Aerospace Structural Metals Handbook* (1989), Metals & Ceramics Information Center, Batelle Columbus Laboratories, Columbus, OH
2. *ASM Metals Handbook* (1990), 10th edition, Materials Park, OH
3. M.E. Backman (1976), *Terminal Ballistics*, Naval Weapons Center, China Lake, CA, NWC-TP-5780.
4. D.R. Curran, L.B. Greszczuk, T. Nicholas, H.F. Swift, J.A. Zukas (1992), *Impact Dynamics*, Krieger Publishing Company, Malabar, FL.
5. W. Johnson (1987), Henri Tresca as the originator of adiabatic heat lines. *Int. J. Mech. Sci.*, **29**(5), pg. 301
6. U.S. Lindholm on discussion of G.H. Daneshi and J. Harding, The high speed punching of a quenched and tempered $1\frac{1}{2}\%$ CrMo steel. *Institute of Physics Conference*, ser. no. 21, pp 404-416
7. H.F. Massey (1921), The flow of metal during forging. *Proc. Manchester Assoc. Engineers*, pp. 21-26
8. H.C. Rodgers (1979), Adiabatic plastic deformation. *Ann. Rev. Mater. Sci.*, **9**, pp. 283-311
9. L. Spicciati (1995), Masters Thesis, University of Notre Dame
10. A.L. Wingrove (1971), *J. Aust. Inst. Met.*, **16**, pp 67-70.
11. C. Zener and J.H. Holloman (1944), *J. Appl. Phys.*, **15**, pp. 22-32
12. A.K. Zurek (1994), The study of adiabatic shear band instability in a pearlitic 4340 steel using a dynamic punch test. *Metallurgical and Material Transactions A*, vol. 25A, pp 2483-2489.

AN INTER-FRAME CONSISTENCY MEASURE
FOR THE EVALUATION OF
MOTION ESTIMATION ALGORITHMS

Sharla Lynne Rohrbacher

Graduate Student

Wright State University

Dayton, OH 45435

Final Report for
Graduate Student Research Program
Wright Laboratories

Sponsored by
Air Force Office of Scientific Research
Bolling Air Force Base, DC
and
Wright Laboratories

October 1995

AN INTER-FRAME CONSISTENCY MEASURE
FOR THE EVALUATION OF
MOTION ESTIMATION ALGORITHMS

Sharla Lynne Rohrbacher
Graduate Student
Department of Electrical Engineering
Wright State University

Abstract

A great deal of useful information can be extracted from a time-varying sequence of images. Motion estimation is an important research field. Its applications can be found in video image coding and enhancement, 3-D structural analysis, robotics, automatic target recognition, and medical image analysis. While different optical flow techniques continue to appear, there has been a lack of quantitative evaluation of existing methods. The future research in motion estimation is limited due to the lack of a standardized measure for motion estimation algorithms. To evaluate the performance of a motion estimation algorithm, the correct optical flows associated with an image sequence must be known. For a real image sequence, accurate optical flows are difficult to obtain due to such complex factors as measurement error in motion speed and direction, camera calibration error, digitization timing errors and lighting source. Image sequences with known optical flows can be synthetically generated, such as the Yosemite sequence. The synthetic processes are difficult, expensive, and the synthetic gray scale image is much different from the real optical intensity received from a camera. Without the knowledge of correct optical flows, researchers can only observe the estimated optical flows and make some subjective comments and qualitative judgements. To evaluate the performance of motion estimation algorithms, a comprehensive scoring system which can provide objective evaluation of such algorithms for real image sequences should be developed. One such measure in this scoring system is inter-frame consistency.

AN INTER-FRAME CONSISTENCY MEASURE
FOR THE EVALUATION OF
MOTION ESTIMATION ALGORITHMS

Sharla Lynne Rohrbacher

Introduction

Optical flow is the distribution of apparent velocities of movement of brightness patterns in an image. Optical flow can arise from relative motion of objects and the viewer. Therefore, optical flow gives important information about the spatial arrangement of the objects viewed and the rate of change of this arrangement.

The optical flow cannot be computed at a point in the image independently of neighboring points without introducing additional constraints, because the velocity field at each image point has two components while the change in image brightness at a point in the image plane due to motion yields only one constraint. The motion of the brightness patterns in the image is determined directly by the motions of corresponding points on the surface of the object. Computing the velocities of points on the object is a matter of simple geometry once the optical flow is known.

To avoid variations in brightness due to shading effects, assume that the surface being imaged is flat. Also, assume that the incident illumination is uniform across the surface. The brightness, or image irradiance, at a point in the image is then proportional to the reflectance of the surface at the corresponding point on the object. Assume that reflectance varies smoothly and has no spatial discontinuities. This latter condition assures that the image brightness is differentiable. Exclude situations where objects occlude one another, in part, because discontinuities in reflectance are found at object boundaries.

A fundamental problem in the processing of image sequences is the measurement of optical flow, or image velocity. The goal is to compute an approximation to the 2-d motion field, a projection of the 3-d velocities of surface points onto the imaging surface from spatiotemporal patterns of image intensity. These techniques can be viewed conceptually in term of three stages of processing. First, prefilter or smooth with lowpass or bandpass filters in order to extract signal structure of interest and to enhance signal to noise ratio. Second, extract the basic measurements such as spatiotemporal derivatives (to measure normal components of velocities) or local correlation surfaces. Third, integrate these measurements to produce a 2-d flow field which often involves assumptions about the smoothness of the underlying flow field.

First define the motion field, which assigns a velocity vector to each point in the image. Neighboring points on an object have similar velocities. The individual motion field in the image is also continuous in most places.

Optical flow is the apparent motion of the brightness pattern. Ideally the optical flow will correspond to the motion field, but this need not always be so.

Consider first a perfectly uniform sphere rotating in front of an imaging system. There will be spatial variation of brightness, or shading, in the image of the sphere, since the surface is curved. This shading, however, does not move with the surface, and so the image does not change with time. In this case the optical flow is zero everywhere, despite a non-zero motion field. Next, consider a fixed sphere illuminated by a moving light source. The shading in the image will change as the source moves. In this case the optical flow is clearly nonzero while the motion field is zero everywhere.

The optical flow is not uniquely determined by local information in the changing image. Consider a patch of uniform brightness in the image that does not change with time. The most likely optical flow is one that is zero everywhere. But in fact within the uniform patch we can assign any pattern of vector displacements.

Let $E(x, y, t)$ be the irradiance at time t at the image point (x, y) . Then if $u(x, y)$ and $v(x, y)$ are the x and y components of the optical flow velocity vector at that point, we expect that the irradiance will be the same at time $t+\delta t$ at the point $(x+\delta x, y+\delta y)$ where $\delta x=u\delta t$ and $\delta y=v\delta t$. That is,

$$E(x+\delta x, y+\delta y, t+\delta t) = E(x, y, t)$$

for a small time interval δt .

When sensor temporal sampling rate is high enough (no temporal error) compared to object acceleration (speed changes) the real object motion is expected to change smoothly in consecutive image frames. Due to spatial-temporal smoothness of optical-flow fields, a good motion estimation algorithm should present gradual change of optical-flow field in the adjacent frames consistently. With this assumption, an interframe consistency measure can be defined to measure the performance of motion estimation algorithms even when the correct optical flow field of the testing image sequences are unknown. The idea is to look at consecutive frames of estimated optical flow field and see if there is drastic motion change, in magnitude of direction, for each pixel. An inter-frame consistency factor can be defined over a spatial area of interest in an image frame to measure the performance of motion estimation algorithms at different areas of the testing images.

Assume that the optical-flow field is expressed as a velocity vector field (u, v) pixels per frame on the image plane. Its time-space expression can be written as $V = (u, v, 1)$ where the third variable indicates one frame. Given an intensity image sequence $E(x, y, t)$, where x and y are the spatial indices and t is the frame index, the optical-flow constraint equation is

$$\frac{\partial E}{\partial x} u + \frac{\partial E}{\partial y} v + \frac{\partial E}{\partial t} = 0$$

based on the assumption of conservation of image intensity. There are many different approaches to solve this equation. This project looked at two of them, both of which are gradient-based.

Motion Estimation Algorithms

Horn & Schunck Algorithm - Horn and Schunck uses an extra constraint on the smoothness of the motion velocity vector field to solve for u and v . This additional constraint tries to minimize the energy function

$$\iint_D \left[\left(\frac{\partial^2 u}{\partial x^2} + \frac{\partial^2 u}{\partial y^2} \right) + \left(\frac{\partial^2 v}{\partial x^2} + \frac{\partial^2 v}{\partial y^2} \right) \right] dx dy$$

over a defined domain D . Combining the conservation of image intensity, the Horn and Schunck algorithm estimates the optical flow velocity field by minimizing the following energy function.

$$\iint_D \left[\left(\frac{\partial E}{\partial x} u + \frac{\partial E}{\partial y} v + \frac{\partial E}{\partial t} \right)^2 + \lambda^2 \left[\left(\frac{\partial^2 u}{\partial x^2} + \frac{\partial^2 u}{\partial y^2} \right) + \left(\frac{\partial^2 v}{\partial x^2} + \frac{\partial^2 v}{\partial y^2} \right) \right] dx dy \right]$$

where the parameter λ is used to place weight on the errors of the conservation of image intensity and of the motion smoothness. The value of λ is usually small if the image intensity measurements are accurate. Minimizing this equation is a problem in the calculus of variations. An iterative solution to the discretized Euler equations is implemented.

The Standard Horn and Schunck algorithm used first-order differences to estimate intensity derivatives. Since this is a relatively crude form of numerical differentiation and can be the source of considerable error, the Non-standard method was also implemented. This method uses spatio-temporal pre-smoothing and 4-point central differences for differentiation.

Lucas & Kanade Algorithm - Derivatives were computed using 4-point central differences. Spatial neighborhoods Ω were 5x5 pixels and the window function $W^2(x)$ was separable and isotropic. The Lucas and Kanade algorithm applies a weighted least-squares fit of the optical flow constraint to a constant model for (u, v) in each small spatial neighborhood Ω by minimizing

$$\sum_{(x,y) \in \Omega} W^2(x, y) \left(\frac{\partial E}{\partial x} u + \frac{\partial E}{\partial y} v + \frac{\partial E}{\partial t} \right)^2$$

where $W^2(x, y)$ is a window function that weights the center of the neighborhood stronger than the periphery.

Image Sequences

Yosemite Sequence - The Yosemite sequence is the most complex test case. The motion in the upper right hand corner is mainly divergent, the clouds are moving to the right with a velocity of 1 pixel/frame while velocities in the lower left hand corner are about 4 pixels/frame. The difficulty of this sequence is due to the range of velocities and the occluding edges between the mountains and at the horizon. There is severe aliasing in the lower portion of the images which, in most methods of motion estimation, produces poor velocity measurements.

Yosemite is a synthetically produced image.

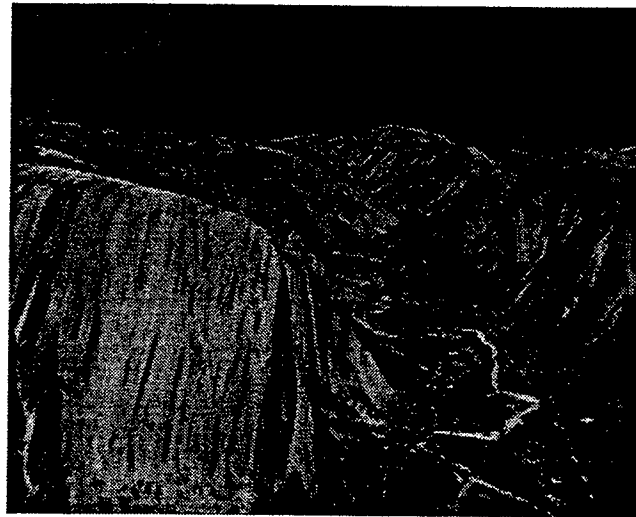


Figure 1. A Frame of the Yosemite Sequence.

Rotating Rubic Sequence - The Rotating Rubic sequence consists of a rubic's cube on a turntable rotating counter-clockwise. The motion field induced by the rotation are velocities less than 2 pixels/frame. Typically, 1.2-1.4 pixels/frame on the turntable and .2-.5 pixels/frame on the rubic's cube.

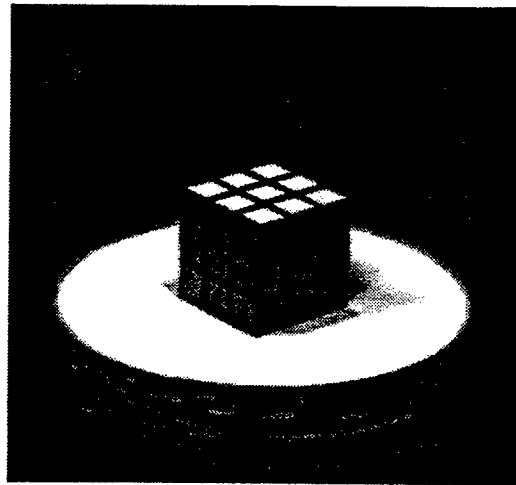


Figure 2. A Frame of the Rotating Rubic Sequence.

Hamburg Taxi Sequence - The Hamburg Taxi sequence is a street scene with four moving objects. The taxi turning the corner at 1 pixel/frame, the car in the lower left driving to the right at 3 pixels/frame, the car in the lower right moving to the left at 3 pixels/frame and the pedestrian in the upper left walking at .3 pixels/frame.



Figure 3. A Frame of the Hamburg Taxi Sequence.

Discussion of problem

Two consecutive frames of optical flow fields are used to calculate the inter-frame consistency factor. Assume that the unit used for $u(x,y,t)$ and $v(x,y,t)$ is pixel/frame. If an adequate temporal sampling rate is used, then $u(x,y,t)$ and $v(x,y,t)$ are constant between the t -th and the $(t+1)$ -th frames. Then the pixel at (x,y) in the t -th frame should have moved to the location $(x+u, y+v)$ at the $(t+1)$ -th frame. The acceleration vector of this pixel is proportional to the vector difference

$$\vec{V}_d(x, y, t) = \vec{V}(x+u, y+v, t+1) - \vec{V}(x, y, t),$$

where the value of $\vec{V}(x+u, y+v, t+1)$ can be obtained from the bilinear interpolation of optical flow field of $\vec{V}(x, y, t+1)$. $\vec{V}_d(x, y, t)$ measures both directional and magnitude inconsistency between estimated optical flow fields $\vec{V}(x, y, t)$ and $\vec{V}(x, y, t+1)$.

An inter-frame consistency factor, $C_f(t)$, can be defined from the magnitude of the vector field $|\vec{V}_d(x, y, t)|$. For areas of interest in an image frame, usually areas with dense optical flow vectors, the magnitude field can be averaged over the areas of interest to produce a scalar at the image frame t . The inverse of that scalar is defined as the inter-frame consistency factor,

$$C_f(t) = \frac{1}{N_A} \sum_{(x,y) \in A} |\vec{V}_d(x, y, t)|$$

where A is the union of areas of interest and N_A is the number of vectors in A . The inter-frame consistency factor is normalized, therefore the closer the value of $C_f(t)$ is to 1, the smoother the optical flow field $V(x,y,t)$, and consequently the better the motion algorithm is for testing an image sequence.

If only the directional error is desired, the inter-frame consistency measure can be defined by using the angular error. Since the angular error only measures the directional errors between two optical flow vectors, the optical flow vectors $V(x+u, y+v, t+1)$ and $V(x, y, t)$ are normalized. The inner product of the two normalized optical

flow vectors now represents the directional error. It ranges from 1 (no error) to -1 (π radian difference). Therefore, the angular error reading can be calculated by using $\cos^{-1}()$.

$$e_\theta(x, y, t) = \cos^{-1} \left[\frac{1}{\sqrt{u(x+u, y+v, t+1)^2 + v(x+u, y+v, t+1)^2 + 1}} \bar{V}(x+u, y+v, t+1) \right. \\ \left. - \frac{1}{\sqrt{u(x, y, t)^2 + v(x, y, t)^2 + 1}} \bar{V}(x, y, t) \right]$$

Similarly, the average angular error over an area of interest can be used as a scalar indicator. The inverse of this scalar is defined as the angular inter-frame consistency factor.

$$\theta_f(t) = \frac{N_A}{\sum_{(x,y) \in A} e_\theta(x, y, t)}$$

where N_A and A are defined as in $Cf(t)$. The angular inter-frame consistency has been normalized. The standard deviation from interframe consistency factor Cf and the angular inter-frame consistency factor θ_f can be calculated as extra indicators to measure the consistency of estimated optical flow vector fields.

Methodology

A motion estimation test suite has been developed by Dr. Kefu Xue and Dr. Jack Jean in association with Spectra Research Laboratories to implement the motion estimation algorithms and images mentioned in this report. The Integrated Motion Analysis Test Suite (IMATS) is a prototype of a standardized test suite to evaluate motion estimation algorithms. IMATS brings existing motion estimation algorithms, test image sequences, and scoring software to a personal computer environment. The inter-frame consistency measure was implemented in two ways. First, it can be directly calculated between two frames by denoting the proper argument in the input argument file when the program is initiated. Second, a menu item was added to IMATS to calculate the inter-frame consistency between two known estimated velocity files.

The inter-frame consistency process will perform the desired motion estimation algorithm (Horn and Schunck, Lucas and Kanade...) on two consecutive frames of an image sequence. The user can chose a desired area over which to calculate the inter-frame consistency factor, usually the most dense section of the image. The process will look at the two velocity components of each pixel of the first frame. It will determine the 'new location' of this pixel in the second frame. The two velocity vectors for this point are then interpolated from the known estimated velocity calculations for the second frame. The value from the first frame and the interpolated value are then compared to give the vector difference. These vector difference are then added up over the desired area.

The inner product of the normalized optical vectors will represent the directional error, θ_f . N_A is the number of vectors found within the desired area and the density is determined by dividing N_A by the total area.

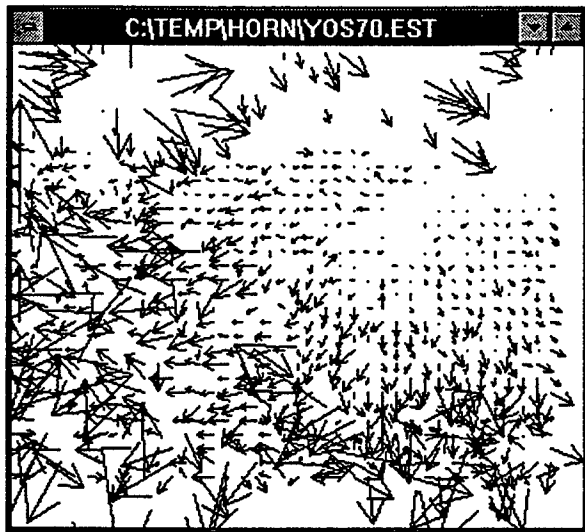
Results

Sequence Used	Standard Horn & Schunck (no threshold)	Standard Horn & Schunck (threshold)	Standard Horn & Schunck (threshold)
Yosemite	$\tau = 0.0$ Area = 63,492 $N_A = 63,492$ Density = 100% $C_f = 0.467$ $\theta_f = 0.548$	$\tau = 3.25$ Area = 63,492 $N_A = 42,958$ Density = 67.6% $C_f = 0.576$ $\theta_f = 0.533$	$\tau = 14.0$ Area = 63,492 $N_A = 19,414$ Density = 30.6% $C_f = 0.695$ $\theta_f = 0.526$
Rubic	$\tau = 0.0$ Area = 51,920 $N_A = 51,290$ Density = 100% $C_f = 0.761$ $\theta_f = 0.488$	$\tau = 0.5$ Area = 51,920 $N_A = 35,464$ Density = 68.3% $C_f = 0.767$ $\theta_f = 0.492$	$\tau = 3.0$ Area = 51,920 $N_A = 16,454$ Density = 31.7% $C_f = 0.916$ $\theta_f = 0.500$
Taxi	$\tau = 0.0$ Area = 40,120 $N_A = 40,120$ Density = 100% $C_f = 0.635$ $\theta_f = 0.479$	$\tau = 2.0$ Area = 40,120 $N_A = 28,368$ Density = 70.7% $C_f = 0.703$ $\theta_f = 0.485$	$\tau = 7.5$ Area = 40,120 $N_A = 12,226$ Density = 30.5% $C_f = 0.795$ $\theta_f = 0.488$

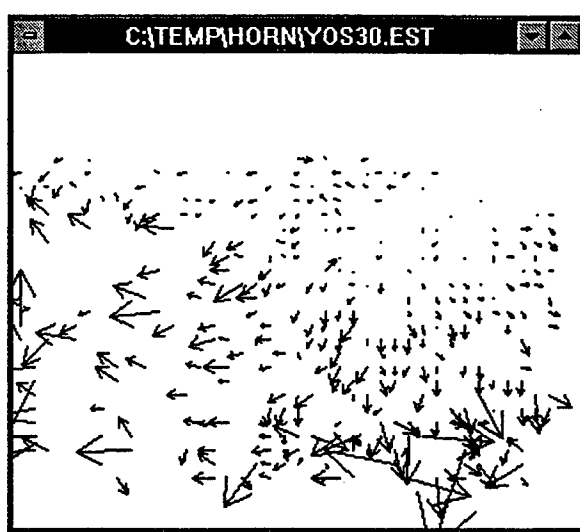
Table 1. Average Inter-frame Consistency Measure for the Horn and Schunck Algorithm.

Sequence Used	Modified Lucas & Kanade (no threshold)	Modified Lucas & Kanade (threshold)	Modified Lucas & Kanade (threshold)
Yosemite	$\tau = 0.0$ Area = 63,492 $N_A = 63,492$ Density = 100% $C_f = 0.570$ $\theta_f = 0.557$	$\tau = 1.0$ Area = 63,492 $N_A = 45,477$ Density = 71.6% $C_f = 0.602$ $\theta_f = 0.532$	$\tau = 2.75$ Area = 63,492 $N_A = 20,918$ Density = 32.9% $C_f = 0.656$ $\theta_f = 0.523$
Rubic	$\tau = 0.0$ Area = 51,920 $N_A = 51,920$ Density = 100% $C_f = 0.880$ $\theta_f = 0.496$	$\tau = 0.58$ Area = 51,920 $N_A = 35,853$ Density = 69.1% $C_f = 0.890$ $\theta_f = 0.498$	$\tau = 0.7$ Area = 51,920 $N_A = 16,421$ Density = 31.6% $C_f = 0.906$ $\theta_f = 0.508$
Taxi	$\tau = 0.0$ Area = 40,120 $N_A = 40,120$ Density = 100% $C_f = 0.800$ $\theta_f = 0.492$	$\tau = 1.4$ Area = 40,120 $N_A = 27,681$ Density = 69% $C_f = 0.816$ $\theta_f = 0.490$	$\tau = 2.0$ Area = 40,120 $N_A = 12,444$ Density = 31% $C_f = 0.823$ $\theta_f = 0.490$

Table 2. Average Inter-frame Consistency Measure for the Lucas and Kanade Algorithm.

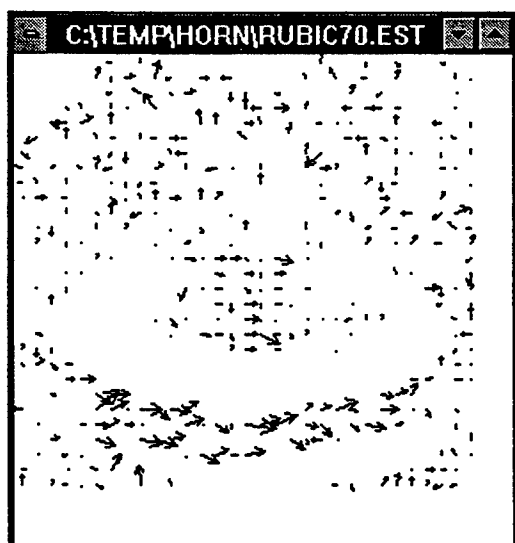


(a)

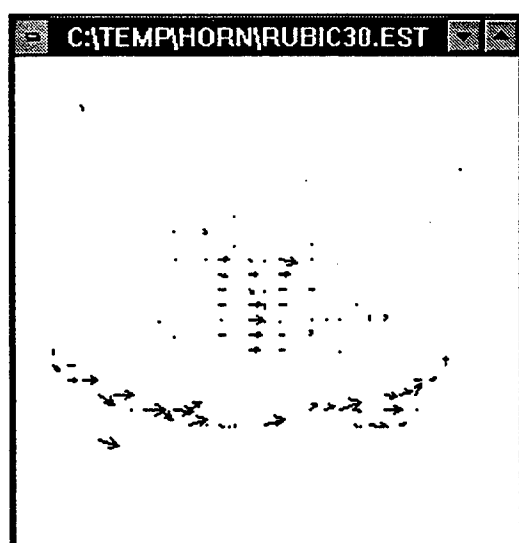


(b)

Figure 4. Needle Plots for the Horn and Schunck algorithm on the Yosemite Sequence with
(a) 70% density and (b) 30% density.

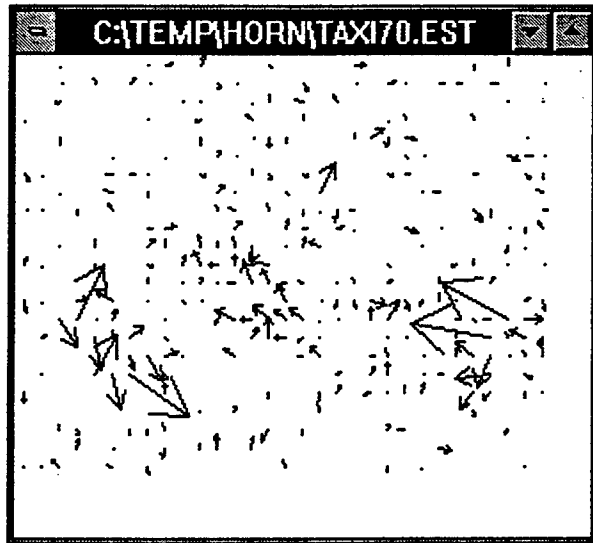


(a)

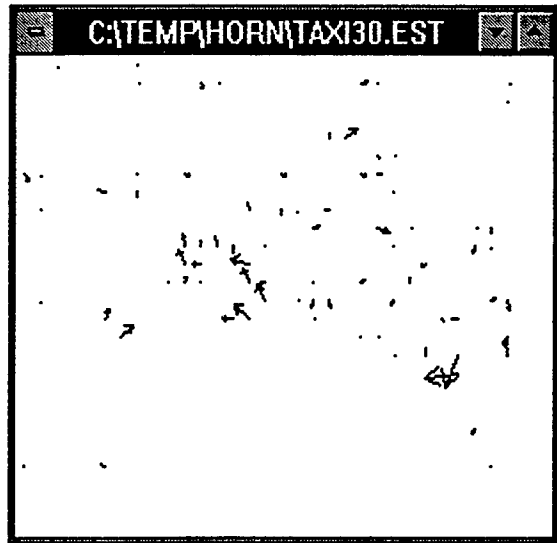


(b)

Figure 5. Needle Plots for the Horn and Schunck algorithm on the Rubic Sequence with
(a) 70% density and (b) 30% density.

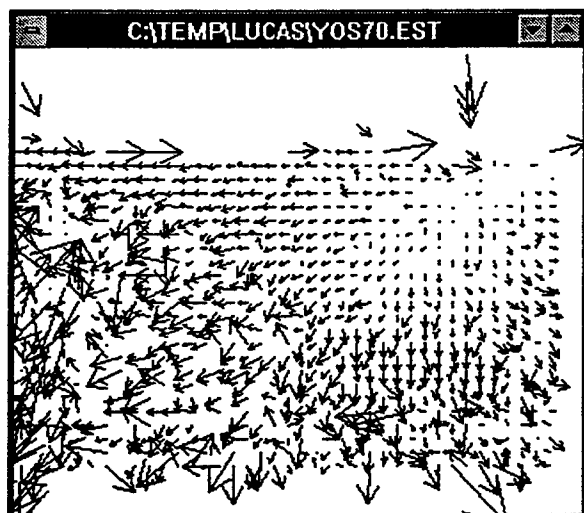


(a)

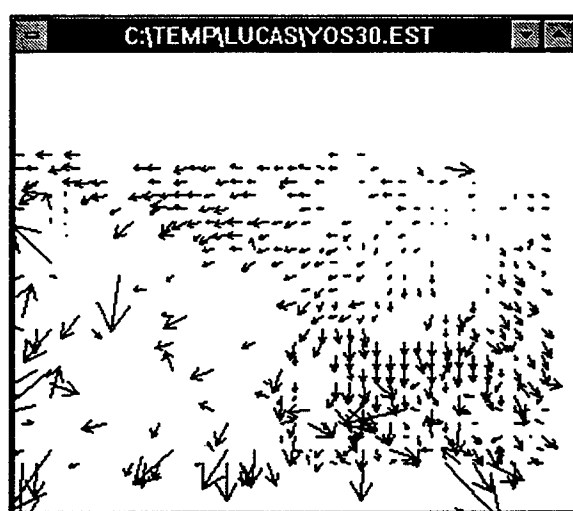


(b)

Figure 6. Needle Plots for the Horn and Schunck algorithm on the Taxi Sequence with
(a) 70% density and (b) 30% density.

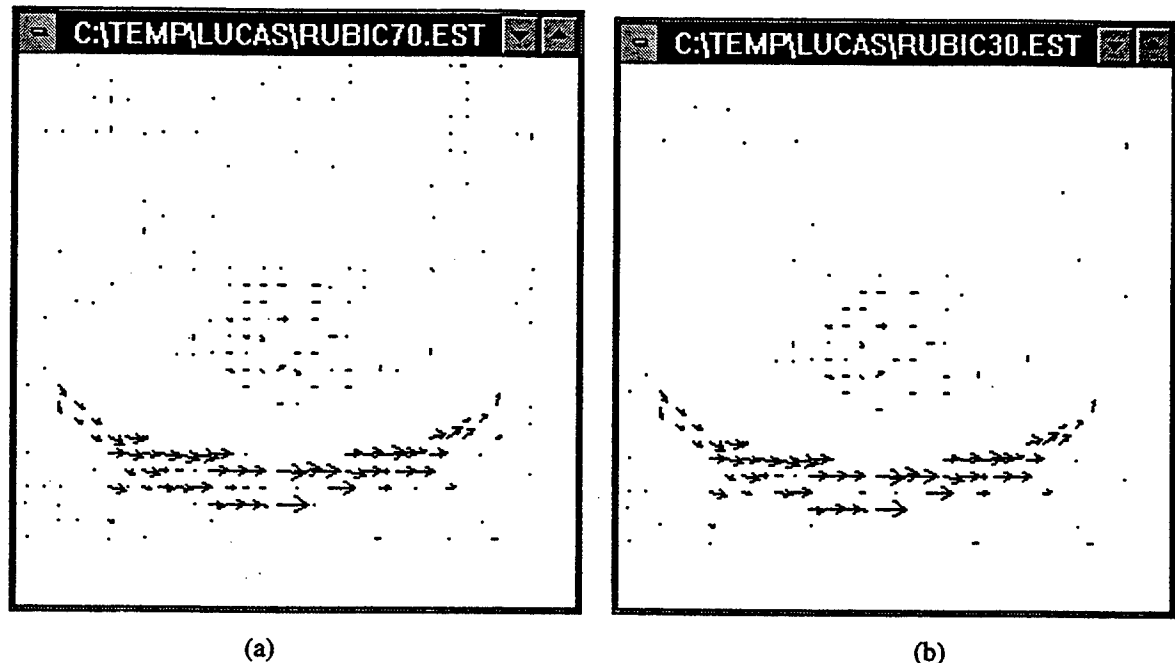


(a)



(b)

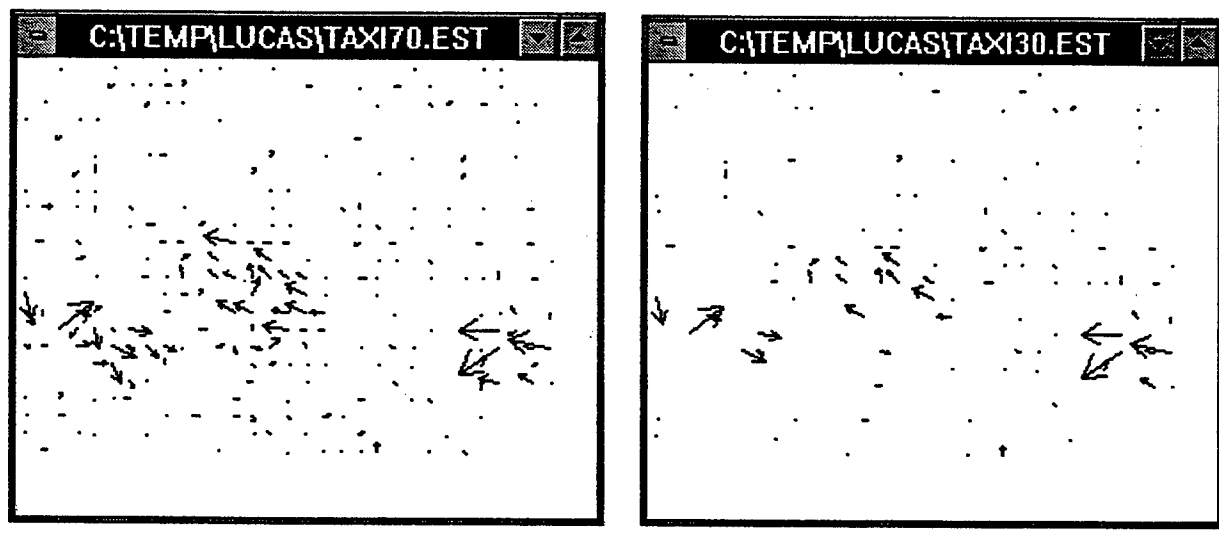
Figure 7. Needle Plots for the Lucas and Kanade algorithm on the Yosemite Sequence with
(a) 70% density and (b) 30% density.



(a)

(b)

Figure 8. Needle Plots for the Lucas and Kanade algorithm on the Rubic Sequence with
(a) 70% density and (b) 30% density.



(a)

(b)

Figure 9. Needle Plots for the Lucas and Kanade algorithm on the Taxi Sequence with
(a) 70% density and (b) 30% density.

Sequence Used	Standard Horn & Schunck (no threshold)	Standard $\ \nabla I\ \geq 5.0$	Modified Lucas & Kanade $\lambda_2 \geq 1.0$	Modified Lucas & Kanade $\lambda_2 \geq 5.0$
Yosemite Area = 63,492	Error = 53.729 St. Dev. = 29.043 Density = 100% ----- $C_f = 0.467$ $\theta_f = 0.548$ $N_A = 63,492$ Density = 100%	Error = 49.710 St. Dev. = 26.658 Density = 57.634% ----- $C_f = 0.602$ $\theta_f = 0.528$ $N_A = 37,454$ Density = 58.99%	Error = 49.732 St. Dev. = 25.956 Density = 61.285 ----- $C_f = 0.603$ $\theta_f = 0.535$ $N_A = 43,950$ Density = 69.22%	Error = St. Dev. = Density = ----- $C_f = 0.587$ $\theta_f = 0.482$ $N_A = 965$ Density = 1.52%

Table 3. Comparing original statistics to the Inter-frame Consistency Measure.

Conclusion

The average inter-frame consistency was determined for the Horn and Schunck and the Lucas and Kanade motion estimation algorithms for three different image sequences. The average inter-frame consistency measure for the Horn and Schunck algorithm can be seen in Table 1. The first column represents the inter-frame consistency measure when the estimated outputs are not thresholded. Tau is the value used to threshold the estimated velocities. Looking down a column, the overall area of the image is smaller. The area used to calculate the inter-frame consistency factor was equal to the total area of the image with a border of approximately ten pixels. The Rubic sequence has the best inter-frame consistency factor mainly due to the simplicity of the motion of the objects in the image. The Yosemite sequence has the worst inter-frame consistency factor, which was expected due to the occluding edges of the mountains and the horizon, and the aliasing that occurs in the image. The major occlusion boundary that introduces error is the horizon. This is evident in the flow fields produced. If the sky is excluded from the analysis, the inter-frame consistency measure would show improved performance. Looking across a row, the inter-frame consistency measure increases as the velocities are thresholded and the number of velocity components found (density) is decreased.

The Lucas and Kanade motion algorithm is more accurate in determining the velocities. The average inter-frame consistency measure for the Lucas and Kanade algorithm can be seen in Table 2. The analysis is similar to the above analysis for the Horn and Schunck algorithm. The Rubic sequence gives the best results, and the Yosemite gives the worst results. Looking across a row, the inter-frame consistency measure increases as the velocities are thresholded and the number of velocity components (density) is decreased.

The needle plots shown in Figures 4-9, show the estimated velocity components of each of the image sequences using both the Horn and Schunck and the Lucas and Kanade algorithms with two different densities. The number of significant velocity vectors decreases as the density decreases and the accuracy of determining these velocity components is increased. Comparing the needle plots from the Horn and Schunck algorithm to the corresponding needle plots from the Lucas and Kanade algorithm demonstrates that the Lucas and Kanade is a more accurate motion estimation algorithm. For example, the Lucas and Kanade needle plots from the Rubic sequence contains a dense number of estimated velocity components located on the turntable and rubic's cube and only a few scattered components from noise in the background of the picture which is stationary. The corresponding Horn and Schunck needle plots show a significant number of estimated velocity vectors in the background which is stationary and should not have any velocity components.

The original program contained a few statistical calculations, such as average error, standard deviation and density. These values for the Yosemite sequence can be found in the first half of Table 3. Comparing them to the corresponding inter-frame consistency measurements, it is determined that in both cases the density is similar and the accuracy increases as the threshold is implemented.

The Inter-frame Consistency Measure is a good standardized measure for the evaluation of motion estimation algorithms. To ensure this theory, other motion algorithms need to be implemented.

References

1. *“Determining the Optical Flow”* Artificial Intelligence 1981 Berthold K.P. Horn and Brian G. Schunck p185-203
2. *“Motion Field and Optical Flow”* Chapter 12 p278-298
3. *“Performance of Optical Flow Techniques”* J.L. Barron, D.J. Fleet, S.S. Beauchemin and T.A. Burkitt July 1992 (Revised July 1993) Department of Computer Science, The University of Western Ontario
4. *“An Inter-frame Consistency Measure for the Evaluation of Motion Estimation Algorithms”* Dr. Kefu Xue Department of Electrical Engineering, Wright State University

SYNTHESIS AND CHARACTERIZATION OF CHAIN EXTENDING MONOMERS FOR
POLYMER DISPERSED LIQUID CRYSTAL SYSTEMS

Michael D. Schulte
Graduate Student
Department of Materials Science and Engineering

University of Cincinnati
Cincinnati, OH 45210-0012

Final Report for:
Graduate Student Research Program
Wright Laboratory

Sponsored by:
Air Force Office of Scientific Research
Bolling Air Force Base, Washington DC

and

Wright Laboratory
Materials Directorate
WPAFB, OH

September 1995

SYNTHESIS AND CHARACTERIZATION OF CHAIN EXTENDING MONOMERS FOR
POLYMER DISPERSED LIQUID CRYSTAL SYSTEMS

Michael D. Schulte

Graduate Student

Department of Materials Science and Engineering
University of Cincinnati

Abstract

The synthesis and characterization of mono and difunctional monomers to be used in a cross-linked matrix for polymer dispersed liquid crystal systems is presented. The focus of this investigation is the synthesis of monomers which will replace the cross-linking *N*-vinylpyrrolidone (NVP) in the polymer dispersed liquid crystal system. Synthesis schemes included cyanobiphenols with dibromoalkanes and DCCI coupling reactions between carboxylic acids and biphenols. The synthesis of four chain extending monomers for polymer dispersed liquid crystal systems are reported, three of which are believed to be novel.

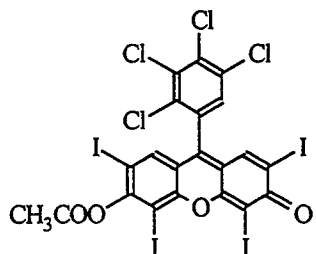
SYNTHESIS AND CHARACTERIZATION OF CHAIN EXTENDING MONOMERS FOR POLYMER DISPERSED LIQUID CRYSTAL SYSTEMS

Michael D. Schulte

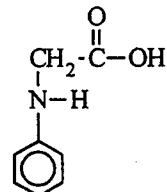
Introduction

Polymer dispersed liquid crystal systems have been the focus of recent investigations to record Bragg reflection gratings by spatially phase separating regions of liquid crystal domains.^{5,9} Gratings are photochemically prepared by exploiting principals of constructive interference in the writing region. Holographic polymer dispersed liquid crystals or PDLC's consist of anisotropic dispersions of microdroplets less than .3 micrometers in a host polymer matrix.^{1,5} Such microdroplets exhibit high anisotropy and birefringence which make them desirable for applications in electrically switchable narrow-notch holographic reflection filters. Thus, liquid crystals offer low switching voltages, high optical densities for protection against visible or near IR laser threats and fast response times.

Acrylate polymers are desirable for PDLC matrix materials since their amorphous structure gives rise to excellent optical properties. PDLC systems considered for this investigation begin with a prepolymer syrup typically composed of the multifunctional monomer dipentaerythrol hydroxy penta acrylate (DPHPA), the chain extender *N*-vinylpyrrolidone (NVP), the photoinitiator dye Rose Bengal (RB), the coinitiator *N*-phenylglycine and E7: a commercially available liquid crystal mixture.⁵ In such systems, the pentacrylate DPHPA is crosslinked using an Ar ion laser. Rose Bengal is attractive for such PDLC applications as it displays a broad absorption spectrum with a peak molar extinction coefficient of $\sim 10^4$, $M^{-1} cm^{-1}$ at about 490 nm. Absorption of radiation by RB results in excited 1s energy state followed by inter-system crossing to the triplet state, resulting in *N*-phenyl glycine producing a radical to initiate polymerization.⁶



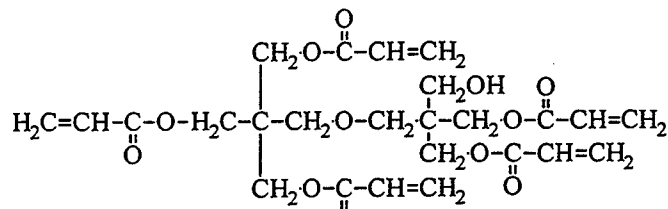
Rose Bengal (RB)



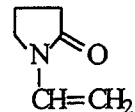
N-phenylglycine (NPG)

The typical PDLC matrix consists primarily of DPHPA in conjunction with NVP to produce a crosslinked matrix with submicron droplets of E7 dispersed throughout.⁵ Due to steric

hindrances associated with DPHPA, NVP is used as a chain extender to promote a highly crosslinked network by scavenging double bonds not yet reacted. Previous work has shown the the concentration of NVP had a drastic effect on the morphology of the phase seperated system.⁹



Dipentae rythrol Hydroxypenta Acrylate (DPHPA)



N-Vinyl Pyrrolidone (NVP)

Thus, the focus of this investigation is the synthesis of monomers which will replace NVP in the PDLC system. A crosslinking monomer which is long about the principal axis and thermodynamically compatible with E7 is desired. The desired length will be achieved by attaching alkane leader groups to thermodynamically favorable elements which posses a high p electron conjugation along the principal molecular axis. Thus, compounds considered for synthesis typically included a biphenyl substituent with variations resulting in fluorinated and difunctional monomers.

Synthesis mechanisms included cyanobiphenols with dibromoalkanes and DCCI coupling reactions between acids and biphenols. 4-Cyanobiphenyl is the most widely used mesogenic core and has been attached to a wide range of backbone types.⁷ The DCCI coupling reaction is a one step esterification method, which allows the conversion of a carboxylic acid at room temperature into an ester. Thus, an alcohol may be reacted with an acid anhydride in the presence of an equivalent amount of dimethylaminopyridine. In the DCCI coupling reaction, the carboxylic acid is converted by DCCI to an acid anhydride, which forms an acylpyridinium species with the catalyst.⁸ This is followed by equilibration of the acylpyridinium species with the alcohol to produce an ion pair. Nucleophilic attack on the acyl group generates the ester and catalyst. The carboxylic acid is recycled by DCCI while the catalyst is reused.⁴ DCCI coupling reactions are attractive due to their one-step scheme, however, removal of the DCU byproduct may be difficult.

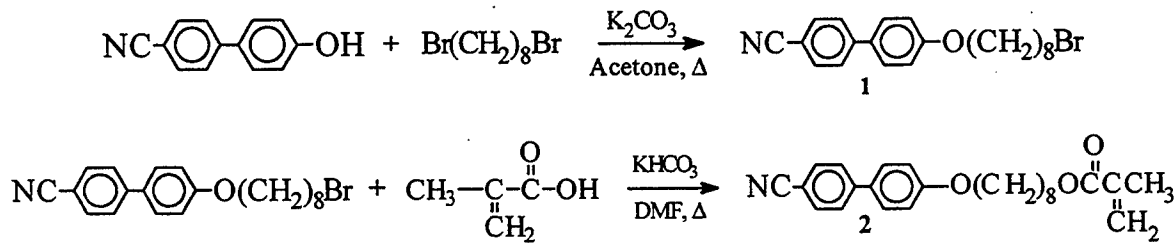
Experimental Section

Materials. 4-hydroxy-4'-cyanobiphenyl, 1,8-dibromo-octane, potassium hydrogen carbonate, hydroquinone, dihydroxybiphenol, DCCI, 4-pentenoic acid, 2,2' 3,3' 5,5' 6,6' Octafluoro-4,4' biphenol monohydrate, dimethylaminopyridine, bisphenol A, (hexafluoroisopropylidene)diphenol and 2-(trifluoromethyl)acrylic acid (all from Aldrich) were used as received. Methacrylic acid and 4,4' bis(2-hydroxyhexafluoroisopropyl)biphenol were used as received from Lancaster Synthesis. Acetone was dried over molecular sieves, distilled and stored with molecular sieves. All other materials were commercially available and were used as received.

Characterization. The proposed structures of all the compounds considered in this investigation were verified using ^1H NMR spectroscopy and FT-IR spectroscopy. The thermal properties of the monomers synthesized were determined using a Thermal Analyst 2920 differential scanning calorimeter (DSC). Transition temperatures were reported at their onset. Heating rates were 10°C/min for all materials. A Nikon Optiphot-Pol polarizing microscope equipped with a Mettler GP 82HT hot stage and a Mettler FP 90 central processor were used to observe thermal transitions and determine if a material displayed a liquid crystal characteristics. ^1H NMR spectra were recorded on a Varian VXR-300 spectrometer with a Varian VXR-4000 Processor. TMS was used as the internal standard. A Perkin-Elmer FT-IR 1725X spectrometer equipped with a GC-IR 1700X Interface was used to obtain infrared transmittance spectra.

Monomer Synthesis.

Scheme 1



1-Bromo-8-(4'-cyanobiphenyl-4-yloxy)octane (1) was prepared using a procedure as described by Attard *et al.*² A 450 ml round bottom flask was equipped with a stir bar and a condenser. To the flask were added 4-hydroxy-4'-cyanobiphenyl (2.5 g, 13 mmol), 1,8-dibromo-octane in large excess (23.9mL, 130 mmol), and potassium carbonate as base (13.5 g, 97.5 mmol) were refluxed with stirring in dry acetone (200 mL) for 24 hours. The reaction mixture was hot filtered, the residue washed with acetone and the solvent removed with a roto-evaporator. Light petroleum (40-60°) was added to the extract and the precipitate collected via vacuum filtration using a .45

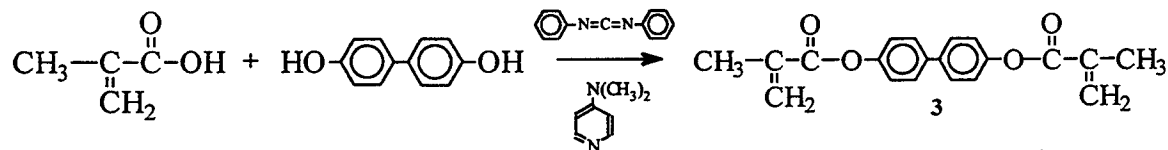
mm filter paper. Thus, the removal of any dimeric side product that may have been formed during the reaction was removed. Experimental DSC, FT-IR and ¹H NMR spectra were in close agreement with previously reported values.³

Yield: 3.38 g, 75%. Melting point: 70.1°C. FT-IR (Kbr) ν/cm^{-1} : 2235 (vs CN). ¹H NMR (CDCl₃): 87.7 (4H, aromatic), 7.5 (2H, aromatic), 7.0 (2H, aromatic), 4.0 (2H, OCH₂), 3.4 (2H, CH₂Br), 1.7-2.0 (OCH₂CH₂, CH₂CH₂Br), 1.2-1.5 (8H, O(CH₂)₂(CH₂)₄(CH₂)₂Br).

8-(4-Cyanobiphenyl-4'-yloxy)octyl methacrylate (2) was prepared using the procedure described by Craig et al. and Imrie.³ Methacrylic acid (0.66 g, 7.7 mmol) was stirred with potassium hydrogen carbonate (0.74 g, 7.4 mmol) for 5 minutes at room temperature to form the potassium methacrylate salt. A 450 ml round bottom flask was equipped with a stir bar and a condenser. To the flask were added the potassium methacrylic salt, 1-Bromo-8-(4'-cyanobiphenyl-4-yloxy)octane (2) (2 g, 5.2 mmol) and hydroquinone (0.015 g, 0.14 mmol) in *N,N*-dimethylformamide (60 ml). The reaction mixture was refluxed with stirring at 100°C for 24 hours. The mixture was poured into water (300 ml) upon cooling and stirred to coagulate the precipitate. The precipitate was collected by vacuum filtration using a 5mm filter paper and dissolved in dichloromethane. The organic solution was washed in 5% aqueous sodium hydroxide and then water. The organic layer was then dried over MgSO₄, filtered and the solvent removed on a roto-evaporator. The product was then recrystallized twice from ethanol. Experimental DSC, FT-IR and ¹H NMR spectra were in close agreement with previously reported values.³

Yield: .93 g, 46%. Melting point: 47.0°C., FT-IR (Kbr) ν/cm^{-1} 2223 (vs CN). ¹H NMR (CDCl₃): δ 7.7 (4H, aromatic), 7.5 (2H, aromatic), 7.0 (2H, aromatic), 6.1 (2H, CH₂=C), 5.6 (2H, CH₂=C), 4.2 (2H, H₂COC(O)), 4.0 (2H, OCH₂), 2.0 (3H, CH₃), 1.6-1.9 (4H, OCH₂CH₂, CH₂CH₂OC(O)), 1.3-1.5 (8H, O(CH₂)₂(CH₂)₂(CH₂)₂C(O)).

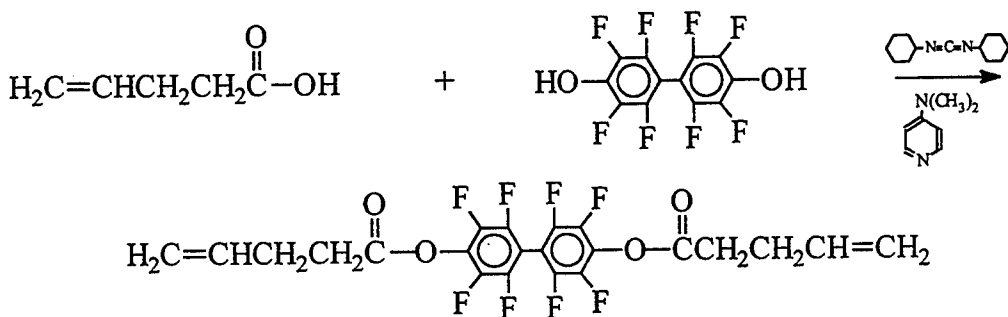
Scheme 2



4,4' Dimethacrylic biphenyl (3) was prepared via DCCI coupling reaction using a modification of the procedures described by Hassner *et al.*⁴ Thus, methacrylic acid (3.2 g), DCCI (8.4 g), 4,4' dihydroxybiphenol (3.8 g) and dimethylaminopyridine (.45 g) were refluxed with stirring in 1,2 dichloroethane (DCE) (240 ml) for 72 hours at 30°C. The reaction mixture was filtered to

remove the DCU and the precipitate rinsed with 15 ml of DCE. About one-half of the DCE solvent was removed and the filtrate vacuum filtered using a .45 mm filter. The solvent was removed from the remaining filtrate and the product recrystallized twice from ethanol. Yield: 1.46 g (25%). FT-IR (Kbr) ν/cm^{-1} : 1736 (vs Ester). DSC: 144°C. ^1H NMR: δ 7.6 (4H, aromatic), 7.2 (4H, aromatic), 6.4 (2H, $\text{C}=\text{CH}_2$), 5.8 (2H, $\text{C}=\text{CH}_2$), 2.1 (6H, $\text{C}-\text{CH}_3$).

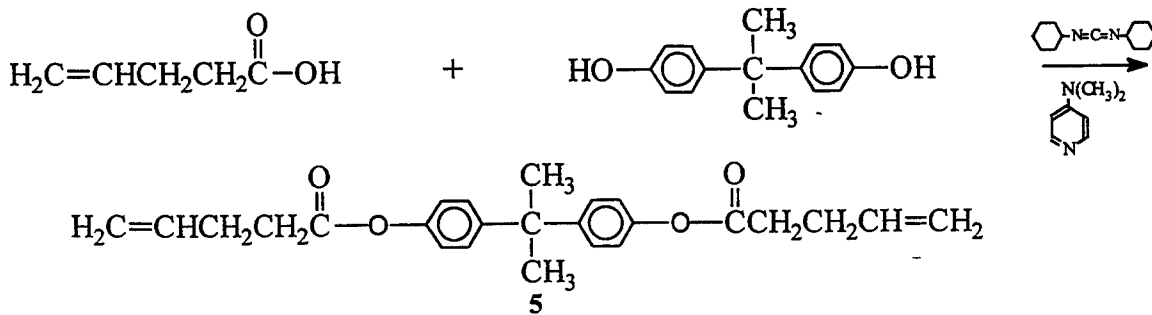
Scheme 3



4,4' (2,2' 3,3' 5,5' 6,6' Octafluoro)biphenyl (4) was prepared via DCCI coupling reaction using a modification of the procedures described above for 4,4' Dimethacrylic biphenyl (3). A 100 mL round bottom flask was equipped with a stir bar and a condenser. Thus 4-Pentenoic acid (.52 g), 2,2' 3,3' 5,5' 6,6' octafluoro-4,4' biphenol monohydrate (1.0 g), dimethylaminopyridine (0.06 g) and hydroquinone (0.00014 g) were refluxed with stirring in dichloromethane (50 mL) for 72 hours at ambient temperature. The reaction mixture was vacuum filtered using a 5mm filter paper. The filtrate was then washed in water, 5% acetic acid and again in water. The filtrate was then dried over MgSO_4 and filtered and the solvent removed with a roto-evaporator. The final product was off-white in color and possessed a sticky texture.

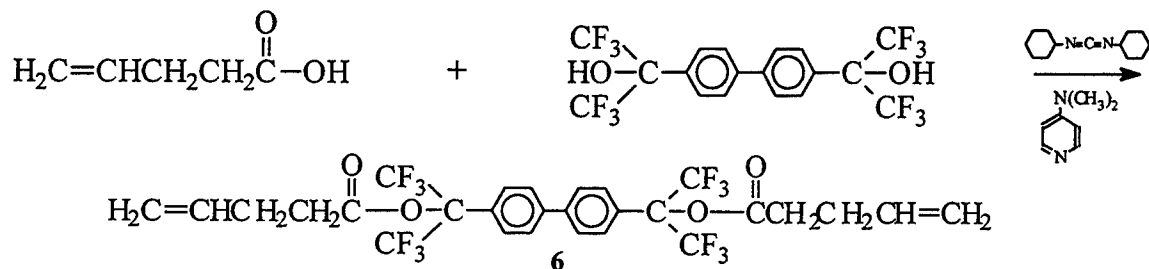
Yield: 1.2 grams (85%). FT-IR (Kbr) ν/cm^{-1} : 1791 (vs Ester). DSC: 40.7°C. ^1H NMR: δ 5.9 (2H, $\text{H}_2\text{C}=\text{CH}$), 5.1-5.2 (4H, $\text{H}_2\text{C}=\text{C}$), 2.8 (4H, $\text{CH}_2\text{C}=\text{O}$), 2.5 (4H, $\text{CHCH}_2\text{CH}_2\text{C}=\text{O}$).

Scheme 4



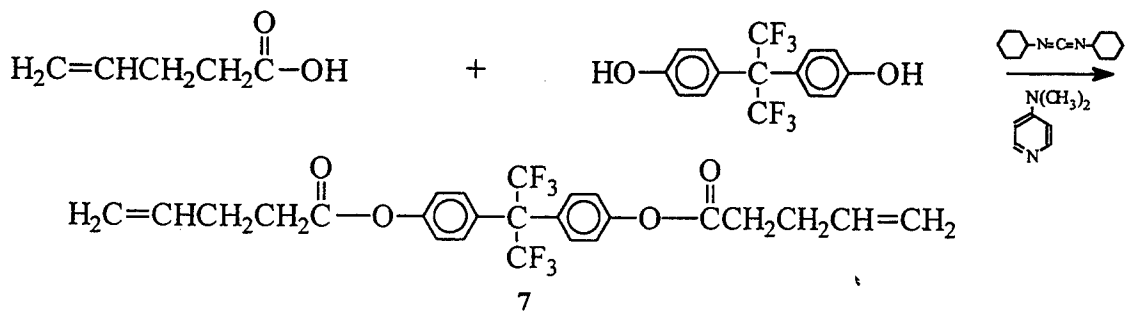
4,4' Dipentenate (bisphenyl A) (5) synthesis was attempted via DCCI coupling reaction using a modification of the procedures described above for 4,4' (2,2' 3,3' 5,5' 6,6' Octafluoro)biphenyl (4). Thus, 4-Pentenoic acid (2 g, 20mmol), DCCI (4.5 g, 22mmol), Bisphenol A (2.5 g, 11 mmol) and Dimethylaminopyridine (.24 g, 20mmol) were added to a 300 ml round bottom flask and refluxed with stirring for 72 hours at 23°C. The reaction mixture was vacuum filtered to remove the DCU byproduct. The filtrate was washed with water, 5% acetic acid then again with water. The organic layer was then dried over MgSO₄, filtered and the solvent removed. FT-IR (Kbr) ν/cm^{-1} : 1758 (vs Ester). DSC: 211.5°C. ¹H NMR: δ 6.9 (4H, aromatic), 7.2 (4H, aromatic), 5.8-5.9 (H₂C=CH), 5.0-5.1 (H₂C=CH), 2.5-2.6 (H₂C=CHCH₂CH₂COO).

Scheme 5



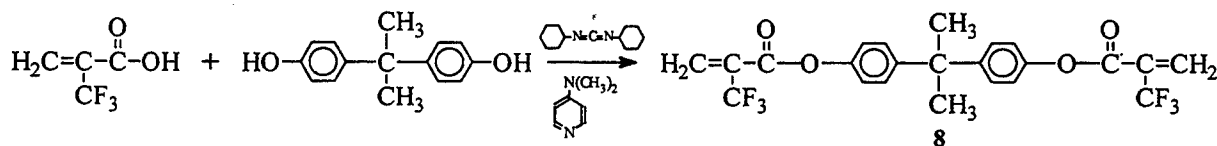
4,4' Dipentenate bis(2-hexafluoroisopropyl)diphenyl (6) synthesis was attempted via DCCI coupling reaction using a modification of the procedures described previously for 4,4'-bis(hydroxyhexafluoroisopropyl)biphenol (5). A 200 ml round bottom flask was equipped with a stir bar and condenser. To the flask were added 4-Pentenoic acid (.617 g), DCCI (1.4 g), 4,4'-bis(hydroxyhexafluoroisopropyl)biphenol (1.6 g) and dimethylaminopyridine (.075 g). The solution was refluxed with stirring for 72 hours in 1,2 dichloroethane (60mL) at 23°C. The reaction mixture was vacuum filtered to remove DCU. 250 ppm hydroquinone was added to the filtrate and the solvent removed under reduced pressure and bath temperature of 38°C. The remaining viscous material was opaque and tan in color.

Scheme 6



4,4' Dipentenate hexafluoroisopropylidene diphenyl (7) synthesis was attempted via DCCI coupling reaction using a modification of the procedures described by Hassner *et al.*⁴ 4-Pentenoic acid (2.0 g, 20 mmol), DCCI (4.5 g, 22 mmol), 4,4'-(hexafluoroisopropylidene)diphenol (3.7 g, 11 mmol), and dimethylaminopyridine (.24 g, 2 mmol) were added to a 300 ml round bottom flask and refluxed for 72 hours at 30°C. The reaction mixture was filtered and the solvent removed under reduced pressure, upon which, a viscous oil-like product remained. Characterization confirmed that the reaction did not proceed as anticipated.

Scheme 7



4,4'-(2-(Trifluoromethyl)acrylic bisphenyl A (8) synthesis was attempted via DCCI coupling reaction using a modification of the procedures used for 4,4' dimethacrylic biphenyl (3). To a 300 mL round bottom flask were added 2-(trifluoromethyl)acrylic acid (2.5 grams, 18 mmol), DCCI (4.05 g, 20 mmol), bisphenol A (2.23 g, 10 mmol) and dimethylaminopyridine (.22 g, 1.7 mmol). The reaction mixture was refluxed with stirring for 72 hours at 30°C.

The reaction mixture was observed to turn yellow in color several hours after the reaction was initiated. After 24 hrs, a viscous precipitate was observed in the bottom of the flask.

Variations of this approach were explored including ambient temperature reactions and adding 250 ppm hydroquinone to inhibit polymerization, however, these approaches were met with little or no success in obtaining the desired product. Characterization methods revealed a stable fluorinated polymer which was virtually insoluble in benzene, acetone, dichloromethane, dichloromethane, and toluene.

Results and Discussion

8-(4-Cyanobiphenyl-4'-yloxy)octyl methacrylate (2) first reported by Craig and Imrie³ was successfully synthesized in this work. The ¹H NMR spectrum may be viewed in **Figure 1.1** in the appendices. Upon polarized microscopic observation (2) exhibited what appeared to be a smectic phase upon cooling. Craig and Imrie reported this behavior after attaching the monomer to a polymer backbone. The differential scanning calorimetry (DSC) thermogram of (2) is shown in **Figure 1.3** in which melting is observed at 47°C. The FT-IR spectrum in **Figure 1.2** shows a very strong peak at 2223 ν/cm^{-1} corresponding to C-N vibrations.

To our knowledge, synthesis of 4,4' Dimethacrylic biphenyl (3) by DCCI coupling has not been previously reported. The structure was confirmed in part by the ¹H NMR spectrum which may be viewed in **Figure 2.1** in the appendices. No liquid crystalline behavior was observed upon examination under the polarizing microscope. The FT-IR spectrum shown in **Figure 2.2** reveals a very strong peak at 1736 ν/cm^{-1} corresponding to the ester group. The differential scanning calorimetry (DSC) thermogram in **Figure 2.3** shows a sharp melting peak at 144°C.

The synthesis of 4,4' (2,2' 3,3' 5,5' 6,6' Octafluoro)biphenyl (4) was confirmed by the ¹H NMR spectrum shown in **Figure 3.1**. The FT-IR spectrum shown in **Figure 3.2** shows a very strong peak at 1791 ν/cm^{-1} corresponding to the ester peak. The differential scanning calorimetry (DSC) thermogram may be viewed in **Figure 3.3** and shows a melting peak at 40.7°C.

The structure of 4,4' dipentenate (bisphenyl A) (5) was confirmed and to our knowledge has not been previously synthesized via DCCI coupling. The product was a viscous liquid, light-brown in color and transparent. The ¹H NMR spectrum shown in **Figure 4.1**, confirms the structure. The FT-IR spectrum which may be viewed in **Figure 4.2** in the appendices reveals a very strong peak at 1758 ν/cm^{-1} which corresponds to the ester group in the product.

The synthesis of 4,4' dipentenate bis(2-hexafluoroisopropyl)diphenyl (6) was not confirmed. The resulting product was a viscous liquid which was opaque and tan in color. The synthesis of 4,4' dipentenate hexafluoroisopropylidene diphenyl (7) was not confirmed. A significant portion of the 4-Pentenoic reactant was recovered from the reaction mixture via short-path distillation. The synthesis of 4,4'-(2-(trifluoromethyl)acrylic bisphenyl A (8) was not confirmed despite attempts at varying reaction temperature and the addition of hydroquinone to inhibit polymerization. Consistently, a fluorinated polymer which was virtually insoluble in all solvents tested, was precipitated after the first few hours of starting the reaction.

Conclusion

The synthesis of four chain extending monomers for polymer dispersed liquid crystal systems has been reported. One of these monomers has been previously reported³ while three others synthesized via DCCI coupling reaction have not been reported previously to our knowledge. Three reaction schemes were attempted via DCCI coupling with no significant findings to support a successful synthesis.

Upon incorporation into the pre-polymer syrup, 8-(4-Cyanobiphenyl-4'-yloxy)octyl methacrylate (**2**) was promising in that it appeared soluble in the syrup. However, after 24 hours, a viscous liquid was remaining which was cloudy in appearance. This is promising in that the monomer is highly reactive in the syrup but the polymerization time must be addressed. To date, none of the three novel monomers have been incorporated in the pre-polymer syrup.

Suggestions for Future Research. Acid chloride reactions should be considered in the future as purification may be easier than those synthesized via DCCI coupling. Column chromatography should be investigated in the removal of the urea byproduct from DCCI reactions. Monomers synthesized in this investigation will be incorporated into the pre-polymer syrup and results reported at a later date.

Acknowledgment. I am grateful to Wright Laboratory: Materials Directorate (WL/MLPJ) and Research and Development Laboratories whose support made this research possible.

References.

- (1) Doane, J.W.; Vaz, N.A.; Wu, B.-G.; Zumer, S. *Appl. Phys. Lett.* **1986**, *48*, 269.
- (2) Attard, G. S.; Imrie, C. T.; Darasz, F. E. *Chem. Mater.* **1992**, *4*, 1246.
- (3) Craig, A. A.; Imrie, C. T. *Macromolecules* **1995**, *28*, 3617.
- (4) Hassner, A. A.; Alexanian, V. *Tetrahedron* **1978**, *44*, 475.
- (5) Sutherland, R. L.; Natarajan, L. V.; Tondiglia, V. P.; Bunning *Chem. Mater.* **1993**, *5*, 1533.
- (6) Neckers, D. C. *J. Photochem. Photobiol. A, Chem.* **1989**, *47*, 1.
- (7) Imrie, C. T.; Karasz, F. E.; Attard, G. S. *Macromolecules* **1993**, *26*, 3803.
- (8) Hassner, A.; Krepki, L.; Alexanian, V. *Tetrahedron* **1978**, *34*, 2069.
- (9) Sutherland, R. L.; Natarajan, L. V.; Tondiglia, V. P.; Bunning, T. J.; Adams, W. W. *The International Society for Optical Engineering: Proceedings Reprint* **1994**, *2152*, 305.

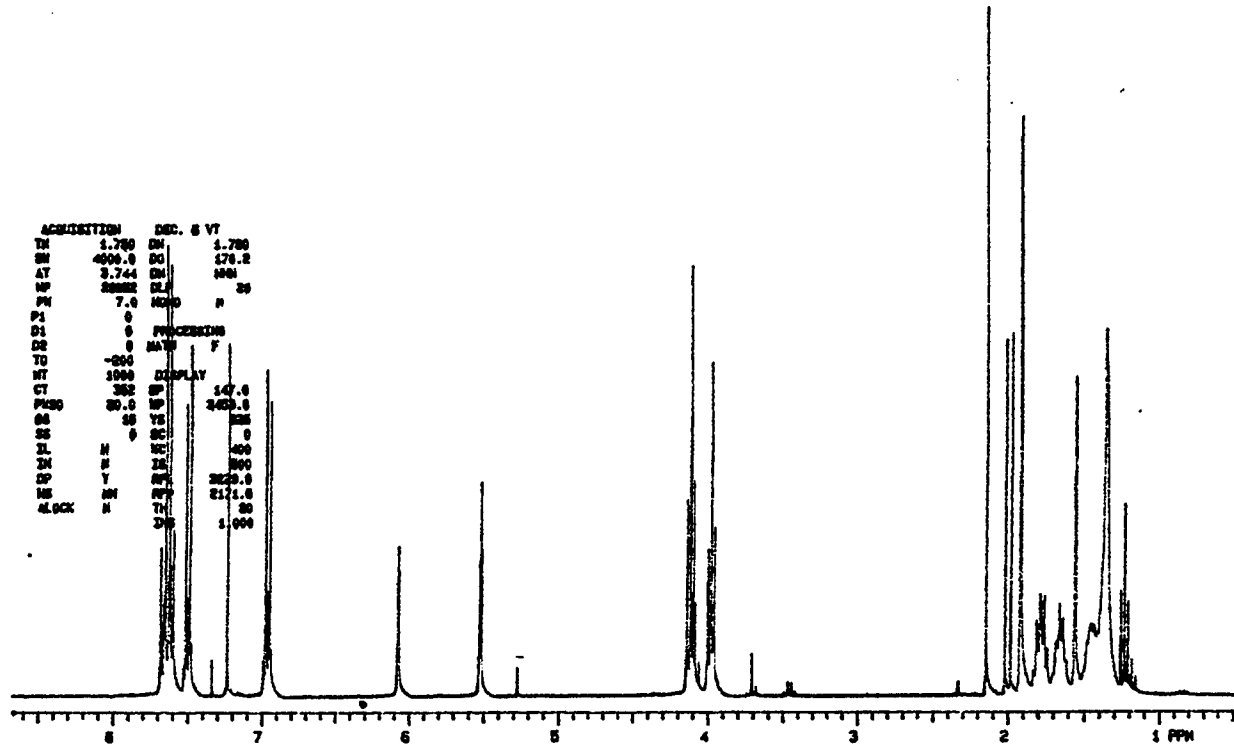


Figure 1.1. ^1H NMR spectrum of 8-(4-Cyanobiphenyl-4'-yloxy)octyl methacrylate (**2**) in close agreement with previously reported values.³ (CDCl_3): δ 7.7 (4H, aromatic), 7.5 (2H, aromatic), 7.0 (2H, aromatic), 6.1 (2H, $\text{CH}_2=\text{C}$), 5.6 (2H, $\text{CH}_2=\text{C}$), 4.2 (2H, $\text{H}_2\text{COC(O)}$), 4.0 (2H, OCH_2), 2.0 (3H, CH_3), 1.6-1.9 (4H, OCH_2CH_2 , $\text{CH}_2\text{CH}_2\text{OC(O)}$), 1.3-1.5 (8H, $\text{O}(\text{CH}_2)_2(\text{CH}_2)_2(\text{CH}_2)_2\text{C(O)}$).

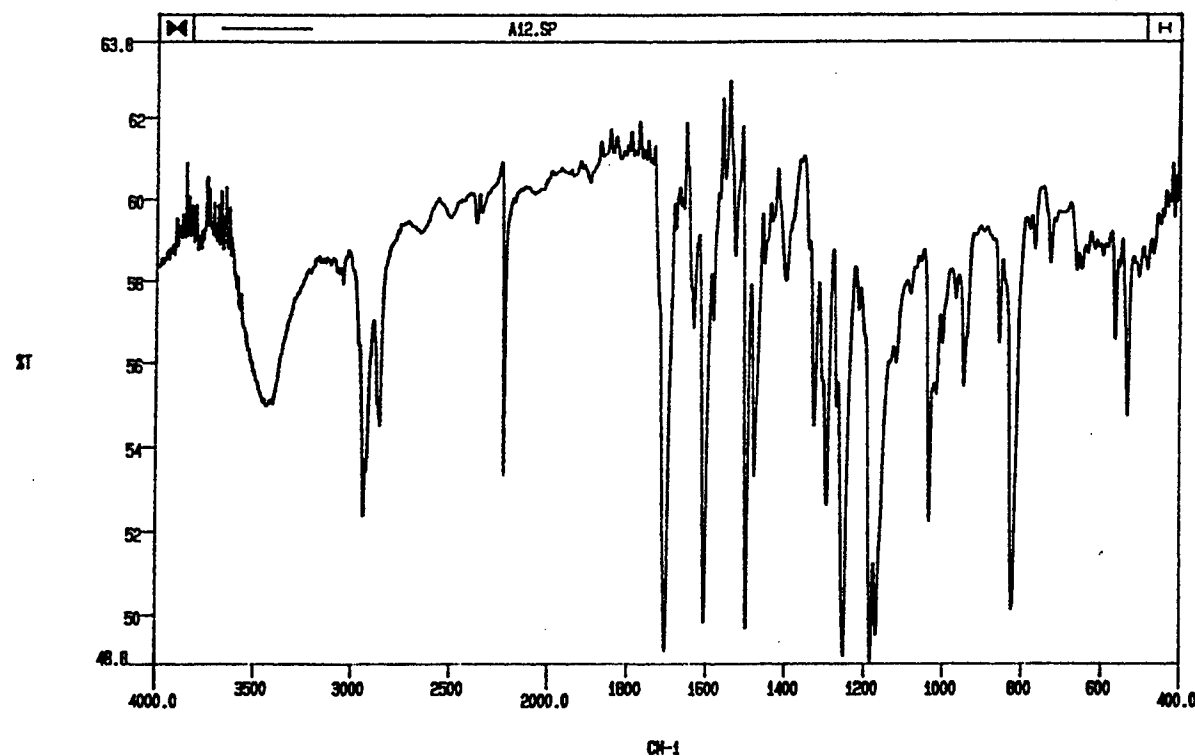


Figure 1.2. FT-IR spectrum of 8-(4-Cyanobiphenyl-4'-yloxy)octyl methacrylate (2). FT-IR (Kbr) ν/cm^{-1} 2223 (vs CN).

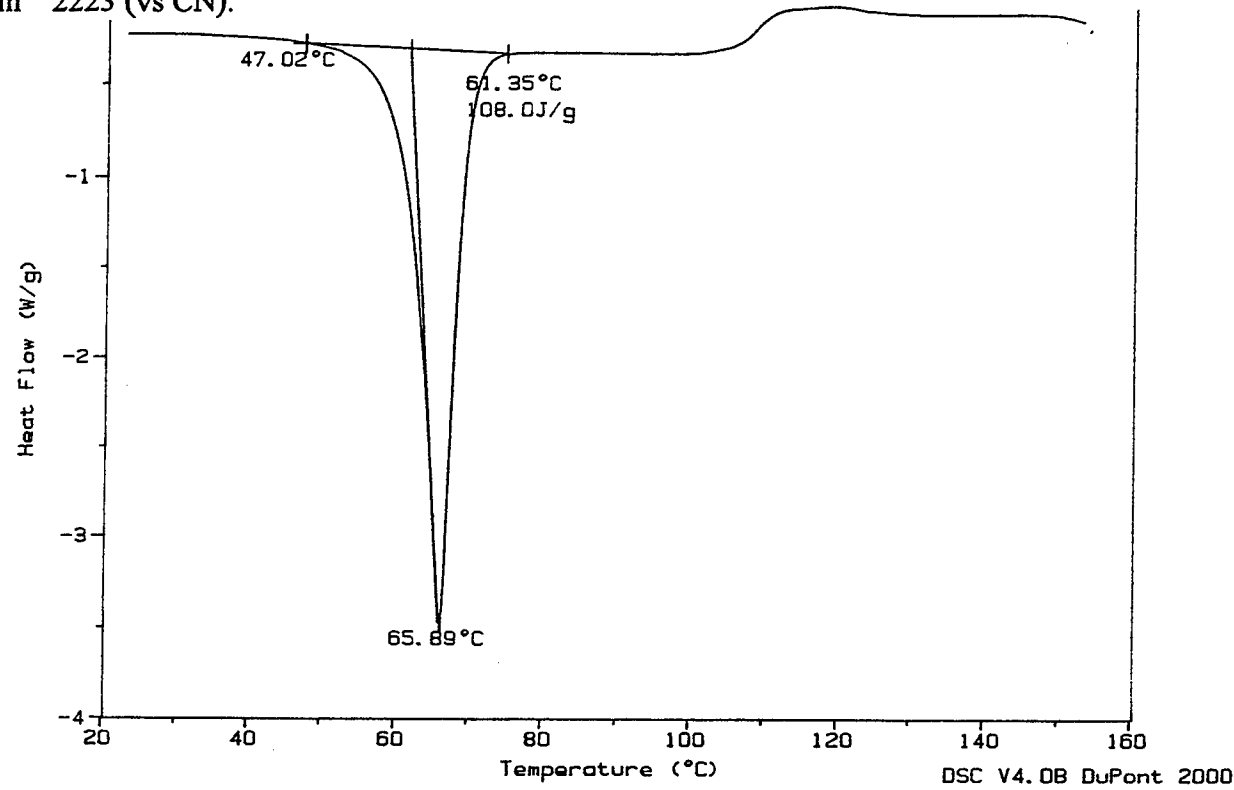


Figure 1.3. DSC thermogram of 8-(4-Cyanobiphenyl-4'-yloxy)octyl methacrylate (2). m.p. 47.0°C.

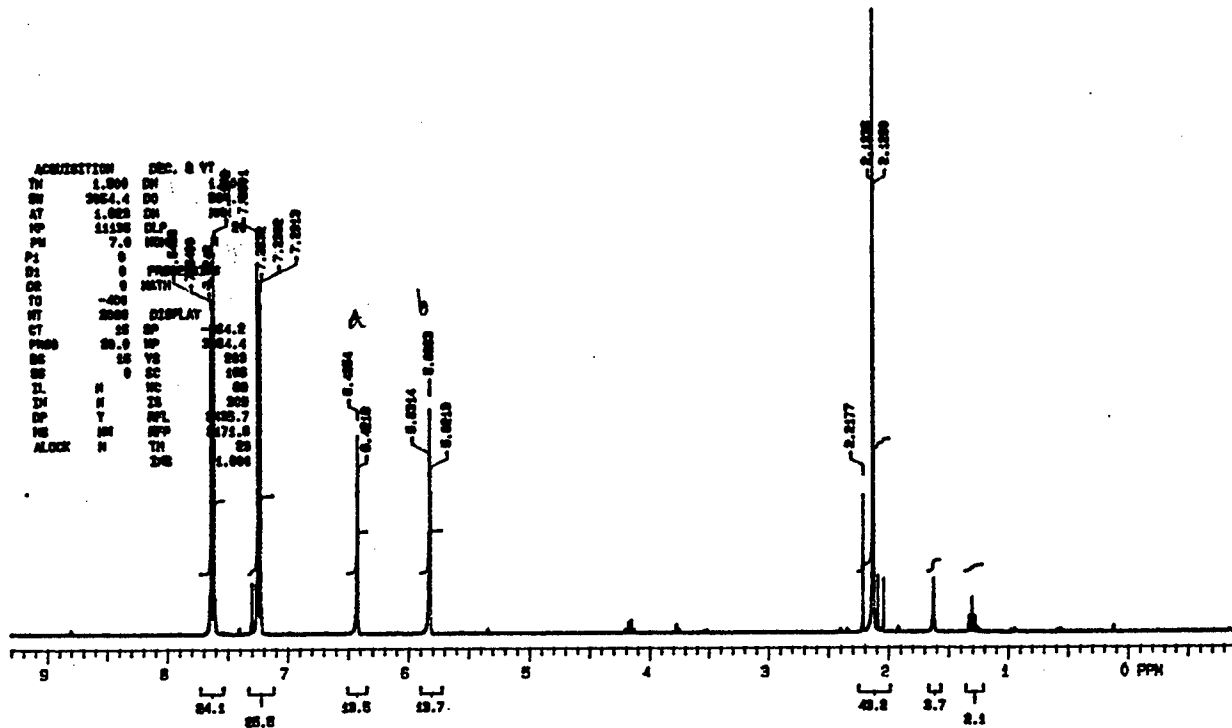


Figure 2.1. ^1H NMR spectrum of 4,4' Dimethacrylic biphenyl (3). ^1H NMR: δ 7.6 (4H, aromatic), 7.2 (4H, aromatic), 6.4 (2H, $\text{C}=\text{CH}_2$), 5.8 (2H, $\text{C}=\text{CH}_2$), 2.1 (6H, $\text{C}-\text{CH}_3$).

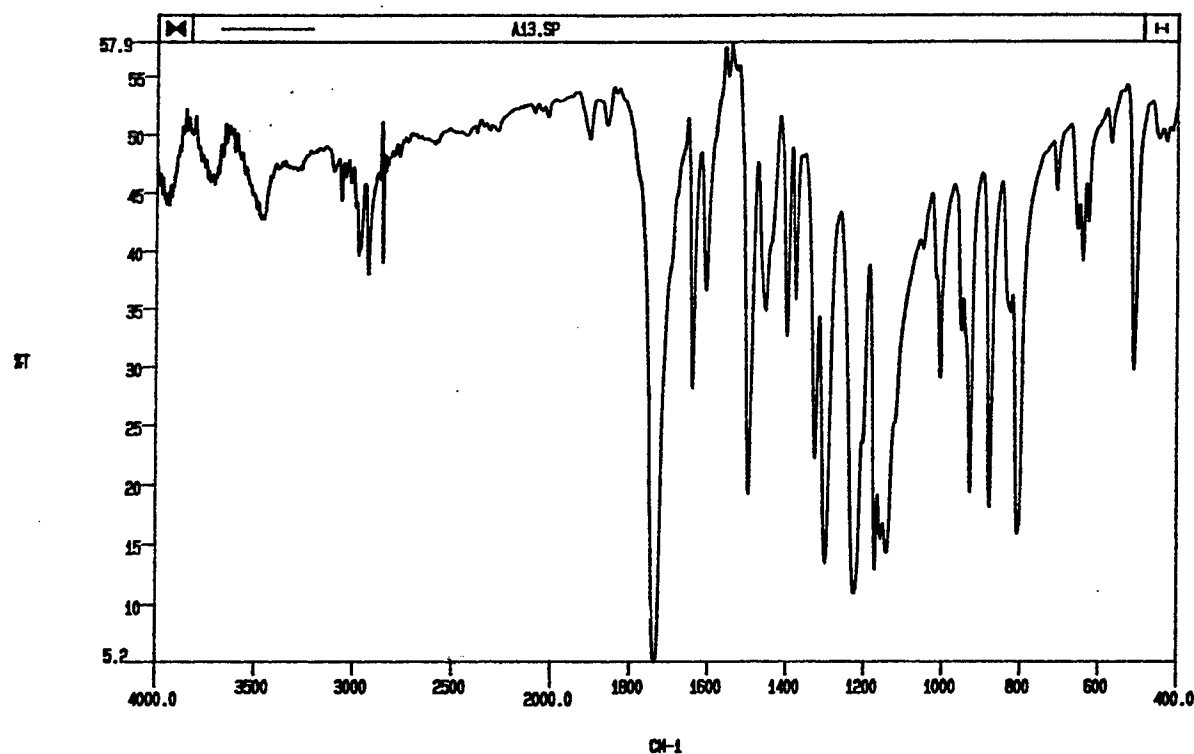


Figure 2.2. FT-IR thermogram of 4,4' Dimethacrylic biphenyl (3). FT-IR (Kbr) ν/cm^{-1} : 1736 (vs Ester).

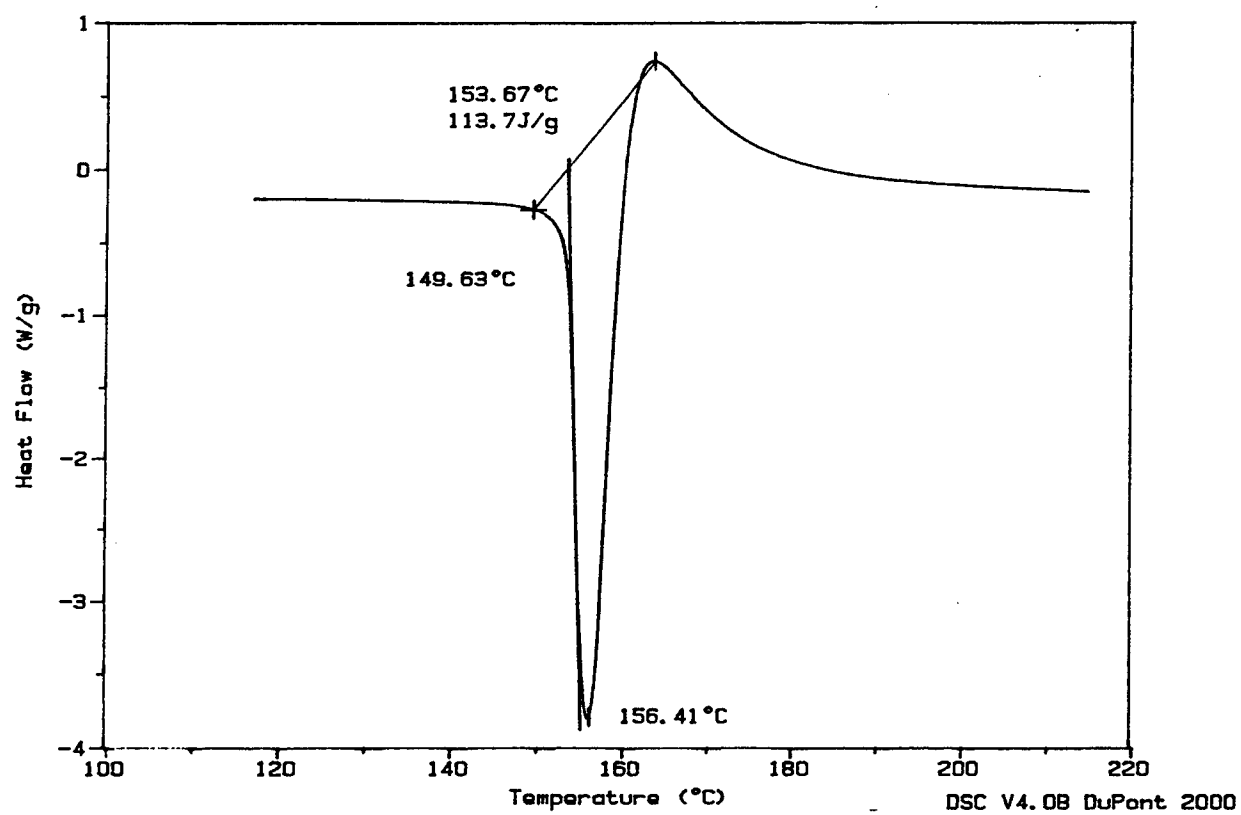


Figure 2.3. DSC thermogram of 4,4' Dimethacrylic biphenyl (3). m.p. 144°C.

IDP1 PULSE SEQUENCE: STD4H
DATE 08-15-95
SOLVENT CDCl₃
FILE H

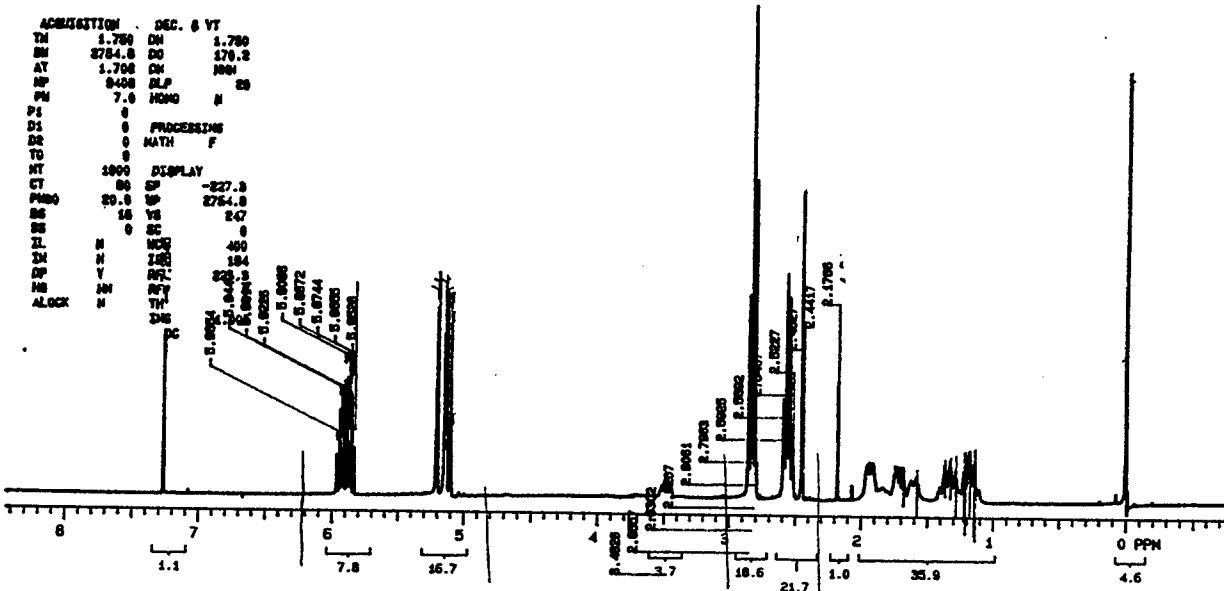


Figure 3.1. ¹H NMR spectrum of 4,4' Dipentenoic(2,2' 3,3' 5,5' 6,6' Octafluoro-biphenyl) (4): δ 5.9 (2H, H₂C=CH), 5.1-5.2 (4H, H₂C=C) 2.8 (4H, CH₂C=O), 2.5 (4H, CHCH₂CH₂C=O).

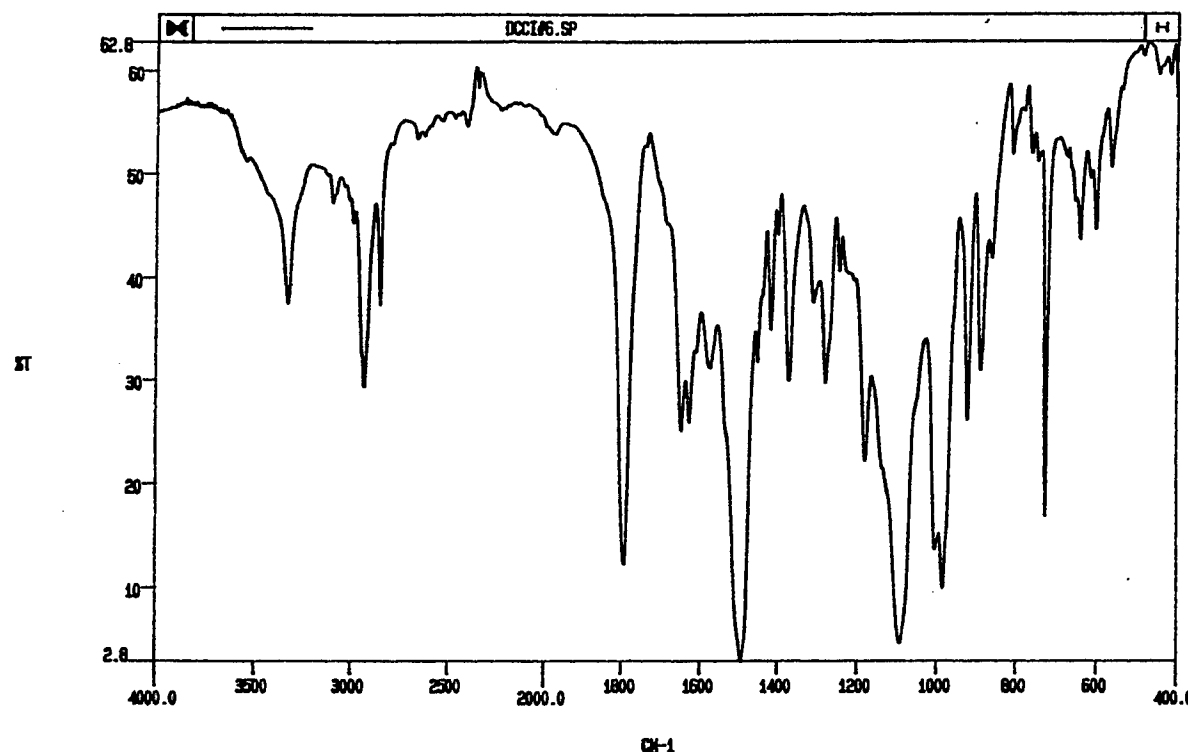


Figure 3.2. FT-IR spectrum of 4,4' Dipentenoic(2,2' 3,3' 5,5' 6,6' Octafluoro-biphenyl) (4): FT-IR (Kbr) ν/cm^{-1} : 1791 (vs Ester).

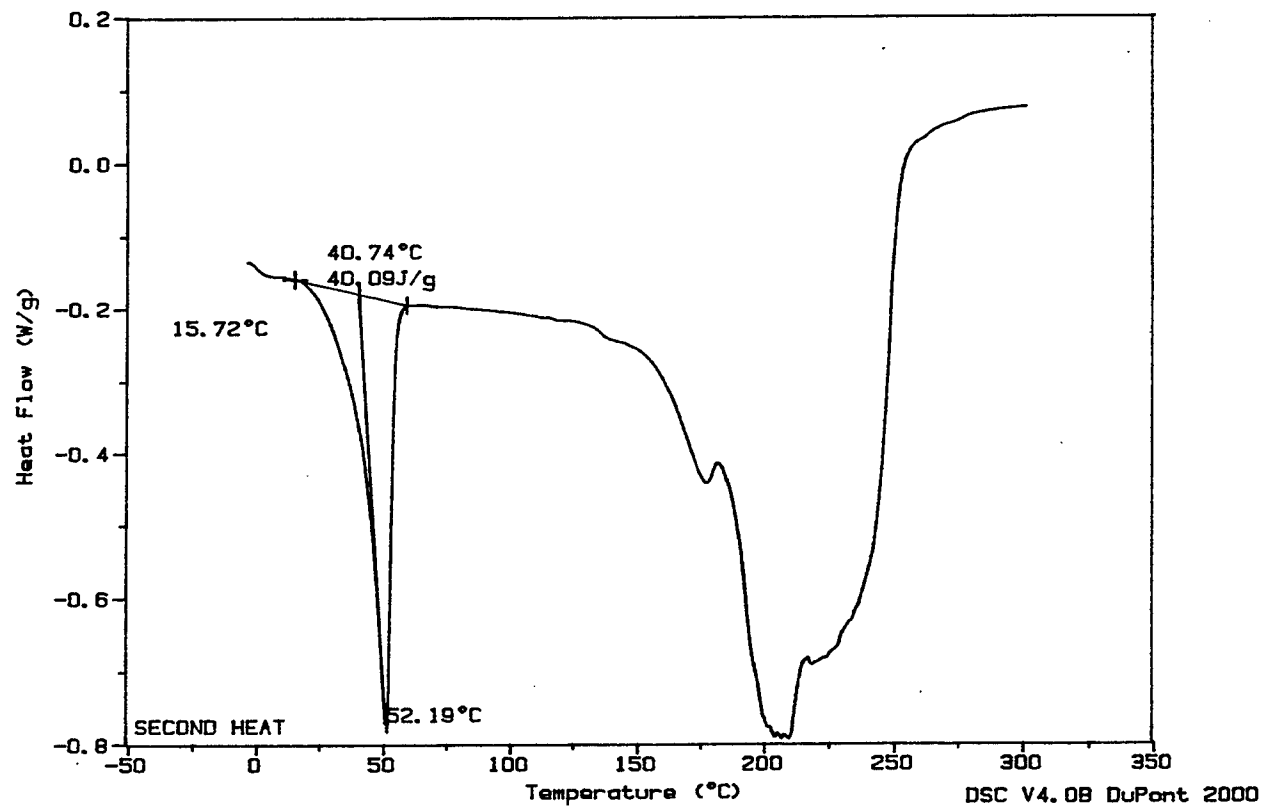


Figure 3.3. DSC thermogram of 4,4' Dipentenoic(2,2' 3,3' 5,5' 6,6' Octafluoro-biphenyl) (4): m.p. 40.7°C.

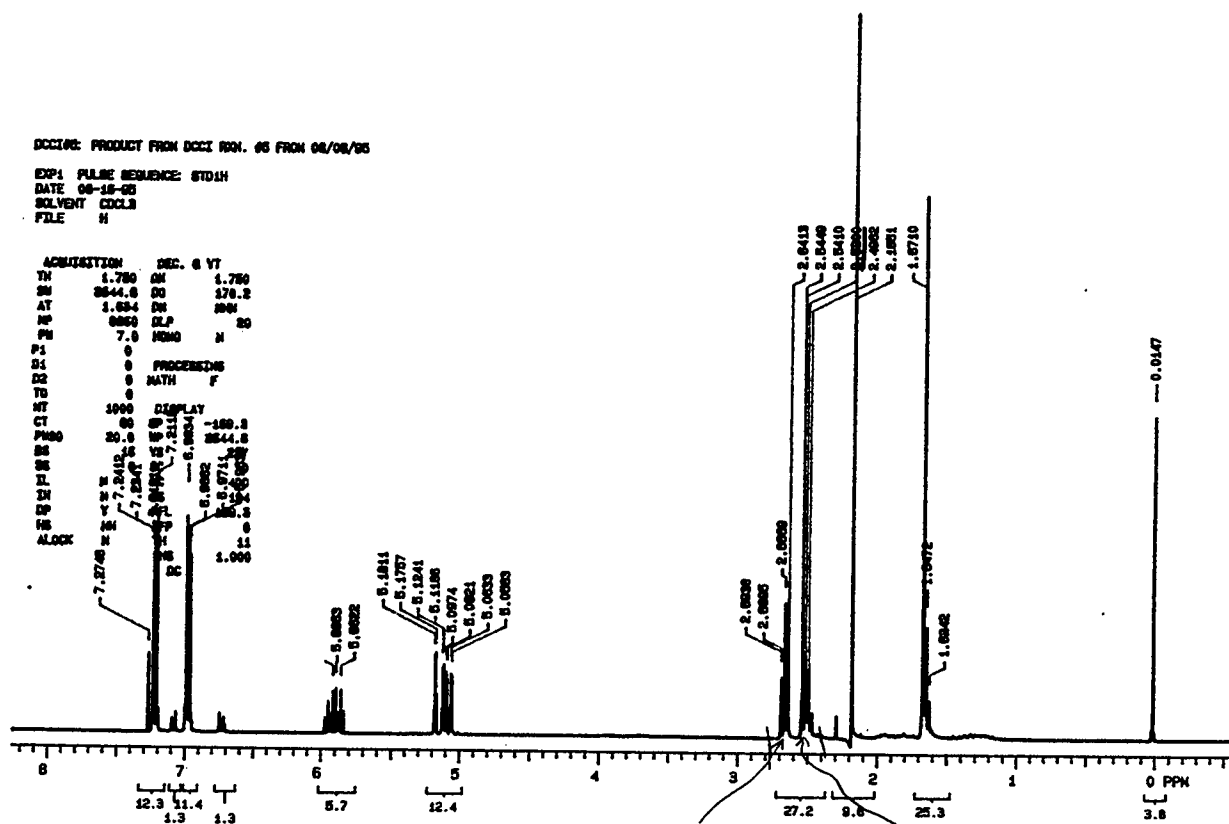


Figure 4.1. ^1H NMR spectrum of 4,4' dipentenate (bisphenyl A) (5): δ 6.9 (4H, aromatic), 7.2 (4H, aromatic), 5.8-5.9 ($\text{H}_2\text{C}=\text{CH}$), 5.0-5.1 ($\text{H}_2\text{C}=\text{CH}$), 2.5-2.6 ($\text{H}_2\text{C}=\text{CHCH}_2\text{CH}_2\text{COO}$).

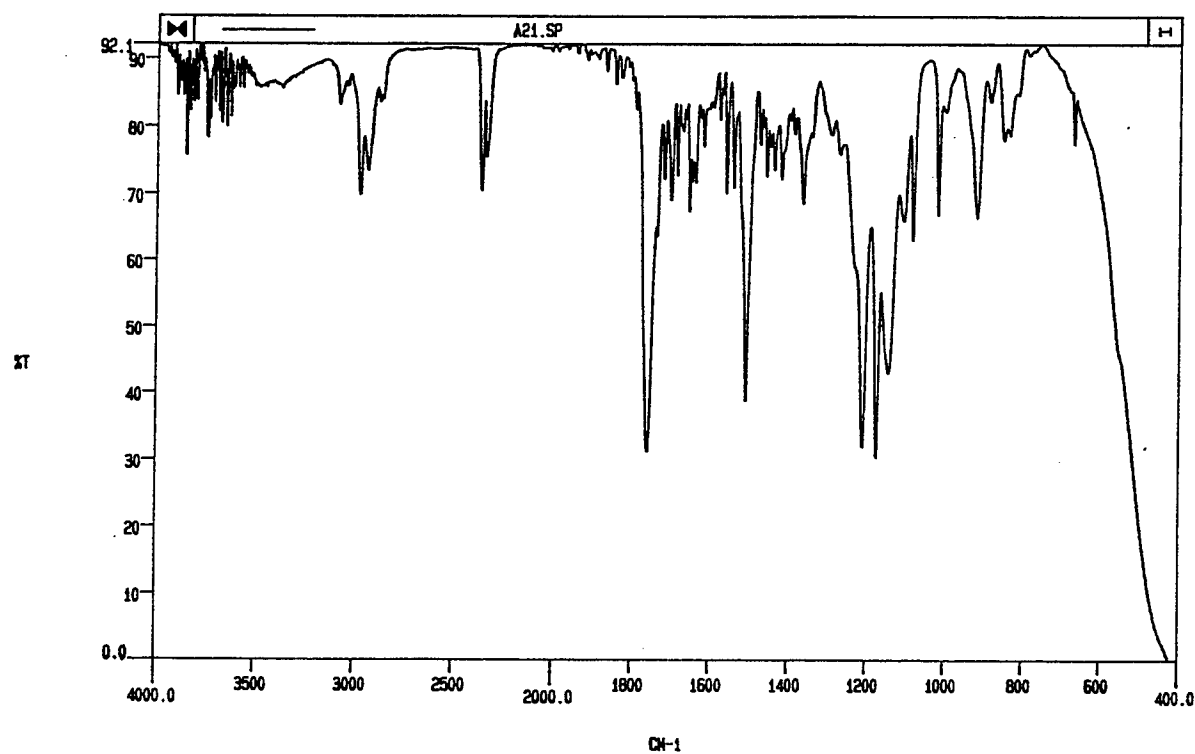


Figure 4.2. FT-IR spectrum of 4,4' dipentenate (bisphenyl A) (5): (Kbr) ν/cm^{-1} : 1758 (vs Ester).

**INVESTIGATIONS INTO THE USE OF THIN-FILM VANADIUM
DIOXIDE AS AN OPTICALLY ADDRESSED INFRARED SPATIAL
LIGHT MODULATOR**

Pankaj Shah
Graduate Student
Department of Electrical and Computer Engineering

Wayne State University
Detroit, MI 48202

Final Report for:
Graduate Student Research Program
Wright Laboratory Materials Directorate

Sponsored by:
Air Force Office of Scientific Research
Bolling Air Force Base, Washington DC

and

Wright Laboratory

September, 1995

INVESTIGATIONS INTO THE USE OF THIN-FILM VANADIUM DIOXIDE AS AN OPTICALLY ADDRESSED INFRARED SPATIAL LIGHT MODULATOR

Pankaj Shah
Graduate Student

Department of Electrical and Computer Engineering
Wayne State University

ABSTRACT

Infrared spatially light modulators (IRSLM) have numerous applications in optical systems for applications including optical computing, target recognition and survivability. One of the critical issues surrounding the use of IRSLM technologies is the interference to the scene caused by conductive control lines needed to control a nonlinear material or micromechanical based device (MEMS). In this study, we have investigated the use of an out-of band laser source to drive the phase transition of thin-film vanadium dioxide (VO_2) in an attempt to remove all control lines from the clear aperture of the device. We have observed control of $10.6\text{ }\mu\text{m}$ radiation emitted from a CO_2 laser by effecting the phase transformation using $1.3\text{ }\mu\text{m}$ radiation from a diode laser. Also, the transient response of this material was investigated. Hysteresis curves of reflectivity vs. temperature, and transmission spectral curves for different temperatures are demonstrated for VO_2 films on a germanium substrate and a sapphire substrate. Other identified areas of research include the use of VO_2 in microwave waveguide devices for noncontact thermally induced changes in the waveguide properties; and electronic logic circuits acting as active substrates for VO_2 thin-films, for spatially addressing and switching different regions of the modulator in a highly controlled manner.

INVESTIGATIONS INTO THE USE OF THIN-FILM VANADIUM DIOXIDE AS AN OPTICALLY ADDRESSED INFRARED SPATIAL LIGHT MODULATOR

Pankaj Shah
Graduate Student
Department of Electrical and Computer Engineering
Wayne State University

INTRODUCTION

Over the past thirty years, there has been continual efforts at investigating vanadium dioxide (VO_2) to take advantage of its ability to undergo a reversible phase transition from semiconductor to metal due to some physical effect. In this transition the reflectivity of the material increases in the infrared region of the spectrum, the transmission decreases, the absorption increases, and the resistivity increases by up to five orders of magnitude.

There are many applications for a material which exhibits this behavior. Optical computing and logic operations can be performed. High speed switches can be created from VO_2 because of its fast switching time. The switching time has been measured to be around 5 ps¹. However this value also depends on the method of initiating the transition. Data storage can be performed because of the hysteresis behavior exhibited in the material. Flash protection can be achieved because of the ability to limit high intensity by performing a phase transformation to the metallic state at high temperatures. Solar efficient windows can be created. One group has reported observing the phase transition around room temperature. Another group has created a bolometer² using VO_2 .

In this report we focus on the near and far infrared regions of the electromagnetic spectrum. We investigate different applications of the phase transition in relation to creation of an IRSIM. Control of light by light is observed as well as transient switching. Other phenomena particular to VO_2 are also investigated. The outline of this report is as follows. In the first section background information will be given about the material. Then the experiments performed and their results will be discussed. Following that, new applications that should be investigated will be discussed.

BACKGROUND INFORMATION ON VANADIUM DIOXIDE

Vanadium dioxide is known as a chromogenic material. These are materials that undergo a transition that is strongly and reversibly depend on some physical effect. If the transition depends on light the material is photochromic. If it depends on applied electric currents or voltages, the material is electrochromic and if it depends directly on heating the material, the transition is thermochromic. In the literature it is observed that Vanadium Dioxide acts as both an electrochromic and thermochromic material.

The transition from semiconductor to metal and vice versa occurs due to several effects in VO_2 . Heating the film through a critical transition temperature will cause the phase change^{3,4}. Doping the material with donors Nb, W, and F will cause the transition⁵. Injection of protons will also cause the transition because protons act as charge compensators and thus will allow more electrons to be injected into the material⁶. This electron gas will give the material its metallic properties. Creating a deviation from stoichiometry with respect to oxygen by ion or electron bombardment will also cause the transformation. This bombardment breaks the V-O bonds after which the oxygen atoms will diffuse to the surface of the grains in the oxide film. The V atoms will then begin to form bonds to each other forming thin filaments in the oxide. This is the metallic state.⁷

In this research project only the transition due to heating will be considered. At low temperatures VO_2 is a semiconductor with a gap of .7 eV. The crystal structure is monoclinic. The V-V bonds have alternate separations of 2.65 and 3.12 angstrom and form a zig-zag chain. This leads to bands composed of bonding d orbitals between closely spaced metal atoms. At high temperature the material enters the metallic phase with a rutile crystal structure. All the V-V bonds now have equal separations of 2.87 angstrom⁸. The change in the bond lengths can lead to stresses in the material. This has interesting effects as will be seen later.

The phase transition can be considered a martensitic transformation which is due to a diffusionless shearlike phase transformation. The transformation can be considered as undergoing an antiferroelectric to paraelectric transition and a change from homopolar to metallic bonding at the same temperature^{9,10}. The primary driving force is the electron-electron correlation.^{11,12}

There is a critical temperature where this transition occurs. Some have defined this as the temperature of the point where some parameter such as reflectivity or resistivity has reached its half way point in the transition, others have defined this as the temperature where the slope is the greatest. There are several ways to change the value of this critical transition temperature. One way is to replace some vanadium atoms by W, Mo, Nb, or Re. Another way is to replace oxygen atoms by F. Also, the application of stress through the substrate or overlayer will change the critical transition temperature.¹³

RESULTS AND DISCUSSION

Two samples were investigated. A vanadium dioxide film (~5000 Å) grown on a germanium substrate, and vanadium dioxide film (~5000 Å) grown on a sapphire substrate. Information on the phase transformation with temperature was obtained using the setup shown in Fig. 1. The laser is a Synrad Inc. model D48-V-115 CW CO_2 laser.

The detectors were pyroelectric detectors connected to a Laser Precision Corp. Universal Radiometer model 6600, which took the ratio of the incident energies. Though the laser's emission varied greatly in time, all measurements were relative to the light emitted. The sample was mounted in a copper holder that had a close thermal contact to the VO_2 film. This holder was heated by an Omega Temperature Controller model CN9000A. This heater was used in all the experiments. The results for both samples are shown in Figs. 2. and 3. These figures demonstrate that at a critical temperature the phase of the material transforms to metallic with the increased reflectivity associated with this phase. Also, the plots demonstrate hysteresis associated with this transition. This hysteresis is due to stresses occurring at the domain boundaries between islands of metallic regions in a semiconductor film or vice versa. The stress is caused by the change of the bond length sizes. The strange behavior near the transition may be due to an excited state which is neither the final metal or semiconductor state of the material. One theory is that this excited state is a semiconductor containing metallic phase inclusions which are electron-hole drops formed in the bulk of the semiconducting phase and consisting of an electron-hole $d_{\parallel}-d_{\parallel}$ plasma¹⁴. This may also be caused by the large change in the imaginary refractive index that occurs in these materials at $10.6 \mu\text{m}$ wavelength¹⁵.

To understand the behavior of the samples over a large region of the spectrum, the transmission spectra of the two samples were plotted vs. wavenumber for four different temperatures, 40, 60, 70, and 80 degrees Celsius as shown in Figs. 4, and 5. These curves were plotted using a Perkin-Elmer model 983 Spectrophotometer with the sample placed in the heater. In these figures the transmission decreased as the temperature increased showing the effect of the phase transformation. The band gap of the semiconductor is .7 eV which corresponds to a point to the left of the left edge of the horizontal axis. The horizontal axis represents energy smaller than that necessary to cause electron transitions by absorption.

To test whether light can be used to control the propagation of light through the film, two experiments were performed. First the curve in Fig. 2. was replotted, but now with a second laser beam heating the region where the first laser beam heated the sample. Fig. 6. shows these results. This second beam also heated the sample, and thus the transition was observed to occur at a lower temperature as shown in the figure. The next experiment was to see if information can be put on a light beam by using the VO₂ film as a spatial and temporal light modulator. The setup for this experiment is shown in Fig. 7. The VO₂ film on Ge substrate sample was used. Here the diode laser made by ATX Telecom Systems, Inc., model 1.3 SBLC with a fiber output, emits 1.3 μm wavelength light which was used to heat the sample. Then the 10.6 μm wavelength light from the Synrad CO₂ laser was transmitted through the heated region. The two spots were overlapped on the sample by first overlapping the spots using a 100 μm pinhole in place of the sample and optimizing the transmission of light from both lasers through it. The transmitted signal was picked up by a pyroelectric detector and sent to an HP Sampling Oscilloscope model 54522A. ZnSe lenses were used as well as high reflecting metallic mirrors. The beam splitter is a 50-50 AR coated Ge window. The 10.6 μm beam was chopped to provide a trigger for the oscilloscope. The result of this experiment is shown in Fig. 8. Here we see that when the 1.3 μm light hits the VO₂ film, the film is heated, and the transmission decreases. At the spot where the beams irradiate the VO₂, they are at their greatest focus with spot sizes of approximately 200 μm for the 10.6 μm beam and 40 μm for the 1.3 μm heating beam which contained 250 mW of power. Thus heating of the film directly causes the phase transition. This transition could also be obtained by heating the substrate which would transfer its energy to the film to also initiate the phase transition. This experiment confirms the possibility that VO₂ films can be used to obtain information about the temperature behavior of certain regions.

To have good modulation depth, several factors have to be considered, first both light beams should have close to equal spot sizes on the sample. Also, the sample should be

biased at the proper point on the transmission vs. temperature curves so that the transmission has a great enough change upon laser heating. If the sample is biased near point A in Fig. 9, a larger change in temperature will be needed from laser heating. If the sample is biased at point C and if the temperature change upon heating with the laser is not large enough it will turn on but not be able to turn off once the heating beam is removed. For optimum performance, the sample should be biased at point D and enough heat due to absorption should be provided from the laser to cause the sample to reach point E on the curve.

It is interesting to observe that the heating caused by the $1.3 \mu\text{m}$ beam does not wash out. If the beams were nonoverlapped by as little as $100 \mu\text{m}$, the effect is not observed, regardless of how long the sample was heated. Thus the heat is very efficiently conducted away from the sample. This shows that great spatial control can be achieved in the amount of information transmitted through the VO_2 modulator. This may be due to the good thermal conductivity of the Ge substrate. Therefore close attention should be paid to the substrate material.

A transient switching experiment using $10.6 \mu\text{m}$ light was performed to find the temporal response of the film. Calculations were performed using formulas from the work of Kuster¹⁶ which showed that to heat VO_2 using $10.6 \mu\text{m}$ light required almost twice as much power or half as small a spot size of the focused heating beam when one includes the latent heat of the phase transition, and the losses at the lenses than what we have available. When we tried to do the experiment anyway using the VO_2 on a Ge substrate sample, we did not observe any phase transformation. The equations were correctly predicting that we did not have enough power in our beam. Therefore since we were unable to heat the film enough using a CO_2 laser, so we had to rely on heating of the film by conduction of heat from a substrate that could absorb more energy when heated by the laser. In this case the substrate was sapphire. This high power pulsed beam was obtained

from a Laser Sci. Inc., model PRF 1500W, TEA CO₂ laser and the Synrad laser provided the CW beam. Again the beams were focused on the sample and overlapped to approximately 200 mm spot sizes. The setup is shown in Fig. 10. Mercury Cadmium Telluride (MCT) detectors were used to pick up the fast signals. Fig. 11. demonstrates the successful switching response showing the incident beam from the TEA laser and the fast modulation of the reflected CW beam due to the fast response of the film and substrate. The transient switching experiment performed demonstrated the time of switching a continuous wave (CW) beam using a high power pulsed beam which heated a substrate that conducted its heat to the film was actually faster than the rise time of the pulses from our pulsed laser which was a few nanoseconds

One last effect observed in the lab was the creation of a superlattice of phases in the VO₂ film on the sapphire substrate. This was first observed by Valiev¹⁷ and explained¹⁸ as being due to the elastic stress field existing at the boundary between the newly formed phase and the preexisting phase. This stress is due to the changes in the bond lengths that occur during the phase transition. The stress fields prevent the newly formed domains from growing, but lower the transition temperature of nearby regions. Thus more and more regions transform but do not grow large and this feedback and control mechanism causes the material to exhibit a diffraction pattern in the transmitted light during the phase transition by creating several spots instead of just one. In the experiment we performed, the pulsed output from the TEA laser was focused on the sample and a diffraction pattern was observed. Due to a lack of time, no further analysis was performed.

FUTURE IDEAS

The phase transition that takes place in VO₂ provides many interesting possibilities for interesting device concepts. If two coherent light beams interfere at the VO₂ film, fringes will form through constructive and destructive interference. If there is enough energy in the laser beam to heat the sample and cause the phase transition to occur where

constructive interference occurs, stripes of mirrors can be written. Light that is incident on these stripes will reflect and the reflection will experience constructive and destructive interference creating a reflected interference pattern.

Another interesting step in the research of VO_2 is to place the VO_2 on a substrate that contains active IC's. Currently substrates for infrared applications of VO_2 include Si, GaAs, ZnSe, and Ge. These can be doped both n and p type. At the junction of n and p regions a depletion region is created which has resistance and thus creates heat. This should be investigated for its ability to cause the phase transition in VO_2 . Large integrated circuits can be created and covered with VO_2 . When different electrical contacts to the substrate are switched on and off using electrical signals, the VO_2 film covering it will have different regions transmitting or reflecting at different instances of time in a controlled fashion.

One final interesting concept is to coat with VO_2 the insides of microwave waveguide elements such as part of a stub tuner as shown in Fig. 12. Then when the element is heated by some method such as a noncontact method using a laser, the tuner will change its effective length because the inside surface will become metallic, and the behavior of the waveguide will change.

CONCLUSION

Thus from the experiments conducted we see that in the near and far infrared regions of the spectrum, VO_2 can perform as a limiter. It can also be used as a modulator to write information onto another light beam. Although further research is required these exponents demonstrated the potential of VO_2 films for use as a IRSIM device. In addition there are other interesting areas where further research should occur in the near future.

ACKNOWLEDGMENT

I would like to thank the people I worked with at Wright Laboratory Materials Directorate, my advisor Dr. Patrick Hood for the interesting topic and guidance, and Dr. Shekhar Guha, Dr. Paul Fleitz, and Dr. Hao Jiang for helpful discussions.

¹ M. F. Becker, B. Buckman, R. M. Walser, T. Lepine, P. Georges, and Alain Brun, *Appl. Phys. Lett.*, vol 65, p. 1507, 1994.

² H. Jerominek, F. Picard, and D. Vincent, *Optical Eng.*, vol 32, p. 2092, 1993.

³ A. S. Barker Jr., H. W. Verleur, and H. J. Guggenheim, *Phys. Rev. B*, vol 17, p. 1286, 1966.

⁴ H. Jerominek, F. Picard, and D. Vincent, *Optical Eng.*, vol 32, p. 2092, 1993.

⁵ A. A. Bugaev, B. P. Zakharchenya, and F. A. Chudnovskii, *Metal-Semiconductor Phase Transition and Its Application*, Nauka, Leningrad, 1979.

⁶ A. I. Gavrilyuk, T. G. Lanskaya, A. A. Mansurov, and F. A. Chudnovskii, *Sov. Phys. Solid State*, vol 26, p. 117, 1984.

⁷ E. I. Nikulin, F. A. Chudnovskii, E. B. Shadrin, and D. A. Myasnikov, *Sov. Phys. Tech. Phys.*, vol 33, p. 1473, 1988.

⁸ W. Paul, *Mat. Res. Bull.*, vol 5, p. 691, 1970.

⁹ J. B. Goodenough, *J. Solid State Chem.*, vol 3, p. 490, 1971.

¹⁰ P. Jin and S. Tanemura, *Jpn. J. Appl. Phys.*, vol 33, p. 1478, 1994.

¹¹ H. K. Kim, H. You, R. P. Chiarello, H. L. M. Chang, T. J. Zhang, and D. J. Lam, *Phys. Rev. B.*, vol 47, p. 12900, 1993.

¹² D. Paquet, P. Leroux-Hugon, *Phys. Rev. B.*, vol 22, p. 5284, 1980.

¹³ C. G. Granqvist, *Materials Science for Solar Energy Conversion Systems*, ed. C. G. Granqvist, Pergamon Press, Oxford, 1991, chap 5, p. 106.

¹⁴ A. A. Bugaev, V. V. Gudyalis, and A. V. Klochkov, *Sov. Phys. Solid State*, vol 26, p. 887, 1984.

¹⁵ P. J. Hood and J. F. DeNatale, *J. Appl. Phys.*, vol 70, p. 376, 1991.

¹⁶ H. Kuster and J. Ebert, *Proceedings of the Boulder Laser Damage Symposium*, p. 141, 1979.

¹⁷ K. A. Valiev, V. G. Mokerov, V. V. Saraikin, and A. G. Petrova, *Sov. Phys. Solid State*, vol 19, p. 1487, 1977.

¹⁸ V. I. Emal'Yanov and A. L. Semenov, *Sov. Phys. Solid State*, vol 32, p. 1790, 1990.

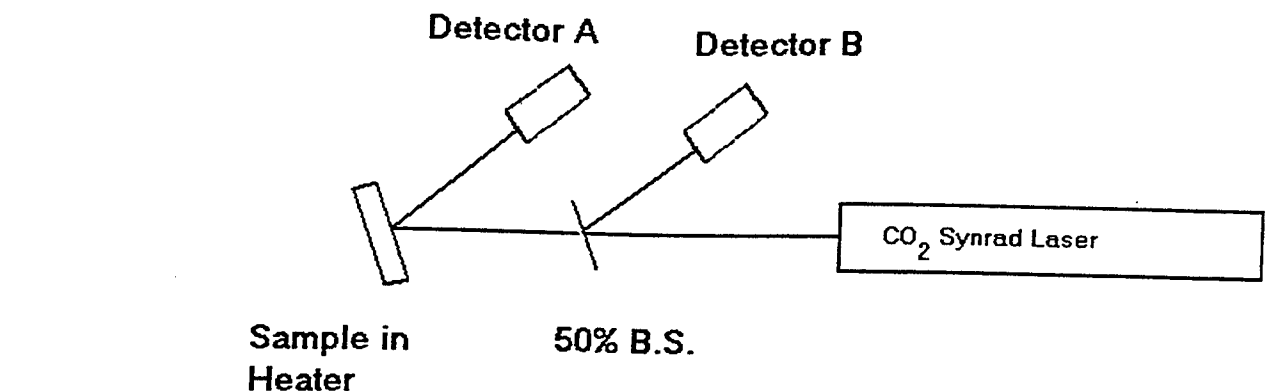


Fig. 1. Setup for reflectance vs. temperature plots.

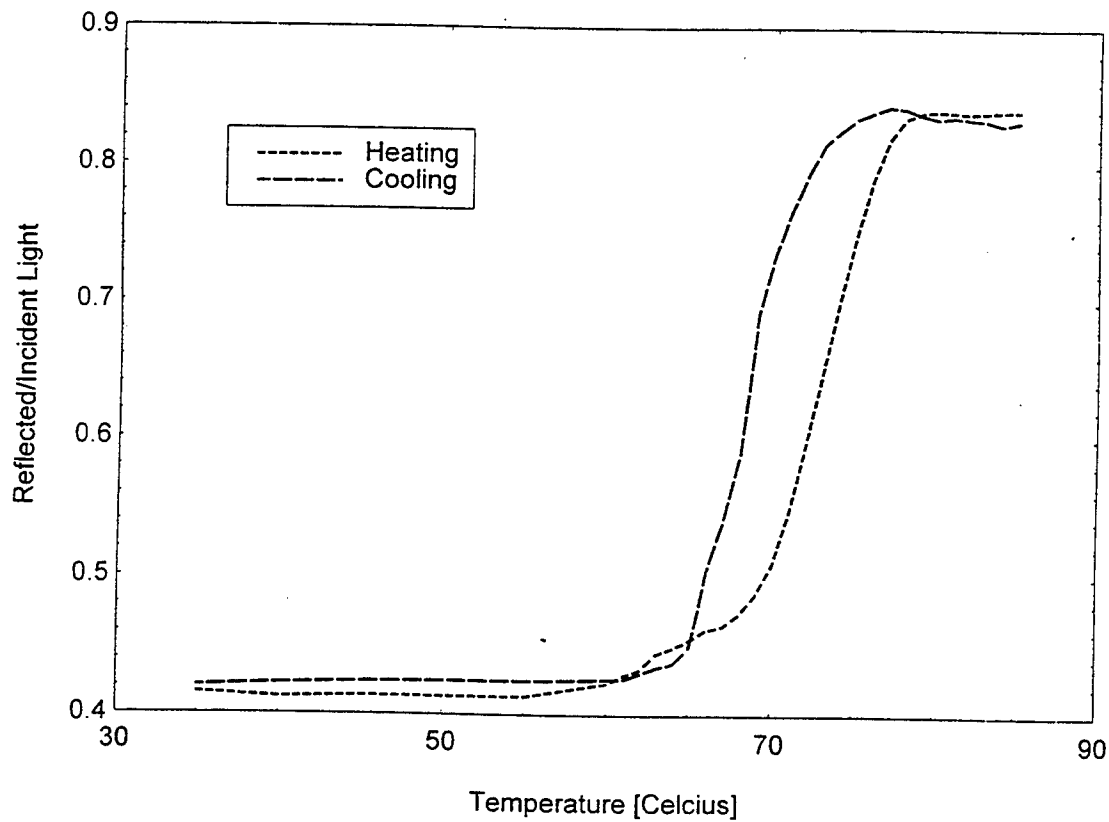


Fig. 2. Reflectance vs. temperature for VO₂ on a sapphire substrate.

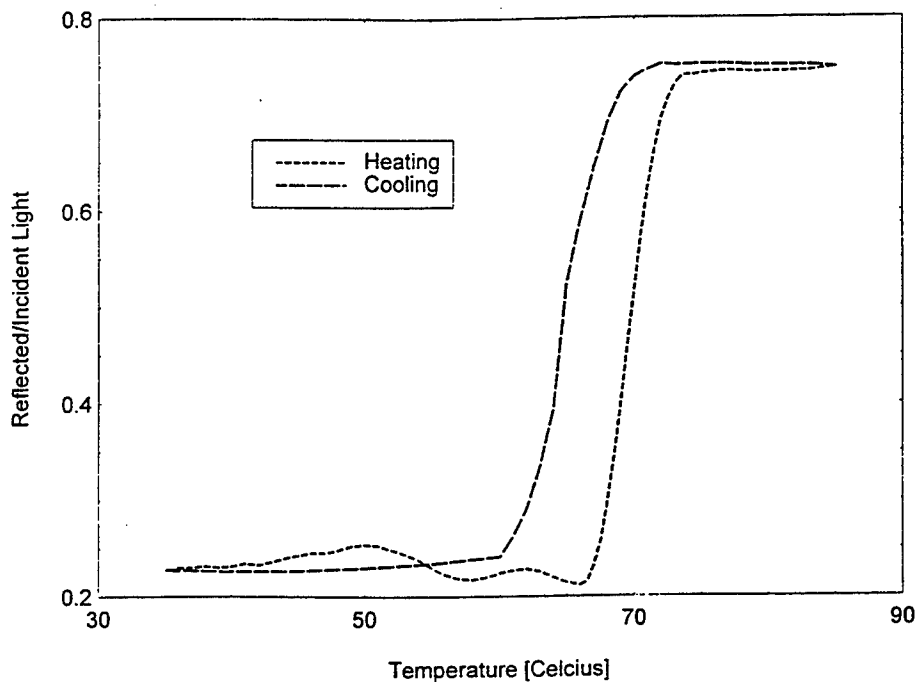


Fig. 3. Reflectance vs. temperature for VO_2 on a Ge substrate.

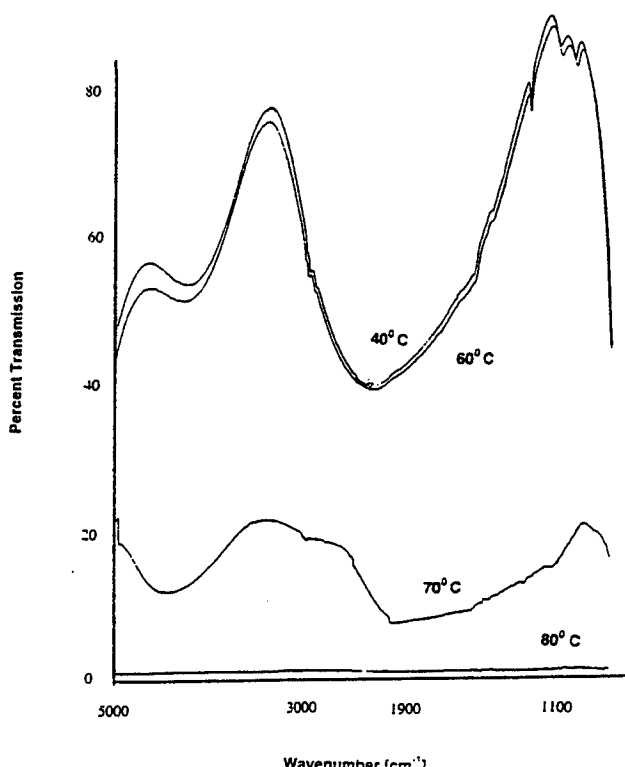


Fig. 4. Transmission spectra
for VO_2 on a Ge substrate
at different temperatures.

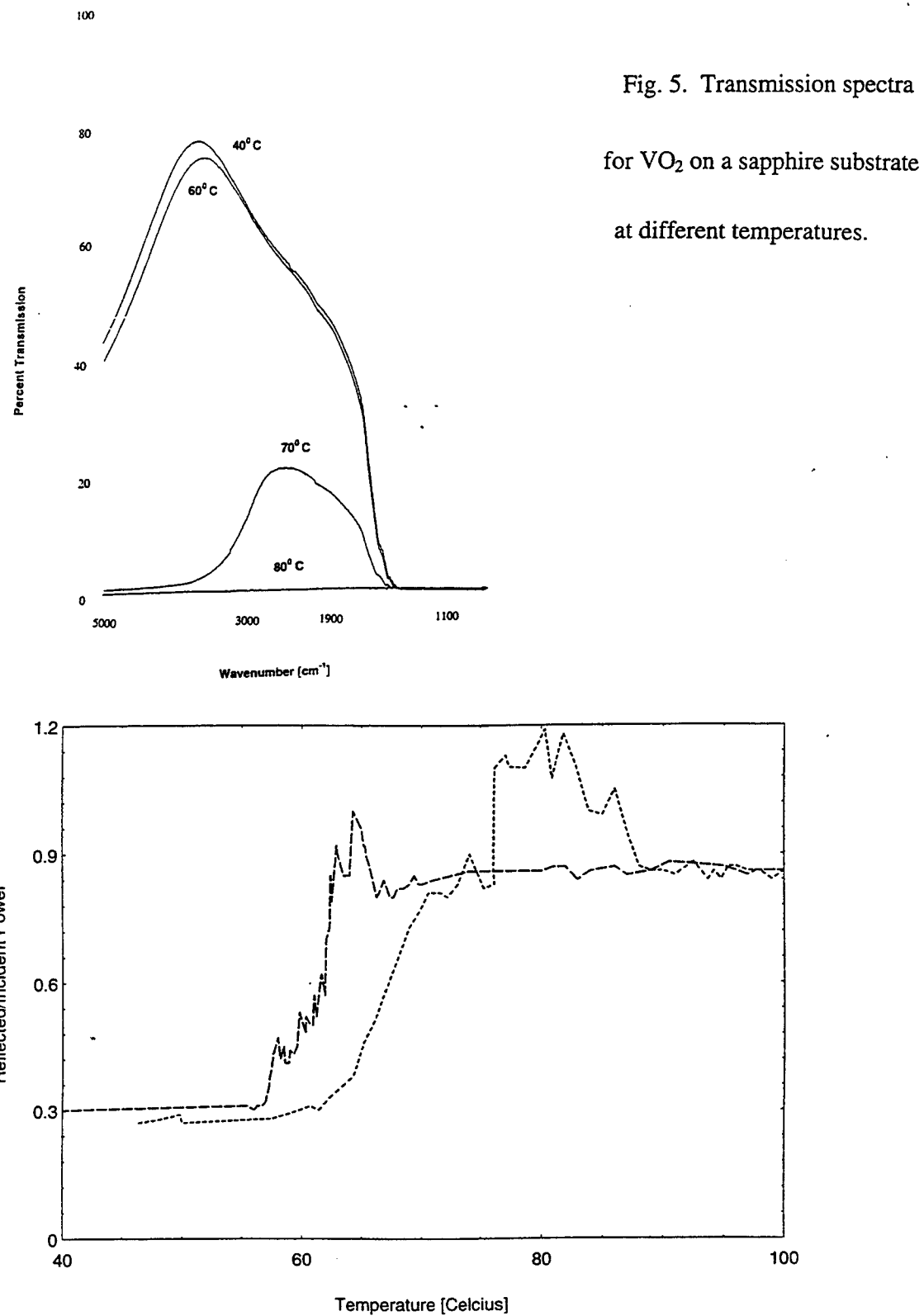


Fig. 5. Transmission spectra

for VO_2 on a sapphire substrate
at different temperatures.

Fig. 6. Reflectance vs. temperature for VO_2 on a sapphire substrate with heating from the heater and another laser beam.

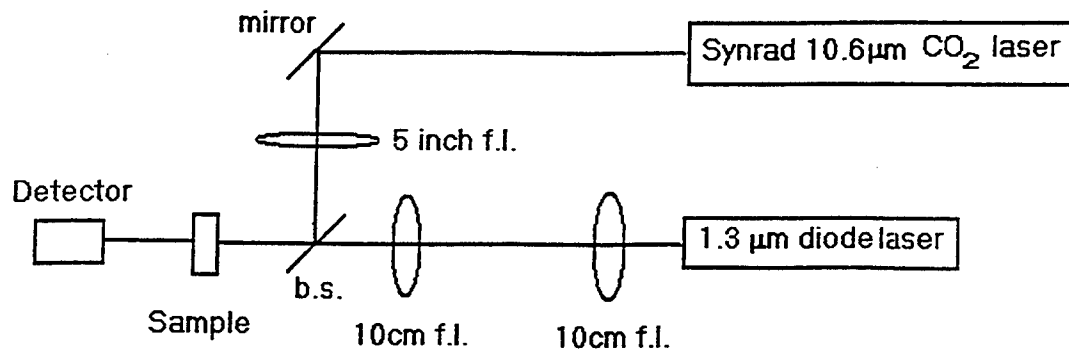


Fig. 7. Setup for light switching light experiment.

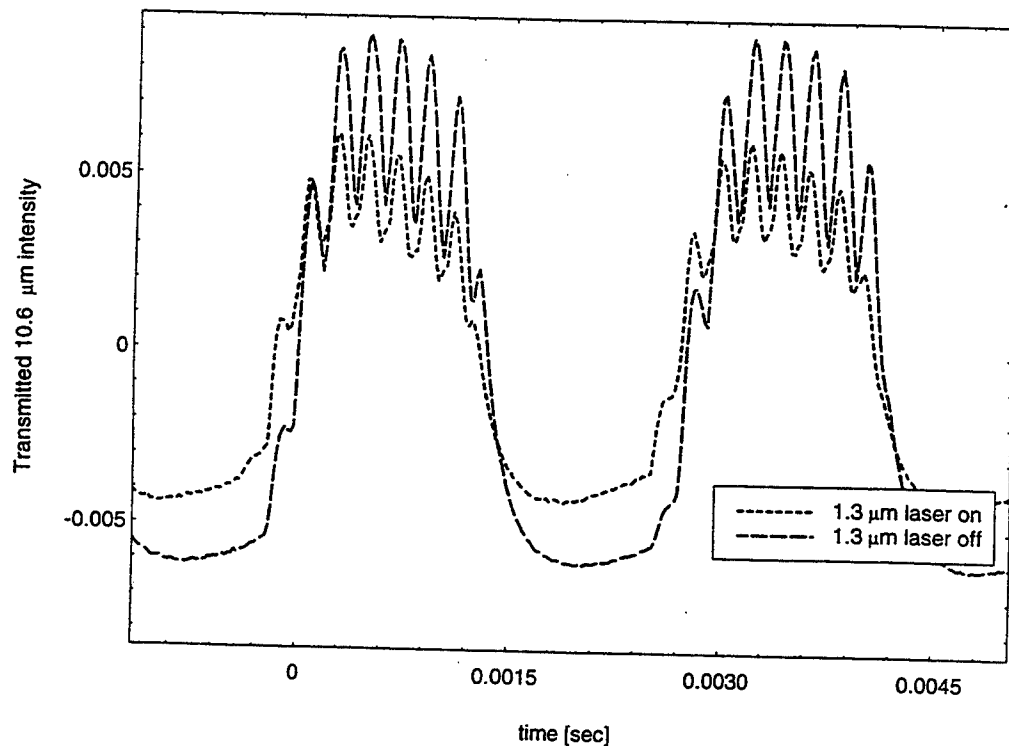


Fig. 8. Switched and unswitched waveforms showing one light beam's transmission is controlled by another.

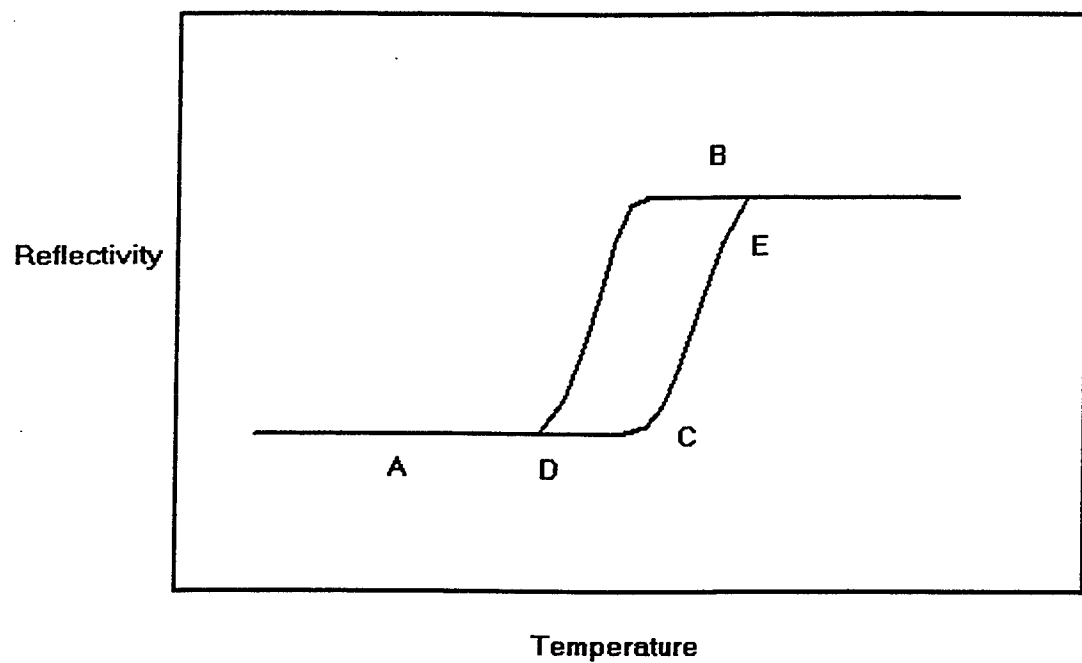


Fig. 9. Hysteresis curves to explain bias location and temperature ranges for ideal performance.

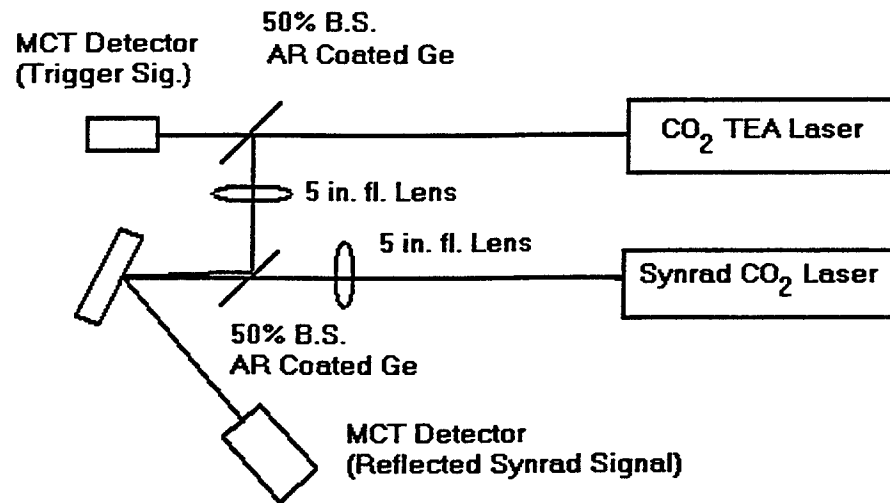


Fig. 10. Setup for transient switching experiment.

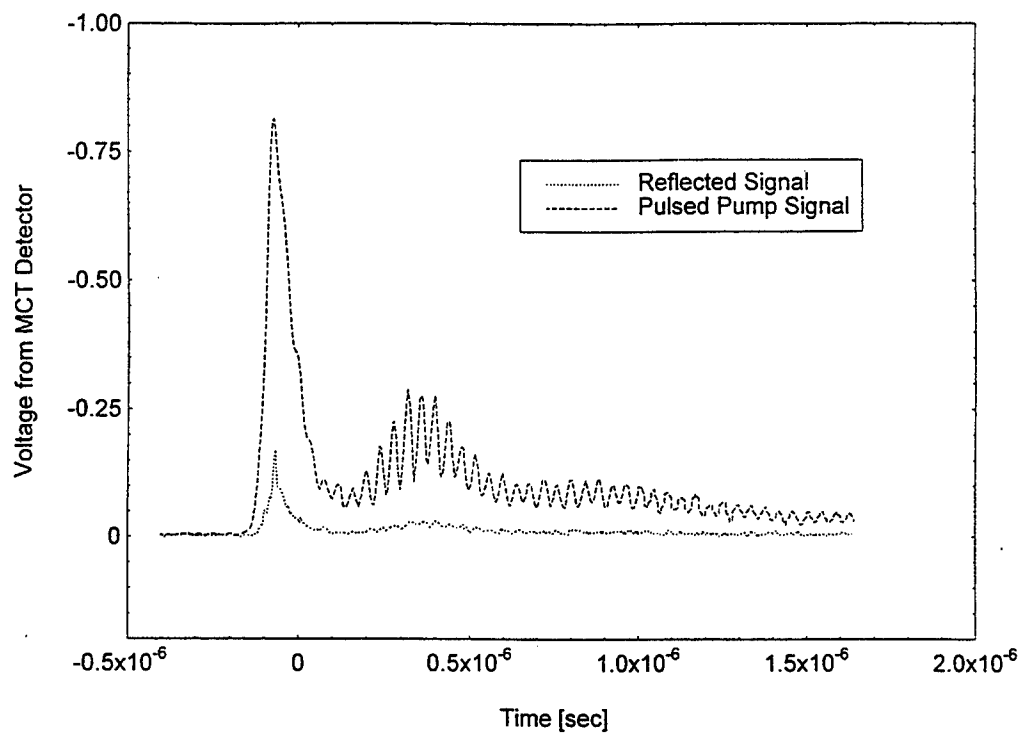


Fig. 11. Result from transient switching experiment.

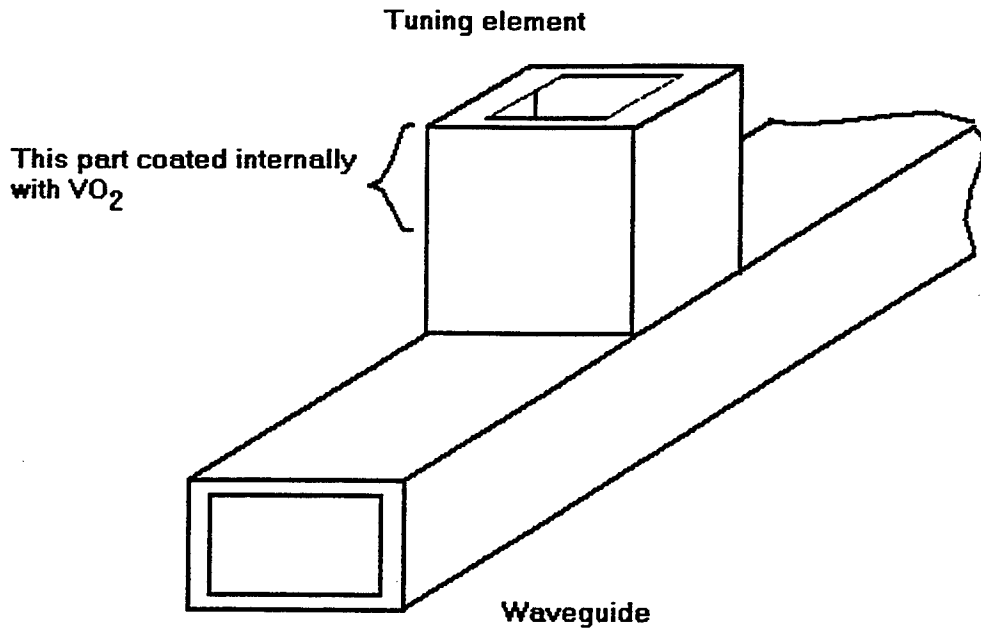


Fig. 12. Illustration of waveguide whose properties can be modified by the phase change in VO_2 .

**A GENERAL METHODOLOGY FOR CLUSTERING AND SEQUENCING
ALGORITHMS WITH APPLICATIONS TO INTELLIGENT KNOWLEDGE-BASED
MANUFACTURING/MACHINING SYSTEMS**

Edward A. Thompson, Doctoral Student

and

Georges A. Bécus, Associate Professor

Aerospace Engineering and Engineering Mechanics Department

University of Cincinnati
Cincinnati, OH 45221-0070

Final Report for:
Summer Faculty Research Program

and

Graduate Student Research Program
Wright Laboratory

Sponsored by:
Air Force Office of Scientific Research
Bolling Air Force Base, DC

and

Wright Laboratory
Wright-Patterson Air Force Base, OH

September 1995

**A GENERAL METHODOLOGY FOR CLUSTERING AND SEQUENCING ALGORITHMS
WITH APPLICATIONS TO INTELLIGENT KNOWLEDGE-BASED
MANUFACTURING/MACHINING SYSTEMS**

Georges A. Bécus and Edward A. Thompson

ABSTRACT

Product design and process planning have been separate activities. Even with the advent of computer aided design, CAD systems have been extensively used in the automation of product design, while process design or planning has remained a separate and primarily manual effort with little or no automation. Although there have been numerous efforts (e.g. group technology involving variant and generative techniques) and research in the area of product design and process planning integration, most research has addressed only a portion of the problem, i.e., either the product design or process planning. The integration of shape, function, material and process design is a goal which offers many challenges to overcome. After reviewing Adaptive Modeling Language (AML), an approach and implementation for integrating product and process design in a virtual manufacturing environment involving competing processes, this report presents a general methodology and general purpose algorithms for clustering and sequencing under (precedence) constraints. These algorithms could easily be integrated in AML or other Intelligent Knowledge-Based-Engineering systems to perform such tasks as setup generation/sequencing and feature/operation sequencing. The algorithms employ an Annealing Genetic strategy together with special purpose operators and repair functions as the optimization engine. Our approach, flexible enough to allow user interaction, finds very quickly (near) optimal solutions of higher quality than existing methods.

KEYWORDS: Intelligent Knowledge-Based Engineering, Adaptive Modeling Language, Process Planning, Operation-Based Design, Machining, Clustering, Sequencing, Annealing Genetic Algorithm.

INTRODUCTION

Today enterprises have to compete in an ever changing global market environment which requires fast appropriate decisions. Process costs and product affordability, which form the basis for competing in the marketplace, are often adversely affected by customer demands dictating quick response and imposing continual changes to the product development cycle thereby lengthening development time. Investigating new materials and processes to lower costs while enhancing product performance is a goal pursued by every manufacturer.

The standard approach to product and process design is the *specify-evaluate-revise* cycle which often involves time-consuming loops. The engineering of a product incorporates numerous stages involving design specification, manufacturing planning, finite element modeling and analysis, and inspection planning. Changes to the design (dimension, tolerance, material, process constraints, etc.) as well as rework procedures (especially costly if revisions are suggested late in the cycle) cause delays in the final production and market deployment. Often, this cycle generates new ideas or product technology. Alternative materials and processes discovered in this stage are tested in an attempt to enhance product functionality and reduce processing costs. Alternative materials and processes benefit new designs but can also affect the design of retrofit parts for maintaining/refurbishing existing systems as in the design and production of aircraft components (either the re-manufacture of parts for maintaining existing aircraft or new parts designed to replace existing ones). There is an opportunity for the inclusion of past knowledge in new designs to explore alternative materials and processes outside the lengthy *specify-evaluate-revise* cycle.

Developing a methodology to handle changes dynamically and to minimize the design cycle could lead to major savings in the product development cycle and thereby benefit product affordability. Such methodology will enable the investigation of alternative materials and processes to lower the production cost and enhance product performance. This methodology will be applied across all steps in the production process and will form the basis for the development of an Intelligent Knowledge-Based-Engineering (IKBE) system for integrating feature-based, memory-driven design, with material specification, manufacturing/inspection process planning, adaptive meshing, and finite element modeling/analysis.

Because nearly all products require some machining, the benchmark process for current efforts in integrating product and process design is machining. Machining, the most common form of material removal, is often an alternative to other processes when dealing with small quantities of parts for structural applications. In addition to functional specifications and geometric shape, process planning of machined parts requires the preparation of an outline describing all machining setups, fixtures, detailed machining operations, tooling, machining data and finally the NC part program to cut the part [1]. For small lot sizes (1-25 parts), the design and process planning steps account for a large percentage of the overall production time so that an integrated system for concurrent design and automated process planning generation will significantly improve productivity, shorten the design to fabrication cycle and lower processing costs. The system should enable the user to interactively design and plan the machining process to cut the part.

The development of an IKBE system integrating automated process plan generation in a feature-based design environment requires solving a number of problems related to setup generation, feature sequencing, fixturing, tooling, tool path logic, and machining parameter computation [2,3]. There are a number of design automation systems for cutting single features. But these systems generally are not geometry driven and often merely provide a

process plan for a limited number of prismatic shapes by generating the machining operation sequence for a single feature [1] or irrespective of feature interaction. The user input is by feature type limiting these systems to a prescribed library of features without any assistance regarding unique setup generation, fixturing, or any other process planning criteria [4]. Such systems, based on the variant approach of comparing, retrieving, and modifying similar pre-stored process plans, are limited to pre-stored patterns and do not offer a suitable solution for integrating product design and process planning.

Other attempts at automating process planning for machining are limited to simple geometry. The machining features are extracted from a computer aided design (CAD) system using a feature recognition methodology, often limited to a set of machining features with simple orientations and attachments [4-12]. Such systems do not offer an integrated solution for design and process planning, because the part design and modifications are done independently on a CAD system.

Computer Integrated Manufacturing (CIM) systems, oriented towards automating tool path generation from the part geometry created by a CAD system, produce a primitive cutting plan by mapping the tool path to follow the contour of a surface. Although they may handle complex surfaces, these systems offer little or no assistance in the selection of the tooling and machining specifications such as speed, feed and depth of cut and they rely heavily on user interactions for isolating and sequencing the surfaces to be cut. This complicates the process plan generation and tool path logic of even simple parts [13].

In contrast, the developing IKBE architecture supports a concurrent engineering system for interactive design and process planning of machined parts for rapid production. The process plan incorporates the selection of setups, their sequence, fixturing recommendations, tooling, and all the machining data for cutting the part, reflecting the part geometry, the part material characteristics, and the machine selection. In addition, the user can interactively inquire about the production plan to view the effect of the part design and characteristic modifications. The system automatically validates the changes and reconfigures the process plan reflecting the user modifications. The IKBE system supports a sophisticated feature-based design environment, enabling the user to interactively design parts with complex geometry. Form features are basically macro level descriptions of fundamental shape features (hole and profile) with position and dimensional constraints that enable the transfer of a part model without transferring the geometric instance. Most CAD systems are complemented by a Feature Based Design Environment (FBDE) providing advanced tools for interactive feature dimensioning, positioning, and orientation specifications. A free-form feature-based capability allows the user to create and customize a suitable design feature library independent of manufacturing features. Finally, the system supports a geometric reasoning algorithm to assist in feature interpretation and instantiation. Whereas previous systems [13] tend to rely heavily on user specifications to guide tool selection, machining parameters computation, and generation of the tool path, the IKBE architecture has the capability to compete alternative part geometry with optimal material selection and process design.

There are two basic approaches for automated process planning: the variant approach and the generative approach [1]. Variant process planning is based on the retrieval and modification of a stored process plan for a similar part. The parts are grouped into classes and standard plans are stored for each class. This approach is useful only when all parts being designed can be classified in a number of categories depending on certain attributes. The process plan of a particular part is generated by identifying the part class, retrieving the plan, and modifying it to fit the new part attributes. Some systems using this approach are CAPPTM, MILTURNTM and MULTIPLANTM.

Generative process planning systems compose a new plan for each part. A generative process plan is synthesized based on information about the part, the machines, tooling fixturing, and certain process planning rules. There are no process plans pre-stored in a data base. The generative approach tends to be more flexible but also more complex so that these systems are not fully automated but tend to rely on human interaction to provide applicable process and material constraints. Several generative process planning systems have been developed such as APPSTM, CPPPTM, XPSSTM, AUTOPLANTM, SURFCAMTM, AdlardTM, GENPLANTM and AUTAPTM.

Of the various recent process planning systems for machining we mention SIPSTM, a feature-by-feature process design system being integrated with the National Institute of Science and Technology's Automated Manufacturing Research Facility. CUTTECHTM, another feature-by-feature system, orders machining operations and chooses tools together with cutting depths, speeds, and feeds on the basis of feature geometry and material machinability data. XCUTTM, a research system similar to SIPSTM, accommodates collective process plans for parts that have a one-sided geometry while decomposing features into separate cuts which use geometry and tolerance information to choose tools.

The integrated process planner reviewed in the next section focuses on more comprehensive process design, i.e., planning at a higher level of set-up organization compared to other systems which are typically limited to one set-up or non-interacting feature-by-feature process plans.

ADAPTIVE MODELING LANGUAGE (AML)

As stated earlier, process design involves several activities that are typically done manually with little or no automation, while CAD and other feature-based design systems enable the user to interactively design and edit part geometry. An integrated feature-based Adaptive Modeling Language (AMLTM) automating the manufacturing, inspection, and analysis of custom parts using Knowledge-Based Engineering methods has recently been developed and implemented. Critical functionalities of AMLTM include a parametric FBDE, a mixed dimensional solid/surface modeler supporting non-manifold topology, and a geometrical reasoning kernel for multi-axis machining and inspection and process planning automation. The system is oriented toward enabling significant reductions in the machining cost and time to produce small quantities of structural components, i.e., automating the breadth and diversity of components typically associated with a small (fewer than 50 employees) job shop.

The AML™ process planner is a generative planner and is oriented toward addressing the above described needs of a typical job shop to enable rapid prototyping and production. AML™ not only enables automated process planning but allows the designer to change or create new parts through the evaluation of alternative process plans. AML™ is based on a single underlying object-oriented architecture incorporating two patented techniques for competing alternative design/material/process constraints. While an engineer is designing the part, AML™ generates the process plan interacting with the system to inquire about alternative materials, processes, and design specifications. Complex part designs with detailed process plans and analysis models will be concurrently developed in hours or days instead of weeks or months. The functionalities of the AML relevant to our work are summarized in the following subsections.

Part Design and Geometry, Feature Instantiation and Interpretation

The FBDE is a parametric, free-form, constraint driven, three dimensional mixed modeling design environment with an icon-based graphic window interface enabling the user to easily create, edit, and modify the part geometry. The system allows the user to create a free-form feature and parametrically associate its dimensions and orientation with other features. AML™ can reason about complex 3D geometry including multiple intersecting features such as a pocket involving edge profiles blended with a number of bosses. Unlike existing systems, AML™ is not limited to features from a library but enables the user to create and customize a feature library suitable to his/her needs. To create a feature, such as a generic 'wall-profiled' pocket, the user begins by creating a 2D profile feature which defines the pocket base, and selects a feature base-point. AML™ provides a number of alternative methods to assist in the creation of the profile and offers a number of tools to assist the user in the interactive selection of the points and vectors. When the designer uses a feature-based part model to describe part geometry, feature interactions could result in a number of different interpretations or valid aggregate feature geometries. The AML™ geometric reasoning engine enables the user to create a surface attachment constraint to limit the feature instance to only one of these interpretations or when several interpretations of the input specification exist, assists the user in the specification of the selection

Process planning

The part model (geometry) generated by the FBDE is basically a description of the part geometry in terms of the starting geometry (stock) and "design features" with their associated dimensions, tolerances and orientations. An equivalent manufacturing part model is required to account for the different (manufacturing) interpretations of the same part geometry (design). Extracting the necessary manufacturing information from the part geometric description is required to produce the process plan. Therefore a manufacturing part model, depicting the part before and after each setup in terms of the manufacturing features and the associated geometry, is generated. Each design feature is mapped into one or several manufacturing features which may be later refined and reclassified depending upon the selected setup and part orientation. A manufacturing feature is represented by a number of

machining operations satisfying the part geometric description including surface finish and tolerances. A successful automated machining process planner, integrated with a FBDE requires the solution to several fundamental problems related to features translation, intersection and sequencing, setup generation and sequencing, and 'part-stock' fixturing. The automated process planner generates a machining process plan with the following details and specifications:

1. the number of setups required to machine a part,
2. the sequence of the setups,
3. the features within each setup and their sequence,
4. the part geometry before and after each setup,
5. the intermediate part geometry after removing each feature within a setup,
6. the detailed machining operations for machining each feature (including cutting dimension, speeds, feeds, horsepower, material removal rate, etc.),
7. the tooling for each operation including alternatives,
8. the feasible sequence for the machining operations for the different features within the same setup, and
9. the recommended part orientation, and valid surfaces for contact with the fixtures.

The first problem addressed in automating the process design is to cluster the features into a number of sequenced setups and determine the appropriate fixtures to be used. A setup establishes the number of features which can be machined while the part is held within the same fixture. Grouping the features to generate the minimum number of setups while minimizing the number of operations associated with machining one setup before another requires careful visualization and analysis as the number of permutations grow exponentially with the number of features. Some features may belong to more than one setup, thus features are initially grouped into potential setups that will be later refined to minimize the overall time required to machine the part.

A manufacturing feature is comprised of a set of machining operations, related to milling and holemaking constrained by part geometry. These constraints involve conditions before and after successive machining operation and are related to the tool access, the part geometry (open-pocket vs. closed-pocket), and machining capabilities (coolant available), etc. Depending on the bounding surfaces, part-stock dimensions, and other characteristics, a feature to be machined is translated into one or more manufacturing features, each representing a number of machining operations. A number of surface and vector objects are created relative to intersections with other features and the part-stock and associated with feature type, dimensions, tolerances and orientation. These objects constrain the range of tool approach directions relative to non-interference access and orientation of tooling in addition to any required safety or preparatory operations such as drilling highly toleranced corner 'cut-in' surfaces. These additional manufacturing features must also be included in setup generation. The manufacturing part model is basically an enhanced object structure representation in terms of the machining

features. The machining operation sequence for each manufacturing feature is generated as constrained by both feature dimensions and tolerances and material machining resources.

Process Optimization - Setups

A part typically consists of several features and grouping the features into a minimum number of setups with appropriate fixtures is a difficult task. The following steps are taken to generate a minimum number of setups from the part geometry: (i) Features Translation, (ii) Potential Setups Generation, (iii) Elimination of the Redundant Setups and (iv) Setup Optimization. The setups that now remain have no common features and, as a consequence, the process plan has been globally optimized for the minimum number of setups. Further optimization can be achieved by sequencing features and operations and by eliminating intersection overlap among features.

Automated Operation Sequencing

Depending on the complexity of the feature, tolerances, material, and desired finish, up to twenty machining operations may be required to machine a feature. Features belonging to the same setup may use the same tools, but in different order. For example, feature 1 may require the use of dls-200 (a drilling tool) before the use of dls-100 (a different drilling tool), while feature 2 may require the use of dls-100 before the use of dls-200. The goal is to provide the machinist with a 'near' optimal operation sequence, taking into account the following criteria: maintaining tool dependency (for a feature), minimizing tool changes, and minimizing tool travel, thereby guaranteeing a high quality part at the lowest possible cost. AML™ uses a Genetic Algorithm to achieve this goal. The problem, a set of operations required to machine the setup, is read from an input file (see illustrative example section below for an example and typical results). The goal is to perform operation sequencing across features. The machinist is provided with a near-optimal solution. The output does not violate any of the dependency constraints and at the same time minimizes tool changes and tool travel. A globally optimal solution cannot be guaranteed.

Process Optimization - Fixturing and Features

The process plan requires the identification of fixturing surfaces, based upon the type of fixture, for holding the part while allowing machine/tool access to cut the features. The inputs to this module are: (i) the starting part-stock, (ii) the features within the setup, and (iii) the tool orientations and feed directions. Depending on the selected fixturing method, such as a vice, certain criteria are used to identify the best fixturing surfaces. AML™ uses an algorithm to analyze the part surfaces before and after the setups. The objective of the analysis is to determine a feasible, yet least time consuming fixturing method to reduce overall processing time and costs.

Within each fixtured setup a preliminary sequence of machining operations is generated for all intersecting features and subsequently adapted to include sequencing of non-intersecting features for optimization of processing

within a setup. Although not immediately apparent, the number and dimensions of the manufacturing features can be different from the associated design features. AML™ uses a patented technique to optimize the machining process by evaluating dimensions and associated machining parameters for all manufacturing features as they are recomputed based on the selected sequence for processing the design features. These machining parameters include: thin wall conditions, thin floor conditions, and tool clearance (axial and radial).

A GENERAL METHODOLOGY FOR CLUSTERING AND SEQUENCING

It should be clear from the above brief review of the salient capabilities of AML™ that clustering or grouping (e.g. of operations into features or of features into setups) and sequencing (e.g. of setups or of operations within a feature or setup) are two tasks which have to be done at different times and at different levels in an IKBE system. The development of efficient, general purpose algorithms to carry out these tasks formed the focus of our research effort for the SFRP/GSRP. The multifaceted methodology we adopted in the solution of these two problems makes, we believe, our approach and our algorithms quite novel and general. Our methodology is detailed in this section.

First, our approach is operation- based, not feature or setup based. Indeed, once geometric features to be machined have been translated into manufacturing features, each comprised of a set of machining operations related to milling and holemaking and constrained by part geometry, a part to be machined can be reduced to a list of machining operations. These are the basic (i.e. lowest level) machining elements which need to be clustered and sequenced both into setups and within setups. This operation-based approach allows for the clustering of operations across features so that operations associated with the same feature could conceivably be done in different setups.

Second, the two tasks of clustering and sequencing in our approach are not treated separately. They are carried out simultaneously. This stems from the realization that clustering and sequencing are essentially the same problem. To see this more clearly we need to distinguish between two kinds of clustering: (1) hard or rule-based and (2) soft or metric-based. Hard clustering is based on a set of (universally) accepted rules (e.g. all operations requiring the same tool are grouped together) and can be implemented with simple logic (if-then, while loops, etc.). Soft clustering, on the other hand, is based on a metric or function which assigns a value to regrouping operations. In the first instance (hard clustering) the clustering is treated as constraints in the sequencing task, i.e. only sequences which do not violate the rule-based clustering are feasible. In the second instance (soft clustering), the clustering metric can be combined with the sequencing metric and the now combined clustering and sequencing problems are solved as one. In this case, the cluster metric is essentially a penalty (or reward) function added to the sequencing cost function. Note that this approach also allows for the simultaneous handling of hard and soft clustering with sequencing by having both clustering constraints (for hard clustering) and clustering penalty/reward (for soft clustering).

A third, unique aspect of our approach is the way in which we handle constraints. These constraints are primarily, but not restricted to, precedence constraints reflecting the order in which operations have to be machined. Here again we can distinguish between hard and soft constraints. Hard constraints, based on a set of (universally) accepted rules (for example: to machine a pocket in a hard material, a machinist has to center drill, drill, rough mill and finish mill) are handled as constraints in the sequencing problem through the introduction of a dependency matrix (see next section). Thus, only sequences which do not violate the rule-based hard constraints are feasible. Soft constraints which express preferences rather than rules can be handled via a penalty/reward approach. Here again the approach allows for the simultaneous handling of hard and soft constraints and sequencing. Note also that clustering is in effect a particular type of constraint. Note further that our treatment of hard clustering and hard constraints makes our approach resource-based. Indeed, many hard clustering rules and hard constraints are the reflection of the resources available to machine the part.

Finally, in order to ensure high quality rapid solutions, the optimization engine selected for our approach is the Annealing Genetic Algorithm as described in [14] and reviewed in the next section.

GENERAL PURPOSE ALGORITHMS FOR CLUSTERING AND SEQUENCING

The approach described in the previous section was implemented in a general purpose algorithm carrying out clustering and sequencing under constraints. Although the algorithm was only tested for operation clustering and sequencing within one setup, we believe it will work equally well for setup generation (clustering of operations into setups) and sequencing once appropriate sets of rules and fitness functions for that problem have been generated. Details of this implementation are now provided.

Annealing-Genetic Algorithm

A hybrid simulated annealing/genetic algorithm called the Annealing-Genetic (AG) algorithm is used as the optimization engine to solve the NP-hard clustering and sequencing problems. The AG algorithm was developed by Lin, Kao, and Hsu [14] to meet the following efficiency goals: (1) the algorithm should converge on a solution which is less than 3% away from the global optimum and (2) the computation time should be bounded by a polynomial function of the problem size. The authors show that the time complexity of the algorithm is empirically $O(n^2)$ for the multiconstraint zero-one knapsack, set partitioning, and traveling salesman problems. The AG algorithm is presented in Table 1 and discussed below.

The AG algorithm, as seen in the block diagram of Figure 1, may be viewed as a genetic algorithm with a Boltzman-type selection operator. An initial quasi population is randomly generated. The genetic operators are then applied to the initial quasi population producing the initial population. After computing the fitness and cost of each member in the initial population, the simulated annealing stage of the algorithm is performed.

Table 1. The Annealing-Genetic Algorithm.

```

1. Initialize the parameters, i.e., population_size,  $T_0$ , and  $\alpha$  ( $0 < \alpha < 1$ );
2. Randomly generate population  $P_0'$ ;
3. Apply genetic operators to  $P_0'$  to create  $P_0$ ;
4. Calculate the fitness and the cost for each point in  $P_0$  (a point is a member of the population);
5. Calculate the average_cost of  $P_0$ ;
6. solution_vector := current_point := the lowest cost point in  $P_0$ ;
7.  $k := 0$ ;
8. while system is not frozen do
9.   no_of_point := 0;
10.  while no_of_point <= population_size do
11.    Generate next_point from current_point by the move generation strategy;
12.     $\Delta C :=$  cost of next_point - cost of current_point;
13.     $Pr := \min[1, \exp(-\Delta C/T_k)]$ ;
14.    if  $Pr > \text{random}[0,1]$  then put next_point into  $P_{k+1}'$ ;
15.    current_point := next_point;
16.    no_of_point := no_of_point + 1;
17.    else pick another point from  $P_k$  as current_point;
18. endwhile
19. Apply the genetic operators to  $P_{k+1}'$  to create  $P_{k+1}$ ;
20. Calculate the fitness and the cost for each point in  $P_{k+1}$ ;
21. Calculate the average_cost of  $P_{k+1}$ ;
22. if the lowest cost point in  $P_{k+1}$  < solution_vector then update solution_vector;
23. if it is the initial stage then determine the initial temperature  $T_1$ ;
24.    $T_1 := (\text{the highest cost} - \text{the lowest cost}) / (\text{population_size}/2)$ ;
25. else  $T_{k+1} := T_k \times \alpha$ ;
26. current_point := the lowest cost point in  $P_{k+1}$ ;
27.  $k := k + 1$ ;
28. if frozen condition is signaled then set system is frozen;
29. endwhile
30. Print out the solution-vector as the final solution;

```

Starting with the best fit member in the initial population, a new member is generated by the move generation strategy. This new member is either placed in a new quasi population or discarded according to some probability,. If kept, the move generation strategy is applied to it to obtain another new member. If the new member is discarded, another member is selected from the initial population based on its fitness. This procedure is repeated until the quasi population is filled. The annealing temperature is then decremented and the genetic operators are applied to the quasi population producing the next generation. The process continues until one of several stopping criteria is met.

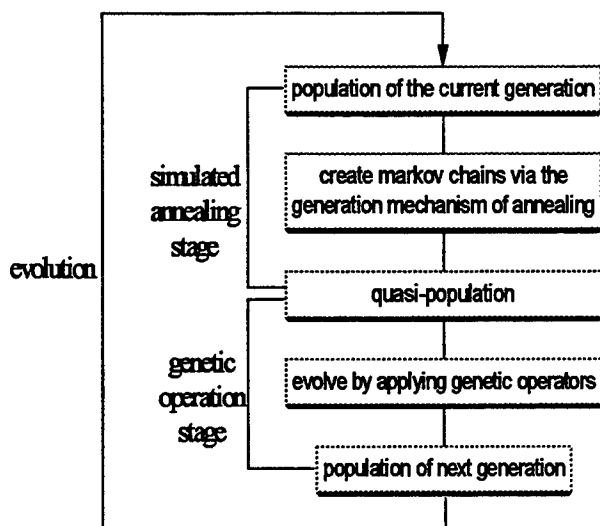


Figure 1. Block Diagram of AG Algorithm

Stopping Criteria/Frozen Condition

There are three separate stopping criterion which signal the frozen condition and stop the algorithm. These are as follows: (1) the maximum number of evolutions has been reached, (2) 80% of the population in a given generation has the same cost as the solution vector, and (3) the temperature in the simulated annealing stage has reached a minimum value. Each of these stopping criteria may be adjusted to yield the desired performance of the AG algorithm. The predetermined values for each of the stopping criterion may also be altered to produce the desired quality of the solution vector.

Genetic Operation Stage

The genetic operators implemented in the AG algorithm modify the members in the quasi population to create a new population. These operators also help to ensure that the average cost of the new population is less than that of the old one (provided the goal is minimization of a cost function). Although other operators such as edge recombination [15] and a newly developed 'forward' edge recombination were implemented, there were no noticeable improvements over the original crossover, inversion, and mutation operators. These three genetic operators are performed in the following steps.

- Step 1. Two parents are selected from the quasi population based on their fitness. The crossover operator is applied to these parents producing two offspring. If the offspring have costs less than the average cost of the old generation, they are placed in the new generation. Otherwise, the parents continue the following steps.
- Step 2. The inversion operator is applied to the two parents reordering their own sequence to produce two offspring. If the offspring have costs less than the average cost of the old generation, they are placed in the new generation. Otherwise, the parents continue to the next step.
- Step 3. The mutation operator is applied to the parents based on a predetermined probability. Finally, the parents are copied to the new generation.
- Step 4. Steps 1-3 are repeated until the new generation is filled.

Crossover Operator

Because the solution representation of the problem is not a simple binary string, a special crossover operator is needed to ensure that the bits in a genetic code are not repeated. In the operations sequencing problem, the machinist does not want to perform the same operation twice. In the traveling salesman problem, the salesperson does not want to visit the same city more than once. The crossover algorithm given in [14] is reproduced below as well as an example of its implementation. The example is a solution tour of a 10-city traveling salesman problem.

- Step 1. Select two parents, Parent1 [1:n] and Parent2 [1:n], from the population based on their fitness values. Initially, Child1 [1:n] := Child2 [1:n] := 0.
- Step 2. Randomly draw two indices p1 and p2 to serve as the crossover points. Then, Child1 [p1:p2] := Parent1 [p1:p2] and Child2 [p1:p2] := Parent2 [p1:p2].

Step 3. Initialize two matching vectors and then set their corresponding indices. That is, $\text{Mating1}[1:n] := \text{Mating2}[1:n] := 0$. Let $\text{Mating1}[\text{Parent1}[p1:p2]] := \text{Parent2}[p1:p2]$ and $\text{Mating2}[\text{Parent2}[p1:p2]] := \text{Parent1}[p1:p2]$.

Step 4. For each $\text{Child1}[i] = 0, 1 \leq i \leq n$, perform the following steps:

```

k := Parent2[i];
while (Mating1[k] != 0)
    k := Mating1[k];
    Child1[i] := k;
endwhile

```

Step 5. For each $\text{Child2}[i] = 0, 1 \leq i \leq n$, perform the following steps:

```

k := Parent1[i];
while (Mating2[k] != 0)
    k := Mating2[k];
    Child2[i] := k;
endwhile

```

Figure 2 below shows an example of the crossover operation.

Step 1	Parent1	= [9 4 1 3 10 6 8 5 7 2]	Parent2	= [8 2 10 6 7 4 3 1 5 9]
	Child1	= [0 0 0 0 0 0 0 0 0 0]	Child2	= [0 0 0 0 0 0 0 0 0 0]
Step 2 p1 = 3, p2 = 8				
	Parent1	= [9 4 1 3 10 6 8 5 7 2]	Parent2	= [8 2 10 6 7 4 3 1 5 9]
	Child1	= [# # 1 3 10 6 8 5 7 2]	Child2	= [# # 10 6 7 4 3 1 # #]
Step 3 Mating1 = [10 0 6 0 1 4 0 3 0 7] Mating2 = [5 0 8 6 0 3 10 0 0 1]				
Step 4 Child1 = [4 2 1 3 10 6 8 5 7 9] Child2 = [9 8 10 6 7 4 3 1 5 2]				

Figure 2. An example of a 10-city traveling salesman tour crossover operation.

Inversion Operator/Move Generation Strategy

The inversion operator and the move generation strategy are identical in the AG algorithm. The inversion operator used in the AG algorithm is a swapping move strategy called the random 2-exchange. Two points in the parent solution vector are randomly selected and the order of the elements between them is inverted. For example,

Parent = [1 2 3 4 5 6 7 8 9 10] p1 = 4, p2 = 9 (chosen randomly)
Child = [1 2 3 | 9 8 7 6 5 4 | 10].

Instead of implementing the random 2-exchange inversion illustrated above for the move generation strategy in the simulated annealing stage of the AG algorithm, other operators such as crossover, edge recombination, and ‘forward’ edge recombination were attempted. We believed that a ‘forward’ edge recombination operator (in which forward edges have a higher probability of being selected) would help preserve the satisfaction of precedence constraints. Unfortunately, this operator was not destructive enough to prevent premature convergence of the algorithm. Since no great advantages were observed, the original inversion operator of [14] (the random 2-exchange shown above) was retained for this problem.

Mutation Operator

The mutation operator is only applied according to some very small predetermined probability, usually set close to one percent. When mutation is invoked, two points in a parent solution vector are selected at random and exchanged. The result is a mutated child. For example,

Parent = [1 2 3 4 5 6 7 8 9 10] p1 = 2, p2 = 8 (chosen randomly)
Child = [1 8 3 4 5 6 7 2 9 10].

Dependency Constraints

Depending on the material and the feature type (shape), certain operations have to be performed in order. For example, to machine a pocket in a hard material, a machinist has to center drill, drill, rough mill, and finish mill. These operations have to be performed in this order. If a machinist tries to plunge with the mill before drilling, the mill might slip and break. The dependency list provided in the data file captures the order in which the operations have to be performed for a single feature.

However, the dependency list is not limited to single feature considerations. Common sense machining may require that certain features be machined before others to ensure the machinist's safety (hard constraints). Also, individual machinists may have their own machining preferences (soft constraints). All of these precedence constraints (i.e. which operations should be performed before others) may be captured by both user interaction/input and intelligent hard-coded rules governing common sense machining and safety considerations. In our algorithm the hard constraint are represented by a (precedence) constraint matrix in which a value of 1 in position [i,j] denotes that operation i must precede operations j.

Repairing Infeasible Solutions

The genetic operators and the move generation strategy do not guarantee that the precedence constraints are satisfied. Thus, infeasible solutions may infect the population. A common approach to avoid violating precedence constraints is to penalize invalid tours with a low fitness value. This is a valid approach but it often requires careful selection of penalizing constants, which can itself be a difficult task. Even with appropriate penalization, the penalty function approach does not guarantee that the final solution will be feasible. The ideal solution to maintaining precedence constraints is to have genetic operators which do not violate them. Until such operators are developed, infeasible solutions in the population must be repaired. In order to preserve the robustness of the genetic algorithm, the repair mechanism must both maintain some of the feasible structure of the infeasible solution and be stochastic in nature. Given such a repair mechanism, the AG algorithm can search only the feasible realm of solutions producing high quality solutions fast. The following discussion explains an inventive repair mechanism which appears to work well for the operations sequencing problem.

Precedence constraints can be handled nicely within the framework of a precedence matrix. Consider the list of operations and dependencies found in Tables 2 and 3. The corresponding precedence matrix in which a value of 1 in position $[i,j]$ denotes a dependency on the order of operations i and j . The precedence matrix may be read as operation in row i should come before operation in column j . For example, operation 3 is performed before operation 4. The precedence matrix may also be read as an antecedent matrix in which operation in column j should come after operation in row i . An example is operation 6 should be performed after operation 5 is performed.

By transforming a simple string of operations into its corresponding precedence matrix, dependency violations can easily be recognized and repaired. Consider the solution sequence of operations $\{3,1,5,0,4,2,6\}$. The precedence matrix for this sequence is shown in Table 4. Dependency constraint violations are easily recognized by comparing the precedence constraint matrix to the precedence matrix of the solution vector. If position $[i,j]$ of the constraint matrix contains a 1, position $[i,j]$ of the solution vector's precedence matrix must also contain a 1. Examining row 4 of the constraint matrix in Table 3 reveals that operation 4 is not required to precede any other operation. However, column 4 requires operation 4 to follow operation 3. To determine if this constraint is satisfied by the proposed solution vector above, the precedence matrix of the solution vector must have a 1 in position $[3,4]$. As seen, there is a 1 located in position $[3,4]$. Thus, this particular dependency constraint is satisfied. If there had been a 0 in position $[3,4]$ of the precedence matrix, the constraint would have been violated and the solution vector would need to be repaired in order to be feasible.

The repair process may be understood through a simple demonstration. Inspecting the possible solution vector of above,

3 1 5 0 4 2 6

several precedence constraint violations are revealed. The constraint matrix requires that operation 0 come before operation 1. This is denoted by a closing bracket.

3]1 5 0 4 2 6

Violation repair is accomplished by simply placing operation 0 randomly before operation 1.

0 3 1 5 4 2 6

The constraint matrix requires operation 1 to precede operation 3 and to follow operation 0.

0[]3 1 5 4 2 6

The violation is eliminated by randomly placing operation 1 within the brackets. In this case there is only one choice.

0[1]3 5 4 2 6

Continuing, the constraint matrix reveals that operation 2 must be executed before operation 3.

0 1]3 5 4 2 6

Again, the violation is eliminated by randomly placing operation 2 before the closing bracket.

0 2 1 3 5 4 6

Next, operation 3 is required by the constraint matrix to precede operation 4 and to follow operations 1,2 and 6. Since operation 6 is furthest to the right, the opening bracket may be placed there without violating the antecedent constraints on operation 3.

0 2 1 3 5 4] [6

When this situation occurs, the brackets must be repositioned without violating any additional constraints to form a closed set. In this example, the constraint matrix dictates that operation 6 must be performed after operation 5. Therefore, it is acceptable to rewrite the solution vector placing operation 6 appropriately after operation 5 such that the brackets are closed.

0 2 1 3 5 6[]4

Operation 3 may now be placed safely within the closed brackets.

0 2 1 5 6[3]4

The above sequence of operations now represents a feasible solution vector.

Table 2.
Operation
dependencies.

Op-ID	Dep-L
0	none
1	1
2	none
3	1,2,6
4	3
5	none
6	3

Table 3. Dependency constraint matrix.

i\j	0	1	2	3	4	5	6
0	0	1	0	0	0	0	0
1	0	0	0	1	0	0	0
2	0	0	0	1	0	0	0
3	0	0	0	0	1	0	0
4	0	0	0	0	0	0	0
5	0	0	0	0	0	0	1
6	0	0	0	1	0	0	0

Table 4. Solution vector precedence matrix.

i\j	0	1	2	3	4	5	6
0	0	0	1	0	1	0	1
1	1	0	1	0	1	1	1
2	0	0	0	0	0	0	1
3	1	1	1	0	1	1	1
4	0	0	1	0	0	0	1
5	1	0	1	0	1	0	1
6	0	0	0	0	0	0	0

Cluster-Preserving Repair

Constraint violations may involve operations belonging to the same cluster (intra-cluster violation) or operations belonging to different clusters (inter-cluster violation). In carrying out the repair algorithm of the previous subsection it is imperative not to destroy the clustering. To this end, in case of an intra-cluster violation, the repair algorithm is carried out on the subset of operations constituting the cluster (intra-cluster repair), while in case of an inter-cluster violation, the repair algorithm is carried out on a string representing the sequence of clusters (inter-cluster repair). Clever methods for tagging operations by cluster id, for collapsing an operation string into a cluster string and for expanding back a cluster string into an operation string greatly facilitate the implementation of this cluster-preserving repair algorithm. In addition, in order to carry out inter-cluster repair, one needs to build the constraint matrix corresponding to cluster strings. This is done by collapsing rows and columns of the operation

constraint matrix corresponding to operations belonging to the same cluster (identified by the cluster id tag).

ILLUSTRATIVE EXAMPLE

The data file (reproduced in Table 5 below) is part of a process plan for a real part (anchor plate for the F-16). It contains the following information for each operation in the setup: Feature name (id), Operation number, Operation Name, Tool id, Coordinates of the clearing starting point, Coordinates of the clearing ending point, and Dependency list. For each operation in the setup the data file contains the following information: Feature name (id), Operation number, Operation Name, Tool id, Coordinates of the clearing starting point, Coordinates of the clearing ending point, and Dependency list. An Operation-Id has been added for easy referencing.

Table 5. Sample input data file.

OP Id	Ft-n	OP#	OP-TYPE	TOOL-id	C-S-Pt	C-E-Pt	DepL
0	PROFILE-1	11	CENTER-DRILL-NON	DLS-007	(-1.76 0.00 1.35)	(-1.76 0.00 1.35)	(0)
1	PROFILE-1	12	CENTER-DRILL-NON	DLS-007	(-0.92 1.50 1.35)	(-0.92 1.50 1.35)	(0)
2	PROFILE-1	13	CENTER-DRILL-NON	DLS-007	(0.92 1.50 1.35)	(0.92 1.50 1.35)	(0)
3	PROFILE-1	14	CENTER-DRILL-NON	DLS-007	(1.76 0.00 1.35)	(1.76 0.00 1.35)	(0)
4	PROFILE-1	15	CENTER-DRILL-NON	DLS-007	(0.92 -1.50 1.35)	(0.92 -1.50 1.35)	(0)
5	PROFILE-1	16	CENTER-DRILL-NON	DLS-007	(-0.92 -1.50 1.35)	(-0.92 -1.50 1.35)	(0)
6	PROFILE-1	17	DRILL-NON	DLS-123	(-1.76 0.00 1.35)	(-1.76 0.00 1.35)	(11)
7	PROFILE-1	18	DRILL-NON	DLS-123	(-0.92 1.50 1.35)	(-0.92 1.50 1.35)	(12)
8	PROFILE-1	19	DRILL-NON	DLS-123	(0.92 1.50 1.35)	(0.92 1.50 1.35)	(13)
9	PROFILE-1	110	DRILL-NON	DLS-123	(1.76 0.00 1.35)	(1.76 0.00 1.35)	(14)
10	PROFILE-1	111	DRILL-NON	DLS-123	(0.92 -1.50 1.35)	(0.92 -1.50 1.35)	(15)
11	PROFILE-1	112	DRILL-NON	DLS-123	(-0.92 -1.50 1.35)	(-0.92 -1.50 1.35)	(16)
12	PROFILE-1	113	DRILL-IN	DLB-005	(-0.35 0.00 1.35)	(-1.67 0.00 1.35)	(0)
13	PROFILE-1	114	R-E-MILL-NON-F&W	MLS-0996	(-0.35 0.00 1.35)	(-1.67 0.00 1.35)	(113 112 111 110 19 18 17)
14	PROFILE-1	115	FIN-END-MILL-WALL	MLS-0198	(-1.67 0.00 1.35)	(-1.67 0.00 1.35)	(114)
15	PROFILE-2	21	CENTER-DRILL-NON	DLS-009	(3.10 0.49 1.35)	(2.95 0.46 1.35)	(0)
16	PROFILE-2	22	DRILL-NON	DLS-152	(3.10 0.49 1.35)	(2.95 0.46 1.35)	(21)
17	PROFILE-2	23	R-END-MILL-F&W	MLS-0996	(3.10 0.49 1.35)	(2.95 0.46 1.35)	(22)
18	PROFILE-2	24	F-END-MILL-WALL	MLS-0198	(2.95 0.46 1.35)	(2.95 0.46 1.35)	(23)
19	PROFILE-3	31	CENTER-DRILL-NON	DLS-009	(-3.10 -0.49 1.35)	(-2.95 -0.46 1.35)	(0)
20	PROFILE-3	32	DRILL-NON	DLS-152	(-3.10 -0.49 1.35)	(-2.95 -0.46 1.35)	(31)
21	PROFILE-3	33	R-END-MILL-F&W	MLS-0996	(-3.10 -0.49 1.35)	(-2.95 -0.46 1.35)	(32)
22	PROFILE-3	34	F-END-MILL-WALL	MLS-0198	(-2.95 -0.46 1.35)	(-2.95 -0.46 1.35)	(33)
23	HOLE-1	41	DRILL-IN	DLB-005	(4.80 0.00 1.35)	(4.80 0.00 1.35)	(0)
24	HOLE-2	51	DRILL-IN	DLB-005	(-4.80 0.00 1.35)	(-4.80 0.00 1.35)	(0)

The coordinates are needed to calculate the distance the tool has to travel,. If a tool change is needed, then the machine has to go back to the tool starting point and perform a tool change. From there, it must go to the clear starting point of the next operation. If a tool change is not needed, then the tool has to travel from the end clear point of an operation to the start clear point of the next operation. Depending on the material and the feature type

machinist has to center drill, drill, rough mill and finish mill. These operations have to be performed in this order. If a machinist tries to plunge with the mill before drilling, the mill might slip and break. The dependency list captures the order in which operations have to be machined.

If this process plan was used as is, then twelve tool changes would be required. But by running this process plan through the algorithm currently implemented in AML™, a process plan that requires less tool changes is produced. This process plan will help greatly in reducing the time it takes to machine the part, and thus reducing the cost of machining it. The following are the two best sequences (listed by Operation Id's although the actual format of the output is Feature name, Tool-id, and Operation number) found by the Genetic Algorithm employing a penalty function approach:

(19, 15, 1, 2, 0, 5, 3, 4, 20, 16, 7, 8, 11, 9, 10, 6, 12, 24, 23, 21, 17, 13, 18, 14, 22), tool_travel=112.797974, tool_changes=6

(0, 5, 4, 1, 15, 19, 2, 3, 20, 16, 7, 8, 11, 9, 10, 6, 12, 24, 23, 21, 17, 13, 18, 22, 14), tool_travel=114.963272, tool_changes=7

Note that the second of these does not have the minimum number (6) of tool changes which is guaranteed by our simultaneous clustering/sequencing approach.

In contrast, the best solution (which we believe to be the globally optimal solution) found by our algorithm is:

(12, 24, 23, 15, 19, 20, 16, 5, 0, 1, 2, 3, 4, 8, 9, 10, 11, 6, 7, 17, 13, 21, 22, 14, 18), tool_travel=100.939133, tool_changes=6

The solution most commonly found by our algorithm is:

(19, 15, 23, 12, 24, 1, 0, 5, 4, 3, 2, 16, 20, 8, 9, 10, 11, 6, 7, 17, 13, 21, 22, 14, 18), tool_travel=101.247757, tool_changes=6

which is only 0.31% away from the believed global optimum). Our approach not only guarantees the minimum number of clusters, but it optimally sequences the clusters both externally and internally producing an operations sequence which minimizes tool travel. The previous GA/penalty approach appears to get trapped in a feasible solution and is not able to optimize further. As shown above, our approach is able to reduce the tool travel an additional 13.9%.

CONCLUSIONS

A review of the issues related to the integration of product design with material and process planning has been presented in the introduction to this report. The research issues have been discussed and a demonstrated solution presented. Previous systems have been designed to take input either from a GT code or from a descriptive file created by a user. In some instances, these previous systems have involved a descriptive language implemented via shape features (holes, pockets, etc.) to interpret the part geometry and convert it into a special format to generate prescribed process planning information.

We have seen a technological leap in the development of CAD systems, leading to a growing gap between design and process planning automation. AML™ is intended to close that gap and provide a process design capability which is completely automated. The process planner generates process specifications based on the part geometry, material, and process constraints. As exemplified by machining, the plan specifications are then passed to the tool path planner that generates and simulates the cutting path. The NC part program is automatically generated accounting for tool geometry, tool changes, machining data, and obstacle avoidance (fixtures). No user interactions are needed, all parameters are automatically extracted or computed. AML™ is capable of validating the recommended vise fixturing surfaces.

The methodology used for developing our general purpose clustering/sequencing algorithm is novel in that (1) it is operation based, (2) it combines the two tasks of clustering and sequencing into a single one, (3) it ensures that hard constraints are satisfied directly (not through a penalty/reward approach which, as illustrated in the example may lead to solutions of a lesser quality), (4) it allows for competing soft clustering and/or soft constraints (often resulting from user 'what-if' scenarios) between themselves or with other objectives, and (5) it is general enough to be applied at every level in the product design and process.

The implementation makes use of clever mechanisms to handle constraints, repair, etc. The illustrative example suggests its superiority over existing algorithms in solving the NP-hard clustering/sequencing problem.

The algorithm can easily be integrated into a KBDE system such as AML™. Future work will concentrate on complementing the algorithm with heuristic, experience based rules. This will allow the system to present the user with suggestions regarding alternative materials and processes and ultimately, .

REFERENCES

1. T. C. Chang, "Expert System Planning for Manufacturing," Addison-Wesley, NY., 1990.
2. Chen, C.L.P., LeClair, S.R., An Integration of Design and Manufacturing: Solving Setup Generation and Feature Sequencing Using Unsupervised Learning Approach, *J. of Computer Aided Design*, 26, No. 1, pp. 59-75, Butterworth-Heinemann Ltd London, UK, 1993.
3. S. R. LeClair, H. N. Kamhawi, and C. L. P. Chen, "Feature Sequencing in the Rapid Design System Using a Genetic Algorithm, " North America Manufacturing Research Conf., NAMRC, XXII, pp. 95-100, May, 1994.
4. M. Kanumury and T. C. Chang, "Process planning in an automated manufacturing environment", *J. of Manufacturing Systems*, 10, No. 1, pp. 67-78, 1992.
5. Caroline Hayes and Paul Wright, "Automating process planning: using feature interactions to guide search", *J. of Manufacturing Systems*, 8, No. 1, pp. 1-15, 1990.
6. K. F. Zhang, A. J. Wright and B. J. Davies, "A feature-recognition knowledge base for process planning of rotational mechanical components", *The Intl J. of Advanced Manufacturing Technology*, 4, pp. 13-25, 1989.
7. P. Prabhu and H. P. Wang, "Algorithms for Computer-Aided Generative Process Planning," *ibid.*, 6, No. 1, 1991.
8. Jonathan F. Bard and Thomas A. Feo, "The cutting path and tool selection problem in computer aided process planning", *J. of Manufacturing Systems*, 8, No. 1, pp. 17-26.
9. Y. H. Pao, F. L. Merat, & G. M. Radack, "Memory-Driven, Feature-Based Design," WL-TR-93-4021 , Materials Directorate, Wright-Patterson AFB, OH, January 1993, Case Western Reserve University, Air Force Contract Number F33615-87-C-5250, Distributed January 1993.
10. Y. H. Pao, K. Komeyli, D. Shei, S. R. LeClair, & A Winn, "The Episodal Associative Memory: Managing Manufacturing Information on the Basis of Similarity and Associativity," *J. of Intelligent Manufacturing*, 4, No. 1, pp23-32, February 1993,
11. T. E. Westhoven, C. L. P. Chen, S. R. LeClair, & Pao, Y.H., Episodal Associative Memory Approach for Sequencing Interactive Features in Process Planning, *Artificial Intelligence for Engineering Design, Analysis and Manufacturing*, 6, No. 4, pp 177-197, December, 1992.
12. Pao, Y., Komeyli, K., Goraya, T. & LeClair, S.R., A Computer-Based Adaptive Associative Memory in Support of the Design and Planning, *Intl J. of Applied Artificial Intelligence*, Hemisphere Publishing Company, Corp., New York, NY.
13. Parametric Technology, Inc., "Pro-Manufacturing", User's Manual, Waltham, MA, 1993.
14. F.T. Lin, C-Y Kao and C-C Hsu,"Applying the Genetic Approach to Simulated Annealing in Solving Some NP-Hard Problems," *IEEE Trans. on Sys., Man, and Cyb.*, 23.,No. 6, pp.1752-1767, Nov/Dec 1993.
15. Michalewicz, Z., "Genetic Algorithms + Data Structures = Evolution Programs," Springer-Verlag, Berlin Heidelberg, 1992.

INSTALLING A LASER FOR
SHADOWGRAPHIC HOLOGRAPHY
OF BALLISTIC IMPACT EVENTS
AT WRIGHT-PATTERSON AFB

William J. Turner
Graduate Student
Department of Mathematics

400 Carver Hall
Iowa State University
Ames, IA 50011-2066

Final Report for:
Graduate Student Research Program
Wright Laboratory

Sponsored by:
Air Force Office of Scientific Research
Bolling Air Force Base, DC

and

Wright Laboratory
Wright-Patterson Air Force Base, OH

August 1995

INSTALLING A LASER FOR
SHADOWGRAPHIC HOLOGRAPHY
OF BALLISTIC IMPACT EVENTS
AT WRIGHT-PATTERSON AFB

William J. Turner
Graduate Student
Department of Mathematics
Iowa State University

Abstract

Wright Laboratory is in the process of obtaining an ANSI Class 4 laser to study ballistic impact events. The laser will provide WL/FIVS with shadowgraphic holography capabilities. Before the laser can be used at WPAFB, certain facility and safety requirements must be met, and the base Laser Safety Officer (LSO) must issue a permit for the approved use of the laser in a proposed location.

Operating this laser is not an easy task, and many materials, ranging from dyes to mirrors to oscilloscopes, are required to maintain the laser. In addition, the film must be developed in a particular manner to get a good holographic image.

Once a the three dimensional image is obtained, it must be digitized to do computer analysis. Basic research on digitizing three dimensional holographic images originated at Sandia National Laboratory, but was never completed due to financial cutbacks and organizational restructuring.

Table of Contents

Abstract.....	2
Table of Contents.....	3
Table of Tables	4
Introduction.....	5
Shadowgraphic Holography.....	5
The Laser	6
Facility Requirements	6
Safety Requirements	7
Laser Eye Examinations	8
Hazard Instruction.....	9
Written Operating Instructions	9
Firing Circuit.....	11
Laser Placement and Considerations	12
Required Materials.....	13
Problems	15
Triggering	15
Making Holograms	16
Developing Holograms	17
Viewing Holograms	18
Digitizing Holograms	18
Alternative Uses.....	19

Table of Tables

Table 1: Components Delivered with System	13
Table 2: Expendable Materials for Maintaining Laser	14
Table 3: Electronics Instrumentation to Maintain Laser.....	14
Table 4: Expendable Materials for Developing Film	14
Table 5: Solution A.....	17
Table 6: Solution B	17

INSTALLING A LASER FOR
SHADOWGRAPHIC HOLOGRAPHY
OF BALLISTIC IMPACT EVENTS
AT WRIGHT-PATTERSON AFB

William J. Turner

Introduction

Wright Laboratory is in the process of acquiring a laser for shadowgraphic holography to study ballistic impact events. In particular, WL/FIVS desires holograms of the spall cloud produced by a projectile penetrating a composite target slightly above the ballistic limit (i.e., where the projectile just penetrates the target plate). These holograms will be used to determine information about the source of individual particles in the cloud. Results will be used to describe energy transfer within the ballistic impact event.

The particular laser that WL/FIVS is considering was purchased by Physical Sciences Inc. (PSI) under an SBIR contract with the Air Force and Phillips Laboratory. PSI then subcontracted to the aerophysics group at the University of Alabama in Huntsville (UAH) to operate the laser and make holograms of aluminum projectiles impacting aluminum targets.

The present task is to determine the setup and operational requirements of the laser when installed at WPAFB, and to evaluate the feasibility of digitally capturing the three dimensional image for computer analysis.

Shadowgraphic Holography

Unlike conventional holography, shadowgraphic holography consists of making a three dimensional image of an object's shadow. To make a hologram two beams of light are required-a reference beam and an object beam. The reference beam directly illuminates the film, while the object beam is directed on a diffusing reflector such that the reflected light causes the object's shadow to fall on the film. The hologram is made by recording the interference pattern made by the object and reference beams on special holographic film.

The Laser

The UAH aerophysics group is using a frequency doubled Neodymium YAG laser designed and manufactured by Continuum Inc. to make the holograms. This type of laser was selected for two reasons. First, unlike a ruby laser, it is possible to use a continuous laser of the same wavelength to view the holograms once they are made. Images will therefore be identical in size to the original objects. Viewing the film with a light wavelength other than that used to acquire the images will cause size differences in the image.

Second, a short pulse time is needed to freeze the motion of small particles traveling at high velocities. The Nd YAG laser has a pulse time of approximately 130 ps, and this pulse can freeze the motion of a $10 \mu\text{m}$ particle traveling at 6 km/s to 10% of the particle's diameter.

This particular laser is a 35 mJ pulsed laser, with a pulse repetition rate of 10 Hz, providing an output power of 350 mW. The laser has a beam diameter of approximately 0.5 cm and a beam divergence of roughly 0.6 milliradians. The above capabilities define the laser as an ANSI Class 4 laser.

The laser is water cooled using a closed water loop. This system, in turn, transfers heat to an external water system supplied by the facility, such as tap water.

Facility Requirements

This laser has certain facility requirements. First, it requires constant temperature and humidity. The laser does not have to be kept at any particular temperature, but any change in temperature can change the laser's alignment. Humidity is not a problem as long provided condensation does not accumulate on any of the mirrors or lenses. Dust is a large problem, however. The laser should be housed in a closed, air conditioned room or tent like at UAH.

The laser also requires a source of water, such as tap water, to cool the closed internal water system. In addition, the laser needs a power source supplying 208 volt, 3 phase, AC

electricity. The plug used at PSI before the laser was transferred to UAH is labeled 250V, 3 Phase, with a NEMA designation of L15-20.

A darkroom is required for film processing. The darkroom location should be conveniently near the laser for rapid developing and assessment of test results.

Safety Requirements

Because this laser is an ANSI Class 4 laser, its use must comply with all applicable requirements of AFOSH Std 161-10 and WPAFBR 161-2. The laser installation must be reviewed and approved for use on-base by 88 ABW/EMB. A permit is issued by the base Laser Safety Officer (LSO) for the approved use of the laser in a specified location. Its use must also be incorporated into the safety permit of the range and reviewed and approved by WL/DOS.

The following is a summary of some of the most significant review criteria which must be addressed:

Facility Requirements

- Define the laser hazard control area (LHCA) using the laser specifications and beam parameters
- Post each entrance to the LHCA with an ANSI Class 4 laser warning sign
- A flashing red light installed or positioned at each entrance to the LHCA
- Insure unauthorized personnel are not allowed access to the LHCA
- Cover windows and other openings to prevent reflections to uncontrolled areas
- Have appropriate laser protective eyewear available for each individual in the LHCA
- Have the ability to lock/secure each entrance to the LHCA

Personnel Requirements

- Define those individuals who are authorized to operate the laser or be present in the LHCA during laser operation
- Document requirements for initial and terminal laser eye exams
- Develop laser operation instructions and hazard notices
- Develop written emergency shutdown procedures
- Insure authorized personnel are familiar with the operating instructions and emergency shutdown procedures developed

Equipment and Setup Requirements

- ANSI Class 4 warning labels on the laser
- Electrical interlocks on laser housing
- Beam path defined and adequate beam stop in place
- Firing circuit designed to prevent unintentional firing
- Beam path free of unnecessary specular and diffuse reflection hazards
- Work area uncluttered and free of trip hazards, etc.
- Review and approval letter (signed by WL/DOS) is posted

One individual is designated as the primary operator for each permitted laser. That person is the point of contact for 88 ABW/EMB concerning all aspects of the specific laser permit. The individual must ensure that all aspects of laser safety are met. This includes ensuring that all individuals authorized to operate the laser have been provided with basic laser safety instruction, have read and are familiar with all written operating instructions, and have had a laser eye examination.

Laser Eye Examinations

Laser eye examinations are required for all military, civilian, and contractor personnel assigned duties in areas where ANSI Class 3b or 4 lasers are used. Visitors are exempted as long as they are adequately protected from the laser beam. The base Laser Safety Office interpretation of this requirement is that visitors will only observe and not operate any lasers and will be provided with and wear laser protective eyewear.

Initial laser eye examinations are required prior to working with lasers or if more than 12 months have elapsed since the last laser physical and the start of new laser duties. Termination laser eye examinations are required for personnel who will no longer be working with lasers at WPAFB because of retirement, PCS/PCA, separation, or assignment to duties which no longer involve laser operation. There are not requirements for annual or other periodic follow-up examinations.

Contractor personnel who have a laser eye examination on file with their current employer do not have to have another examination performed at WPAFB, but the person designated as the primary operator of the laser must request verification of the exam. The LSO recommends contractor personnel provide a written statement that they have a laser eye examination on file with their current employer. This statement should include when and where this examination was performed.

Laser eye examinations are given at no charge to military and civilian employees of WPAFB and to contractor personnel. The examinations are performed in the Med GP/SGPO ophthalmology clinic located in Building 40, Area B. To request an eye examination, it is only necessary to send a brief letter to 88 ABW/EMB including the individual's name, social security number, organization, office symbol, work phone number, and the type of laser(s) an individual will be working with. One letter may be used for several individuals as long as all information is supplied. The base LSO will then contact the Med GP/SGPO, which will in turn contact each individual named in the letter to schedule an examination.

Hazard Instruction

All personnel authorized to be in the LHCA during laser operation must be provided with basic laser safety instruction. This instruction can be provided by either the base LSO or WL/DOS and can take the form of lectures, question and answer sessions, films, slides, computer software, or combinations of the above.

Documentation must be kept on file that all authorized personnel have received these instructions.

Written Operating Instructions

Written operating instructions must be developed for the laser, and all authorized personnel must be familiar with them. The following is a guide for developing operating

instructions. It is not intended to be inclusive, and there may be other safety considerations which should be included for a specific laser.

1. List the name and telephone number of the individual in the organization who is primarily responsible for the safe operation of the laser and the names of any other people who have been trained, received laser eye examinations, and are authorized to operate the laser.
2. Include instructions on how to prevent the laser from being operated by unauthorized personnel (such as control measures involving the key to the laser power supply, locking the laser in a cabinet when not in use, etc.)
3. Specify what actions operators will take to ensure the LHCA is secure prior to laser firing and that no unauthorized personnel are present.
4. If applicable, include instructions to cover windows, portals, or other openings from the LHCA during laser operation.
5. Include instructions to ensure that a proper beam stop or attenuator is used so the beam is terminated at the end of its useful path.
6. If applicable, include instructions on the use of moveable barriers, partitions, curtains, or other beam enclosure devices.
7. Include specific instructions on the use of protective eyewear during laser operation.
8. In areas where different types of lasers with varying wavelengths are being used, ensure that individuals are instructed to wear the appropriate protective eyewear. A combination of protective eyewear may be required if various lasers are running simultaneously.
9. If applicable, specify what control measures are necessary when visitors or other individuals are present in the LHCA during laser firing or demonstrations.
10. Include instructions to ensure that individuals are aware of specular reflection hazards and the fact that wearing jewelry (including watches) is not permitted around open laser beam operations.
11. Advise individuals, if applicable, that viewing certain visible and near infrared laser beams with magnifying optics can increase the ocular radiation hazard and is prohibited unless appropriate attenuating filters are utilized.

12. Include instructions to ensure that individuals are aware of the fact that lasers are generally approved for operation only in the location specified on the laminated laser permit tag. Operation in other areas is prohibited unless reviewed and approved by the base Laser Safety Officer.
13. Most laser incidents occur when performing beam alignment. If applicable, include step-by-step instructions which must be followed when performing beam alignment procedures.
14. If applicable, include information and instructions on the electrical shock hazards associated with the laser. When electrical work must be performed on high voltage power supplies, two individuals should be present and both should be trained in CPR.
15. Include instructions on what operators should do in case of an emergency such as a fire, accidental injury, or a suspected overexposure to laser radiation.
16. Include instructions to notify the Base Laser Safety Officer at 257-2010 and the organization's safety representative as soon as possible following an accidental injury or suspected overexposure to laser radiation.
17. If the laser must be left unattended during operation, include specific instructions that operators shall take to ensure the LHCA is secured against unauthorized entry.
18. Some laser dyes are carcinogenic. If applicable, include instructions on what personnel protective measures shall be used to safely prepare dyes and clean up spills.
19. For ANSI Class 4 lasers, include instructions to turn on the laser warning light(s) prior to laser firing and to turn off the light(s) when the laser is not in use.
20. Include a step-by-step Emergency Shutdown Procedure as an attachment to your site-specific operating instructions for ANSI Class 4 lasers.

Firing Circuit

The firing circuit must be designed to prevent unintentional firing. Normally, this consists of some type of lock and key mechanism, and the key must be stored away from the laser to prevent someone from unintentionally turning it on.

Laser Placement and Considerations

If holograms of Range 4 (Building 63) are desired, the laser itself would have to be located in the control room. Range 4 is not sufficiently sanitary for the laser's operation. Range 4 is also too narrow to house the laser adjacent to the test arena. By placing the laser in the control room, the beam will have to be routed down range to where the hologram is to be made. Such a set-up will require boring holes in the concrete wall between the control room and the range. If beam confinement is desired, the beam could be routed through conduit to the test site. The most difficult part would be adjusting the beam within enclosed directional joints.

The proposed range in Building 22B is much cleaner, and it would be a much better choice for setting up the laser. At least in the short term, the laser could be placed on the range near where the hologram is to be made. Thus the beam would not have to be routed as far, making it simpler to direct and adjust the beam. In addition, the proposed range is very large, and a shelter might be required for the laser to help keep the environmental conditions constant at the laser.

In either range, the LHCA would have to be defined and isolated from the rest of the building. In Range 4 this would include covering the windows, while in Building 22B the range would have to be isolated from the laboratories (Rooms A113A and A113B) at the far end. Regardless of the LHCA location, electrical interlocks will have to be placed on the doors, flashing lights installed, and ANSI Class 4 warning signs posted.

Required Materials

There are many items required to run this laser. Some will be delivered with the laser as listed in Table 1. There are also many expendable materials needed to maintain the laser and develop the holograms. (See Tables 2-4.)

Table 1: Components Delivered with System

Component	#	Vendor	Catalog Number
Optical Breadboard	1	Newport	CSD-35-4
Optical breadboard stand or home built stand to achieve correct height	1	Newport	VW-3660
Mirror holders	4	Newport	MM2-1A
Post holders	4	Newport	VPH-4
Posts	2	Newport	SP-2 (6) SP-4 (6)
Beamsplitter	2	CVI Laser	BS-532.0-75-1025-45P LW-3-1037-C
Mirrors	3	CVI Laser	Y2-1025-45-P
Film holder assembly	1	In house	
Bases	2	Newport	B-2
Beamsplitter holder	2	Newport	MM2-1A
Patchbox for external triggering	1	In house	
Laser	1	Continuum	PY-61
Laser Power/Energy Meter	1	Ophir	Nova

Table 2: Expendable Materials for Maintaining Laser

Component	Vendor
Q-switch Dye No. 1	Exciton
1,2 Dichloroethane, 99.8% HPLC grade	Aldrich
Deionizing cartridge	Continuum
Hypodermic needle and syringes	Locally available
Filters for hypodermic syringes	Locally available
100 ml glass beakers	Locally available
Rubber gloves	Locally available
Balston DFU AAQ Filter	Continuum
Flash Lamps for laser	Continuum

Table 3: Electronics Instrumentation to Maintain Laser

Component
Fast Oscilloscope, 350 MHz bandwidth with 50 Ω input (Tektronix 7834 or equivalent)
Oscilloscope, 1 MHz bandwidth

Table 4: Expendable Materials for Developing Film

Elon Developing Agent	e.g., Kodak 146 3025
Sodium Sulfite, anhydrous	e.g., Fisher Chemical S430-500
Sodium Carbonate, anhydrous	e.g., Fisher Chemical S495-500
Distilled Water	
Rapid Fixer	e.g., Kodak 146 4106
Stop Bath	e.g., Kodak 146 4247

In addition, safety glasses and external triggers for the laser must be provided. The safety glasses that PSI provided for UAH are made by Glendale Protective Technologies, Inc., Lakeland, FL 33801, and they are marked with the following:

Argon/Nd-GaAs

5,000 - 11,000 nm OD > 7
35-14

850 - 1080 nm	OD > 7
750 - 850 nm	OD > 5
710 - 750 nm	OD > 3
532 nm	OD 7
190 - 520 nm	OD > 9

Also, it might be a good idea to get a second power/energy meter so that both the direct and reflected power and energy can be read at the same time. This would help insure that the correct energy is in the final pulse, and it would eliminate the need to continually reposition the meter that reads the reflected power and energy.

Problems

UAH has experienced several problems getting the laser to operate correctly. Some problems have been identified as bad hardware. (They are currently on their third controller for the laser.) According to the repairman from Continuum, most of the problems have resulted from a combination of moving the system from Massachusetts to Alabama and in training people who are not familiar with the system. Once the system is set up, these problems should disappear. (The laser does appear to now be working satisfactorily at UAH.)

Other problems involve acquiring satisfactory holograms on a consistent basis. This may be due in part to the home-built stand they are using for the optical bench. A commercially built stand would probably provide better support for the laser and diminish any vibrations that may be present (causing a change in the beam path).

Triggering

To trigger the laser externally, a pulse train at 10 pulses per second must be supplied to flash the flash lamps (necessary to provide a correct thermal environment for the laser). These pulses must go from high to low voltage. This pulsing must be done for at least 10 minutes.

Between 100 ms and 250 ms before the desired lasing, this pulse train must stop. This allows the capacitors to be recharged and keep the voltage from decaying too much. Then, approximately 275 ms before the lasing, a final flash lamp trigger pulse is supplied to the same input as the pulse train. At UAH, this final flash lamp trigger is supplied by a He-Ne laser light sheet that is interrupted by the passing projectile.

Finally, a trigger pulse is applied to the external Q-switch trigger input when the laser output is desired. Lasing will then occur less than 200 ns after this pulse. At UAH, this trigger is provided approximately 15 ms after impact. This delay allows the debris to travel approximately 7.5 cm at 5 km/s.

Making Holograms

Several factors are required to make a hologram. First, the optical paths must be stable, and there must be sufficient spatial and temporal coherence in the two beams to produce a stable interference pattern with a high fringe contrast ratio. Second, there must be correct laser power to expose the film. Third, the film must have sufficient spatial frequency capability to record the interference pattern. Finally, the hologram must be made in darkness.

Because a very short pulse laser is used, the optical elements would have to move at a velocity greater than 1 km/s to wash out the fringes. So, the stability of the optical paths is not an issue.

Because the coherence length of this laser is much less than the diameter of the film holder/diffuser, it is necessary to match the optical path lengths of the object and reference beams. To do this, PSI and UAH has used separate optical paths for the object and reference beams.

PSI and UAH are using an AGFA 8E56 film with approximately 5,000 lines per mm spatial resolution to make their holograms. This particular type of film requires an energy of 6.75 mJ is required to expose a square area of 215 cm^2 .

Developing Holograms

Because of the special film used in developing holograms, there are some special developing instructions. Two developing solutions, Solutions A and B, are required. (See *Tables 5 and 6.*) Both have a long shelf life and should be prepared in advance.

Table 5: Solution A

Chemical	Quantity
Boiling Water (distilled)	1000 ml (1 liter)
Metol (Elon) from Kodak	10 grams
Sodium Sulfite	50 grams

To make Solution A, start with boiling water. Add the Metol and stir until thoroughly mixed. Then add the Sodium Sulfite to this mixture and stir until thoroughly mixed.

Table 6: Solution B

Chemical	Quantity
Boiling Water (Distilled)	1000 ml (1 liter)
Sodium Carbonate	50 grams

To make Solution B, once again start with boiling water. Add the Sodium Carbonate and stir until thoroughly mixed.

When ready to develop the exposed film, measure equal amounts of Solutions A and B, then mix Solution B into Solution A. Then dilute 5 times with distilled water, and stir until thoroughly mixed. For instance, to make slightly less than one liter of developing solution, mix 80 ml of Solution A, 80 ml of Solution B, and 800 ml of distilled water.

The developing procedure is then performed in complete darkness. First, develop a single sheet of exposed film in the freshly mixed developer solution for 8 to 10 minutes. Then,

place it in the stop solution (Kodak 146 4247) for 30 seconds. Next, place it in the fix solution (Kodak 146 4106) for 3 to 4 minutes. Dry it using three alcohol/water mixtures for 15 to 20 seconds each. The alcohol/water mixtures are defined as follows. The first mixture is 25% alcohol and 75% distilled water. The second mixture is 50% alcohol and 50% water. The last mixture is 100% alcohol. Finally, hang up the film to dry.

Viewing Holograms

To view the holograms, a continuous laser will have to be obtained, preferably of the same wave length as the Nd YAG that makes the holograms. It is possible to view them using a different wavelength laser, i.e. a He-Ne, but there will be some scaling of the image.

The best way to view the holograms is by using the light source from which the images were generated. Then viewing the film, it should be held at the same radius as when exposed, and the light should fall on it exactly as it did during the exposure. To achieve this, it is necessary to build a holder for the film that will hold it in the same radius as it was when it was exposed and that will reflect the laser light off a ball bearing in the same fashion as was done when the images were generated.

Another scheme for viewing the hologram is to illuminate the film in exactly the opposite way as when it was exposed. This would cause the image to appear to float in the air, thus allowing cameras to get arbitrarily close to it. However, lighting the hologram in this way is much more difficult.

Digitizing Holograms

To get information about the position and velocity of spall particles, it is important to be able to digitize the image. To get all the information needed about the three dimensional spall cloud into two dimensional images, two separate views must be used. The holder for the film

(providing the correct radius) should be placed on some sort of rotational table so that the hologram can be turned by 90 degrees to get two orthogonal views.

In addition, everything in the camera's view must not reflect any light, and the laser used for viewing the hologram must be very bright. Otherwise, any light reflected off the holder or other objects can blind the camera to the hologram.

Work on digitizing a three dimensional image was previously conducted at Sandia National Laboratories under contract with the US Army before Sandia's gun range was shut down. They originally planned to use one viewing angle and focus the camera in one plane to get information about the third dimension. They then decided to modify the system to use diffuse illumination and allow for multiple viewing angles. However, the particle analysis task became much more difficult because the particle images became shadows against a speckle background, rather than bright scatters against a dark background.

Sandia NL's gun range has been shut down and its personnel have been reassigned. The man most familiar with their holography project is Bruce Hansche, who can still be contacted at SNL at 505/844-3469.

There may also be a project to digitize three dimensional images taking place at Eglin AFB under the direction of Joe Gordon (904/882-5375), but I was unable to contact him about it.

Alternative Uses

The laser may be applied to several alternative uses. For instance, it could be used as a flash for high-speed photography. The short pulse length allows standard still cameras to be used instead of more expensive high-speed cameras. This technique has been proven by both the University of Alabama in Huntsville and Sandia National Laboratory.

MODELING EFFECTS IN AIRCRAFT CONTROL DESIGN AND ANALYSIS FOR
MICROBURST PENETRATION

Eric Wemhoff
Graduate Student
Department of Mechanical Engineering

University of California, Berkeley
Berkeley, CA 94720

Final Report for:
Graduate Student Research Program
Wright Laboratory, Armament Directorate

Sponsored by:
Air Force Office of Scientific Research
Bolling Air Force Base, Washington DC
and
Wright Laboratory, Armament Directorate

September 25, 1995

MODELING EFFECTS IN AIRCRAFT CONTROL DESIGN AND ANALYSIS FOR MICROBURST PENETRATION

Eric Wemhoff
Graduate Student
Department of Mechanical Engineering
University of California, Berkeley

Abstract

The issue of controlled flight through a particularly hazardous form of windshear, called a microburst, is considered. A considerable amount of work has been done in recent years towards calculating optimal trajectories and developing guidance laws for flight through a microburst. These works typically differ in the choice of aerodynamic, dynamic, and wind shear models, as well as the problem formulation. Several of these papers are summarized and discussed with attention to these differences. Emphasis is placed on the effect of the aerodynamic modeling differences, and how inaccuracies in aerodynamic modeling might affect various results and their applicability to real-world implementation. In the future questions related to the choice of aerodynamic model will be explored in order to ascertain the validity of assumptions made in the currently existing literature, and to try to improve upon it.

MODELING EFFECTS IN AIRCRAFT CONTROL DESIGN AND ANALYSIS FOR MICROBURST PENETRATION

Eric Weinhoff

1 Introduction

Controlled flight through wind shears is important for safety of flight as well as for structural integrity of the aircraft. In general, when designing a control scheme for a particular system, a mathematical model of the system is employed in the process. Evaluation of the resulting controller may also be done using the model. The optimality of the implemented controller will depend on the deviation of the actual system from the mathematical model, the robustness of the control scheme to uncertainties in the model, and external disturbance characteristics (in this case the wind shear field).

1.1 Aerodynamic Models

In the case of control of aircraft, one of the largest sources of inaccuracy in the plant model is due to simplified or incorrect models of aerodynamic effects. Often, unsteady and nonlinear effects are left out because these terms in the model are hard to derive analytically and in closed form. Therefore design of control systems is often based on these simplified aerodynamic models, and testing is historically done either by simulation using these models (which can be inaccurate) or in-flight testing (which is expensive and dangerous).

A modern tool which may be useful in improving this situation is that of computational fluid dynamics (CFD). First, CFD is useful for the identification of aerodynamic models because realistic aerodynamic flight data can be gathered cheaply, and the flight trajectory can be controlled exactly in order to emphasize the effects one is trying to model. Secondly, CFD allows for inexpensive "flight testing". Simulations of the aircraft-controller system can be performed and evaluated to determine if and when the system does not perform as predicted by the analytic model. Because CFD produces realistic results, the insight gained from simulations should apply to actual flight conditions. Allan has used CFD for this purpose [1].

A particular area of aerodynamics which seems to have not been dealt with very carefully is that of the effects of wind shear. Wind shear, by definition, involves flight through varying atmospheric winds (both speed and direction); this may be due to variations in wind velocity in either space or time. Because the aircraft's velocity *relative* to the wind is the most important factor in determining aerodynamic forces and moments, wind shear can cause unexpected flight path deviations. Plainly, these deviations are unwanted and can be dangerous.

The nonlinear, unsteady aerodynamics associated with wind gusts is not well modeled or understood. These aerodynamics were studied extensively in the 1950's [2, 3]. Most of the progress was due to the use of linearized approximations to the aerodynamics, which allowed the linear response to sharp edge or random gusts to be calculated analytically. Since then, the nonlinearity of the full problem has prevented significant further advances in modeling. Another approach in modeling is to transform the problem of

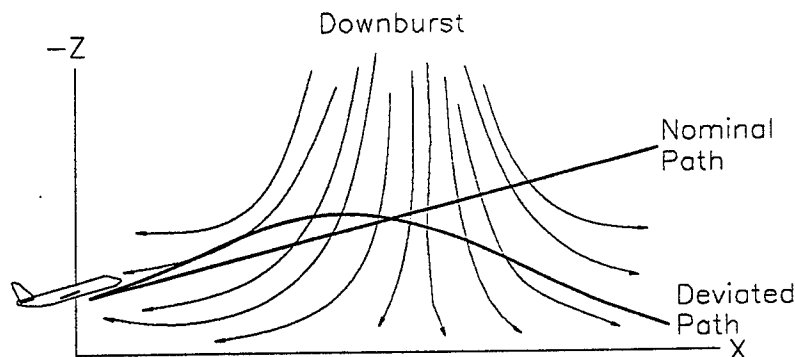


Figure 1: Microburst encounter during takeoff.

an aircraft flying through air of varying velocity to an aircraft moving through steady air with a resultant velocity equal to the actual velocity minus the velocity of the surrounding atmosphere. This method is fundamentally unsound because this is a transformation to a noninertial reference frame when the velocity of the surrounding air is unsteady (especially when the velocity time derivative or gradient is large as it may be when microbursts occur); hence the computed forces and moments will in general be incorrect.

1.2 Microburst Wind Shear

In recent years several flight incidents have been attributed to an atmospheric phenomenon known as a microburst. This is strong, highly localized wind shear that occurs when a mass of cold air descends through the surrounding air in a narrow column and then spreads out radially as it nears the ground. This situation represents a hazard for aircraft that are at low altitude, such as in a takeoff or landing situation, due to a loss of lift (which can be viewed as an air-relative energy loss). Several accidents have been attributed to this phenomenon in recent years [4, 5, 6].

The effect is even greater when the pilot acts in the standard way. In the typical flight through a microburst on a takeoff or landing path (near the ground), the aircraft first encounters a strong headwind (see Figure 1). This causes a sudden increase in airspeed, and correspondingly, lift and drag, so that the plane will rise above the flight path and groundspeed decreases. The reflex reaction of a pilot experiencing this will be to pitch down and throttle back to maintain a constant airspeed and glide path angle. As the aircraft traverses the microburst, the headwind will be replaced by a downdraft followed by a tailwind. These last two phases both contribute to a loss of lift. Even if an aircraft has the physical ability to fly through a downburst with the proper control inputs, without the correct guidance strategy the deviations from the flight path can be large and sometimes catastrophic. The problem then is how to determine what is the best control strategy for safety and/or performance in these situations.

1.3 Control Systems and Strategies

Work on control strategies for penetrating or surviving a microburst has recently been done by several groups of authors. As this work indicates, there are two basic ways one can look at the problem. The first is to determine the best possible, physically realizable, course of action for flying through a given wind field. Studies of this type use global knowledge of the velocity field, and since in a typical flight situation this information is not available, these strategies are not implementable in reality. Furthermore, for complex nonlinear problems such as this, the optimal trajectory can only be computed numerically and the resultant control history is not an explicit function of the state, hence the control is open loop and not implementable for this additional reason. These types of studies generate *optimal* trajectories, that is the trajectory which minimizes a chosen performance index, given the physical description of the aircraft and wind shear.

The second way to look at the problem of penetrating microbursts is to find control strategies which use only local wind information, and are therefore implementable. The resulting strategy is called a guidance law. The two approaches are complementary in that the optimized trajectory is the one associated with the best possible performance of the aircraft, and one would therefore like a guidance law to approximate this trajectory. See Section 6 for more details about optimal controls and guidance laws.

Some authors have taken the approach of first deriving the optimal control and associated state trajectory for a given performance index, microburst description, and aircraft model (the mathematical description of the rigid-body dynamics and aerodynamics of the aircraft). Subsequently a practical guidance scheme which attempts to mimic the optimal trajectory with only local knowledge of the windshear is developed.

Others have directly developed guidance laws (as opposed to first computing the optimal control) based on intuitive, practical ideas such as air-relative energy based feedback, and then have simulated these control schemes to determine their effectiveness [7] [8] [9].

The following groups, among others, have worked on control systems and strategies for flight control in microbursts:

- Psiaki, Stengel, et al. [10, 11, 12, 13, 14].
- Miele, Wang, Melvin et al. [15, 16, 17, 18, 19, 20].
- Bailey, Krishnakumar [7, 8]
- Zhao and Bryson [21, 22]
- Gera [9]

1.4 Overview

It is important to determine how critical the aerodynamic approximations are in control system design for aircraft (as well as many other situations involving control of fluid systems); a system that performs well in simulation using a simplified aerodynamic model may or may not perform satisfactorily in the actual implementation. There are two sides to this question: first, does the performance of a control

system designed using simplified aerodynamics degrade substantially when implemented in a physical system, and secondly could the performance of the closed loop system be improved substantially by basing the control design on more accurate aerodynamics in the first place. Note these are very similar questions, and can be called performance robustness issues.

If the effects are small, then control design based on the simpler aerodynamic models (such as the work in this area that has been done to date) should perform well and is adequate. On the other hand if the effects are large, then additional work is needed to take advantage of knowledge of these effects.

In order to ascertain the effects of the model used for control system design, the optimal trajectories based on different aerodynamic models might be compared. This should give a feel for how large an effect the aerodynamics have; if, for a given problem formulation, the optimal trajectories are substantially different, then the choice of aerodynamic model is important. This is in the sense that if the optimal trajectories differ, then for a real life windshear penetration, applying the optimal control that was based on more accurate aerodynamics should yield a lower cost function than if the optimal control based on the simpler aerodynamics was used. A question to be answered is how large the difference in cost functions might potentially be.

This difference will of course depend on the details of the problem formulation. So another interesting question is, where are the aerodynamic approximations most crucial—for instance for different flight regimes, wind models, wind fields, control laws, and flight scenarios (such as takeoff, landing, or aborted landing). This may be assessed by looking at the relative magnitude of the extra aerodynamic terms in these different situations, by comparing optimal trajectories, or by comparing resulting performance index values.

We also want to look at how a particular controller will perform in real life. This has not been done in the work on controlled flight through microbursts thus far; instead, simulations of controller performance have typically been based on the same simplified aerodynamic models which were used to develop the controller. Obviously, these simulations will not reveal poor controller performance which is due to unmodelled aerodynamics.

To find how a particular controller is going to perform in real life, one may choose to do flight testing. An easier choice, however, is to do CFD simulation, which should give very accurate results without the expense of actual flight testing. The controlled aircraft will be simulated using CFD algorithms which simulate not only the fluid motion but also the control law and dynamic response of the aircraft. Because an optimal control history is an objective result of the problem formulation which utilizes aerodynamic understanding for best results, it is a good candidate for use in comparing the effectiveness of controllers based on aerodynamic models of differing accuracy. This is in contrast to guidance laws, which typically are based mainly on engineering judgement (due to the complexity of the aircraft/wind shear system) and therefore are highly subjective. In other words, there is no obvious method for guidance law design which isolates the effects of the aerodynamic model used from the subjective features of the guidance law which are based on the designer's judgement.

As mentioned above, optimal control histories are, for a problem with complex models such as this one, open loop and therefore not suitable for implementation as control laws. We may get around this by computing the optimizing control trajectory $u(t), t \in [t, t_f]$ at each time step, where the initial condition for the optimal control problem is the current state. Only the first element in this control history is used, and at the next time step the optimal control trajectory is recomputed based on the new state of

the aircraft. Because the optimizing control is an implicit function of the initial state this is closed-loop control. Granted, this is rather computationally expensive to do and could not be implemented in real time. But it can be implemented in a CFD simulation, and provides an objective measure of the merits of basing control design on accurate aerodynamic models.

Obviously, to do any of these things, one must first know what the more accurate aerodynamic models look like. To find these models is a large task in itself where work needs to be done.

2 Aerodynamic Model Identification

It is difficult to derive accurate aerodynamic models for flight regimes where unsteady motion occurs or the aerodynamic forces are nonlinear functions of the state. The equations of fluid motion do govern the aerodynamic forces, but these equations are not suitable for use as a model of the system. This is because in general, the solutions to these equations (lift, drag, and pitching moment for longitudinal motions) are *functionals* of the entire state and atmospheric properties; that is, they depend on all past values of these variables. This infinite dimensional problem is intractable unless simplifying assumptions are made.

Tobak's indicial function method uses response functions to describe the aerodynamic force dependency on the state and atmosphere functionals [23, 3]. The following simplifying assumptions are usually made: the forces are only weak functions of motions that occurred far in the past and this dependence may be neglected, and terms that are high order in frequency are small because characteristic frequencies of the aircraft are small. With these assumptions then, the method can be used to formulate a functional form of the aerodynamic model without finding the indicial functions, which in general is a large task. This functional form contains parameters which must then be evaluated by using experimental data.

Another approach is to express the functionals as functions of the coefficients of a Taylor-series expansion of the state and atmosphere histories; this leaves another infinite-dimensional problem which again is in a form suitable for simplification. Chapman has developed this method for the general case involving unsteady motions and an atmosphere which may be varying with space and time [24]. As with the indicial function method, simplifying assumptions are introduced: rates are slow and time histories and spatial variations may be truncated to some order. Once again this leaves a functional form of the aerodynamic model which includes free parameters to be estimated.

Aerodynamic parameters may be determined in either of four ways: wind tunnel testing, ballistic range data, flight testing, or CFD simulation. A general discussion of this topic is given in [25], and methods for extracting parameters from data gathered in either of these methods are presented in [26, 27, 28]. It is difficult to estimate parameters dealing with the effects of unsteady motions and varying atmospheric properties using the first three methods because of the need to create elaborate experiments in order to gather data for these cases. In using CFD one gains the advantage of controlling the environment and maneuvers of the aircraft with relative ease, so that unsteady and atmospheric effects may be isolated. Of course, CFD is only a simulation of reality, so that results obtained must somehow be validated by any of the other methods.

Work is currently being done to program the appropriate boundary conditions and geometry for simulating wind shear by Tom Olsen at AEDC, to be continued at the University of California, Davis

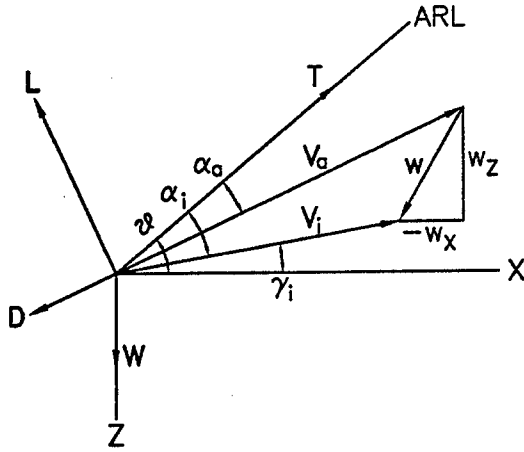


Figure 2: Geometric relationships used in the dynamics model.

[29]. For the purposes of this work, the aircraft will be a wing-tail combination based on the geometry of a large jet transport. The geometry will be a simplification of the full geometry of an aircraft yet should provide the salient aerodynamic features. The simulation of the fluid system will be three-dimensional, while the motion will be restricted to the longitudinal plane. Outer boundary conditions will be specified to simulate the effects of wind shear.

3 Control Design Issues

When computing optimal trajectories or designing guidance laws, the following choices are important and will affect results achieved and the validity of conclusions drawn (for real-life application): dynamic model; aerodynamic model; wind model; problem formulation, including the performance index, boundary conditions, and physical constraints on the aircraft; guidance law structure, when designing guidance laws.

3.1 Dynamic Model

The rigid-body longitudinal dynamics of the aircraft are modeled by six first-order equations, two equations per degree of freedom which are the horizontal position, vertical position, and pitch. Velocities may be expressed either relative to an inertial axes system or to a body-fixed system. Here we have chosen (for the moment) to represent velocities in the inertial axes; inertial-relative quantities are indicated by the subscript i , whereas air-relative quantities have the subscript a . See Figure 2 for the geometrical relationships used in the dynamic model.

The equations of motion to be used, in a form given by Psiaki and Stengel [10], are

$$m\dot{V}_i = -q_d S [C_D \cos(\alpha_i - \alpha_a) + C_L \sin(\alpha_i - \alpha_a)] + T \sin \alpha_i - mg \sin \gamma_i \quad (1)$$

$$mV_i \dot{\gamma}_i = q_d S [C_L \cos(\alpha_i - \alpha_a) - C_D \sin(\alpha_i - \alpha_a)] + T \sin \alpha_i - mg \cos \gamma_i \quad (2)$$

$$\dot{q} = q_d S \bar{C}_M / I_{yy} \quad (3)$$

$$\dot{\alpha}_i = q - \dot{\gamma}_i \quad (4)$$

$$\dot{h} = V_i \sin \gamma_i \quad (5)$$

$$\dot{r} = V_i \cos \gamma_i \quad (6)$$

along with the following geometrical relations which give the air-relative angle of attack (α_a) and velocity (V_a):

$$\alpha_a = \alpha_i + \gamma_i - \tan^{-1} \left(\frac{V_i \sin \gamma_i + w_v}{V_i \cos \gamma_i + w_h} \right) \quad (7)$$

$$V_a^2 = V_i^2 + w_v^2 + w_h^2 + 2V_i(w_v \sin \gamma_i + w_h \cos \gamma_i) \quad (8)$$

Here the aerodynamic forces L , D and M are expressed in the usual coefficient form: $L = q_d S C_L$, $D = q_d S C_D$, and $M = q_d S \bar{C}_M$; L and D are perpendicular and parallel to the air-relative velocity V_a , as usual. All of the aerodynamic modeling is expressed through the functional form of these coefficients.

In their work, Miele, Wang, Melvin et al. use a simplified form of these dynamics (with velocities expressed in body axes); they assume that the angle of attack can be specified and hence use it as the control for their problem. This simplification is accurate when the response of the angle of attack to the actual physical control (elevator angle or applied torque) is sufficiently fast compared to translational response to the actual control, provided that the aerodynamic model used is accurate for the maneuvers involved. The assumption eliminates the dynamic equations governing the pitch angle since θ and α are algebraically related; hence the airplane is a point mass. This form of the equations is also used by Zhao and Bryson.

4 Aerodynamic Model

The choice of aerodynamic model will affect the control design and performance results. Historically, aerodynamic models have been developed for the case of flight through a steady atmosphere, and are applicable in a rigorous sense only if this assumption holds. In particular, attempts to handle unsteady winds by replacing the aircraft's velocity with an air-relative velocity, while approximately correct under certain assumptions, have not been carried out rigorously. Also, due to the complexity of the infinite-dimensional fluid system, many simplifying assumptions must clearly be made if the resulting aerodynamic model is to be manageable. These usually involve the assumption that certain higher order terms are small. In the present study, we would like to improve upon the usual model; this basically involves including more of these higher order terms.

The goal is to formulate a model for the aerodynamic forces and moments which correctly includes unsteady wind effects and some higher order approximation. In order to do this we will start from an expression for the model which makes no assumptions about the effects of unsteady wind or size of higher order terms. This approach has been taken by Chapman [24] and Etkin [30].

It is reasonable to assume that in general, the aerodynamic forces on an aircraft depend on the state of the fluid system around it; this in turn can be assumed a function of the aircraft's past motion and configuration (including any changes of the aircraft which may affect the external fluid velocity field) as well as the history of the atmosphere. The motion of the aircraft at time t is specified by its

(inertial) velocity $\mathbf{v}(t)$ and its angular velocity $\boldsymbol{\Omega}(t)$. Let $\boldsymbol{\delta}(t)$ be a parameter vector which specifies the configuration of the aircraft. There are many atmospheric quantities that may effect the aerodynamics; here it will be assumed that effects due to variations in density, temperature, etc. are small, and that only atmospheric wind velocities are important. The wind velocity field is expressed as $\mathbf{w}(t, x, y, z)$, a function of time and position ρ .

Taking for example the nondimensionalized aerodynamic lift force $C_L(t)$ (other forces and moments are analogous), its functional dependence on the above quantities is written as

$$C_L(t) = C_L[\mathbf{v}(\zeta), \boldsymbol{\Omega}(\zeta), \boldsymbol{\delta}(\zeta), \mathbf{w}(\zeta, \rho)], \quad \zeta \in [0, t].$$

The lift at time t is a *functional* of its arguments and depends upon the values they took on during the time interval $[0, t]$; this is expressed by letting the variable ζ be an element of $[0, t]$. For longitudinal motion we only need to consider the x - and z - components of the aircraft and wind velocities, and the y - component of the angular velocity, q . In the present study the configuration vector $\boldsymbol{\delta}$ contains the control variables, which are elevator deflection δ_e and possibly thrust setting δ_t , so we have

$$C_L(t) = C_L[v_x(\zeta), v_z(\zeta), q(\zeta), \delta_e(\zeta), \delta_t(\zeta), \mathbf{w}(\zeta, x, z)], \quad \zeta \in [0, t].$$

A functional for C_L is not very useful for modeling; since a function may be represented by the coefficients of its Taylor series, we may replace the functional with a function by expressing each of the arguments as a Taylor series about time t and location of the aircraft at time t , $\mathbf{r}(t)$:

$$C_L(t) = C_L \left(\mathbf{v}(t), \frac{\partial \mathbf{v}}{\partial \zeta} \Big|_t, \frac{\partial^2 \mathbf{v}}{\partial \zeta^2} \Big|_t, \dots, \boldsymbol{\Omega}(t), \frac{\partial \boldsymbol{\Omega}}{\partial \zeta} \Big|_t, \frac{\partial^2 \boldsymbol{\Omega}}{\partial \zeta^2} \Big|_t, \dots, \boldsymbol{\delta}(t), \frac{\partial \boldsymbol{\delta}}{\partial \zeta} \Big|_t, \frac{\partial^2 \boldsymbol{\delta}}{\partial \zeta^2} \Big|_t, \dots, \mathbf{w}(t, \mathbf{r}(t)), \frac{\partial \mathbf{w}}{\partial \zeta} \Big|_{t, \mathbf{r}(t)}, \frac{\partial \mathbf{w}}{\partial \rho} \Big|_{t, \mathbf{r}(t)}, \frac{\partial^2 \mathbf{w}}{\partial \zeta^2} \Big|_{t, \mathbf{r}(t)}, \frac{\partial^2 \mathbf{w}}{\partial \rho^2} \Big|_{t, \mathbf{r}(t)}, \frac{\partial^2 \mathbf{w}}{\partial \zeta \partial \rho} \Big|_{t, \mathbf{r}(t)}, \dots \right)$$

Now it is usually argued that some of these terms will be small enough to drop out. For example if terms of second order and higher are left out,

$$C_L(t) = C_L \left(\mathbf{v}(t), \frac{\partial \mathbf{v}}{\partial \zeta} \Big|_t, q(t), \frac{\partial q}{\partial \zeta} \Big|_t, \boldsymbol{\delta}(t), \frac{\partial \boldsymbol{\delta}}{\partial \zeta} \Big|_t, \mathbf{w}(t, \mathbf{r}(t)), \frac{\partial \mathbf{w}}{\partial \zeta} \Big|_{t, \mathbf{r}(t)}, \frac{\partial \mathbf{w}}{\partial \rho} \Big|_{t, \mathbf{r}(t)} \right) \quad (9)$$

Notice that this may still be an arbitrary function of its arguments; nothing has been said or assumed about the functional form. Usually another Taylor-series expansion is used, this time for C_L itself in terms of its arguments. It is most beneficial to take the expansion about some reference flight condition so that higher terms in the resulting expansion will be small for small deviations from this condition. Which terms will be small and which combinations of variables to use in the model is a question to be answered through simulation or flight testing. For example, the combinations of variables V and α (velocity magnitude and angle of attack) are usually used instead of the Cartesian velocity components. Simulation using CFD could possibly be the most efficient way to find the best model.

Authors who have looked at the microburst penetration problem have used what amount to commonly used simplifications of this model in which the coefficients on the right hand side are constants,

independent of α_a and δ_e . Psiaki and Stengel include the unsteady $\dot{\alpha}$ term:

$$C_M = C_{M_0} + C_{M_\alpha} \alpha_a + C_{M_{\dot{\alpha}}} \dot{\alpha}_a + C_{M_q} q_i + C_{M_\delta} \delta_e \quad (10)$$

$$C_L = C_{L_0} + C_{L_\alpha} \alpha_a + C_{L_{\dot{\alpha}}} \dot{\alpha}_a + C_{L_q} q_i + C_{L_\delta} \delta_e \quad (11)$$

$$C_D = C_{D_0} + \epsilon C_L^2 \quad (12)$$

Miele, Wang, Melvin, et al. include terms which are nonlinear in angle of attack

$$C_D = B_0 + B_1 \alpha + B_2 \alpha^2, \quad \alpha \leq \alpha_{**},$$

$$C_L = C_0 + C_1 \alpha, \quad \alpha \leq \alpha_{***},$$

$$C_L = C_0 + C_1 \alpha + C_2 (\alpha - \alpha_{**})^2, \quad \alpha_{**} \leq \alpha \leq \alpha_{**}.$$

Although nonlinear in form, these aerodynamics include no unsteady or atmospheric gradient effects, nor even a dependence upon δ_e or q . Bailey and Krishnakumar make this same simplifying assumption.

We would like to look at results obtained with each of these three degrees of aerodynamic model complexity, give by equations (9), (10 – 12), and the last form in which the forces are functions of α only.

5 Wind Model

A model of the microburst is needed to generate optimal trajectories and also to simulate flight through the microburst. Because of recent interest in the microburst penetration problem, several studies of the atmosphere have been conducted and many analytic models of downbursts have been formulated.

Psiaki and Stengel use two models throughout their papers; one is an engineering approximation that captures gross characteristics of a typical downburst. This specifies both the horizontal and vertical winds as sinusoidal functions of the range x only (and not altitude, which real-world winds are a function of); w_x is one period of a sinusoid and w_z has a $(1 - \cos)$ form. They also use models based on wind fields measured by the Joint Airport Weather Survey (JAWS) using Doppler radar [31, 32]. These are real-world wind measurements which are typically not as smooth as analytic models for the wind. Stengel has also done work based on the Osegueda-Bowles model [33].

Miele, Wang, Melvin et al. also use an engineering approximation in [15] which is similar to that mentioned above, with the difference that w_x and w_z are linear rather than sinusoidal functions of range. In later work they add a term that is linear in altitude [18].

Zhao and Bryson [21] use an Ivan ring-vortex model in their work; it specifies a three-dimensional axisymmetric wind field as a function of range and height [34].

Finally, Krishnakumar and Bailey employ a Zhu-Etkin three-dimensional doublet sheet model [35].

Initially the Osegueda-Bowles model will be used here: it expresses wind velocities as relatively simple analytic functions, yet matches real-world wind measurements based on JAWS. The velocity field is axisymmetric along the vertical Z axis, a function of both range and height, and satisfies continuity in three dimensions.

The equations governing this model are:

$$w_x = \frac{\lambda R^2}{2x} [1 - e^{-(x/R)^2}] (\epsilon^{z/z^*} - \epsilon^{z/\epsilon}) \quad (13)$$

$$w_w = \lambda e^{-(x/R)^2} [\epsilon (\epsilon^{z/\epsilon} - 1) - z^* (\epsilon^{z/z^*} - 1)] \quad (14)$$

See Table 1 for a short description of the parameters used in these equations.

R	radius of downburst shaft
z^*	characteristic height, out of boundary layer
ε	characteristic height, in boundary layer
λ	scaling factor

Table 1: Parameters in Osegueda-Bowles downburst model.

6 Control

We would like to know, given the physical properties of the aircraft and the wind velocity field, what is the best way to fly through the wind. For instance, is it possible to survive flight through a given wind shear in a given airplane. Or, what is the maximum altitude gain possible in a given time; this criterion might be used in a takeoff situation (although it might not be the wisest choice). These are optimal control problems.

The usual way to state the general optimal control problem is:

For a system described by the state equations

$$\dot{\mathbf{x}} = \phi(\mathbf{x}, \mathbf{u}, \boldsymbol{\pi}, t)$$

find the function \mathbf{u} which minimizes

$$J[\mathbf{x}_0, \mathbf{u}] = g(\mathbf{x}(t_f), t_f) + \int_{t_0}^{t_f} f(\mathbf{x}, \mathbf{u}, t) dt$$

subject to the constraints

$$\chi(\mathbf{x}, \mathbf{u}, \boldsymbol{\pi}, t) = 0$$

$$\psi(\mathbf{x}, \mathbf{u}, \boldsymbol{\pi}, t_f) = 0$$

$$\mathbf{h}(\mathbf{x}, \mathbf{u}, t) \geq 0$$

$$\mathbf{g}(\mathbf{x}, t) \geq 0$$

In the state equation, \mathbf{x} is the state, \mathbf{u} is the control vector, and $\boldsymbol{\pi}$ is a vector of system parameters that may be optimized along with the control. For instance, in problems where the final time is variable and is to be optimized, such as landing an airplane, $\boldsymbol{\pi}$ may include final time. Here χ are nondifferential constraints on the state and control, ψ are final time constraints among the state and control, \mathbf{h} and \mathbf{g} are inequality constraints on the control and state, respectively. The cost function J can consist of an integrated part, f , and/or a penalty on the final state, g .

Given the initial state \mathbf{x}_0 , along with the functional form of the above equations, J will be a functional of \mathbf{u} and $\boldsymbol{\pi}$ only. Therefore if the problem is well posed, then a solution \mathbf{u}^* and $\boldsymbol{\pi}^*$ exists which minimizes J . The optimizing control history, \mathbf{u}^* , will be a function of t , for $t \in [t_0, t_f]$.

Problems with a different initial states will result in different control history solutions; therefore u^* is a function of x_0 . When the optimal control problem can be solved analytically, the solution u^* can be expressed as an *explicit* function of the initial state and time. This form of the optimal control is called a control law because it can be used for closed-loop feedback control, since the optimal control is specified as an explicit function of the state.

But in general, such as when the state equations contain nonlinearities or when nonlinear (including inequality) constraints are present, it is not possible to solve this problem analytically. Numerical procedures must usually be employed to derive the solution u^* . This solution will be an implicit function of the initial state rather than explicit: it depends on the initial state, but to find the control history solution for a given initial state, the optimal control problem must be solved numerically and the solution is in the form of a time history rather than a function of the initial state. In other words it is an open loop solution, and so cannot be directly applied to the real system where uncertainties are present. However, optimal control *could* be used to form a feedback controller. For instance, the controller might periodically recalculate the optimal control using the current state as the initial state in the optimal problem formulation, apply the resulting control history for some time period, and then repeat. Feedback is introduced by recalculating the optimizing control periodically. To do this requires the ability to numerically solve the optimal control problem within the selected time step, which typically would be small. This is a practical obstacle to implementation of this method in real time. Note that when CFD is used to simulate the aerodynamics this method could be used to introduce feedback control, because the simulation is not performed in real time.

Another implementability issue, for the case of an aircraft flying through a windshear, is that the optimal control solution uses global knowledge of the wind velocity field, whereas in real life only local knowledge is available with present technology (if even that). This is a fundamental obstacle to the calculated optimal control being of any practical use as controllers, until such time as sensors are available to provide global wind velocity field knowledge. A controller based on local knowledge utilizes less information than the optimal control, and therefore will be suboptimal.

Although the optimal solution cannot be implemented, it is useful as a benchmark solution against which *implementable* control laws can be compared. Implementable control laws are called guidance laws. The optimal solution, using complete knowledge of the aircraft and wind field, is the control history which does the best job possible of minimizing J . No other control, no matter how derived, could do better, where ‘better’ is of course measured by the performance index and depends upon the various equations describing the system. Therefore a guidance law which generates a state trajectory and performance which are close to that produced by the optimal control solution can be considered to generate near-optimal performance, at least for the system described by the equations that the optimal control is based upon.

7 Optimal Control Work

This section describes some work that involves the application of optimal control to the microburst penetration problem. It is an attempt to present different issues that arise in formulating and analyzing the optimal control problem. In an early paper, Psiaki and Stengel pose the optimal control problem

for several microburst penetration scenarios involving either a jet transport or general aviation aircraft in the takeoff or landing situation, using either the engineering approximation or JAWS microburst models [11]. Their general cost function contains a weighted sum of terms penalizing deviations in V_i , γ_i , q , α_i , α_a , V_a , and distance from the glide path; for the numerical solution presented, deviation from glide path is emphasized.

Also included in the cost function are “soft constraint” terms, which in effect create inequality constraints which keep the controls, δ_e and δ_t , within saturation limits, and α_a and V_a within stall limits. The form of these soft constraints are such that the controls, angle of attack, and velocity are not penalized when they satisfy the desired constraints: the penalty becomes nonzero when the soft constraints are violated. This is a reasonable way to effectively get inequality constraints by using penalty terms. (In most of the numerical algorithms used to calculate optimal trajectories, it is much easier to deal with additional penalty terms rather than inequality constraints on the state or control variables.) In contrast, some authors include a squared control term in an effort to enforce soft constraints; this results in a simpler function but is less desirable because the part of the cost function due to the control will be minimized at the expense of the actual performance component of the cost function.

The control variables used here are thrust and elevator angle. In the calculated optimal trajectories, the thrust input leads the wind, in expectation of air speed losses. Hence the ability to use global information is plainly used to obtain the trajectory. In addition, the angle of attack varies with the airspeed in order to maintain a nearly constant lift. This empirical finding is later used to approximate the optimal trajectory by a guidance law; this is one example where a general observed characteristic of the optimal trajectory and control is used as a basis for guidance law synthesis.

For a case where airspeed rather than glide path deviations are emphasized in the cost function, which is similar to a standard piloting technique, tracking of the glide path was poor. This demonstrates that the best way to transit a downburst is typically unintuitive.

The emphasis of a later paper by Psiaki and Stengel [12] is to evaluate the effects of microburst characteristics on the optimal trajectories and the ability of an aircraft to survive encounters with various microbursts. This is done by computing the optimal trajectories for microbursts of varying length scales and intensities. Their engineering approximation model for a downburst is used, the aerodynamic model has the form of equations (10–12), and both takeoff and landing are considered. The optimization problem is formulated with fixed final time, free end point, true inequality constraints to get throttle saturations and angle-of-attack limits, and penalties on the control action. As before, the main emphasis of the cost function is to penalize deviations from the intended flight path.

Different indications of the safety of a particular flight were looked at; these include maximum altitude deviation (which affects where the plane touches down in the landing case), minimum airspeed (too low an airspeed causes loss of stability, loss of control, and/or stall), vertical velocity (deviations from the intended descent or climb rate can cause undesirable ground impact), and inertial velocity (an excess of which may be dangerous when landing). Analysis showed that for a given one of these factors, some microburst length scales are more crucial than others. For instance, the minimum airspeed for an optimal trajectory tends to be lower for smaller microburst lengths; this is intuitive because there is less time to use the thrust to adjust the groundspeed as the wind changes. In other words the airspeed is more “vulnerable” to windspeed changes. The altitude deviation and vertical velocity factors are found to be most crucial at length scales between those of the short-period and phugoid oscillations for the aircraft

in question, and at microburst scales longer than this the goundspeed becomes the crucial quantity. This study demonstrates that the choice of microburst parameters will affect the assessment of the safety of the resulting optimal trajectory.

Another paper that was reviewed, by Mulgund and Stengel [14], calculates optimal trajectories for an abort maneuver in which the pilot, realizing the aircraft has flown into a downburst while landing, aborts the landing in order to increase the chances of surviving the encounter. One interesting feature of this maneuver is the transition from the landing glide path to a trajectory that carries the aircraft through the downburst; Mulgund and Stengel introduce pitch rate, elevator deflection, and rate of elevator deflection terms into the cost function to give the ability to shape this transition. For instance, large vertical accelerations and hence structural stresses are not desirable. Also in the cost function is a term which penalizes deviations from a climb rate objective. Their results indicate that some optimal trajectories may specify large angles of attack, pitch rates, and vertical accelerations, depending on the chosen cost function. It is noted that the shape of calculated optimal trajectories depends heavily on the chosen cost function and microburst severity.

The work done by Zhao and Bryson [21] differentiates between a "survival" and "performance" case during takeoff flight. As expected, a performance-oriented cost function emphasizes maintenance of the desired flight path, while a survival-oriented penalty emphasizes not hitting the ground. To promote survival, Zhao and Bryson argue that the appropriate goal is to maximize the "pseudoenergy" of the aircraft, defined as $E = h + v_a^2/2g$; here h is altitude and v_a is the air-relative velocity. The performance flight tries to minimize deviations from a desired climb rate. In both cases, a minimum altitude constraint is enforced because it is found that the optimal trajectory solution for both survival and performance flight through severe downbursts is to trade altitude for airspeed, i.e., it is more effective to increase air-relative energy by dropping to a lower altitude and increasing airspeed, rather than attempting to follow an intended flight path.

One rationale for this finding is that near the ground, microburst wind velocities tend to be smaller; therefore it is easier to fly through the microburst near the ground. As mentioned in Section 5, their choice of wind model uses potential flow elements and is fairly detailed; in particular it captures the feature of real downbursts that winds decrease near the ground. It would be interesting to see if similar results would have been obtained while using some of the simpler engineering approximations of Psiaki and Stengel or Miele et al.

Other details of the Zhao/Bryson approach include: maximum thrust is assumed and flight control begins after the aircraft has transited about a quarter of the microburst (which gives a pilot time to realize the situation and is therefore more conservative than the other studies). It is noted that the imposition of terminal constraints do not greatly effect optimal flight trajectories, except near the end time. They also note that the landing case presents a much more delicate problem; the survival goal here cannot be to simply maximize energy, because the aircraft's final goundspeed as well as descent rate must be limited in order to land safely. Hence the energy must be controlled more carefully.

Lastly, two papers by Miele et al. which present optimal control trajectories for takeoff and landing were reviewed. In their formulation of the problem the aircraft is modeled as a point mass (as mentioned in Subsection 3.1); angle of attack is the control variable. True inequality constraints are imposed on angle of attack and its derivative. Engineering approximations for the windshear profile are used which include variables for length scale and intensity but do not have a vertical wind component, only

horizontal; the aerodynamic model is described in Section 4.

For the takeoff case [15], different final-time boundary conditions are tried, involving combinations of constraints on final velocity, flight path angle, and angle of attack. Thrust is held constant at the maximum setting. The paper concentrates on results obtained from using a cost function which penalizes deviations from the desired flight path angle.

Numerical optimal trajectories are obtained which are very similar to those obtained by Psiaki and Stengel in [11]. Different final time boundary conditions primarily affect the latter half of the optimal trajectory and control the balance between final altitude and velocity. Angle of attack changes as much as .5 deg/s, most of the optimal trajectories are at angles of attack greater than 10 degrees, and significant amounts of time are spent at α_a as high as 15 degrees; for these high values the aerodynamics may be significantly different from the linear, steady aerodynamic approximation.

Another paper deals with landing [18]. For this case it is more realistic to let the thrust be a control in order to get better groundspeed control at touchdown; both constant and controlled thrust are explored. It turns out that for the controlled-thrust case, thrust is gradually decreased near touchdown, which reduces the final groundspeed. Final time is free, velocity is bounded, flight path angle at touchdown is specified, and the touchdown location is bounded; these are very realistic flight specifications. The angle of attack and thrust are subject to inequality constraints. The microburst is modeled with both vertical and horizontal wind components; aerodynamic modeling includes effects of flap setting and undercarriage position, but the form is still the simple one given in Section 4. The integrated portion of the optimal control problem cost function penalizes deviations from an intended flight path which features a flare maneuver at the end.

Numerical results are better for the case where thrust is controlled instead of held constant, as expected, because the multiple conditions imposed on the flight are more easily met. Some qualitative aspects of the optimal trajectories are also presented. A noteworthy feature of this work is that the various constraints, cost functions, and boundary conditions make this a very realistic case of landing, which is a much more detailed process than taking off. However, the dynamic, aerodynamic, and microburst models used are very simple.

8 Discussion

As stated above, the primary goal of the current work will be to assess how crucial the accuracy of the chosen aerodynamic model is when investigating the microburst penetration problem. Whenever nonlinear, unsteady, or windshear-related effects are large, one would expect that a knowledge of these terms can be used for better understanding and more efficient control efforts; the optimal control is expected to be different, and guidance law strategies might be devised which take the extra information into account.

The extra terms are nearly zero in steady, constant-wind, small-angle flight, since for these conditions the steady linearized aerodynamic model is accurate; they should be most significant in nonlinear, unsteady, and varying-wind flight regimes. For instance they will be large during rapid maneuvers such as the pull-up associated with the abort maneuver or the rapid change in angle of attack to maintain constant lift in a rapidly changing headwind. In downbursts of smaller scale or higher intensity, spatial

gradients and rates of change of the wind field around the aircraft will be larger. In addition, the larger the aircraft, the larger the spatial gradient effects will be. A further consideration is that real-life winds are not as smooth as the velocity fields resulting from engineering approximations or simple analytic models, and therefore velocity gradients and unsteady effects might be expected to be larger in real life. Because of this, another interesting comparison to make would be how important the extra aerodynamic terms are when using simple analytic models versus models that more closely approximate real-life winds, such as JAWS or other formulations with higher-frequency components.

From the discussion of previous optimal control work that has been done, it can be seen that there are many different ways to formulate the downburst penetration problem. The variations to be considered include the type of flight (takeoff, landing, or abort), cost function, control and/or state constraints, terminal constraints, and microburst model, size, and intensity. In particular the cost function may have terms involving altitude, descent rate, velocity, energy, control variables, and angle of attack, among others. The actual function chosen must reflect the final design goals, which in the case of an aircraft encountering windshear is probably safety. However the form of a cost function which penalizes "unsafe" flight is not immediately obvious and so this choice is very subjective. Concerning choice of wind shear model, the optimal trajectory should be expected to be highly dependent on the wind field, so that the more accurate, the better. The point is that in order to ascertain the importance of accurate aerodynamic modeling for optimal flight control, a good representative case or cases needs to be chosen, and then the aerodynamic model varied to find how the optimal trajectory responds.

On the practical side, one might expect that the use of more accurate aerodynamics would not lead to a great improvement in existing guidance laws or piloting strategies. This is because both current guidance laws and pilots necessarily provide "rough" control, whereas using the more accurate aerodynamic model to formulate better control strategies would be a fine tuning effect on a control scheme that is approximately correct already. The roughness is a result of the fact that guidance laws are typically designed using intuition and pilots are not capable of computing some sort of numerical control algorithm.

To put it another way, the difference between an optimal trajectory and a trajectory generated through a guidance law, in the microburst penetration problem at least, is expected to be much larger than the difference between an optimal trajectory based on the simpler versus the more accurate aerodynamics. The relative sizes of these differences, however, remains to be determined.

References

- [1] B. G. Allan, C. A. Atwood, and A. Packard. Control System Analysis in Nonlinear Flight Regimes. *AIAA Paper 94-3544*, 1994.
- [2] M. Tobak and L. B. Schiff. On the Formulation of the Aerodynamic Characteristics in Aircraft Dynamics. Technical Report R-456, NASA, 1976.
- [3] M. Tobak. On the Use of the Indicial Function Concept in the Analysis of Unsteady Motions of Wings and Wing-Tail Combinations. Report 1188, NACA, 1955.

[4] Pan American World Airways, Inc., Clipper 759, Boeing 727-235, N4737, New Orleans International Airport Kenner, Louisiana July 9, 1982. National Transportation Safety Board, Aircraft Accident Report 83/02, March 1983.

[5] R. E. Bach, Jr. and R. C. Wingrove. The Analysis of Airline Flight Records for Winds and Performance with Application to the Delta 191 Accident. *AIAA Paper 86-2227*, 1986.

[6] T. T. Fujita and F. Carcena. Analysis of Three Weather-Related Aircraft Accidents. *Bulletin of the American Meteorological Society*, 58(11):1164-1181. 1977.

[7] J. E. Bailey and K. S. Krishnakumar. Total Energy Control Concepts Applied to Flight in Wind Shear. *AIAA Paper 87-2344*, 1987.

[8] K. Krishnakumar and J. E. Bailey. Inertial Energy Distribution Error Control for Optimal Wind-Shear Penetration. *Journal of Guidance*, 13(6):944-951. November-December 1990.

[9] J. Gera. Longitudinal Stability and Control in Wind Shear With Energy Height Rate Feedback. NASA TM 3342, November 1980.

[10] M. L. Psiaki and R. F. Stengel. Analysis of Aircraft Control Strategies for Microburst Encounter. *Journal of Guidance*, 8(5):553-559, September-October 1985.

[11] M. L. Psiaki and R. F. Stengel. Optimal Flight Paths Through Microburst Wind Profiles. *Journal of Aircraft*, pages 629-635, August 1986.

[12] M. L. Psiaki and R. F. Stengel. Optimal Aircraft Performance During Microburst Encounter. *Journal of Guidance*, 14(2):440-446, March-April 1991.

[13] M. L. Psiaki and K. Park. Thrust Laws for Microburst Wind Shear Penetration. *Journal of Guidance, Control, and Dynamics*, 14(4):968-975. July-August 1992.

[14] S. S. Mulgund and R. F. Stengel. Optimal Recovery from Microburst Wind Shear. *Journal of Guidance, Control, and Dynamics*, 16(6):1010-1017, November-December 1993.

[15] A. Miele, T. Wang, and W. W. Melvin. Optimal Take-Off Trajectories in the Presence of Windshear. *Journal of Optimization Theory and Advances*, 48(1):1-45, April 1986.

[16] A. Miele, T. Wang, and W. W. Melvin. Guidance Strategies for Near-Optimum Take-Off Performance in a Windshear. *Journal of Optimization Theory and Advances*, 50(1):1-47, July 1986.

[17] A. Miele, T. Wang, and W. W. Melvin. Optimization and Acceleration Guidance of Flight Trajectories in a Windshear. *Journal of Guidance*, 10(4):368-377. July-August 1987.

[18] A. Miele, T. Wang, H. Wang, and W. W. Melvin. Optimal Penetration Landing Trajectories in the Presence of Windshear. *AIAA Paper 88-0580*. January 1988.

[19] A. Miele, T. Wang, and W. W. Melvin. Penetration Landing Guidance Trajectories in the Presence of Windshear. *Journal of Guidance*, 12(6):806-814. November-December 1989.

- [20] A. Miele, T. Wang, W. W. Melvin, and R. L. Bowles. Acceleration, Gamma, and Theta Guidance for Abort Landing in a Windshear. *Journal of Guidance*, 12(6):815–821, November–December 1989.
- [21] Y. Zhao and A. E. Bryson Jr. Optimal Paths Through Downbursts. *Journal of Guidance*, 13(5):813–818, September–October 1990.
- [22] Y. Zhao and A. E. Bryson Jr. Control of an Aircraft in Downbursts. *Journal of Guidance*, 13(5):819–823, September–October 1990.
- [23] M. Tobak and L. B. Schiff. Aerodynamic Mathematical Modeling-Basic Concepts. In *AGARD Lecture Series No. 114 on Dynamic Stability Parameters, Lecture No. 1*. March 1981.
- [24] G. T. Chapman. A Report on a Formal Approach to Aerodynamic Modeling for Store Separations and an Evaluation of Delta Correction Methodologies. Private Communication.
- [25] G. T. Chapman and L. A. Yates. Nonlinear Aerodynamic Parameter Estimation and Model Structure Identification. *AIAA Paper 92-4502*, 1992.
- [26] G. T. Chapman and D. B. Kirk. A Method for Extracting Aerodynamic Coefficients from Free-Flight Data. *AIAA Journal*, 8(4):753–758, April 1970.
- [27] H. L. Stalford. High-Alpha Aerodynamic Model Identification of T-2C Aircraft Using the EBM Method. *Journal of Aircraft*, 18(10):801–809, October 1981.
- [28] M. Sri-Jayantha and R. F. Stengel. Determination of Nonlinear Aerodynamic Coefficients Using the Estimation-Before-Modeling Method. *Journal of Aircraft*, 25(9):796–804, September 1988.
- [29] T. Olsen. Private Communication.
- [30] B. Etkin. *Dynamics of Flight*. John Wiley, New York and London, 1959.
- [31] W. Frost and H. P. Chang. Simulated Flight Through JAWS Wind Shear: In-Depth Analysis Results. *AIAA Paper 84-0276*, 1984.
- [32] W. Frost, H. P. Chang, K. L. Elmore, and J. McCarthy. Microburst Wind Shear Models from Joint Airport Weather Studies (JAWS). Federal Aviation Administration, PM 85-18, Washington, DC, June 1985.
- [33] R. M. Osegueda and R. L. Bowles. A Simple, Analytic Three-Dimensional Downburst Model Based on Boundary Layer Stagnation Flow. NASA TM 100632. 1988.
- [34] M. Ivan. A Ring-Vortex Downburst Model for Flight Simulations. *Journal of Aircraft*, 23(3):232–236, 1986.
- [35] S. Zhu and B. Etkin. Fluid-Dynamic Model of a Downburst. University of Toronto, UTIAS Rept. 271, CNISSM 0082-5255, Toronto, Canada, 1983.

**NEURAL NETWORK APPROXIMATION OF DYNAMIC VISCOSITY--
IMPROVING THE QUALITY OF COMPOSITE STRUCTURES**

Richard M. Salasovich
Graduate Student
Department Of Electrical And
Computer Engineering

University Of Cincinnati
Cincinnati, OH 45221

Final Report For:
Graduate Student Research Program
Wright Laboratories

Sponsored By:
Air Force Office Of Scientific Research
Bolling Air Force Base, DC

And

Wright Laboratories

September 1995

**NEURAL NETWORK APPROXIMATION OF DYNAMIC VISCOSITY--
IMPROVING THE QUALITY OF COMPOSITE STRUCTURES**

Richard M. Salasovich
Graduate Student
Department Of Electrical And
Computer Engineering
University Of Cincinnati

Abstract

Various attempts are made to apply adaptive schemes to improve the quality of composite structures. On-line identification and approximation methods are explored to identify processing parameters and approximate dynamic viscosity in autoclave curing of composites. Problems encountered with each method are discussed. Dynamic viscosity of thermoset resin (generated by the Strother Dynamic Model) is approximated using a discretized multilayer neural network.

NEURAL NETWORK APPROXIMATION OF DYNAMIC VISCOSITY-- IMPROVING THE QUALITY OF COMPOSITE STRUCTURES

Richard M. Salasovich
Graduate Student
Department Of Electrical And
Computer Engineering
University Of Cincinnati

Introduction

The application chosen for this adaptive control study was autoclave curing of composite materials. In the manufacture of polymeric composites, tows of fibers (which are usually composed of glass or graphite) are either laid side-by-side unidirectionally or woven into a fabric. Then, they are impregnated with a polymeric resin and partially cured in order to improve handling characteristics. Layers of this prepreg are stacked to form the shape of the desired part and enclosed in a vacuum bag. The assembly is then placed in an autoclave where heat and pressure are applied to lower the resin viscosity so that the polymer fully coats the fibers. This initiates an exothermic reaction in the resin which is called a cure. The process is complete when the polymeric resin is fully cured.

Current models for the curing of polymeric resin are very complicated and require precise definition of chemical reaction kinetics. Therefore, the goal of this study is to simulate proposed cure procedures for new resin systems using a simple model. Various approaches for on-line identification and approximation are explored: identification of a second-order linear model; identification of the Strother Model; approximation by the polynomial method; and approximation by a multilayer neural network.

Procedure

Approach 1: For the initial effort, an attempt is made to model the curing of a part in an autoclave as a second-order linear ordinary differential equation:

$$\dot{T}_{\text{resin}} = A_1 T_{\text{resin}} + B_1 T_{\text{autoclave}} \quad (1)$$

$$\dot{V} = A_2 V + B_2 T_{\text{resin}} \quad (2)$$

with T=temperature, V=viscosity, and A₁, B₁, A₂, B₂=time varying parameters. This approach is abandoned because it simplifies the problem to the point that it becomes meaningless. It was determined that equations (1) and (2) are unrealistic in modeling the cure of resin. Also, the A₂ parameter can not be readily sensed on-line. It must be inferred from other data (i.e. dielectric constant) and is somewhat imprecise, thereby introducing excessive error in an adaptive scheme.

Approach 2: The Strother Dynamic Model for thermoset resins is used in the following four approaches. For new resin materials, process development centers around resin viscosity and reaction rate for a given processing condition. Only after making a “good” test part does heat of reaction and optimum cure time become critical. The Strother Macrokinetics Model predicts resin reaction before the gel point. Isothermal gel time for a resin is given by:

$$GelTime = ae^{bT} \quad (3)$$

where T=temperature and a and b are matrix dependent constants. During any small time increment (dt) the Gel Fraction (amount of reaction that has occurred) can be expressed as:

$$GelFraction = G = \frac{dt}{ae^{bT}} \quad (4)$$

so:

$$\dot{G} = \frac{1}{ae^{bT}} \quad (5)$$

The dynamic case (temperature changing over time) is treated as a series of isothermal steps. The gel fraction for each step is calculated. The reaction fraction (total amount of reaction that has occurred) is the sum of these gel fractions over the dynamic range.

$$ReactionFraction = \sum GelFraction \quad (6)$$

When the reaction fraction equals 1 then the matrix has gelled. The viscosity profile of a resin system heated linearly at 2-3°C/min is generally a U-shaped curve, as shown in Figure 1 of Appendix A. For the left leg of the U, little chemical reaction has occurred and the classical inverse relationship of temperature and viscosity for the starting resin is observed. The right leg of the U represents a more complex case. Significant reaction has occurred, therefore the viscosity increases. At the same time system viscosity is decreasing due to increasing temperature. Strother proposes the total resin viscosity be modeled as a simple mixture:

$$Ns = K1e^{K2(1-RF)/T} \quad (7)$$

$$Nr = K3e^{K4RF/T} \quad (8)$$

$$N_{total} = Ns + Nr \quad (9)$$

where Ns =starting resin viscosity; Nr =reacted product viscosity; N_{total} =total resin viscosity; RF =reaction fraction; T =temperature; and $K1, K2, K3, K4$ are resin dependent constants. These equations predict the system viscosity at any temperature and reaction fraction up to the system gel point. Applying them beyond the gel point produces erratic results. The Strother Model is coded in MATLAB as shown in Appendix A. This generates data needed for the adaptive schemes.

Using the Strother Model, an attempt is made to use on-line identification techniques to estimate the parameters $a, b, K1, K2, K3, K4$. However, the system can not be linearly parameterized as:

$$\dot{y}(t) = -ay(t) + br(t) \quad (10)$$

because the states are functions of logs and exponents.

Approach 3: Next, on-line approximation is attempted using the polynomial method. As seen from Figures 2 and 3 of Appendix A, the inputs to the polynomial method (temperature and reaction fraction) continually increase. In order to guarantee persistency of excitation so that the parameters will converge to their real values, the cure cycle of the autoclave has to be driven unrealistically hard. Even if this were implemented, parameter convergence might not occur because the cure process is such a slowly migrating one. Therefore, the polynomial method is abandoned.

Approach 4: On-line approximation is attempted using a multilayer neural network. However, this is not realizable because reaction fraction can not be calculated continuously with the adjustable weights.

Approach 5: Finally, an off-line discretized multilayer neural network is implemented to approximate resin viscosity as a function of temperature. The equations for a 2 layer feedforward neural network are given in Appendix B, along with the neural network architecture of Figure 4. These are coded in MATLAB as shown in Appendix B. Inputs (temperature and reaction fraction) are generated using the Strother Model shown in Appendix A. Data sets of 12 and 113 exemplars were used to train networks with 3, 6, 9, 12, and 15 neurons. The output is viscosity. The magnitudes of the inputs and outputs vary by orders of magnitude (temperature=50-175°C; reaction fraction=0-1; viscosity=3-15,000 poise). These values have to be normalized to between zero and one so that the network can be trained effectively.

Otherwise, training takes an excessively long time. Even with data normalization, the error never converged to < 0.05 with up to 14 hours of training.

Results

An example of Viscosity vs. Temperature and Error vs. Epoch is given in Figure 5 of Appendix B. Networks with 3, 6, 9, 12, and 15 neurons are trained to ten-thousand epochs with 12 and 113 data sets. Error values are given in Table 1. Error is seen to decrease with increasing number of neurons, however it also increases the training time.

Data Sets	# Neurons	Error
12	3	1.92
12	6	1.72
12	9	1.62
12	12	1.49
12	15	1.42
113	3	22.68
113	6	16.58
113	9	15.98
113	12	14.92
113	15	14.85

Table 1. Error Values After 10,000 Epochs

Conclusion

Various approaches for on-line identification and approximation for autoclave curing of composites are explored: identification of a second-order linear model; identification of the Strother Model; approximation by the polynomial method; and approximation by a multilayer neural network. The Strother Model is coded to generate data sets to train a discretized 2-layer feedforward neural network. The network is trained with 3, 6, 9, 12, or 15 neurons and data sets consisting of 12 or 113 exemplars. It is determined that increasing the number of neurons improves the error. The trained network can be used to predict dynamic viscosity during the autoclave cure cycle.

References

LeClair, S. R. "Qualitative Process Automation." *Int. J. Computer Integrated Manufacturing*, 1989.

Strother, R. K. "Elementary Empirical Process Modeling For Thermoset Resins." *Proceedings of the 31st International SAMPE Symposium and Exhibition*, 1986.

Zurada, J. M. Introduction To Artificial Neural Systems. West Publishing Co., 1992.

Appendix A

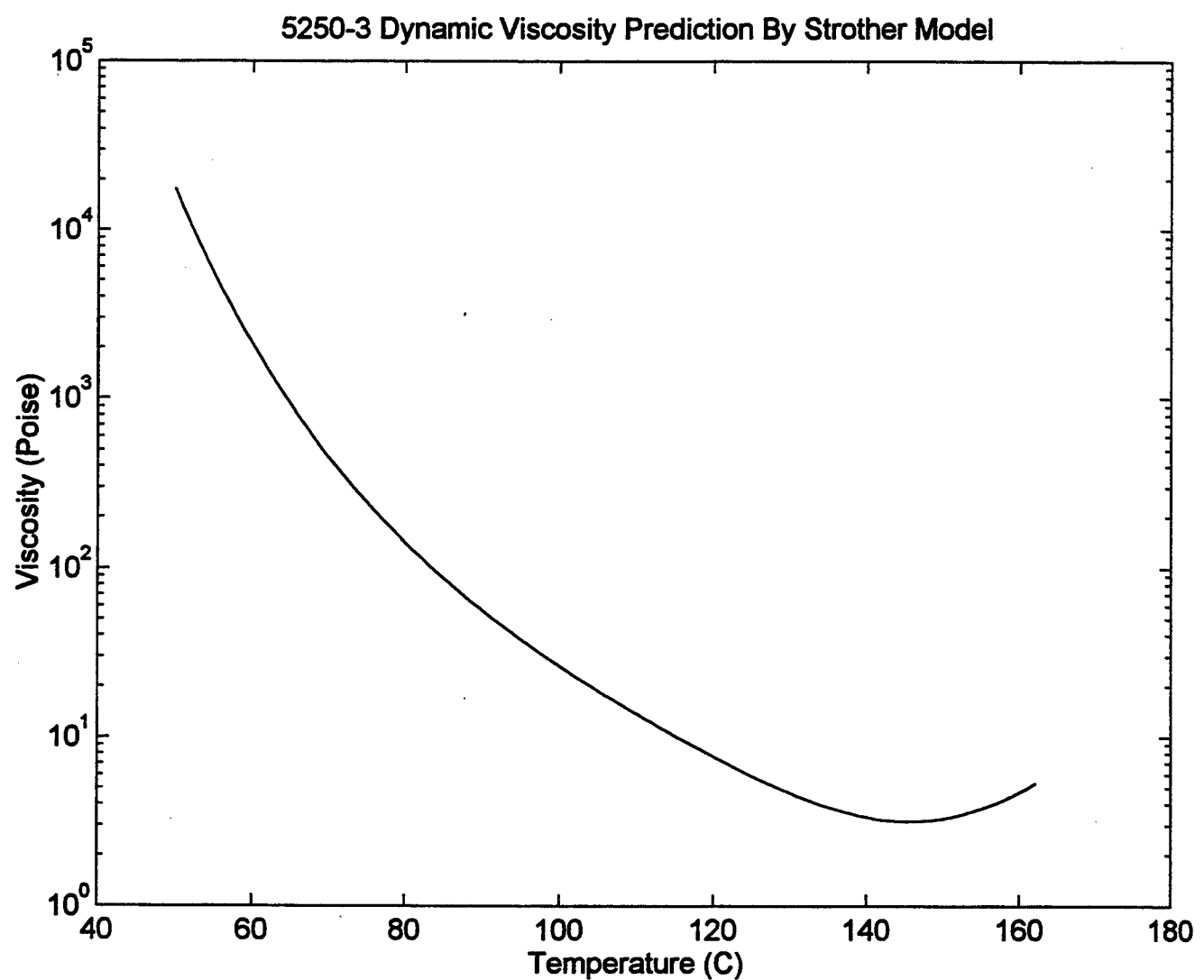


Figure 1

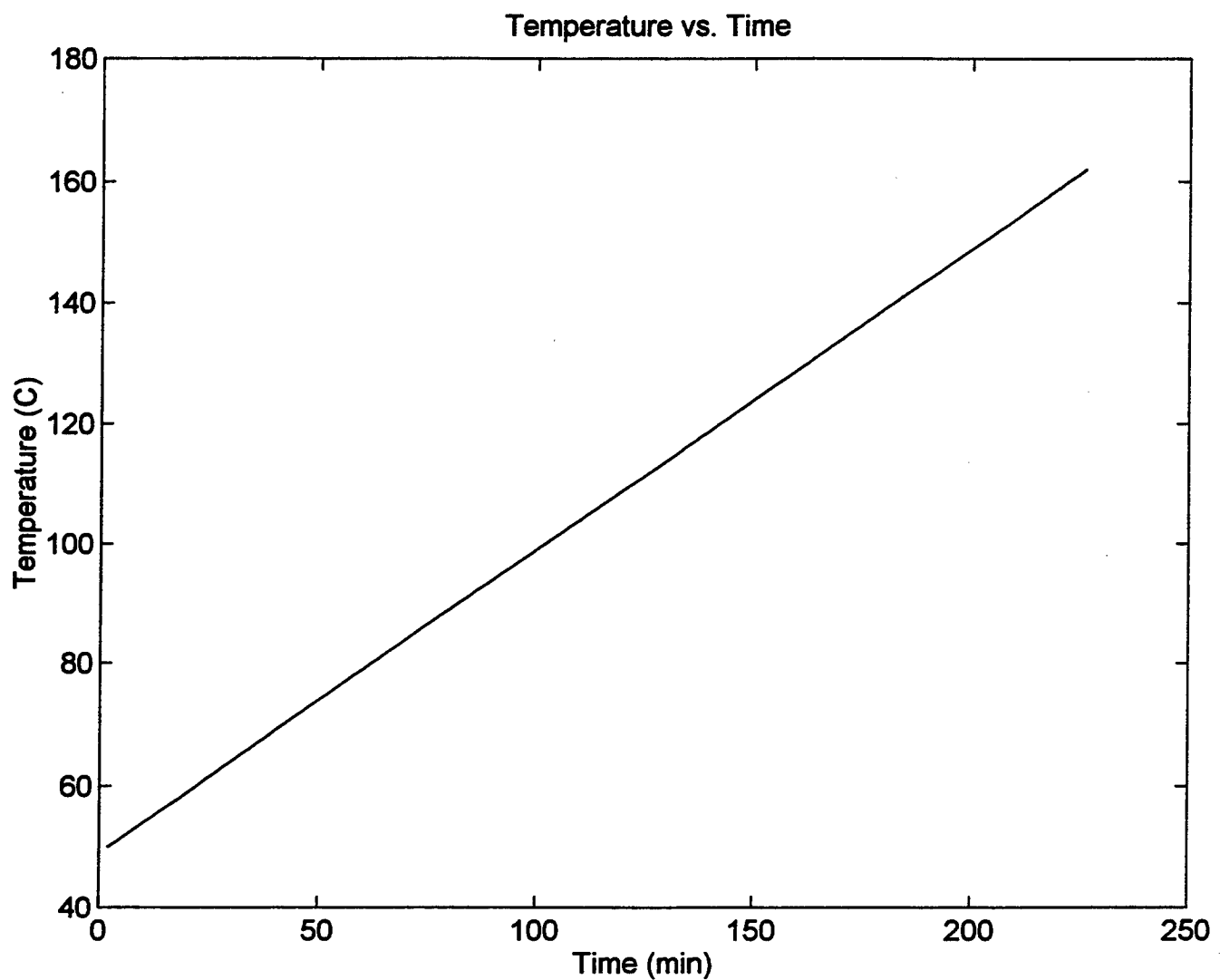


Figure 2

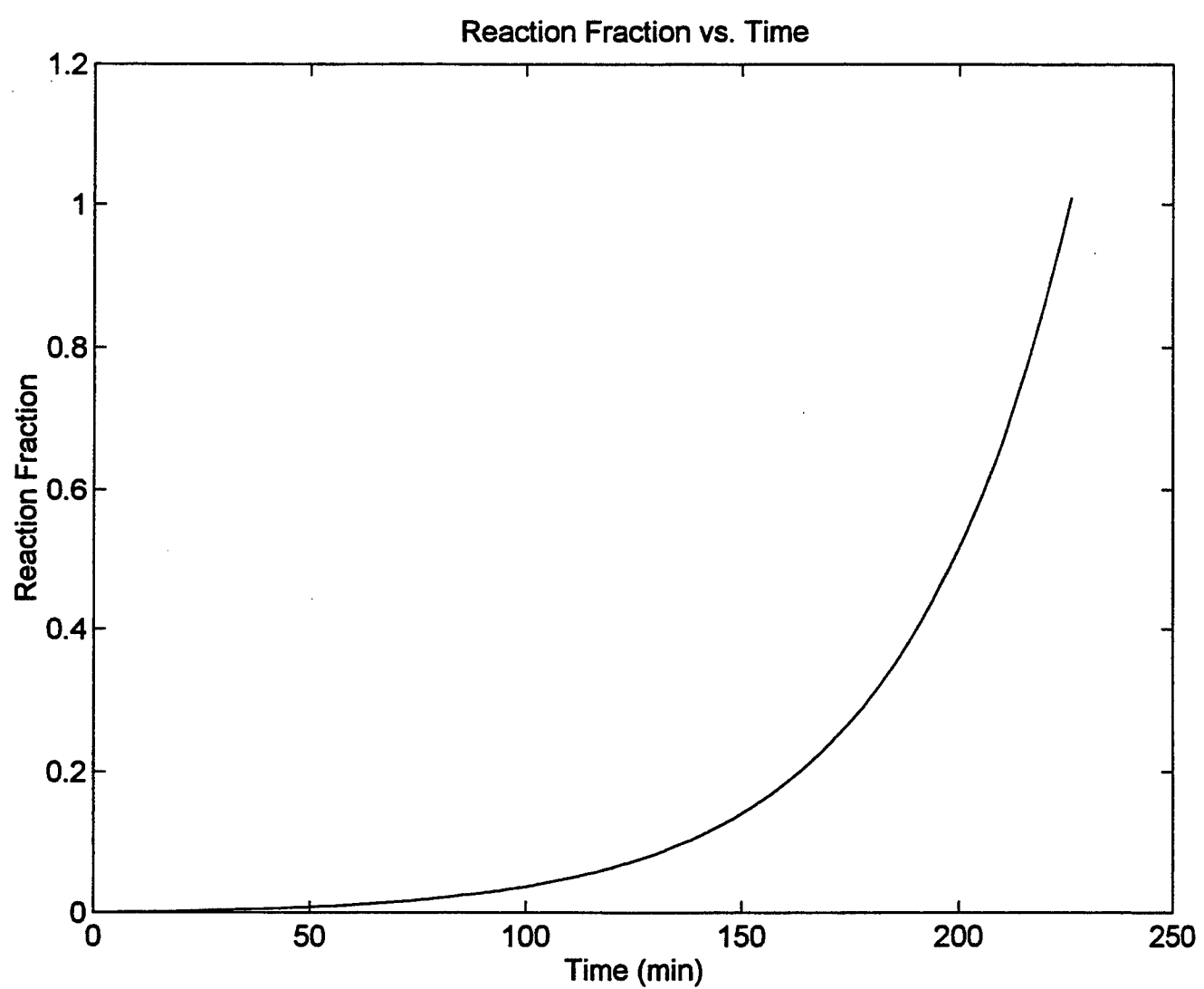


Figure 3

```

% Viscosity Prediction By Strother Model

clear;
a=83333; b=-0.0512; R=2;
K1=0.0579; K2=631.4423; K3=1.2649; K4=229.0746;
RF=0;
TT1=[50,62.5,75,87.5,100,112.5,125,137.5,150,162.5,175];
VV1=[11000,1700,200,45,17,6,3,2,2.5,7,60];
p=polyfit(TT1,VV1,10);
T=50:175;
VV2=polyval(p,T);

for count=1:size(T,2)
    if RF<1
        RF=RF + 1/(a*exp(b*(T(1,count) + R/2)));
        junk(1,count)=count;
        junk(2,count)=T(1,count);
        junk(3,count)=RF;
        junk(4,count)=RF/T(1,count);
        junk(5,count)=VV2(1,count);
        Nm=K1*exp((K2*(1-RF))/T(1,count));
        Nr=K3*exp((K4*RF)/T(1,count));
        Ns(1,count)=Nm + Nr;
    end
end
semilogy(junk(2,:),Ns(1,:))
title('5250-3 Dynamic Viscosity Prediction By Strother Model')
xlabel('Temperature (C)')
ylabel('Viscosity (Poise)')
junk1=[junk(1,:)',junk(3,:)',junk(4,:')];
junk2=[junk(1,:)',junk(5,:')];
junk3=[junk(2,:)',junk(3,:)',Ns(1,:')];

function xdot=viscous(T,x)
a=83333; b=-0.0512;
xdot=[1/(a*exp(b*T))];

```

Appendix B

2-Layer Feedforward Neural Network Equations (3 Neurons)

Input Data Set : $\begin{bmatrix} T \\ RF \end{bmatrix}$ (2 x 113) Output Data Set: $[V]$ (1 x 113)

$$ybar = A \begin{bmatrix} T \\ RF \\ 1 \end{bmatrix} \quad (1 \times 3)$$

$$y = \begin{bmatrix} \sigma(ybar) \\ 1 \end{bmatrix} \quad (1 \times 4)$$

$$\sigma(ybar) = \frac{2}{1 + e^{-\lambda ybar}} - 1 \quad (1 \times 3)$$

$$zbar = Cy \quad (1 \times 4)$$

$$V = \sigma(zbar) \quad (1 \times 1)$$

Adjust Weights:

$$\Delta_{output} = \frac{1}{2}(V_{actual} - V)(1 - V^2) \quad (1 \times 1)$$

$$C = C + \delta \Delta_{output} y \quad (1 \times 4)$$

$$\Delta_{hidden} = \frac{1}{2}(1 - y^2)(C \Delta_{output}) \quad (1 \times 4)$$

$$A = A + \delta [\Delta_{hidden} [T \quad RF \quad 1]]^T \quad (3 \times 3)$$

Use these weights to step through all input data sets

$$Error = \sum |V_{actual} - V| \leq 0.05 \quad (1 \times 1)$$

Neural Network Architecture

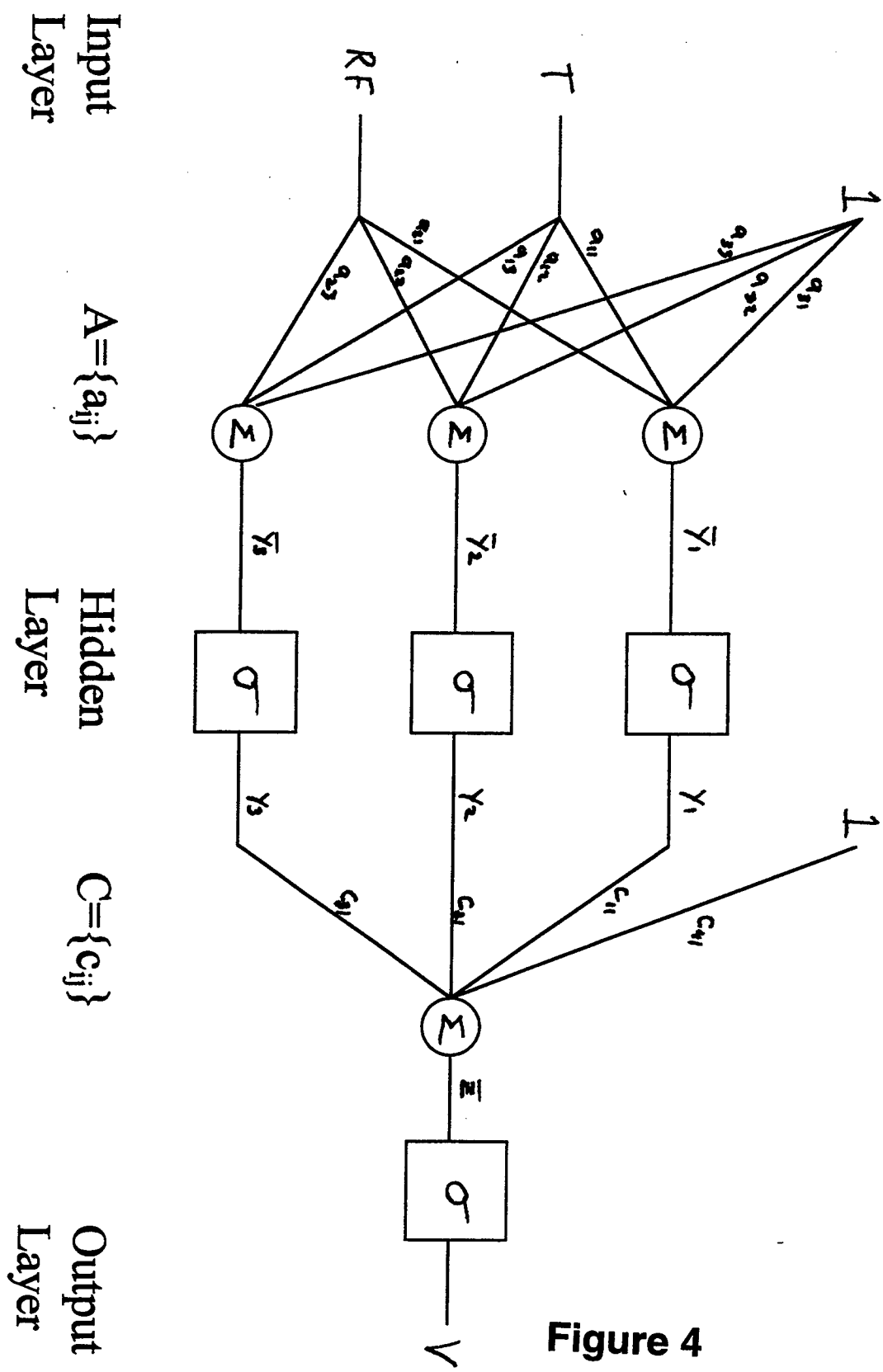


Figure 4

```

% Multilayer Feedforward Neural Network

clear;
load data2.ascii;          % exemplars
z = data2;
P = 12; % number of exemplars
addz = ones(1,P);
z = [z;addz]; % inputs with bias input
load d2.ascii; % desired output
I = 2; % number of inputs
J = 3; % number of hidden
K = 1; % number of outputs
n = 0.01; % learning rate
errmax = 0.05;
lam = 1.0;
V = (rand(I+1,J)-0.5)*2; % weights from input to hidden
W = (rand(J+1,K)-0.5)*2; % weights from hidden to output
error = 100.0 % initialize error
k1 = 1; % indicates exemplar to use for training
epoch = 0;
while error > errmax;
    for cou = 1:1000
        y = V' * z(:,k1); % hidden neuron output
        y = ( 2.0 ./ ( 1 + exp(-lam .* y)) ) - 1;
        y(J+1,1) = 1; % bias for hidden neuron
        o = W' * y; % network output
        o = ( 2.0 ./ ( 1 + exp(-lam .* o)) ) - 1;
        delout = 0.5 .* (d2(:,k1) - o) .* (1 - o.^2);
        delhid = (0.5 .* (1 - y.^2)) .* (W * delout);
        W = W + (n .* (delout * y'))';
        V = V + (n .* (delhid(1:J) * z(:,k1)''));
        if k1 >= P
            k1 = 0;
        end
        epoch = epoch + 1;
        k1 = k1 + 1;
        error = 0;
        k2 = 1;
        while k2 <= P;
            y = V' * z(:,k2); % hidden neuron output
            y = ( 2.0 ./ ( 1 + exp(-lam.* y)) ) - 1;
            y(J+1,1) = 1; % bias for hidden neuron
            o = W' * y; % network output
            o = ( 2.0 ./ ( 1 + exp(-lam .* o)) ) - 1;
            out(k2) = o;
            error = error + sum(abs( o-d2(:,k2) ));
            k2 = k2 + 1;
        end
        track(epoch) = error;
    end
    plot(track)
    sum(abs(d2-out))
    out
    epoch
end
out

```

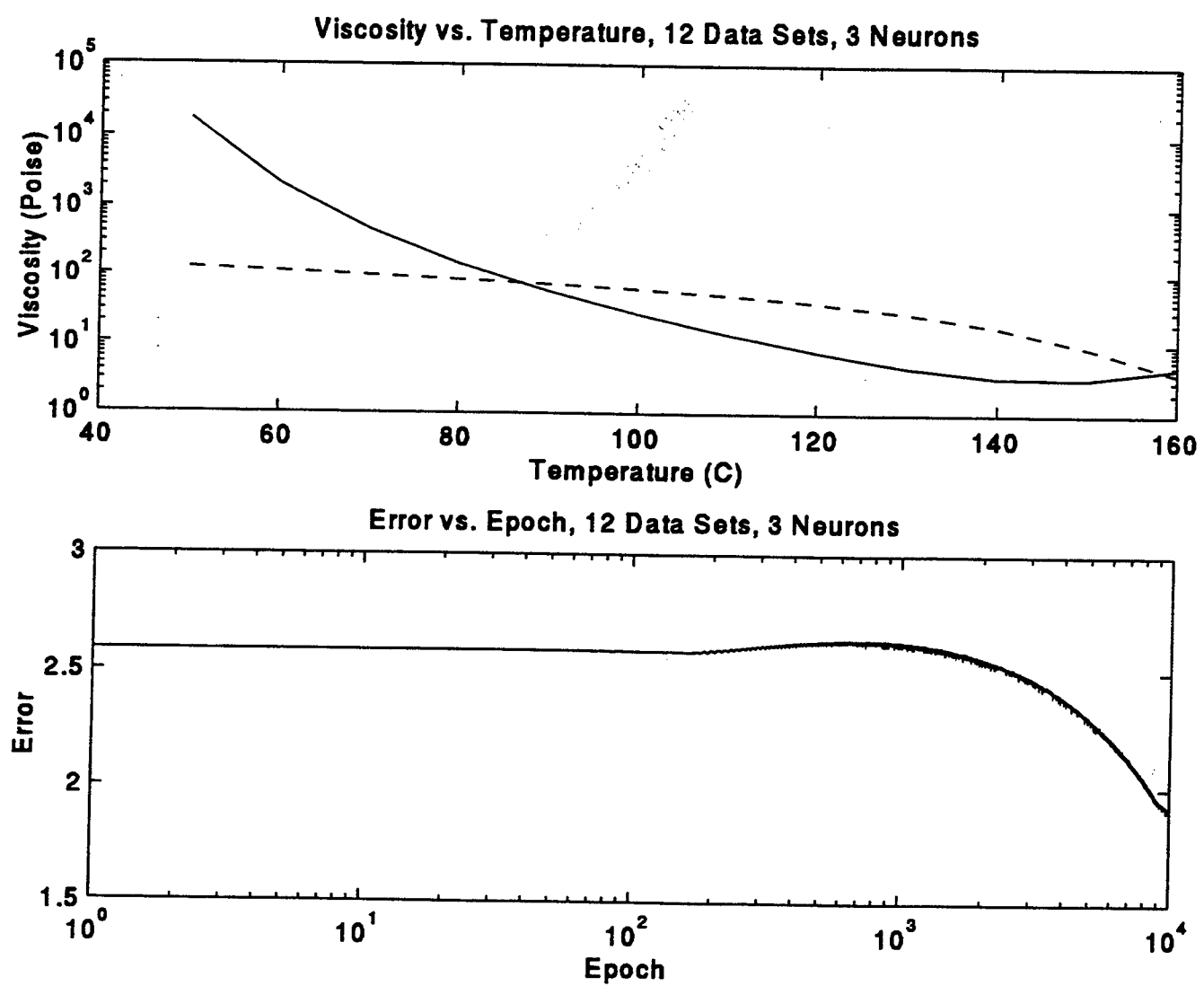


Figure 5